THE UNIVERSITY *of* EDINBURGH

Sensitivity Projections for Hidden Photons and Axion-like Particles in the LUX-ZEPLIN Experiment

Athoy Nilima

Doctor of Philosophy
The University of Edinburgh
Feb 2020

Dedicated to

My mom,
holding whose hands my passion for physics has evolved;

My mom-in-law,
whose words of inspiration enabled me to fight against all odds;

and

Jewel,
my beloved husband,
for being by my side, always ...

Abstract

The particle nature of dark matter is one of the yet unresolved puzzles in contemporary physics. The properties of dark matter, as revealed by several types of cosmological evidence, are inconsistent with the Standard Model of particle physics and imply a new physics beyond. The multi-ton scale, low threshold LUX−ZEPLIN (LZ) experiment aims to detect prospective dark matter particles, particularly the weakly interacting massive particles (WIMPs), by their interactions with liquid xenon nuclei. Apart from WIMPs, LZ is also sensitive to dark matter candidates that may interact with atomic electrons, e.g. the hidden photons (HPs) and the axion-like particles (ALPs). The sensitivity of rare dark matter searches, however, is critically limited by the unavoidable detector backgrounds – the majority of which sit in the electron recoil (ER) band. An accurate modelling of ER backgrounds with a proper treatment of the atomic binding is thus crucial, particularly for the low energy ER searches. The present work addresses some of these exciting issues (e.g. the studies of solar neutrino and low energy electromagnetic backgrounds) in the context of the LZ detector and evaluates the sensitivity reach of the experiment (for 5600 kg fiducial volume and a 1000 live-day run) for HPs and ALPs in the $2 - 70\ keV/c^2$ mass range.

Lay Summary

Cosmological evidence strongly suggests that the ordinary matter (i.e., neutrons, protons etc.) of the visible world contributes only about 5% of the total mass of the Universe. The rest of the universe consists of mysterious ′invisible′ substances called dark matter (26.5%) and dark energy (68.5%). Being non-interactive with electromagnetic radiation, dark matter is invisible to the entire electromagnetic spectrum and hence the name ′dark′. Despite the well-accepted fact of its existence, very little is known about the particle nature of the dark matter. The properties of dark matter, as revealed by several types of cosmological evidence, are inconsistent with the Standard Model of particle physics and imply a new physics beyond.

A wide range of new particles often appear in BSM theories, and many of them fit well within the dark matter paradigm. Direct detection experiments like the Large Underground Xenon (LUX) and LUX−ZEPLIN (LZ) projects aim to detect prospective dark matter particles, mainly the weakly interacting massive particles (WIMPs), by their interactions with liquid xenon nuclei. Apart from WIMPs, several other dark matter candidates, such as hidden photons (HPs) and axion-like particles (ALPs) can also be probed via their interactions with atomic electrons in the detecting medium. The sensitivity of rare dark matter searches, however, is critically limited by the unavoidable detector backgrounds. The majority of the backgrounds are of electron recoil (ER) type, i.e. they interact with atomic electrons. Accurate modelling of the ER backgrounds (e.g. solar neutrinos and trace radioactivity in various detector components) with a proper theoretical treatment of the atomic binding is thus crucial in HP/ALP searches.

This thesis addresses some of these exciting issues in the context of the LZ detector and evaluates the sensitivity reach of the experiment for HPs and ALPs in the $2 - 70\ keV/c^2$ mass range.

Acknowledgements

"If I have seen further it is by standing on the shoulders of Giants."

-Sir Issac Newton, letter to Robert Hooke, 1675.

Yes, Newton said it all – knowledge is cumulative. My first and foremost gratitude is, therefore, to all great minds in the history of physics, without whom I would not be here conducting research on dark matter in the first place.

I express my heartfelt gratitude and deepest appreciation to my PhD supervisor, Professor Alex Murphy, for his patient guidance and encouragement throughout the past three and a half years. He is the most optimistic person I have ever seen – his positive outlook, insightful comments and advices at each and every stage of my work supported me to make this dissertation finally possible.

I would like to extend my sincere thanks to Professor Franz Muheim, my second supervisor, for his continuous support and compassionate feedbacks on my progresses throughout the PhD. Many thanks to Professor Peter Clarke and Dr Matthew Needham, for their advices and critical evaluations of my work in the annual reviews.

It was the *journey of a lifetime* to work within EdiDM, the dark matter research group at the University of Edinburgh. My heartfelt thanks to all EdiDM members, past and present, especially Dr. Paolo Beltrame, who has been a reliable mentor in the first few months of my first year, and Maria Francesca (Dr. Maria Francesca Marzioni), who was the best ′senior′ a PhD student can ever hope for. Thanks to Xin (Dr. XinRan Liu), Nicolas, Chiara and Ellen – it was a pleasure to work with you all. There were times when things did not turn out the way I hoped: codes got bugs, jobs got killed, results got crazy and an epic fight of physics, math, statistics and coding algorithms began in my head. The best thing of PhD is to have someone to share all these work stress with, and Elizabeth was that someone for me. My heartfelt thanks to you, Elizabeth, for being a true ′physics′-sister.

Thanks to the entire Particle Physics Experiment (PPE) group, including them whom I shared the PhD office with: Mahdi, Jenn, Emmy, Matt, Emily, Elena and others. Elena – I will miss our late evening ghost-chats in the empty office.

Working in a big science collaboration was a dream of my younger self. Thanks to each and every member of the LUX-ZEPLIN (LZ) collaboration – it was a real honour to work with you all.

I express my sincere gratitude to the Commonwealth Scholarship Commission in the UK, for granting me the prestigious Commonwealth PhD Scholarship. Both of my grand-dads, *Dada* and *Nana* were Commonwealth scholars and it is a real honour to be their successor.

No word will suffice to express my indebtedness and love for my grandparents (*Dada*, *Dadi*, *Nana*, *Nani*). *Dada* and *Dadi*, although I can't share the happiness with you in person, I know you see me from somewhere beyond the sky with blessings in your heart. *Nana* and *Nani*, my heartfelt thanks for your unconditional love and inspiring words over phone throughout the entire time. *Choto Dada* (my grand-uncle) and *Choto Dadi*, my life in the UK would be incomplete without your blessings and love. I will cherish all our times together – the festivities of Eid, celebration of Christmas and many more.

I express my appreciation to the entire Bangladeshi Community in Edinburgh – especially Dickens *Vaia* and Fancy *Apu* who treated us a family from the very first day we met. Koly – words are insufficient to say how much I will miss you and our coffee-trips. Mumu – thanks a lot for your inspiring words over the last few months, I will miss you. A big ′thank you′ to all my friends back in Bangladesh – Pinky, Runa, Proma, Monon, Rumi, Abonty, Nitun, Aurin, Anne, Monika and all others who never got tired to make me smile by their texts over the messenger. A special appreciation goes for my student and friend Gergana, whose diligence has always encouraged me.

My deepest tribute to them who left us while I was here – my great grand father (*Boro Abba*), my eldest uncle (*Boro Fupa*), my aunt (*Mejo Fupi*) and many others. I could not be there in your last days, but you were in my heart, you are and will always be.

Ammu (mom), *Abbu* (dad), *Ma* (mom-in law) and *Baba* (dad-in-law), words are not enough to thank you for your love, affections and the sacrifices you made for me, my dreams and my aspirations. Thanks to *Ammu*, for being there when everyone else laughed at my dream of being a physicist. Thanks to *Ma*, for embracing my dream at once and making it your own. And thanks to Jewel, my beloved husband, whose constructive guidance, unconditional love and continuous support encouraged me to complete this incredible journey – together.

Contents

List of Figures

List of Tables

Chapter 1

Dark Matter: an Introduction

Overwhelming evidence from cosmology and astrophysics indicates that dark matter (DM) exists. Yet, very little is known about the true particle nature of DM. None of its properties, as inferred by cosmology, fits well within the framework of Standard Model (SM) – pointing to a beyond the Standard Model (BSM) nature. Numerous SM extensions and BSM theories exist in the literature that hypothesise yet-undiscovered particles and many of these particles, e.g. weakly interacting massive particles (WIMPs), hidden photons (HPs) or axion-like particles (ALPs) are also viable DM candidates. The validity of any of these theories can only be confirmed by direct observation of the associated DM candidate. The multi-ton scale, low threshold LUX-ZEPLIN (LZ) detector is a cutting-edge direct detection experiment that aims to serve this purpose by searching for dark matter interactions with liquid xenon (LXe) nuclei (e.g. nuclear recoils by WIMPs) or atomic electrons (e.g. electron recoils by HPs and ALPs).

Given the weak couplings and nearly-at-rest nature of galactic DM, detecting a rare DM interaction is not a straightforward task. A wise selection of target material with an appropriate mass, sufficient background suppression (by state-of-the-art reduction techniques and by going deep underground) and a precise background modelling are essential to enhance the detector sensitivity. Alongside the search for the unseen, direct detection experiments also offer complementary research opportunities to study new physics of already-known particles, e.g. neutrinos. The potential of next generation dark matter experiments like LZ to study neutrino interactions or measure solar neutrino flux is of increasing interest.

This PhD dissertation addresses some of the above aspects, mainly the electron recoil (ER) background modelling, solar neutrino-electron scattering studies and HP and ALP sensitivity projections with the LZ detector.

1.1 Cosmological evidence for dark matter

1.1.1 Dynamical evidence

The first dynamical estimate of the amount of dark matter in the universe was put forward by Lord Kelvin more than a hundred years ago, in his Baltimore lectures (1904) [1]. Consider a simple spherical closed surface S of radius r and volume V with numerous moving bodies within. Let M be the sum of all masses within S and ρ be the mean matter density. The simplest scenario one can imagine is that all the bodies distributed within S had been at rest for twenty five million years[†††]. For $r = 1\ parsec^{*} = 3.09 \times 10^{16}\, m$, $M = 1000 M_{\odot}{}^{\dagger}$ and a uniform normal force on the surface S, bodies on or near S would experience an inward gravitational acceleration of

$$\begin{aligned} Q &= \frac{1000 M_{\odot}}{r^2} = \frac{1000 \times 3.24 \times 10^5 \times M_{Earth}}{(3.09 \times 10^{16}\, m)^2} \\ &= \frac{3.24 \times 10^8 \times (r_{Earth})^2 \times g}{(3.09 \times 10^{16}\, m)^2} \\ &= 1.37 \times 10^{-13}\, km/s^2, \end{aligned} \tag{1.1}$$

using $r_{Earth} = 6.37 \times 10^3\, m$, $g \approx 1000\, cm/s$ and a unit universal gravitational constant ($G = 1$). The equation results in a velocity of $4.32 \times 10^{-6}\, km/s$ per year. According to this calculation, if there are 1000 million[‡‡‡] ′Sun-like′ celestial bodies in S, the root mean square velocity of the distribution by today should be around 50.4 km/s, a value similar to the experimentally measured velocities of visible stars. But the masses of the visible stars alone do not add to the mass of a thousand million ′Suns′, thus indicating a huge mass discrepancy. Kelvin attributed this discrepancy to some apparent ′dark bodies′ in the galaxy which the telescopes could not ′see′.

No matter how fascinating Kelvin's idea was, Henri Poincare disagreed with him [4], immediately by arguing that as the velocity deducted by Kelvin matched

[†††] A controversial [2] estimate of the age of the Earth in Lord Kelvin's time.

[*] parsec: the distance at which one astronomical unit (AU) (1 AU =distance from the Sun to the Earth= 149.6 million km) subtends an angle of one arcsecond ($\frac{1}{3600}$of a degree).

[†] $M_{\odot}$: 1 Solar Mass= 2×10^{30} kg. It was estimated as $3.24 \times 10^5 \times M_{Earth}$ in Kelvin's time.

[‡‡‡] Another estimation by Lord Kelvin of the visible universe [3]. Note that the current estimate is 250 ± 150 billion stars in the Milky way.

that which was observed, there should not be any ′dark matter′. This was the first explicit use of the term ′dark matter′, interestingly, by someone who did not believe in ′dark matter′ himself.

1.1.2 Galaxy clusters

The first major observational hint came with the work of Swiss-US astronomer Fritz Zwicky in 1933. While studying red-shifts of the Coma cluster with Hubble and Humason's data [5], Zwicky noticed [6] a velocity dispersion (1000 km/s) unusually larger than expected (80 km/s). Though Hubble and Humason were already aware of this peculiar fact, it was Zwicky who first investigated this problem using the virial theorem. His analysis arrived at a surprisingly high mass-to-light ratio which he discussed later in his famous 1937 paper [7].

The virial theorem is a technique to calculate the time averaged kinetic energy $\langle K_T \rangle$ of a stable system of N particles as

$$\langle K_T \rangle = -\frac{1}{2} \sum_{k=1}^{N} \langle \vec{r_k} . \vec{F_k} \rangle, \tag{1.2}$$

where $\vec{F_k}$ is the total force on the k-th particle with a position $\vec{r_k}$. For a stable galaxy cluster, the virial theorem simply yields

$$\langle V_{ir} \rangle = -2 \langle K_T \rangle, \tag{1.3}$$

where $V_{ir} = \sum_\sigma \vec{r_\sigma} \, . \, \vec{F_\sigma}$ is the virial of the cluster and indices σ refer to individual galaxies within. Applying Newton's inverse square law to the intergalactic gravitational interactions, one can identify V_{ir} as E_P, the total gravitational potential energy of the cluster. Equation 1.3 can thus be rewritten as

$$\langle E_P \rangle = -2 \langle K_T \rangle = \sum_\sigma M_\sigma \langle v_\sigma^2 \rangle, \tag{1.4}$$

where v_σ is the velocity of the mass M_σ. For an uniform distribution of galaxies throughout a spherical cluster of radius R, Zwicky determined [7] the total mass of the cluster, $M_{cluster}$ to be

$$M_{cluster} = \frac{5R\overline{\overline{v^2}}}{3\Gamma}, \tag{1.5}$$

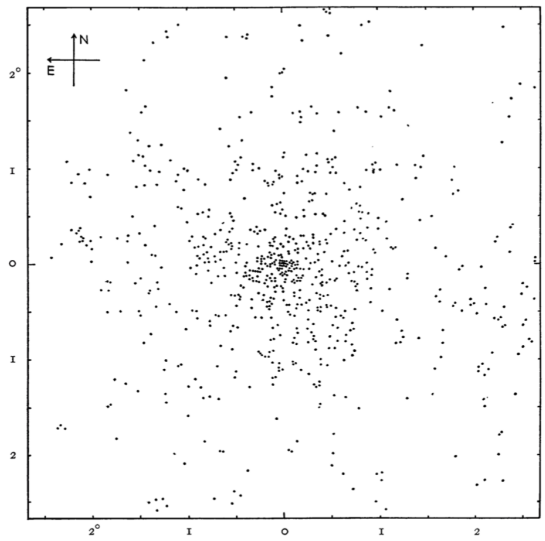

Figure 1.1: *Distribution of galaxies (represented by dots) in the Coma cluster, as used by Zwicky in his original paper [7]. The axes represent angular co-ordinates on the sky.*

where

$$\sum_{\sigma} M_{\sigma} \langle {v_{\sigma}}^2 \rangle \equiv M_{cluster}\, \overline{\overline{v^2}}, \tag{1.6}$$

and the double bars indicate a double average taken over time and over mass. The symbol Γ refers to the universal gravitational constant (G, by the convention used today).

However, in reality, galaxies are distributed non-uniformly within a typical cluster, e.g. the Coma cluster studied by Zwicky (fig 1.1). In such cases, the lower limit of $M_{cluster}$ becomes

$$M_{cluster} > \frac{R\overline{\overline{v^2}}}{5\Gamma}. \tag{1.7}$$

Observational data, however, do not provide velocities v of individual galaxies, rather they give the velocity components v_s along the observer's line of sight. For spherically symmetric velocity distributions, the approximation $v_s \approx \frac{1}{3}v$ leads to

$$M_{cluster} > \frac{3R\overline{\overline{v_s^2}}}{5\Gamma}. \tag{1.8}$$

The Coma cluster has around 1000 component galaxies. Using observational values of v_s for the Coma cluster, a lower bound for the average mass of a component galaxy becomes

$$(M_{Coma})_{avg} > 4.5 \times 10^{10} M_{\odot}\,. \tag{1.9}$$

This was a surprising result because the observed luminosity ($8.5 \times 10^7\ M_\odot$) of an average galaxy is far much smaller, leading to a mass-to-light ratio as

$$\gamma \approx 500\,. \tag{1.10}$$

This huge discrepancy could not be accounted for as being due to the approximations made in above calculations. Zwicky tried several other corrections and methods to resolve this problem, but either they further enhanced the γ or led to contradictory and unphysical solutions. Similar conclusions were also arrived by other contemporary researchers, including Sinclair Smith (1936) [8] and Martin Schwarzschild (1954) [9]. Despite all ongoing controversies [10] at the time, it is this work that is now recognised as providing the first compelling evidence for the existence of dark matter.

1.1.3 Galactic rotation curves

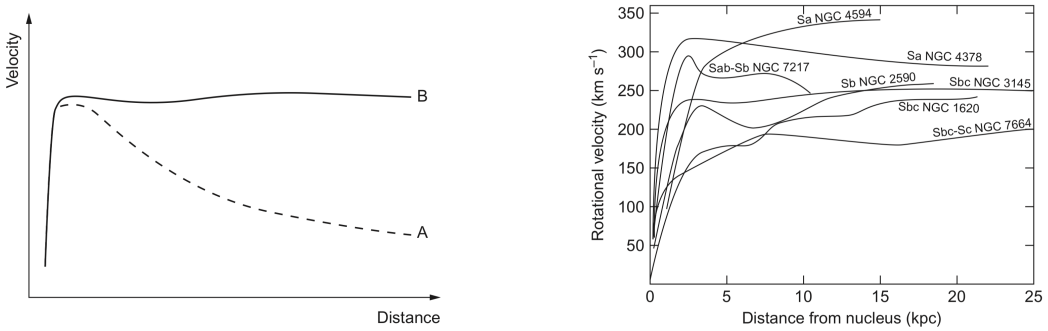

Figure 1.2: *(a) Rotation curve of a typical spiral galaxy: predicted (A) and observed (B). Figure Courtesy [11].*
(b) Rotation curve of seven galaxies from V. Rubin's original paper [12].

The peculiar irregularities in the mass-to-light ratios of individual galaxies were first noticed by Lundmark [13] in 1930. A few years later, Babcock (1939) and Oort (1940) also noticed a radial increase of mass-to-luminosity ratio in a galaxy instead of the expected Keplerian decrease [14, 15]. A series of similar analyses followed, by different groups of astronomers including Kahn and Woltjer [16], Freeman [17], and Rogstad and Shostak [18] in the next few decades. However, the major breakthrough came in the late 70s, by American astronomers Rubin and Ford. Their revolutionary studies of spiral galaxies with a new sensitive spectrograph [12, 19] revealed an approximately linear increase of galaxy mass with radius, well beyond the galactic bulge that contains the visible celestial bodies. A schematic representation is shown in fig. 1.2a where curves A and B

depict predicted and observed rotation curves, respectively, for a typical spiral galaxy. Fig. 1.2b shows the rotational curves for seven galaxies as originally published by Vera Rubin in her famous 1978 paper [12].

Spiral Galaxies consist of a flat, rotating disk containing stars, gas and dust, and a central concentration of stars known as the bulge. Most of the mass of the galaxy has to be in the galactic bulge near the centre and the stars and gas in the disk portion should orbit the centre at decreasing velocities with radial distance from the galactic center. From a Newtonian point of view, the velocity is expected to scale as $1/\sqrt{r}$, r being the radial distance, just by equating the gravitational and centripetal forces acting upon it. Thus, one should expect a rotation curve much like the curve A in fig. 1.2a , unike B, the observed flat one. A reasonable solution to this inconsistency is the existence of an unseen dark matter, alongside the known visible ones.

1.1.4 Gravitational lensing

Another robust piece of evidence for dark matter came through the development of gravitational lensing, a technique based on the bending of light around massive bodies. Followed by Lodge's first use of the term ′lens′ [20], Russian physicist Orest Chwolson in 1924 provided an argument [21] that if the source of light is distant enough, a massive body can deflect the light to produce observable images. Even Zwicky, in his famous 1937 paper, also discussed the possibility of using gravitational lensing to measure total mass of large galaxy like structures.

In general relativity, a massive object (or more generally, the presence of any matter or energy) bends the space-time fabric and this curvature manifests itself as the gravity we know. If a light ray moving along its light-like geodesics (i.e. the curve of ′shortest length′) encounters a massive object, the curvature of the space-time around the object will cause the light ray appearing to be ′deflected′. If the object is massive enough, it can converge several light rays toward a single point, i.e. the observer, and effectively acts like a lens. This is similar to the lens theory in classical optics, the main difference being that the source, object and observers should be at cosmological distances for the effect to be detectable.

When a single massive ′lens′ deflects light to a large deflection angle and produces largely distorted images of distant galaxies, it is called a strong lens. Strong lensing often results in multiple images, arcs or even in Einstein's rings and

allows the modelling of mass distribution of the lens from the distortion geometry. Weak lensing, in contrast, consists of multiple faint lensing effects caused by the intervening matter. Weak lensing manifests itself through minute distortions of distant galaxies and serves as a means of mapping dark matter density distributions.

Figure 1.3: *Composite X-ray (Pink)/ optical image of the Bullet cluster. Blue area shows the distribution of mass as determined by gravitational lens analysis. (Images from: X-ray: NASA/CXC/CfA/ M.Markevitch et al.; Lensing Map: NASA/STScI; ESO WFI; Magellan/U.Arizona/ D.Clowe et al. Optical: NASA/STScI; Magellan/U.Arizona/D.Clowe et al.).*

A noteworthy example is the Bullet Cluster (1E0657-56) [22], which was formed by the collision of two galaxy clusters about 150 million years ago. When two clusters collide, stars are not affected by the collision because of the enormous distance in between. They simply pass next to each other with slightly changed accelerations or velocities. On the other hand, the intracluster gas-dust plasma interacts more strongly, leading to heating and the formation of shocks. These hot gaseous halos emit energies in the x-ray regime, allowing them to be detected by x-ray space telescopes (pink regions in fig. 1.3). The visible stars can be seen in the usual optical images (white spots in fig. 1.3).

If dark matter did not exist, the intracluster plasma would be the dominant part of the total mass of the cluster and hence would be the dominant contributor to the lensing effect. But the mass distribution (shown by the blue region in fig. 1.3) responsible for weak lensing effect of Bullet cluster shows that this is not the case, supporting the existence of the ′unseen′ dark matter.

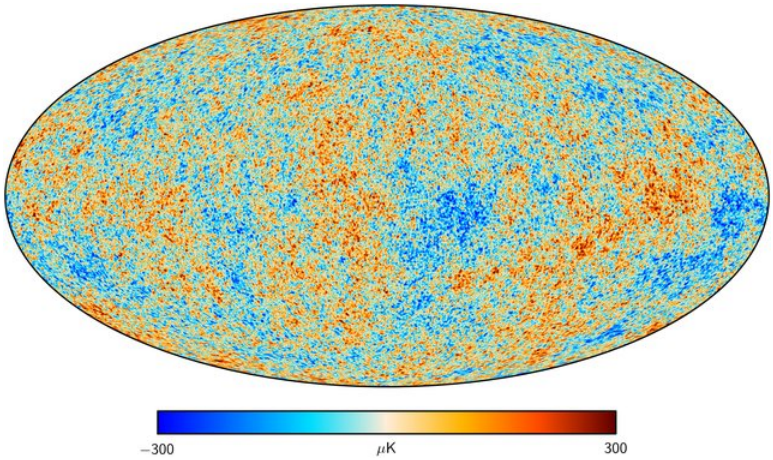

Figure 1.4: *All-sky map of the CMB temperature based on Planck's 2013 data [26]. The z-axis represents the CMB temperature.*

1.1.5 Cosmic microwave background (CMB) anisotropies

The cosmic microwave background (CMB) is the almost-uniform black body thermal radiation that comes from all directions in space. First predicted [23] by Alpher and Herman (1948) and later rediscovered independently by Zel′dovich and Dicke in the early ′60s, the CMB was firmly proposed to be a detectable phenomenon in a brief paper by A. G. Doroshkevich and Igor Novikov, in 1964 [24]. In the same year, Penzias and Wilson, with the Dicke radiometer constructed by them at Bell Telephone Laboratories, made their first measurement clearly showing the presence of CMB [25], which brought them a Nobel Prize in physics in 1978.

The origin of the CMB is associated with the recombination era in early cosmic history. This was the epoch when the previously hot, dense and opaque universe had cooled down to a temperature $\sim 3000\,K$[‡] allowing electrons and protons to (re)combine[§§§] into hydrogen atoms. The photons which were unable to travel freely beforehand were finally released (′photon decoupling′). These photons are visible today, red-shifted ($z = 1100$) due to the expansion to a temperature of $\sim 2.73\,K$. The CMB signal first observed by Penzias and Wilson in 1965 was indeed described as ′isotropic′ by them. However in 1992, NASA's COsmic Background Explorer (COBE) satellite announced [27] the detection of faint anisotropies in CMB. Soon after this discovery, several other CMB experiments

[‡]estimated from Saha equation of weakly ionised plasma for a 90% ionization fraction.

[§§§]This is the first combination of electrons and protons in the history of the universe, so the word ′recombination′ might be misleading.

or space missions have been conducted to map this anisotropy in detail. NASA's Wilkinson Microwave Anisotropy Probe (WMAP), launched in 2001, provided more precise measurements of the anisotropies and estimates of dark matter abundance. The European Space Agency (ESA) launched another space mission named Planck Surveyor in 2009, and its 2013 all sky map (Fig. 1.4) revealed the universe to be slightly older than previously estimated [26].

The CMB anisotropies are understood in terms of the small density fluctuations in the primordial plasma just before the photon decoupling epoch. These anisotropies manifest as an intriguing oscillating pattern, i.e. peaks and troughs in the CMB power spectrum (section 1.2.3) one sees today. Known as baryonic acoustic oscillations (BAO), these oscillations were directly caused by the inward gravitational compression and an outward radiation pressure of the primordial baryon-photon fluid and continued until the complete release of primordial photons.

But how could those density perturbations possibly occur in the ionized plasma? Electrostatic forces should have opposed any tendency of ordinary matter to $'$clump$'$ together, and unless they could clump together, density fluctuations would not occur. So one needs some electrically neutral matter, apart from the ionized ones, to make this happen. This type of neutral matter cannot be some simple atoms ($'$baryonic$'$, i.e. made of protons, neutrons) because the first atoms were only formed during recombination. Hence alongside the ordinary baryonic matter, the primordial plasma must have had some other type of matter that does not interact electromagnetically but does interact gravitationally. Consequently, this provides further evidence for dark matter.

1.2 ΛCDM model

It was not until the early 1980s when cosmologists started to develop comprehensive models to build a common ground for big bang cosmology, CMB observations and the missing dark matter in the universe. In general, these models can be distinguished by the nature (i.e. speed and mass) of the dark matter particles involved (e.g. hot, warm or cold dark matter models), and are summarised in table 1.1. Models with mixed cold and hot scenarios also exist in the literature [28]. This dissertation will focus on the cold dark matter (CDM) candidates.

Table 1.1 *Hot, warm and cold dark matter.*

Model	Speed	Mass	Leading candidates
Hot	Ultra-relativistic	a few tens of eV [29]	SM neutrinos
Warm	intermediate to cold and hot	$\sim keV$ [30, 31]	sterile neutrinos
Cold	non-relativistic	$10^{-5}\,eV$ [32] - GeV, TeV [33–35] or more	WIMPs, ALPs, HPs

Historically developed in early ′80s and widely accepted by the scientific community in the 21st century, the ΛCDM model is currently the leading ′double dark′ big bang cosmological model that includes both the ideas of dark matter and dark energy. Based on three basic components (ordinary matter, a cosmological constant Λ and the CDM), it can explain the galactic structure formation [36], observed acceleration of the galactic expansion (section 1.2.1) and the present day CMB anisotropy (section 1.2.3).

1.2.1 Cosmological constant

1.2.1.1 Preliminaries

In cosmology, the expansion of the universe is described by the Friedmann equation

$$(\frac{\dot{a}}{a})^2 = \frac{8\pi G}{3}\rho - \frac{\kappa}{a^2} + \frac{\Lambda}{3} \qquad \text{(in natural units, i.e. c=1)}, \tag{1.11}$$

where $a(t)$ is the scale factor[¶] of the universe, G the gravitational constant, ρ the energy density[‖] and Λ the cosmological constant. The parameter κ is a measure of the geometry of the universe, known as the curvature[**]. The left hand side of the eq. 1.11 can further be identified as the square of the Hubble's parameter H.

[¶]The scale factor is a measure of the expansion rate of universe and is related to the Hubble parameter as

$$H = \frac{\dot{a}(t)}{a(t)}.$$

[‖]with $c = 1$, the terms matter density ρ and energy density ϵ are interchangeable, according to Einstein's mass-energy relation $\epsilon = \rho c^2$.

[**]There are three possible values of κ: $\kappa = -1$ for open, $\kappa = 0$ for flat and $\kappa = 1$ for closed universe.

The density ρ as a function of time is given by the fluid equation

$$\dot{\rho} + 3\frac{\dot{a}}{a}(\rho + p) = 0, \tag{1.12}$$

where p is the pressure of a fluid with a mass density ρ and the equation is in natural units. A third equation, derived from the above two, is called the acceleration equation which expresses the acceleration of the scale factor as

$$\frac{\ddot{a}}{a} = -\frac{4\pi G}{3}(\rho + 3p) + \frac{\Lambda}{3}. \tag{1.13}$$

The density ρ for a given value of H that makes the universe flat, i.e., $\kappa = 0$ (in the absence of Λ) is known as the critical density ρ_c:

$$\rho_c(t) = \frac{3H^2}{8\pi G}. \tag{1.14}$$

The dimensionless quantity expressed by the ratio ρ/ρ_c is termed as the density parameter (Ω). It can be defined for the universe as a whole or for its individual components, e.g. for the i-th component of the universe,

$$\Omega_i(t) \equiv \frac{\rho_i}{\rho_c}. \tag{1.15}$$

1.2.1.2 Why need Λ?

So far it has not been discussed how the cosmological constant Λ comes in eqs. 1.11 and 1.13 in the first place. The idea of a cosmological constant (Λ) was originally put forward by Einstein to ensure a static universe (which is not correct, as it is now known for sure that the universe is expanding) in the formulation of general relativity. The concept was reincarnated in 1998 after the surprising discovery of the accelerated expansion of the universe, independently by the High-Z Supernova Search Team [37] and the Supernova Cosmology Project [38] through type 1a supernovae observation.

To understand the significance of Λ in connection with an acceleration, a close scrutiny of eq. 1.13 is needed. It shows that the positive values of ρ and p (i.e. greater gravitational forces) decelerate the expansion, but a positive Λ has a $'$replusive$'$ effect. If sufficiently large, a positive Λ can overcome the gravitational term, resulting in an accelerating universe. In the absence of a Λ term it would be impossible for eq. 1.13 to provide an accelerated expansion of the universe.

1.2.1.3 Possible physical interpretation

The cosmological constant can be interpreted as a fluid with a pressure p_Λ, energy density ρ_Λ and a density parameter Ω_Λ:

$$\rho_\Lambda \equiv \frac{\Lambda}{8\pi G}, \qquad \Omega_\Lambda = \frac{\Lambda}{3H^2}. \tag{1.16}$$

The Friedmann equation thus can be rewritten as

$$\sum_i (\Omega_i + \Omega_\Lambda) - 1 = \begin{cases} 0, & \text{for flat universe.} \\ \frac{\kappa}{a^2 H^2}, & \text{for non-flat universe.} \end{cases} \tag{1.17}$$

Here Ω_i is the density parameter of the i'th component. The fluid equation for cosmological constant reads

$$\dot{\rho_\Lambda} + 3\frac{\dot{a}}{a}(\rho_\Lambda + p_\Lambda) = 0. \tag{1.18}$$

This implies a negative effective pressure of cosmological constant ($p_\Lambda = -\rho_\Lambda$), i.e. energy is needed to expand the fluid, not to compress it. With the expansion of the universe, work is done on the Λ fluid keeping the ρ_Λ constant. The estimated values of Ω_Λ by Planck Collaboration based on their 2018 data [39] is 0.685 ± 0.007.

Physically, it might be interpreted as an energy (i.e. the dark energy) with constant density permeating the space and time and is equivalent to the quantum vacuum energy from the quantum mechanics. However, the cosmological constant predictions from quantum field theories are much greater[§] than the experimental values [40].

1.2.2 Cold dark matter (CDM)

The concept of cold dark matter was first developed, independently, by three groups of cosmologists: James Peebles [41]; J. Richard Bond, Alex Szalay, and Michael Turner [42]; and George Blumenthal, H. Pagels, and Joel Primack [43] in 1982. Peebles was awarded [44] half of the Nobel Prize in Physics in 2019 for his contributions to theoretical discoveries in physical cosmology.

[§]In a basic theory, the scale of the discrepancy is a factor of $\sim 10^{110}$; in other reasonable models, it's still enormous (e.g. $\sim 10^{30}$ or so at least).

The basic properties of cold dark matter are [36]:

- **Cold**: If the dark matter particles that constitute the vast majority of the mass of the universe were moving at relativistic speeds, then the remaining ordinary matter would not have sufficient gravity to form large scale galactic structures like galaxies, galaxy clusters etc. This implies that the dark matter particles were non-relativistic ($'$cold$'$), at least at the epoch of structure formation.

- **Non-baryonic**: The primordial light isotope (e.g. deuterium) abundances predicted from the present day observations give strongest limits [45] on the present day baryonic physical density parameter (defined in section. 1.2.3) as

$$0.014 \leq \Omega_B h^2 \leq 0.035 \qquad (h = H_0/100\, kms^{-1}Mpc^{-1}), \tag{1.19}$$

  which is inconsistent with observational values of physical density parameter for total matter ($\Omega_m h^2 \geq 0.1$) [36].

- **Gravitationally and/or weakly interacting**: Dark matter does not interact electromagnetically, otherwise it would be seen. It is also very unlikely for dark matter to interact $'$strongly$'$ because all strongly interacting Standard Model particles (e.g. quarks and hadrons that are made of quarks) interact electromagnetically. There remains two fundamental interactions: gravitational and weak. Dark matter obviously interacts gravitationally as it was discovered via its gravitational effect. Interacting weakly is another viable possibility which justifies why dark matter particles are yet to be directly detected.

- **Cosmologically stable**: Dark matter is stable or long-lived (with a lifetime comparable to the age of the universe), as its presence can still be seen today.

1.2.3 CMB measurements and DM abundance

Precise measurement of CMB anisotropies (section 1.1.5) serves as a key to glance back at the early universe and estimate the dark matter relic abundance. In general, the studies consist of measuring the temperature of CMB in a given direction (i.e., in terms of angular co-ordinates, θ, ϕ) on the sky. The dimensionless temperature anisotropy can be expressed in terms of spherical harmonics $Y^l_m(\theta, \phi)$ as [46]

$$\frac{\Delta T}{T}(\theta, \phi) = \sum_{l=1}^{\infty} \sum_{m=-l}^{l} a_{lm} Y^l_m(\theta, \phi), \tag{1.20}$$

where $\Delta T(\theta, \phi) \equiv T(\theta, \phi) - T_{avg}$ are the fluctuations of temperature $T(\theta, \phi)$ with respect to the average CMB temperature today ($T_{avg} \sim 2.73K$). The coefficients a_{lm} are a measure of the size of these anisotropies. A statistically useful quantity is C_l, known as the angular power spectrum and defined as

$$C_l = \langle |a_{lm}|^2 \rangle. \tag{1.21}$$

The statistical average on the right hand side of eq. 1.21 is an average over all possible values of m. Due to rotational invariances, it results in values of C_l that are independent of m, i.e. is a function of l only. The index l gives a measure of the angular scale: larger l indicates smaller angular scale and vice versa (i.e. $l \propto \frac{1}{\theta}$).

Fig. 1.5 illustrates the CMB temperature power spectrum, $\mathcal{D}_l^{TT}$ as a function of multipole l by the Planck collaboration [39] based on their 2018 data. $\mathcal{D}_l^{TT}$ is related to C_l by

$$\mathcal{D}_l^{TT} \equiv \frac{l(l+1)C_l^{TT}}{2\pi} \tag{1.22}$$

with index TT representing $'$full Planck temperature-only$'$ analysis.

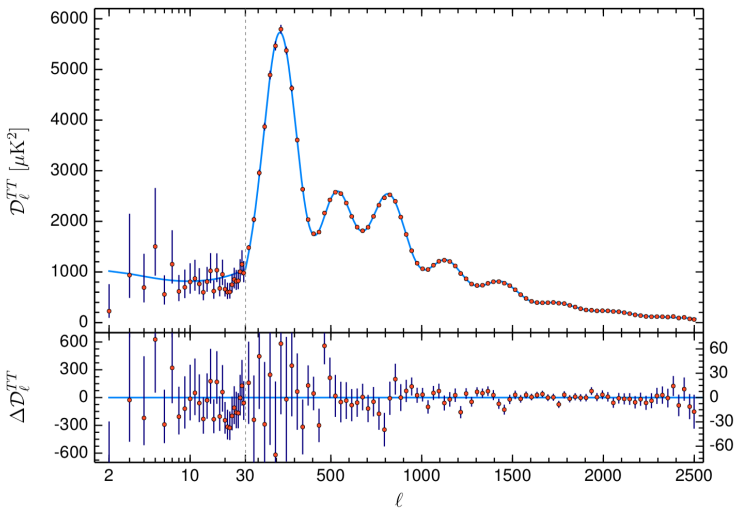

Figure 1.5: *Temperature power spectrum of the CMB based on Planck's 2018 data [39].*

For smaller l ($l \leq 100$) the variation of $\mathcal{D}_l^{TT}$ is quite constant showing the $'$intial conditions$'$ of the early universe. The lower part of the region ($l \leq 15$) was first probed by COBE [27]. This almost flat region is the direct result of the random quantum fluctuations in photon energy densities and gravitational potential in the early universe, the combined effect being known as the Sachs-Wolfe effect and the region as Sachs-Wolfe plateau. The tilt in the almost flat curve is caused by

the rapid ′inflation′ period, during which these tiny fluctuations had evolved into notable density perturbations.

At larger l (i.e. smaller scales), a broad peak is seen around $l \approx 200$, followed by a series of smaller peaks. These are the ′acoustic peaks′, originated from complicated acoustic oscillations in cosmic baryon-photon fluid, when the CMB was being released. These oscillations were due to the combined effect of compression by the gravity (odd numbered peaks) and rarefaction by the radiation pressure (even numbered peaks). Note that the events of photon decoupling and recombination were not instantaneous. As the early photons started to get released, the baryon-to-photon ratio of the oscillating fluid kept increasing resulting in an asymmetric oscillation with enhanced ′gravitational′ effect. This is why the odd peaks are actually seen to be ′enhanced′ over the even ones in the power spectrum. However, the emission of photons also caused a subsequent damping (′diffusion damping′) in the oscillation pattern resulting in reduced frequencies. The oscillation froze out when all early photons were released, leaving behind a shell of baryons with over-dense dark matter in the centre. This is when the universe switched into a transparent one.

The location of the first acoustic peak is sensitive to the geometry of the universe, with the observed location ($l \approx 220$) consistent with a flat universe with $\kappa = 0$. Smaller values of l would indicate a closed universe ($\kappa > 0$) and larger values would indicate an open one ($\kappa < 0$). The relative heights of first and second peak indicate the increase in baryon-to-photon ratio due to photon releases and hence are important sources of information on early baryonic matter density. Because odd number peaks are associated with gravitational compressions mainly governed by the massive dark matter, the third peak can suffice as a footprint of dark matter content in the early universe.

The Planck 2018 data (red points in fig. 1.5) was fitted with the standard 6 parameter[††] ΛCDM Model (blue curve in fig. 1.5) with a flat geometry and the fit was remarkably good[‡‡]. Based on the fits, several density parameter values, Hubble constant and other parameters have been calculated. The physical density

[††]The smallest number of free parameters to get an acceptable fit between ΛCDM Model and observed CMB data is six: physical baryonic density parameter $\Omega_B h^2$, physical dark matter density parameter $\Omega_c h^2$, age of the universe t_0, scalar spectral index n_s, amplitude of curvature fluctuation Δ^2_R and re-ionization optical depth τ.

[‡‡]Fits with some extended ΛCDM Model were also investigated but no satisfactory result was found to favour them [39].

Table 1.2 *Physical Density Parameters from combined Planck 2018 TT,TE, EE+ lowE+ lensing analysis, with* 68% *confidence limit.*

	Parameters	Symbol	Value
Physical Density Parameters	Total matter	$\Omega_m h^2$	0.143 ± 0.001
	Baryon	$\Omega_B h^2$	0.0224 ± 0.0001
	Dark matter	$\Omega_c h^2$	0.120 ± 0.001
	Dark energy	$\Omega_\Lambda h^2$	0.311 ± 0.008
Others	Hubble Constant	H_0	$67.4 \pm 0.5\ kms^{-1}Mpc^{-1}$

parameter is a measure of the relic abundance of the particle concerned, i.e., the amount of that particle remaining in the present universe. For example, $\Omega_c h^2$ represents the dark matter relic abundance, where $h = H_0/100\ kms^{-1}Mpc^{-1}$.

Planck's 2018 standard ΛCDM results from combined TT, TE, EE+ lowE+ lensing analysis (with 68% confidence limit) are summarised in the table 1.2. According to Planck's 2018 measurements, our known universe consists of 68.5% dark energy and 31.5% total matter (26.5% dark matter, 4.9% baryonic matter and rest are other non-baryonic matter like leptons).

1.3 Dark matter in galactic halo

The distribution of dark matter in a galactic neighbourhood is often modelled in the form of a halo. A dark matter halo permeates all the space in a galaxy and extends far beyond its luminous components. To design a direct detection experiment, it is essential to map out the dark matter distribution throughout the Milky way galaxy, especially in the neighbourhood of the solar system.

The Milky way is a medium sized (mass $\sim 10^{12}\, M_\odot$) barred[¶¶¶] spiral galaxy with a diameter $\sim 46 - 61\, kpc$ $(150 - 200\, kly)$ which contains about 250 ± 150 billion stars and over 100 billion planets. Our Sun is located at a distance of $8\, kpc$ from the galactic centre on one of the spiral arms. A steady-state spherically symmetric DM halo with an isotropic velocity dispersion will be considered in the present discussion.

The DM particles in the halo are assumed to be collisionless, moving in orbits determined by a spherical potential solely generated by the mass distribution of

[¶¶¶]has a central bar-shaped region of stars.

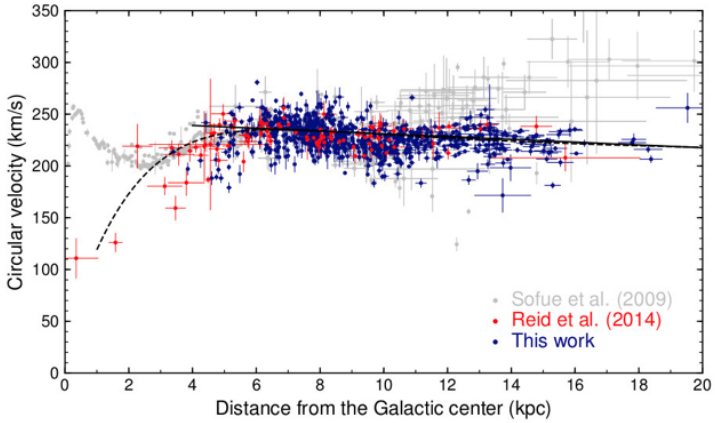

Figure 1.6: *Rotation curve of Milky Way galaxy [47]. The dashed line represents the universal best-fitting model.*

the particles. The total potential Φ can be found by the integration

$$\Phi = G \int_0^r \frac{M(r)}{r^2} dr, \tag{1.23}$$

where G is the gravitational constant and $M(r)$ is the mass at a distance r.

1.3.1 Halo profiles

Fig. 1.6 shows the observed rotation curve of the Milky Way galaxy. The almost flattened[¶¶] ($v = constant$) orbital velocity distribution at higher radii instead of a Keplerian decline ($v \propto \sqrt{r}$) indicates the existence of a mass that is still increasing linearly with radius. The corresponding density profile ($\rho \propto m/r^3 = 1/r^2$) closely resembles to that of an isothermal sphere. This is the well-known pseudo-isothermal halo model with a density profile

$$\rho(r) = \frac{\rho_0}{1 + (\frac{r}{r_c})^2}. \tag{1.24}$$

Such variation led to the concept of a constant density (ρ_0) $'$core$'$ (i.e. a region near the centre (small r) of the galaxy) with a radius r_c. Caldwell and Ostriker in 1981 [48] worked out a value of local DM halo density $\rho_\odot \sim 0.23\, GeV/cm^3$ based on this cored halo distribution. Rotation curves of gas-rich dwarf galaxies strongly favoured this scenario [49, 50].

[¶¶]such flatness is more prominent in dwarf galaxy rotation curves.

However, the density ρ in eq. 1.24 diverges as $r \to \infty$. Also, high resolution numerical simulations found no firm evidence of the $'$cored$'$ scenario. They rather inferred a steep power-law density distribution [51–53] in the inner region ($\rho \propto r^{\alpha}$ where $\alpha = -1$). This is known as the $'$cuspy$'$ DM scenario which induced a long-standing puzzle of core-cusp problem. It has been recently proposed [54] to be resolved by some DM heating models.

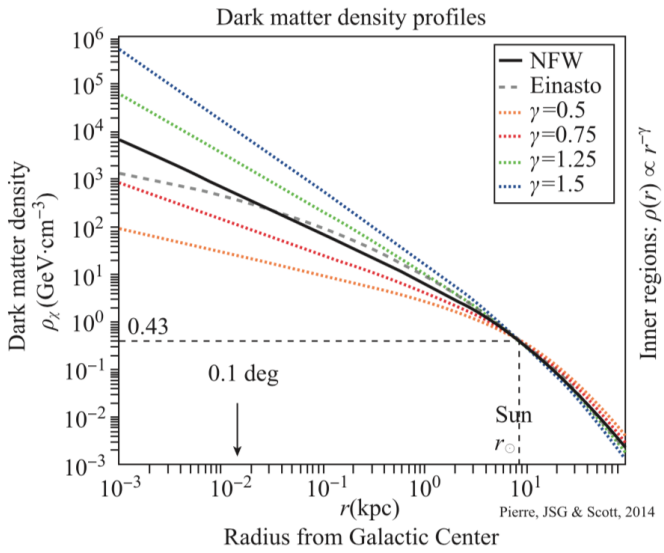

Figure 1.7: *Comparison of different dark matter density profiles. Figure from [55].*

Numerical simulations typically use more advanced profiles, e.g. the universal (works for a large variety of halo masses) Navarro–Frenk–White (NFW) density profile [56]

$$\rho_{NFW}(r) = \frac{\rho_c \delta_c}{(r/r_s)(1 + r/r_s)^2}, \tag{1.25}$$

where $\rho_c \approx 0.5 \times 10^{-5}\, GeV/cm^3$ is the critical density, δ_c is a dimensionless constant and r_s is a characteristic radius. A more generalised version follows as

$$\rho_{gNFW}(r) = \frac{\rho_c \delta_c}{(r/r_s)^{\gamma}(1 + r/r_s)^{3-\gamma}}. \tag{1.26}$$

Another halo profile of interest is the Einasto profile [57]:

$$\rho_{Einasto}(r) = \rho_0 \exp\left(-\frac{2}{\alpha}\left(\left(\frac{r}{r_s}\right)^{\alpha} - 1\right)\right), \tag{1.27}$$

where r is the spatial radius and ρ_0, α, n are constant. Fig. 1.7 shows a comparative plot by [55] which reveals that the local DM density near the Sun is pretty much the same ($\rho_{\odot} \sim 0.43\, GeV/cm^3$), regardless of a particular choice of the density profile. This value was computed kinematically in a model dependent way [58].

A more widely used value is, however, $\rho_\odot \sim 0.39\,GeV/cm^3$ (see PDG 2018 [59]) with a factor 2 uncertainty.

Once a particular DM density profile is chosen, one can determine the velocity dispersion by solving the Jeans equation [60]

$$\frac{d(\rho\sigma_r^2)}{dr} + \frac{2\rho}{r}\beta\sigma_r^2 = -\rho\frac{d\Phi}{dr}, \tag{1.28}$$

where $\sigma_r^2 = \overline{(v_r - \overline{v_r})^2}$ is the velocity dispersion, $\overline{v_r}$ is the mean radial velocity in a spherical shell of mean radius r, $\beta = 1 - \sigma_t^2/\sigma_r^2$ is the anisotropy of dispersion and σ_t^2 is the tangential velocity dispersion. Eq. 1.28 can be numerically solved upto some virial radius, defined [61] from the critical density for a flat universe ρ_{crit} as

$$\frac{M_{vir}}{(3/4)\pi r_{vir}^3} = 178\,\Omega_0^{0.45}\rho_{crit}, \tag{1.29}$$

or by observational data sets [62].

Current LZ analyses assume [63] the standard isothermal halo model following the formalism of [64] with $\rho_\odot \sim 0.3\,GeV/cm^3$ (which was the previous 'standard' value of the local DM density used only until recently [65]). Moreover, a Maxwell-Boltzmann distribution truncated at the Milky Way's escape velocity ($v_{esc} = 544km/s$) is considered for the WIMP velocity distribution in the galactic frame.

1.3.2 Annual Modulation

The flat galactic disk of the Milky way, which contains the Sun and thus the solar system, is rotating through a non-rotating DM halo. This relative motion, between the Sun and the DM halo, appears as an effective 'dark matter wind' to an observer on the Earth. Also, the Earth is rotating around the Sun and the orbit makes an angle of 60° with the plane of the galactic disk (fig. 1.8). The velocity of the Earth in the rest frame of non-relativistic DM halo can be calculated by the Galilean velocity addition

$$\vec{v}_{obs}(t) = \vec{v}_\odot + \vec{v}_{orb}(t), \tag{1.30}$$

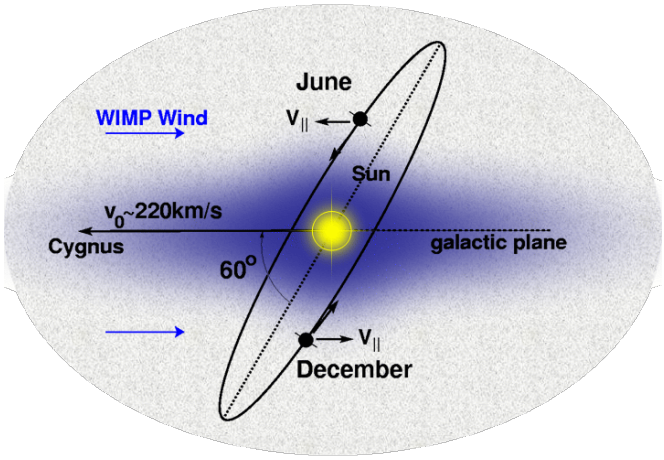

Figure 1.8: *Orbit of Earth around the Sun which is rotating around the galactic centre through the non-rotating DM halo.*

where $\vec{v}_\odot$ is the velocity of Sun with respect to the DM halo and $\vec{v}_{orb}$ is the Earth's orbital velocity around the Sun. $\vec{v}_\odot$ can be further expressed [66] as

$$\vec{v}_\odot = \vec{v}_{LSR} + \vec{v}_{\odot,pec}, \tag{1.31}$$

where $\vec{v}_{LSR} \approx 220\,km/s$ (disk rotation speed) [67] is the motion of the local standard of rest in the galactic co-ordinates*** (i.e. motion of the Sun with respect to the galactic centre) and $\vec{v}_{\odot,pec}$ is the Sun's peculiar velocity owing to its intrinsic motion with respect to the galactic rest frame. However, more recent studies place a $5\% - 15\%$ higher value of $\vec{v}_{LSR}$ as $\vec{v}_{LSR} \approx 235\,km/s$ [68–70].

Owing to the periodic variation of the Earth's velocity $\vec{v}_{orb}$ around the Sun, the relative velocity of the Earth with respect to DM halo also shows a periodic behaviour. Using approximate values of $v_{orb} \sim 30\,km/s$ (the Earth's orbital speed) and $T = 1\,year$, $v_{obs}(t)$ can be expressed as [71]

$$v_{obs}(t) \approx v_\odot\left(1+\frac{v_{orb}\cos(60^\circ)}{v_\odot}\cos\left(\frac{2\pi(t-t_0)}{T}\right)\right) \approx v_\odot\left(1+0.07\cos\left(\frac{2\pi(t-t_0)}{T}\right)\right), \tag{1.32}$$

changing the flux by a few %. The characteristic time $t_0 \sim 150\,\text{day}$ [72] corresponds to the summer time (June 2) when the Earth and Sun move in the

***The local galactic co-ordinates, centred at the Sun, are chosen such that the galactic disk is in the xy plane with x axis pointing to the direction of galactic center from the Sun and y axis coinciding with the rotational direction of the galactic disk. z axis, as obvious, is orthogonal to the disk plane.

same direction and $v_{obs}(t)$ is the maximum. $v_{obs}(t)$ attains a minimum when the Earth and the Sun moves opposite to each other in winter ($\sim$ early December). A detector based on Earth, will thus have more incoming DM particles in June than in December. The subsequent annual modulation of the DM signal in the detector, however, is subject to the particular DM candidate that is being searched for. For WIMP searches, the differential WIMP-nucleus scattering rate can be approximated as [71]

$$\frac{dN}{dE_R}(E_R, t) = S_0(E_R) + S_m(E_R)cos\left(\frac{2\pi(t - t_0)}{T}\right), \tag{1.33}$$

where $S_0(E_R)$ is some time averaged rate and the second term embeds the effect of modulation. The modulation amplitude S_m depends on the incoming energy of the DM particle and on the energy threshold of the particular detector.

However, for HP (ALP) searches by hidden photoelectric (axio-electric) effect, the rate of HP (ALP) absorption is independent of the velocity distribution in the galactic halo, suggesting an absence of modulation terms to an experimentally relevant level [73]. See chapter 6 for details.

1.3.3 Diurnal modulation

In the previous section Earth's rotation around its own axis was ignored. The idea of a second kind of modulation owing to the Earth's daily/diurnal motion was first put forward by Collar and Avignone in 1992 [74, 75]. The corresponding calculations of modulation amplitude will be similar to those in section 1.3.2 but with an extra rotational velocity ($\sim 0.5\,km/s$ near the equator) term in eq. 1.30. Obviously, the amplitude of diurnal modulation is much smaller than the annual one, making it very hard to detect [76]. However, the effect of daily modulation on recoil direction is much larger and forms the basis of the directional detectors. Also, Earth's spinning can manifest into a $'$shielding$'$ effect [77] enhancing the modulation amplitude which can be probed in direct detection experiments [78].

1.4 Chapter summary

This chapter addressed various cosmological aspects of dark matter, such as:

- The present-day universe has 4.9% ordinary baryonic matter, 68.5% dark energy and 26.5% dark matter in it. The rest are other non-baryonic matter

like leptons.

- The ΛCDM model assumes the dark matter to be cold, non-baryonic and stable, and gives predictions consistent with the CMB observations.
- Galactic dark matter is modelled as a halo that extends farther than the visible matter. The relative motions of the Earth and the Sun with respect to the dark matter halo lead to a time-varying incoming dark matter flux to an Earth-based detector.

Cosmological observations are solely based on the gravitational effects of dark matter and do not uniquely characterise its particle nature. This is exactly why particle physics is needed in the picture. Chapter 2 will re-evaluate the dark matter from a particle physicist′s point of view. Chapter 3 will discuss the experimental techniques of dark matter direct detection with LZ, followed by the chapters of my detailed experimental work, background analyses and HP/ALP sensitivity studies. The dissertation will end with a final summary chapter.

Chapter 2

Particle Candidates of Dark Matter

The cosmological observations and precise CMB measurements strongly suggest that dark matter exists, but provide very little information on its fundamental nature. In the absence of an experimental detection, a few theoretical alternatives exist in the literature, e.g. modified gravity [79], modified Newtonian dynamics (MOND) [80] and its relativistic extensions [81]. However, extensive tests against gravitational lensing data [82] indicate the inadequacies of these models to account for the missing mass alone, and further foster the dark matter paradigm. Another idea was to recognise dark matter as massive astrophysical compact halo objects (MACHOs). MACHOs (such as neutron stars, brown dwarfs etc) are large, heavy and non-luminous astrophysical objects made of ordinary baryonic matter. However, the galactic survey of 7 million stars by EROS-2 collaboration ruled out MACHOs to a small fraction ($< 8\%$) of that required [83].

With astrophysical alternatives ruled out, a particle-physics solution may be considered that the dark matter consists of one or more yet undiscovered particles, naturally arising from theories beyond the Standard Model (BSM). An ideal dark matter candidate must possess some distinguishing properties:

- **Observational properties:** A good candidate must explain all the dark matter properties inferred from cosmological observations, e.g., it must be stable or long-lived, non-baryonic and massive enough to account for the missing mass of the universe. It must be gravitationally acting and may be weakly interacting. A brief discussion of these properties in context of the cold dark matter paradigm was discussed in section 1.2.2.

- **Relic abundance:** The production mechanism of the particle in the underlying model should result in a correct dark matter relic abundance ($\Omega_c h^2$ in Table 1.2).

- **Experimental constraints:** The model should be consistent with all the constraints imposed by previous (and current) dark matter experiments.
- **Minimal arbitrary choices of parameters:** The model should be optimized with a minimum number of arbitrary parameters.
- **Testable predictions:** Finally, the model should foreshadow one or more plausible DM interaction signatures. This may be within the reach of current and next generation detection experiments.

Keeping all these properties in mind, this chapter will review some popular dark matter candidates, e.g. weakly interacting massive particles (WIMPs) and weakly interacting slim particles (WISPs). This will be followed by a detail discussion on ALP and HP dark matter models, the central interests of this dissertation.

2.1 WIMPs and WISPs

2.1.1 Weakly interacting massive particles (WIMPs)

The inadequacy of SM to provide an appropriate dark matter candidate indicates the BSM nature of dark matter. Well motivated candidates exist in literature that interact weakly with ordinary matter, naturally produce correct DM relic abundance and fit well within the CDM paradigm. These particles (such as neutralinos, Kaluza-Klein particles etc.) comprise the leading class of CDM candidates to date, known as the weakly interacting massive particles (WIMPs). As the name implies, WIMPs are

- weakly interacting, i.e. the interaction is no stronger than the order of the weak scale;
- massive: typically from GeV/c^2 [33, 34] to a couple orders of TeV/c^2 [35];
- stable (or long-lived) enough;
- thermally produced in the early universe, and can explain the present day dark matter abundance.

Particles with such characteristics often occur in supersymmetry (SUSY), extra dimensions and string theories, such as:

- **SUSY WIMPs:** Phenomenologically motivated by gauge hierarchy problem and coupling unifications, SUSY theories assume a $'$super-partner$'$ for every SM particle, with a spin differing by a half integer. The unified picture of SM and SUSY is known as the minimal supersymmetric Standard Model (MSSM). A new quantum number called R-parity is defined in terms of the baryon number B, lepton number L and spin s as

$$R = (-1)^{3(B-L)+2s}. \tag{2.1}$$

  Each SM particle has a positive R-parity and its superpartner has a negative R-parity. The conservation of R-parity leads to a stable lightest supersymmetric particle (LSP) [84]. Stringent constraints on LSP charge by experimental exotic isotope searches [85, 86] point to an electrically neutral LSP, marking it eligible as DM candidate. Sneutrino, originally proposed as the superpartner of ordinary SM neutrino, has been already ruled out as a DM candidate by direct detection experiments [87, 88]. However, models with sterile sneutrinos [88] and neutralinos (in the mass range $0.1 - 1\ TeV/c^2$) [89] are also being considered.

- **Kaluza-Klein particles:** A theory of universal extra dimensions (UED), originally speculated by Kaluza and Klein in early 1920s [90] and further developed in recent times [91], provides another class of new particles (Kaluza -Klein states) – the lightest of which is a suitable WIMP DM candidate. In such theories, the propagation of SM particles to extra dimensions creates a tower of heavier Kaluza-Klein partner states with identical quantum numbers. The lightest Kaluza-Klein state is stable with a mass in between $400\ GeV - 1.2\ TeV$, can lead to an appropriate DM relic density [92, 93] and might be within the reach of experimental searches.

The WIMPs are assumed to be produced in the pre-big bang nucleosynthesis (BBN) era, via thermal collisions within the primordial gluon-quark plasma. At very high temperatures ($T >> m_\chi$[†]) there was a thermal equilibrium between the continuous annihilation and production processes of WIMPs (χ) and SM particles (ϱ):

$$\chi\bar{\chi} \longleftrightarrow \varrho\bar{\varrho}, \tag{2.2}$$

[†]m_χ is the mass of a χ particle and both T and m_χ are expressed in units of energy.

where the bars represent the antiparticles. The common rate of χ-production and χ-annihilation at equilibrium can be expressed as

$$\Gamma_{eq} = \langle \sigma_A v \rangle n_{eq} \quad \text{(at equilibrium)}, \tag{2.3}$$

where n_{eq} is the equilibrium density of WIMP dark matter, σ_A is the total cross-section of the annihilation process ($\chi\bar{\chi} \longrightarrow \varrho\bar{\varrho}$), v is the relative velocity and the angular brackets represent a thermal average. Because the ϱ particles (mass m_ϱ) need enough energy to generate heavy dark matter particles (assuming that the WIMP mass $m_\chi > m_\varrho$), the rate of χ-production ($\varrho\bar{\varrho} \longrightarrow \chi\bar{\chi}$) is critically dependent on the temperature: the lower the temperature, the more suppressed is the process. Thus, with the universe's expansion and a subsequent temperature drop, the χ-production was Boltzmann-suppressed*. The expansion also lowered the number density (n_χ), resulting in a decrease in the χ-annihilation rate ($\Gamma_A = \langle \sigma_A v \rangle n_\chi$). The entire scenario can be expressed [94] in terms of the Boltzmann transport equation:

$$\frac{dn_\chi}{dt} = -3Hn_\chi - \langle \sigma_A v \rangle (n_\chi^2 - n_{eq}^2), \tag{2.4}$$

where the expansion of the universe is embedded in the term H, the Hubble parameter for a radiation-dominated Universe. When Γ_A was dropped below the expansion rate ($\Gamma_A \lessapprox H$), the Hubble term became primarily dominant and the annihilation practically came to a halt ('WIMP freeze-out'). Since then the decrease of n_χ has been solely due to the universe's expansion. In co-moving co-ordinates‡, the comoving yield or number density ($Y \equiv n_\chi/s$ where s is the entropy density) attained a constant value at freeze-out. A schematic illustration of the variation of Y as a function of a dimensionless variable $x = m/T$ (where m is the WIMP mass and T is the photon temperature) during the freeze-out epoch is shown in Fig. 2.1.

A present day WIMP relic density can be obtained by a numerical solution of the Boltzmann equation. For a velocity independent σ_A, a rough approximation is

$$\Omega_\chi h^2 \simeq \frac{3 \times 10^{-27} cm^3 s^{-1}}{\langle \sigma_A v \rangle}. \tag{2.5}$$

*decreased exponentially with a factor of $e^{-m_\chi/T}$.

‡in co-moving co-ordinates the observer 'comoves' with the Hubble expansion. If d is the physical distance and $a(t)$ is the expansion rate of the universe, a comoving distance x is defined as $x = d/a(t)$.

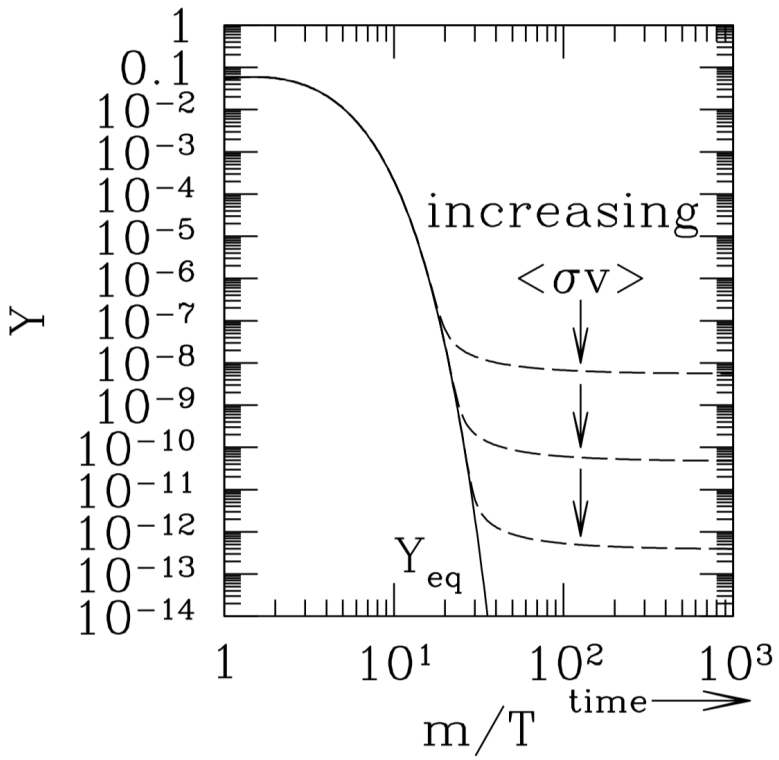

Figure 2.1: *Typical evolution of comoving WIMP yield (or abundance) as a function of m/T for a standard freeze-out scenario. Dashed curves show density after freeze out. Image from [94].*

In order to match $\Omega_\chi h^2$ to the correct dark matter relic density ($\Omega_c h^2$ in Table 1.2), $\langle \sigma_A v \rangle$ needs to be of the order of $\sim 3 \times 10^{-26} cm^3 s^{-1}$. Intriguingly, this is a value similar to electroweak scale WIMPs with a mass around $\sim 100\, GeV/c^2$. This seemingly remarkable 'coincidence' ('WIMP miracle') has been disfavoured by decisive exclusions from direct detection experiments [95–97]. However, one expects from dimensional analysis [98, 99] that only the ratio g_X^4/m_X^2 determines the $\langle \sigma_A v \rangle$ value, i.e.

$$\langle \sigma_A v \rangle \sim \frac{g_X^4}{m_X^2}, \tag{2.6}$$

where g_X is the coupling associated with the process that drives the WIMP annihilation ($\chi\bar{\chi} \longrightarrow \varrho\bar{\varrho}$). Thus, apart from electroweak scale WIMPs, other combinations of (m_X, g_X) that are consistent with the freeze-out mechanism can equally match the correct dark matter relic density in eq. 2.5. In other words, lower-mass WIMPs can still be DM if their interactions are weaker than the weak scale. An exhaustive review follows in [99].

2.1.2 Weakly interacting slim particles (WISPs)

The WIMP realization of dark matter suffers from a non-trivial challenge: the underlying theory needs additional symmetries to ensure the cosmological stability of WIMPs. These symmetries often lead to new interactions inconsistent with the strengths required. An alternative approach is to consider a different class of smaller-mass particles called the weakly interacting slim particles (WISPs). The small WISP mass reduces the interaction phase space and ensures its cosmological stability, i.e. makes the lifetime longer. Typical properties of WISPs are

- *very* weakly interacting;
- have a mass sufficiently smaller than WIMPs ($\sim$ *sub-*eV/c^2 to MeV/c^2);
- stable (long-lived) in cosmological time-scale;
- were produced non-thermally in the early universe.

A plethora of non-WIMP particles already exists in a variety of BSM theories. Many of them act as WISPs in certain mass ranges, e.g. QCD[¶] axions, axion-like particles (ALPs) (see section 2.2) and hidden photons (HPs) (see section 2.3).

Non-thermal productions of WISPs are often described in terms of a misalignment mechanism, though other production techniques exist in the literature. Originally introduced for QCD axions [100–102] and later generalised [103] for other WISPs, the misalignment mechanism can be summarised in a series of events starting from the cosmic inflation. Consider the simplest case of a real scalar field ϕ with a Lagrangian [103]

$$\mathcal{L} = \frac{1}{2}\partial_\mu\phi\partial^\mu\phi - \frac{1}{2}m_\phi^2\phi^2 + \mathcal{L}_I, \tag{2.7}$$

where $\mathcal{L}_I$ governs the interactions of ϕ with itself and all other particles in the primordial bath and m_ϕ is the scalar mass. Assume that the universe underwent an inflationary epoch when the Hubble parameter was very much larger than the WISP mass ($H >> m_\phi$). Fields in the post-inflation universe were (approximately) spatially uniform, with a single but random (probably due to quantum fluctuations during the inflation) initial value $\phi_{initial}$. The inflation was followed by the reheating, and then by a period of radiation dominated expansion. Assuming a Friedmann-Robertson-Walker (FRW) universe (i.e. assuming the field

[¶]quantum chromodynamics.

ϕ to be homogeneous and isotropic) the equation of motion for ϕ in an expanding universe is governed by the Klein-Gordon equation** [104] as [103, 105]

$$\ddot{\phi} + 3H(t)\dot{\phi} + m_{\phi}^2\phi = 0. \tag{2.8}$$

Thermal corrections from $\mathcal{L}_I$ implies $m_\phi = m_\phi(t)$, i.e. m_ϕ evolves with time t. Equation 2.8 has solutions in two different regimes:

- When $3H(t) >> m_\phi$, the oscillation is overdamped with a negligible mass term and the field is approximately constant. In other words, the field ϕ gets frozen at its initial value and $\dot{\phi} = 0$.
- At a later time (t_1) when $3H(t_1) = m_\phi(t_1)$, the damping becomes undercritical. The field ϕ attempts to minimise the potential, and starts oscillating around the minimum. In the absence of any significant damping by decays, the energy density dilutes by the expansion of the universe ($\rho \propto a^{-3}$, where a is the scale factor).

This variation is similar to that expected from a non-relativistic matter. A present day dark matter relic density can be achieved through fine-tuning of the initial misalignment, $\phi_{initial}$. Thus the behaviour of ϕ field oscillations can be attributed to that of a CDM fluid. This simplest scenario can also be generalised for pseudo Nambu-Goldstone Bosons (pNGBs) (e.g. axions, ALPs) and vector fields (e.g. HPs) as shown by Nelson and Scholtz in [106].

2.2 Axion-like particles (ALPs)

Axion-like particles (ALPs) are a general type of (massless) Nambu-Goldstone bosons (NGBs) or (massive) pseudo Nambu-Goldstone Bosons (pNGBs) that appear in many BSM theories as a result of spontaneous breaking§ of additional

**For a homogeneous and isotropic field $\Phi(t)$ with a Lagrangian $\mathcal{L}_\Phi = \frac{1}{2}\partial_\mu\Phi\partial^\mu\Phi - V(\Phi)$, the Klein Gordon equation in an expanding universe is $\ddot{\Phi} + 3H(t)\dot{\Phi} + \frac{\partial V}{\partial \Phi} = 0$.

§Spontaneous symmetry breaking (SSB): Symmetry of the system is not shared by the ground state or vacuum (in perturbative quantum field theory states are built up from vacuum). Thus, the equation of motion is invariant, but the ground state is not, i.e. symmetry breaks. Spontaneous breakdown of an exact global symmetry results into a massless Nambu-Goldstone boson (NGB). If instead, the global symmetry is approximate, the resulting Goldstone particle acquires a small mass and is then called pseudo Nambu-Goldstone Boson (pNGB). The chiral Peccei-Quinn symmetry is approximate. For details, see [107].

(and/or approximate) global symmetries, e.g. majorons from lepton number [108] symmetry and familons from family [109] symmetry. Similar symmetries also occur naturally in string theories and often spontaneously break at string scales producing stringy particles behaving like axions [110, 111].

Although they share some qualitative properties, couplings of generic ALPs to SM particles are far less constrained [112] than axions, e.g. ALP mass and their coupling to photons are not related. This makes the parameter space for ALPs much wider and less-restricted in the experimental context. Another difference is that ALPs are a more general type than axions and have nothing to do with the Peccei–Quinn (PQ) mechanism in QCD. Thus, while axions acquire mass from mixing with neutral pseudoscalar mesons ($m_A f_A \sim m_\pi f_\pi$), ALPs do not, i.e. the quantity $m_{ALP} f_{ALP}$ is less restricted than the QCD axions.

2.2.1 ALP cosmology

Being neutral, non-baryonic and weakly interacting, an ALP can be considered as a cold dark matter candidate. However, the possibility of ALPs comprising the entire CDM critically depends on their behaviour during cosmic inflation. Consider a pre-inflation scenario[¶¶¶], i.e. the PQ-like symmetry was spontaneously broken before inflation and was never restored[††]. The resulting ALPs had random initial field values ϕ_i in different discrete regions, which was later $'$smoothed$'$ out by the inflation, leading to a homogeneous ALP field (i.e. same initial conditions everywhere) ϕ_i. A subsequent misalignment mechanism could have caused a cold ALP population, as discussed in section 2.1.2. The initial misalignment is often expressed in terms of a phase angle Θ. The expected fraction of ALP contribution to CDM is [113]

$$\frac{\Omega_\phi\, h^2}{\Omega_c\, h^2} \approx 1.4 \times \left(\frac{m_\phi}{eV}\right)^{1/2} \times \left(\frac{f_\phi}{10^{11}\, GeV}\right)^2 \left(\frac{\Theta_\phi}{\pi}\right)^2, \tag{2.9}$$

where m_ϕ is the ALP mass and Θ_ϕ is the initial misalignment angle which lies in the range $-\pi$ to π. This evolution of relic density from homogenisation of ALP field by inflation is often termed as the $'$zero momentum mode$'$ [114].

[¶¶¶]Note that post-inflation scenarios are also possible. See appendix A.

[††]If the symmetry is restored afterwards, a misalignment mechanism is still possible with a random initial angle, but the randomness may lead to some different phenomenology [115] .

An important bound comes directly from eq. 2.9. It clearly implies a SSB energy scale of $f_\phi \sim 10^{12}\,GeV$ to reproduce the present day DM abundance. This in turn, constrains the initial misalignment angle Θ_ϕ as a function of the ALP mass. Also, ϕ can not be larger than πf_ϕ[‖] theoretically. Combining, a conservative constraint of $\phi \leq f_\phi$ at $m_\phi > 3H(t_1)$ is obtained.

2.2.2 Generic ALP couplings and constraints

In general, coupling of ALPs with SM gauge bosons (e.g. gluons, photons, and electroweak bosons) are very much suppressed [116, 117] at low energies by a cut-off scale Λ (new physics scale). Despite being feeble, interactions of ALPs with SM particles give rise to a variety of effects that can be probed by astrophysical or laboratory experiments. Most of these experiments are based on ALP couplings to photons, electrons and gluons and/or quarks. Constraints on their couplings to $W^\pm$ bosons have also been obtained in some recent works [118, 119].

2.2.2.1 Coupling with gluons

Interactions of ALPs with gluons in the QCD-scale (i.e. MeV-GeV scale) have received considerable interests in recent times. Novel approaches have been developed to determine their hadronic interaction strengths with experimental implications. The effective Lagrangian for coupling of QCD ALP to two gluons is [116]

$$\mathcal{L}_{eff} \supset -\frac{4\pi\alpha_s c_{Agg}}{\Lambda}\phi\, G^{\mu\nu}\widetilde{G}_{\mu\nu}, \tag{2.10}$$

where c_{Agg} is a dimensionless coupling constant, Λ is a cut off scale, ϕ is the ALP field, G is the gluon field-strength tensor and $\widetilde{G}_{\mu\nu} \equiv \frac{1}{2}\epsilon_{\mu\nu\alpha\beta}G^{\alpha\beta}$ is its dual.

High energy colliders are sensitive probe to ALP-gluon interactions. Experimental constraints exist from kaon decay ($K^+ \to \pi^+\phi$) searches mediated by ALP-pion mixing [120] and LHC searches for mono-jets [121] and di-jets [122]. The first laboratory constraint on axion/ALP-gulon coupling was reported by Abel et al. in 2017 through a nuclear spin precession technique [123].

[‖]Theories with NGBs or pNGBs at low energies often involve a phase term ϕ/f_ϕ, a combination of the NGB or pNGB field ϕ and the SSB scale f_ϕ. The range of ϕ/f_ϕ is $(-\pi, \pi)$ and the scale $f_\phi \sim$ intermediate or GUT($\sim 10^{16} GeV/c^2$) scale in field theories and $\sim$ Planck ($\sim 10^{19} GeV/c^2$) or string (in between GUT and Planck scale) scale in string theories.

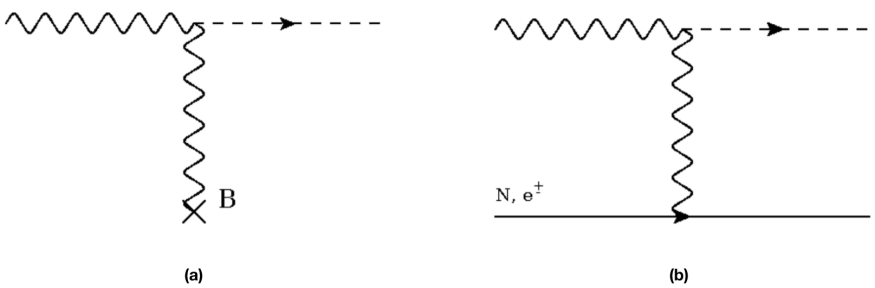

Figure 2.2: *ALP-photon coupling in (a) conversion of photon into ALP in an external magnetic field and (b) ALP production by photon scattering off a nucleus/electron. e.g. Primakoff process.*

2.2.2.2 Coupling with photons

A particularly interesting interaction is an ALP coupling with two photons. Unlike axions, a non-zero coupling is not guaranteed in this case. The interaction Lagrangian [124] is

$$\mathcal{L}_{A\gamma\gamma} = \frac{1}{4} g_{A\gamma\gamma} F_{\mu\nu} \widetilde{F}^{\mu\nu}\, \phi = -g_{A\gamma\gamma} \vec{E}.\vec{B}\, \phi, \tag{2.11}$$

where $g_{A\gamma\gamma}$ is the dimensionful coupling parameter, F is the electromagnetic (EM) field tensor and $\widetilde{F}$ is its dual, ϕ is the ALP field, $\vec{E}$ is the photon electric field and $\vec{B}$ is an external magnetic field. The Lagrangian $\mathcal{L}_{A\gamma\gamma}$ thus induces ALP-photon conversion or oscillations [125] in a strong external magnetic field (Fig.2.2a). Note that such conversion is only possible if the magnetic field is transverse to the ALP (spin 0) and photon (spin 1) propagation direction.

The reason for focussing on ALP-photon coupling is two-fold. Firstly, production of axions or ALPs from thermal photons in a stellar plasma is dominantly driven by such coupling [126], known as the Primakoff process ($\gamma + q \rightarrow a + q$, fig. 2.2b). The second reason is experimental: most searches dedicated to axions or ALPs are based on such interactions.

The possibility of ALPs as dark matter can be tested against their coupling to photons, the corresponding parameter landscape is shown in fig 2.3. The region labelled ′Standard ALP CDM ($m_1 = m_0$)[§§]′ is obtained from the simplest ALP model assuming a constant mass m_ϕ throughout the expansion of the universe. To

[§§] $m_1 \equiv m_\phi(t_1) \equiv 3H(t_1)$ is the mass at matter-radiation equality, m_0 is the present day mass.

account for present day DM abundance, the lifetime τ of ALP decay ($\phi \to \gamma\gamma$) cannot be shorter than the age of the universe, excluding the region labelled $'\tau_{ALP} < 10^{17}s'$. The impact of ALP decays on reionization history of the universe, as computed in [103], yields the exclusion region x_{ion}, which is compared against the extragalactic background light (EBL) [127], optical and X-rays. Experimental exclusion bounds from helioscope searches[¶¶] (e.g. CERN Axion Solar Telescope (CAST) [128, 129], Tokyo Axion Helioscope (SUMICO) [130]), 'light shining through wall'[***] [131] experiments (e.g. Any Light Particle Search (ALPS) [132]) and haloscope[†††] [133] searches are also illustrated in the figure. Unlike haloscope searches, the 'ALPS' and 'CAST+Sumico' bounds are quite generic and do not require ALPs to be the dark matter.

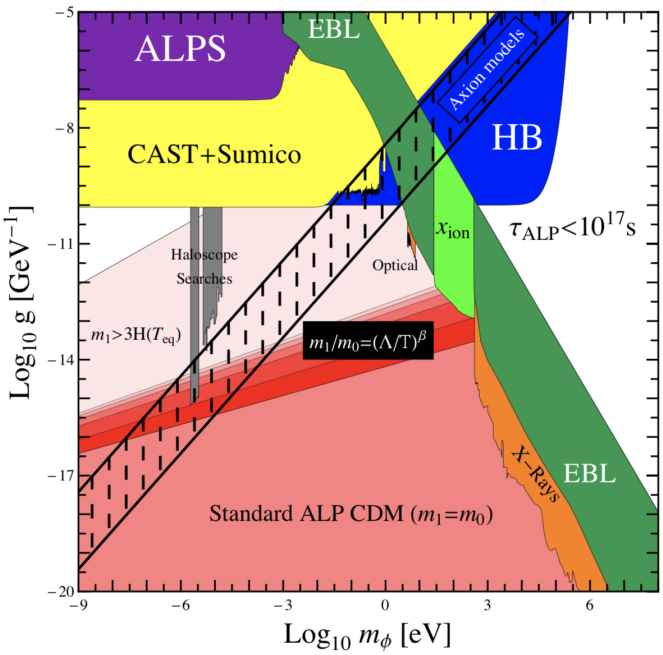

Figure 2.3: *Experimental bounds from [103] on ALP-photon coupling (g). Different shades of red are the allowed region of ALPs as DM. m_ϕ is the ALP mass. Details in text.*

Comparison of observed cooling rates of horizontal branch (HB) stars to those expected comprises an astrophysical probe to constrain [134, 135] energy losses

[¶¶]where a strong magnetic field is used to convert solar axions approaching the earth into detectable photons.

[***]where strong magnetic fields induce photon-ALP oscillations in a laser light fired against a wall. ALPs, being very weakly coupled, pass through a wall while photons get blocked. On the other side, ALPs can oscillate back into detectable photons.

[†††]exploit microwave cavities to search for axion/ALP in the local galactic dark matter halo.

in stellar cores due to ALP productions. Currently they provide the strongest astrophysical bounds, nearly probing the ALP DM region.

2.2.2.3 Coupling with electrons

Besides their generic interactions with gauge bosons, ALPs can also interact with fermions, especially with the electrons. The effective Lagrangian of the interaction is [136]

$$\mathcal{L}_{Ae} = g_{Ae}\frac{\partial_\mu \phi}{2m_e}\bar{\psi}_e\gamma^\mu\gamma_5\psi_e = -i\, g_{Ae}\bar{\psi}_e\gamma_5\psi_e\phi, \tag{2.12}$$

where g_{Ae} is the dimensionless coupling constant, m_e the electron mass, and ψ the electron spinor field. Some interesting interactions involving ALP-electron coupling are the Compton conversion ($ALP + e^- \rightarrow e^- + \gamma$), Axio-electric effect ($ALP + e^- + Z \rightarrow e^- + Z$) etc. The axio-electric effect in the context of LZ experiment will be discussed in detail in chapter 6.

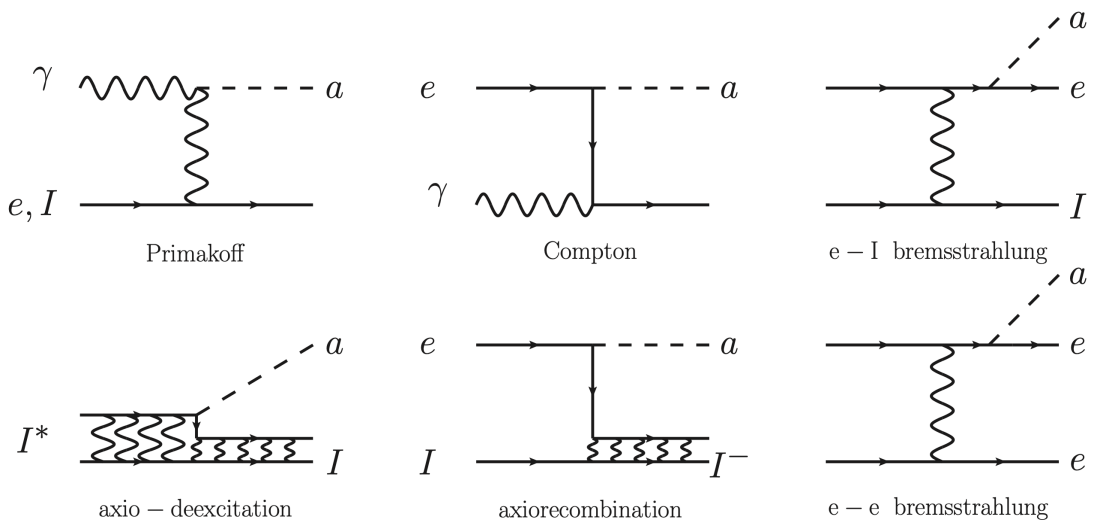

Figure 2.4: *Feynman diagrams of solar productions of axion/ALP in non-hadronic models. Figure from [136].*

ALP-electron couplings are particularly more model dependent. For example, tree-level couplings are possible in non-hadronic models (e.g. Dine-Fischler-Srednicki-Zhitnitsky (DFSZ) [137]) while hadronic models (e.g. Kim-Shifman-Vainshtein-Zhakharov (KSVZ) [138]) allow only loop-level ones. This creates a significant difference in stellar production of axion/ALPs [136]. For example, DFSZ-like models open up additional channels (see fig. 2.4) of stellar axion/ALP productions, e.g. electron-ion bremsstrahlung ($e + I \rightarrow e + I + \phi$),

electron-electron bremsstrahlung ($e + e \rightarrow e + e + \phi$), Compton scattering ($\gamma + e \rightarrow e + \phi$), axio-recombination ($e + I \rightarrow I^- + \phi$) and axio-deexcitation of ions ($I^* \rightarrow I + \phi$). For low mass stars, the Primakoff production is suppressed and the major contributions come from axio-recombination, bremsstrahlung and Compton (ABC) processes. g_{Ae} thus plays a dominant role in solar axion/ALP flux in non-hadronic models, allowing a way to constrain g_{Ae} by low mass star observations. Stringent limits come from different white dwarf cooling observations and studies of enhanced luminosity of red giant stars for axion-induced energy loss in the core. Outputs of some recent studies of the M5 global cluster [139] gave a limit $g_{Ae} < 4.3 \times 10^{-13}$. A combined analysis [140] of M5 and white dwarf data was also reported in 2017, and their fit gave $g_{Ae} = 1.6^{+0.29}_{-0.34} \times 10^{-13}$. Direct detection prospects of ALP-electron coupling will be discussed in detail in chapter 6.

2.3 Hidden photons (HPs)

Most of the theories of particle dark matter are particularly focussed on their weak coupling with the SM sector. The predicted cross-sections for DM-SM interactions are typically very small, but within the reach of sensitive detectors. However, null results from DM experiments over the years have developed a relatively new idea that DM actually resides in a ′hidden sector′ – a sector that does not interact with SM particles through known SM forces. The hidden sector has a characteristically rich structure and forces of its own. If the hidden sector is particularly motivated to solve the puzzle of dark matter and dark energy, it is also called the ′dark sector′. Nevertheless, the terms ′hidden sector′ and ′dark sector′ are often used interchangeably in the literature.

An exciting candidate for DM in the hidden sector is the hidden photon (HP), a hypothetical $U(1)'$ gauge boson that interacts with the visible sector via a loop-induced kinetic mixing with SM hypercharge $U(1)_Y$ gauge boson. Extra hidden $U(1)'$ symmetries often appear in supersymmetric extensions of the SM and is a generic feature of string theories [141].

Hidden photon can obtain a mass either via a hidden Higgs [142] or a Stückelberg mechanism [141, 143]. The first case, inspired by SM Higgs mechanism, introduces a new hidden Higgs (h') field in the hidden sector, which upon SSB, generates a hidden photon mass. In addition to mass generation of hidden sector particles, h'

can also pick up a minicharge (see section 2.3.2.3) allowing additional interactions with the SM sector. Unsuppressed hidden Higgs-SM Higgs interactions are also possible, providing a 'Higgs portal' [144] to probe the hidden sector. An alternative mechanism is the Stückelberg one, where an additional scalar field B generates masses of abelian vector bosons and preserves gauge invariance at the same time. The Stückelberg-like field appears naturally in large scale string compactifications. However, the hidden Higgs case also reduces to the Stückelberg if the h' mass is larger than energy scale in question [145].

2.3.1 HP cosmology

Being a WISP, HPs can be non-thermally produced via the misalignment mechanism [106] in the early universe. The underlying concept of misalignment has already been discussed in section 2.1.2 for a scalar/pseudoscalar case. Consider now a vector field V with a Lagrangian

$$\mathcal{L} = -\frac{1}{4}V_{\mu\nu}V^{\mu\nu} + \frac{m_V^2}{2}V_\mu V^\mu + \mathcal{L}_{grav} + \mathcal{L}_I, \tag{2.13}$$

where V^μ is the HP field and $V^{\mu\nu}$ is its field strength. $\mathcal{L}_I$ encodes HP interactions with SM particles, and $\mathcal{L}_{grav}$ governs a non-minimal coupling to gravity:

$$\mathcal{L}_{grav} = \frac{k}{12}RV_\mu V^\mu. \tag{2.14}$$

In eq. 2.14, k is a prefactor that parametrise the strength of such coupling and R is the Ricci scalar. In FRW universe,

$$\frac{R}{6} = -(2H^2 + \dot{H}). \tag{2.15}$$

In comoving co-ordinates (i.e. $\bar{V}_i = V_i/a(t)$), the equation of motion for V attains the form [103]

$$\ddot{\bar{V}}_i + 3H\dot{\bar{V}}_i + \left(m_V^2 + (1-k)(2H^2 + \dot{H})\right)\bar{V}_i = 0. \tag{2.16}$$

The indices i correspond to the spatial components, while the time component is zero as long as $m_V \neq 0$ [106]. Equation 2.16 has solutions in two different regimes:

- For $(3H >> m_V)$ and in the absence of the non-minimal coupling to gravity, $2H^2$ and $\dot{H}$ terms would dominate in eq. 2.16 and generate a large effective

mass for hidden photons. However, the situation would conflict with the flat potential requirement in the slow roll over regime of the standard inflation scenario. Inclusion of the non-minimal gravitational coupling (eq. 2.14) resolves this issue. For the simplest case of $k = 1$, the geometric contribution to the vector mass is precisely cancelled [103] in eq. 2.16. The situation resemblances the scalar case (described in section 2.1.2) and the fields $\bar{V_i}$ are approximately constant i.e. frozen. Study of the cases where $k \neq 1$ is of interest [103].

- For $(m_V >> H)$ and $(m_V^2 >> \dot{H})$, eq. 2.16 simply reduces to eq. 2.8 and the components V_i behave much like independent scalars. The subsequent underdamped oscillations show a non-relativistic behaviour (i.e. energy density varies as $\propto a^{-3}$), similar to that described in section 2.1.2, irrespective of the value of the prefactor k.

Nevertheless, the situation is essentially different than that for ALPs, which were pNGBs with an additional constraint of $\phi \leq \pi f_\phi$. HPs, in contrast, do not have a natural initial value for V_i. Note that if the HP mass is generated via Higgs mechanism, the inflationary misalignment might not work [106] to produce a DM condensate. In the Stückelberg case, on the other hand, no such problem exists [103].

Note that alternative mechanisms for HP production, both thermal and non-thermal, also exist in literature and are summarised in appendix A. The values of HP kinetic mixing (defined in section 2.3.2.1) required for the correct thermal relic abundance are bigger than the experimental limits by several orders of magnitude [146]. However, HPs can still be the dark matter if its early-universe production is contributed by the misalignment mechanism and/or inflationary fluctuations (appendix A). For details, see [146].

2.3.2 HP interactions and constraints

By definition, SM particles are not charged under the hidden $U(1)'$ symmetry and thus no direct coupling to HPs is allowed. However, several portals endowing very weak coupling between hidden and visible sectors still exist. The most thought-through portal is the kinetic mixing one, first proposed by Okun [147] and Holdom [148] in the early $'$80s. Such mixing appears in vacuum polarization diagrams in the field theories and is a natural assumption in the string theories.

2.3.2.1 Kinetic mixing

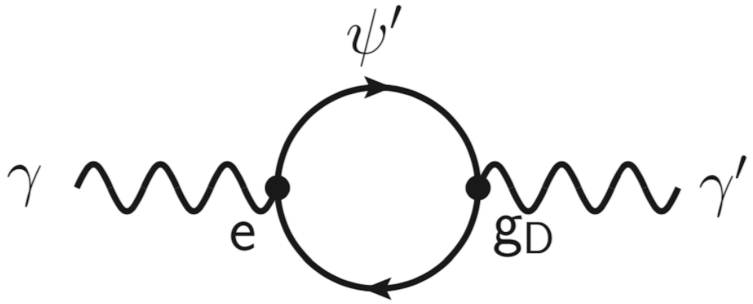

Figure 2.5: *Feynmann diagram of kinetic mixing.*

Hidden photons can couple [141, 149] to an SM hypercharge boson (or, below electroweak scale, a photon or a Z^0 boson) via kinetic mixing generated at high energies from loops of heavy particles (ψ' in fig. 2.5) charged under both $U(1)_Y$ and $U(1)'$. For n heavy Dirac fermions in the loop, the Lagrangian is

$$\mathcal{L} = \sum_n (i\bar{\psi}_n \gamma^\mu \partial_\mu \psi_n - m_n \bar{\psi}_n \psi_n - i g_n A^\mu \bar{\psi}_n \gamma^\mu \psi_n - i g'_n V^\mu \bar{\psi}_n \gamma^\mu \psi_n), \tag{2.17}$$

where the fermion species are labelled by $n = 1, 2....$ etc. g and g' are couplings to SM and hidden sector respectively. An integration over the loop momentum results in a fundamentally divergent integral (unless the diagrams add destructively) which, in full high energy theory, can be treated by a standard renormalization method [150]. In low energy (below the electroweak scale) effective theory, an explicit dimension-four operator,

$$\mathcal{O}_{KM} = -\frac{\kappa}{2} F_{\mu\nu} V^{\mu\nu}, \tag{2.18}$$

is induced in the effective Lagrangian [145]:

$$\mathcal{L}_{eff} \supset -\frac{1}{4} F_{\mu\nu} F^{\mu\nu} - \frac{1}{4} V_{\mu\nu} V^{\mu\nu} - \frac{\kappa}{2} F_{\mu\nu} V^{\mu\nu} + \frac{m_V^2}{2} V_\mu V^\mu + e J^\mu_{em} A_\mu. \tag{2.19}$$

J^μ_{em} is the EM current and $F_{\mu\nu}$, $V_{\mu\nu}$ are the field strength tensors[‡‡‡] of photon (A_μ) and HP (V_μ) fields respectively. Note that the direct HP-photon mixing in eq. 2.19 is valid as long as $m_V << m_Z$ (mass of Z^0 boson). Otherwise, additional mixing with hypercharge component of Z^0 should also be included.

The parameter κ represents the strength of the kinetic mixing and is usually

[‡‡‡]e.g. for photon, the field strength tensor is defined as $F_{\mu\nu} = \partial_\mu A_\nu - \partial_\nu A_\mu$.

non-vanishing [151] with a natural value of

$$\kappa \approx \frac{e g_h}{16\pi^2}, \tag{2.20}$$

where e and g_h are the visible and hidden gauge couplings respectively. In field theories $g_h \approx 1$ and κ attains an approximate value as $\sim 10^{-3}$ [152]. In large volume string compactifications, smaller g_h are possible and κ can be anywhere within the range $10^{-12} - 10^{-3}$ [141].

2.3.2.2 Photon-HP oscillation

The HP mass m_V in eq. 2.19 can be generated either by hidden Higgs or a Stückelberg mechanism. For simplicity, a Stückelberg generated m_V will be considered in the following. The kinetic part of 2.19 can be diagonalised by a field redefinition

$$V_\mu \to S_\mu - \kappa A_\mu, \tag{2.21}$$

with a resulting Lagrangian as

$$\mathcal{L}_{eff} \supset -\frac{1}{4} F_{\mu\nu} F^{\mu\nu} - \frac{1}{4} S_{\mu\nu} S^{\mu\nu} + \frac{m_V^2}{2} (S_\mu - \kappa A_\mu)^2 + e J^\mu_{em} A_\mu + \mathcal{O}(\kappa^2). \tag{2.22}$$

The kinetic mixing term is now absent, but the mixing parameter κ is shifted into a mass term that mixes the photon like state A_μ and a sterile state S_μ. These states are not actually the propagation eigenstates, but the interaction ones. A_μ interacts with ordinary electric charge while the sterile S_μ does not (hence named $'$sterile$'$). The non-diagonal mass term

$$\mathcal{L}_m = \frac{m_V^2}{2} (S_\mu - \kappa A_\mu)^2 = \frac{1}{2} m_V^2 S^\mu S_\mu - \kappa m_V^2 S^\mu A_\mu + \frac{1}{2} m_V^2 A^\mu A_\mu \tag{2.23}$$

allows a HP-photon oscillation where pure photon like states (A_μ) produced by electrons can oscillate into sterile states S_μ and vice versa. Substituting eq. 2.23 into eq. 2.22, an effective interaction term is obtained:

$$\mathcal{L}_{int} = -\kappa m_V^2 S^\mu A_\mu + e J^\mu_{em} A_\mu. \tag{2.24}$$

2.3.2.3 Interaction with SM electromagnetic charge

Instead of shifting the hidden gauge field V_μ (eq. 2.21) one can also shift the SM photon field A_μ:

$$A_\mu \to A_\mu^{shifted} - \kappa V_\mu. \tag{2.25}$$

Then the Lagrangian becomes

$$\mathcal{L}_{eff} \supset -\frac{1}{4}F_{\mu\nu}F^{\mu\nu} - \frac{1}{4}V_{\mu\nu}V^{\mu\nu} + \frac{m_V^2}{2}V_\mu V^\mu + eJ_{em}^\mu(A_\mu^{shifted} - \kappa V_\mu) + \mathcal{O}(\kappa^2). \tag{2.26}$$

The kinetic terms are still diagonalised, but instead of a mass term (eq. 2.23) carrying the mixing, a direct coupling $eJ_{em}^\mu(A_\mu^{shifted} - \kappa V_\mu)$ between SM EM current and the HP field V_μ is obtained.

However, the physical picture behind both redefinitions (eqs. 2.21 and 2.25) are equivalent. The choice of a particular approach is subject to computational convenience only, the physical observables will always have the same value.

2.3.2.4 Hidden photons as mediator

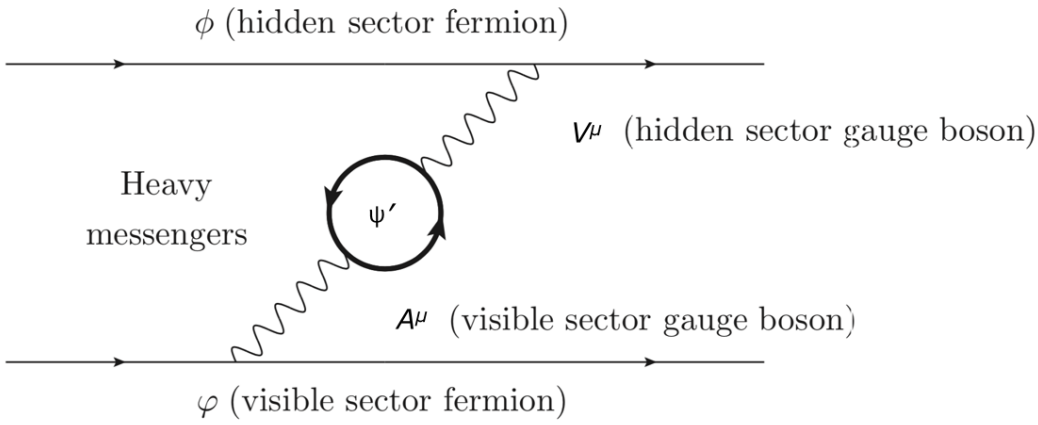

Figure 2.6: *Effective interaction between visible and hidden sectors via kinetic mixing. Figure from [150].*

HPs can also be considered as a 'mediator' of hidden sector-SM sector interactions. Particularly interesting is the case for a massless HP which is schematically represented in fig. 2.6. Consider a single species of hidden Dirac fermion (ϕ in fig. 2.6) that is charged under the hidden U' symmetry. It is possible for ϕ to interact with a SM fermion via the portal of HP-SM photon kinetic mixing. This

corresponds to an interaction Lagrangian

$$\mathcal{L} \supset -ig_h V^\mu \bar{\phi}\gamma_\mu \phi + i\kappa g_h A^\mu \bar{\phi}\gamma_\mu \phi. \tag{2.27}$$

The second term in eq. 2.27 is analogous to the SM photon-electron coupling, except that the charge is now modified by an order κg_h. From the viewpoint of effective field theory, κ is a completely arbitrary parameter, i.e. no quantisation condition is imposed on it. Hence the charge obtained by the hidden fermion ϕ under the SM electromagnetic field, i.e.

$$\epsilon = \frac{\kappa g_h}{e} \tag{2.28}$$

is not quantised as well. In other words, hidden fermions integrally charged under hidden $U(1)'$ have obtained a rational charge (often called 'minicharge') under the SM $U(1)$ field. This can be further generalised into wider hidden sector physics, where a particle residing in the hidden sector interacts with the SM particles through an additional new mediator particle (that may or may not be massless). For example, in the secluded HP scenario [153], the mediator (HP) mass is lighter than that of the DM and they cannot decay into DM, hence the name 'secluded'.

2.3.2.5 Constraints on HP parameter space

The question of experimental interest is what the accessible parameter space (m_V, κ) for HP is. The cosmological constraints for the thermal production scenario is discussed in appendix A. This section will consider a more general landscape (fig. 2.7), with the constraints on heavy thermal HP shown in an orange band at the far right side of the plot. Bounds from number of effective neutrino studies (N_ν^{eff}), solar HP studies ('Solar lifetime') and Far-InfraRed Absolute Spectrophotometer (FIRAS) results (labelled 'CMB') have also been shown.

The bound on optical depth $\tau_2 > 1$ computed in [103] comes from the 'resonance crossing' [155] arguments on photon-HP oscillations in an expanding universe. The region labelled 'Coulomb' comes from tests of Coulomb's law at low mass regions. Experimental constraints from CAST, ALPS and haloscope searches are also shown.

Note that 'Coulomb', 'CMB', 'ALPS', 'CAST' and 'Solar Lifetime' exclusion regions do not require HP to be dark matter. The light pink region, on the other

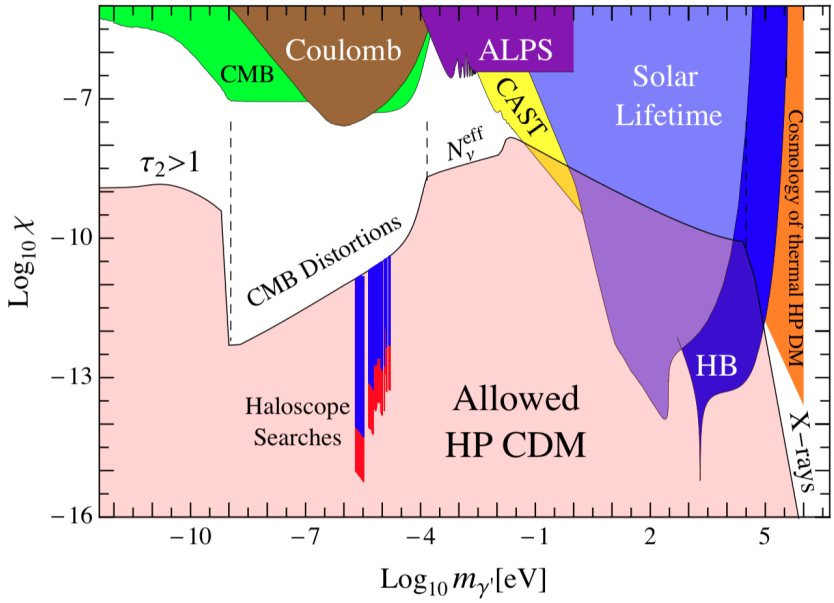

Figure 2.7: *Experimental bounds on hidden photon kinetic mixing [103].*

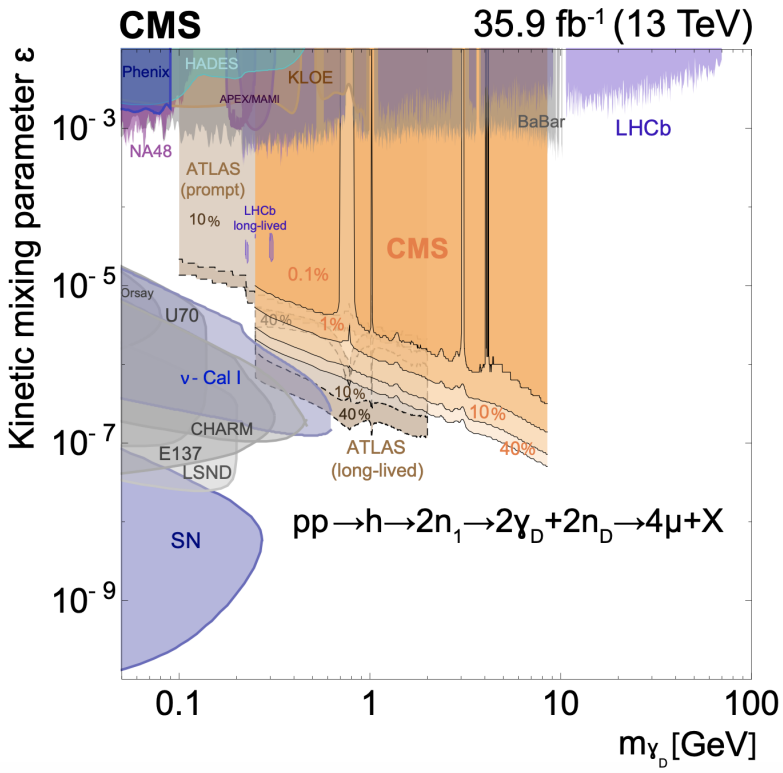

Figure 2.8: *Collider bounds on hidden photon kinetic mixing (denoted by ϵ) from [154, and references therein] in a dark SUSY scenario for the process $pp \to h \to 2n_1 \to 2\gamma_D + 2n_D \to 4\mu + X$ with $m_{n_1} = 10\,GeV$ and $m_{n_D} = 1\,GeV$. The coloured contours correspond to different values of the branching fraction $\mathcal{B}(h \to 2\gamma_D + X)$ in the range 0.1–40%. Details in [154].*

hand, is the allowed parameter space for HP as CDM. Direct detection prospects of HP CDM will be discussed in detail in chapter 6.

High energy colliders (e.g. A Toroidal LHC ApparatuS (ATLAS) [156] and the Compact Muon Spectrometer (CMS) at the Large Hadron Collider (LHC) [154]) probe GeV/c^2 - TeV/c^2 scale HPs in general, via HP production and decays. For example, fig. 2.8 shows the 90% CL upper limit on kinetic mixing parameter (black solid curves) from CMS search for new light bosons decaying into muon pairs via the dark SUSY process [154]:

$$pp \to h \to 2n_1 \to 2\gamma_D + 2n_D \to 4\mu + X, \tag{2.29}$$

where h is a Higgs boson, γ_D is the light hidden photon, n_1 is the lightest non-dark neutralino, n_D is an undetected dark neutralino and X are the spectator particles predicted in several models [157]. The coloured contours correspond to different values of the branching fraction $\mathcal{B}(h \to 2\gamma_D + X)$ in the range 0.1–40%.

2.4 Chapter summary

The topics covered in this chapter are:

- A wide landscape of particle dark matter candidates, including both WIMPs and non-WIMPs, exists beyond the Standard Model.
- A good DM candidate must satisfy the cosmological, astrophysical and existing experimental constraints to date and reproduce the DM relic abundance.
- ALPs and HPs are viable dark matter candidates. ALPs can be detected via their weak coupling to the SM sector. HPs, despite residing in a hidden sector, can couple to the visible sector via kinetic mixing with SM photons.

Basically, these yet-undetected particles (WIMPs, ALPs or HPs) can reside anywhere in their wide parameter spaces. Experimental DM detection thus have been an emerging field of interest in recent years. The goal of the direct or indirect searches is two fold: either to detect (i.e. $'$discover$'$) the hidden dark matter or to exclude certain region of the parameter space providing important constraints. The following chapter will illustrate specific experimental techniques that have been developed to achieve these goals.

Chapter 3

Direct Detection of Dark Matter: the LUX-ZEPLIN (LZ) Experiment

The landscape of theoretically motivated DM candidates is huge – probing them all is beyond the capability of a single detector. A synergistic effort is thus required from a diverse array of detection experiments. Three different lines of approach can be adopted, as shown schematically in fig. 3.1a. Despite having a common goal of detecting the dark matter, each of these approaches has its own pros and cons. Collider probes of dark matter are based on DM production in a controlled laboratory environment (typical detector time-scales are $\sim 100\,ns$) but can not determine its cosmological stability ($\sim$ age of the universe). Indirect searches look for primary or secondary products of self-annihilation or decays of cosmological DM but suffer from unavoidable astrophysical backgrounds. A third and alternative option is to detect the DM around the Earth in an Earth-based low-background environment, directly via their interactions with ordinary material.

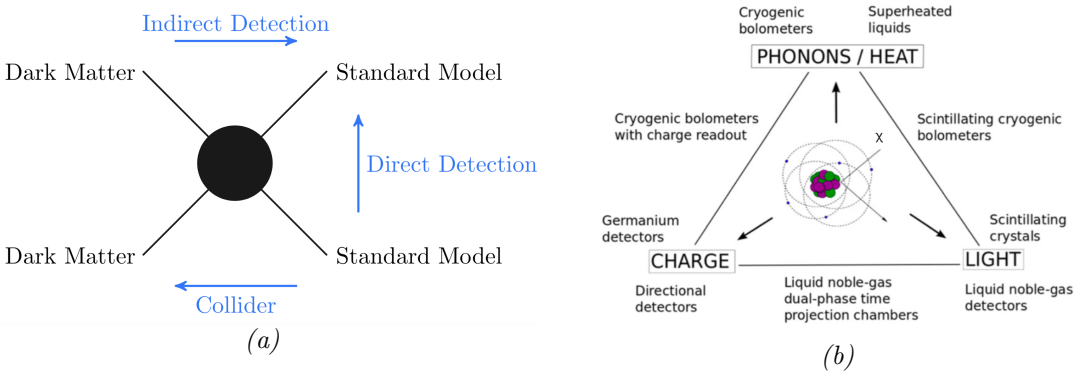

Figure 3.1: *(a) Three routes of dark matter detection. (b) Direct detection technologies [72].*

Depending on the interaction type, target material and energy deposition, three

different signatures can be searched for in a direct detection experiment – atomic ionization of target material, release of scintillation photons from excited target atoms and the heat production (phonons in crystal). Use of all three signatures in a single detector would be ideal, but it is very difficult in reality. Direct detection experiments to date are either based on one particular signature or on a powerful combination of two (positioned in between the corresponding signatures in fig. 3.1b). In the later case, the relative size of the two signatures facilitates identification of the particle that deposited the energy, enabling a better electron recoil (ER) - nuclear recoil (NR) discrimination. Since most backgrounds sit in the ER band, an ER-NR discrimination facilitates the background rejection in the data collected. The Large Underground Xenon (LUX) experiment and its successor LUX-ZEPLIN (LZ) are leading direct detection experiments in this context.

This chapter is mainly devoted to technical details of the LZ experiment. A brief summary of other direct, indirect and collider DM searches will be covered in section 3.5 at the end.

3.1 Recoil kinematics

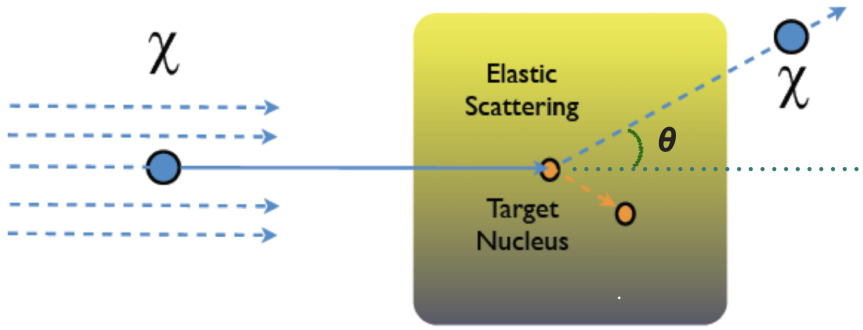

Figure 3.2: *Elastic scattering of a DM particle (χ) with a target nucleus.*

Conventional direct detection is mainly focussed on the elastic scattering of a DM particle (χ) with a target nucleus N (fig. 3.2). The nucleus N is initially at rest, which is a good assumption at room temperatures and below. χ particles from the CDM halo are moving with non-relativistic speeds. Non-relativistic calculations for two-body elastic scattering yield a recoil energy of

$$E_{NR} = \frac{v^2 \mu^2}{M_N}(1 + \cos\theta) \tag{3.1}$$

for a single nucleus of mass M_N, where M_χ is the dark matter mass, v is the dark matter velocity, θ is the scattering angle (defined in fig. 3.2) and

$$\mu \equiv \frac{M_\chi M_N}{(M_\chi + M_N)} \tag{3.2}$$

is the reduced mass of the DM-nucleus system. For WIMP searches, μ lies within $1 - 133\,GeV$. Assuming a typical DM velocity, $v \sim 10^{-3}c$ and ignoring the annual modulation, the maximum possible recoil energy in direct detection is roughly $E_{NR}^{max} \simeq 20$ - $200\,keV$.

Direct detection via NR is less effective for low dark matter masses, as they produce nuclear recoils with very small E_{NR}. An alternative way is to search for an ER signal caused by, for example, the scattering of a χ particle with an electron of the target atom [158] or absorption of a DM particle by a bound electron (chapter 6). The later will be discussed in detail in chapter 6, in the context of HP and ALP searches with the LZ detector.

3.2 Liquid xenon as a detection medium

Liquid xenon (LXe) is a sensitive detection medium with a unique** capability to produce both the charge carriers and scintillation photons upon particle interactions. This facilitates the use of LXe in dual phase time projection chambers (e.g. LZ) enabling particle identification and a better ER-NR discrimination.

3.2.1 Physical properties

Scintillation properties of liquefied noble gases and their suitability as radiation detectors are well-known since the mid-twentieth century [160]. Noble gas detectors to date make use of liquid xenon (LXe) and liquid argon (LAr), whereas some research and development (R&D) activities are being developed to utilize liquid neon (LNe) [161] as well.

Table 3.1 presents some selective properties of LXe, LAr and LNe in the direct detection context. Liquid noble gases are stable, dense, homogeneous, very good dielectrics and chemically inert. Their $\sim K$-scale boiling points make the

**The only other liquid rare gas that share this capability is liquid argon (LAr) [159].

Table 3.1 *Comparison of some selective properties of noble liquids. Numbers are taken from [162].*

Properties	Xe	Ar	Ne
Atomic number, Z	54	18	10
Molar mass (g/mole)	131.3	39.95	20.18
Boiling point T_b at 1 atm (K)	169	87.26	27.102
Liquid density at T_b (g/cm^3)	3.10	1.40	1.20
Scintillation wavelength (nm)	175	125	78
Scintillation yield (photons/MeV)	42	40	30
1st ionisation energy (eV)	12.1	15.8	21.6
Long lived radioactive isotopes	^{136}Xe	^{39}Ar,^{42}Ar	none
Price	High	Low	Moderate

liquefaction and the detector operation easier than the $\sim mK$ scale cryogenic bolometers. They have very high scintillation yields (allowing a low energy threshold) and are transparent to their own scintillation (with wavelengths in the ultra-violate regimes). In general, LNe and LAr detectors require wavelength shifters[†] to detect the scintillation light in the visible blue wavelength region ($\sim 400\,nm$). For LXe, photo-sensors with quartz windows transparent to Xe scintillation light are used. Both LXe and LAr have high ionisation capabilities, facilitating a dual channel (ionisation and scintillation) detector configuration. A good ER-NR discrimination can be achieved via the charge/light ratio and pulse shape discrimination of scintillation light pulse. Additionally, liquid noble gases have modest NR quenching factors, high electron mobilities and low electron diffusions.

All liquid noble gases have a high stopping power (i.e. short attenuation length) for penetrating radiations. This property, known as the ′self-shielding′, naturally ′shields′ the inner (′fiducial′) detector volume against the external backgrounds. The larger the detector is, the more effective is the self-shielding. Use of liquid noble gases as detection media thus foster large volume detectors, which can be easily constructed at reasonable costs and practicalities.

Among the noble liquids, LXe has the highest scintillation and ionisation yields and the highest stopping power (owing to its atomic number and density) for γ-rays. Natural Xe is highly radio-pure (except for $^{136}Xe\,2\nu\beta\beta$ decay [163, 164]) and any ^{85}Kr contamination can be reduced by charcoal or cryogenic distillation

[†]to convert the scintillation photons into UV or visible light so that comparatively inexpensive PMTs can be used for light detection.

process. The neutron-odd isotopes (^{129}Xe, ^{131}Xe) with high mass number allow to probe both spin-independent (SI) WIMP-nucleon and spin-dependent (SD) WIMP-neutron interactions. All these properties make LXe an excellent medium for dark matter direct detection.

3.2.2 Scintillation mechanism

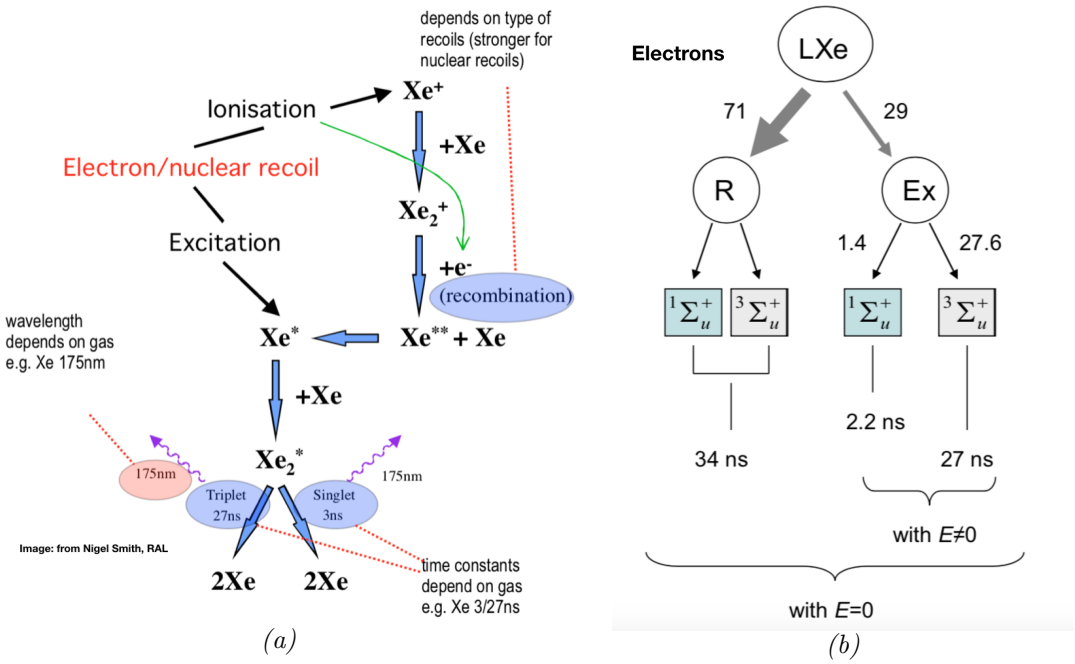

Figure 3.3: *(a) Energy deposition channels in liquid xenon. (b) Observed energy distribution (in %) to recombination (R) and excitation (Ex) channels for fast electrons. Decay times of singlet and triplet states are also shown. Figure from [165].*

Scintillation of LXe, upon particle interaction, can be produced in two processes:

1. **Diatomic excitation:** Excitation of Xe atoms, either by an electron or nuclear recoil, can form excited diatomic molecules called excimers ($Xe_2^{*,v}$ in eq. 3.3). Both vibrational (superscript v in eq. 3.3) and electronic (superscript $*$ in eq. 3.3) excitations are possible. Vibrational relaxations are mostly non-radiative (infra-red emissions are also possible). Electronic relaxation of Xe_2^*, however, from one of its two lowest electronic excited states ($^3\Sigma_u^+$, $^1\Sigma_u^+$) to the ground state $^1\Sigma_g^+$ emits an vacuum ultraviolet (VUV) scintillation photon. The ground

state is unstable, thus causing a dissociation of Xe_2 molecule.

$$\begin{aligned} X + Xe &\rightarrow Xe^* + X && \text{(impact excitation)} \\ Xe^* + Xe &\rightarrow Xe_2^{*,v} && \text{(excimer formation, } \sim \text{ps)} \\ Xe_2^{*,v} + Xe &\rightarrow Xe_2^* + Xe && \text{(vibrational relaxation)} \\ Xe_2^* &\rightarrow Xe + Xe + \gamma && \text{(VUV emission, } \sim \text{ns)} \end{aligned} \tag{3.3}$$

Here X is the recoiling electron or nucleus initiating the process.

2. **Recombination:** Ionisation of Xe atoms by an incoming particle is followed by subsequent recombinations of ionised electrons, mostly with molecular ions. Relaxation of the resulting excited Xe^{**} states to Xe^* is non-radiative and some heat is generated in the process. Xe^* then forms an excimer ($Xe_2^{*,v}$) which de-excites (similarly as in eq. 3.3) by release of a VUV photon.

$$\begin{aligned} X + Xe &\rightarrow Xe^+ + e^- + X && \text{(ionisation)} \\ Xe^+ + Xe + Xe &\rightarrow Xe_2^+ + Xe \\ e^- + Xe_2^+ &\rightarrow Xe^{**} + Xe && \text{(recombination, } \sim \text{ps)} \\ Xe^{**} + Xe &\rightarrow Xe^* + Xe + heat \\ Xe^* + Xe &\rightarrow Xe_2^{*,v} && \text{(excimer formation} \sim \text{ps)} \\ Xe_2^{*,v} + Xe &\rightarrow Xe_2^* + Xe && \text{(vibrational relaxation)} \\ Xe_2^* &\rightarrow Xe + Xe + \gamma && \text{(VUV emission, } \sim \text{ns)} \end{aligned} \tag{3.4}$$

The relative populations of $^3\Sigma_u^+$ and $^1\Sigma_u^+$ states are different than in the diatomic excitation case and depend on the type and energy of the incoming particle causing the recoil. The corresponding difference in the pulse shape of VUV photons (shorter for singlet de-excitation and longer for triplet de-excitation) can be used to discriminate between ER and NR. For single phase detectors, this is the only means of ER-NR discrimination. The pulse shape discrimination (PSD), although more difficult for LXe than in LAr, has been used before in ZEPLIN-I detector [166].

The relative contribution of scintillation yield in the excitation and recombination channels due to fast electrons is shown in fig. 3.3b. In LXe, a significant time delay occurs for the slow recombination process (fig. 3.3b) that creates a non-exponential component in the decay curve. This can be removed by applying an electric field, E. In the absence of an electric field, the scintillation yield decreases by a factor of ~ 3.

3.2.3 Effective scintillation efficiency

The total energy (E_{dep}) deposited by an incoming particle in LXe, either via nuclear or electron recoil, is divided in three channels (fig. 3.3a): ionisation, excitation and heat [159]. Only the first two channels cause the scintillation, i.e. they yield detectable quanta. The scintillation yield is given by [159]

$$\frac{E_{dep}}{W_{ph}} = f(n_i + n_{ex}), \tag{3.5}$$

where n_i and n_{ex} are, respectively, the number of electron-ion pairs and the number of excimers. W_{ph} is the work function, i.e. the minimum energy needed to produce a scintillation photon. An error-weighted average of the values calculated by Doke et al. [167] and Dahl [168] is $W_{ph} = 13.7\,eV$. f is a quenching factor to account for the effects that suppress ($'$quench$'$) the scintillation yield, e.g. energy loss via heat production. Quenching in ER is negligible and it is conventional to take $f_{ER} = 1$. The effect of heating due to kinetic energy ($4.65 - 5.35\,eV$ [165]) of ionised electrons is absorbed in the value of W_{ph} itself. Comparing the forms of eq. 3.5 for ER and NR, the quenching factor for NR can be expressed as

$$\begin{aligned} \frac{1}{f_{NR}} &= \frac{[(n_i + n_{ex})/E_{dep}]_{NR}}{[(n_i + n_{ex})/E_{dep}]_{ER}} \\ &= \frac{\text{scintillation per unit energy for NR}}{\text{scintillation per unit energy for ER}}. \end{aligned} \tag{3.6}$$

Some particularly interesting quenching factors are:

- **Nuclear quenching:** For nuclear recoils, a considerable amount of energy is spent in the recoiling effect (i.e. atomic motion, producing heat) which does not result in excitation or ionization. The fractional energy loss in this process is given by the Lindhard's [169] factor,

  $$q_{ncl} = \frac{k\,g(\epsilon)}{1 + k\,g(\epsilon)}. \tag{3.7}$$

  For a nucleus ${}^{A}_{Z}X$, $k = 0.133\,Z^{2/3}\,A^{-1/2}$, the reduced energy $\epsilon = 11.5\,E^{NR}_{dep}\,Z^{-7/3}$ and the function $g(\epsilon)$ can be fitted by $g(\epsilon) = 3\epsilon^{0.15} + 0.7\epsilon^{0.6} + \epsilon$.

  For LXe, $Z = 54$, $A = 131$ and q_{ncl} is non-negligible for $E^{NR}_{dep} < 10\,MeV$.

- **Bi-excitonic/electronic quenching:** Hitachi proposed [170] a second type

of quenching due to the ′bi-excitonic′ collisions of the type

$$Xe^* + Xe^* \rightarrow Xe + Xe^+ + e^-. \tag{3.8}$$

In the absence of such collisions, each of the two Xe^* would produce one excimer ($Xe_2^{*,v}$) and emit one VUV photon. But a bi-excitonic collision reduces the number of potential photons from two to one (if the resulting electron-ion pair recombines) or zero (if the resulting electron escapes the recombination by drifting away). In either case, the scintillation yield is reduced.

Based on Birk's saturation law [171], the bi-excitonic quenching factor is

$$q_{el} = \frac{1}{1 + k_b \frac{dE}{dx}}, \tag{3.9}$$

where dE/dx is the linear energy transfer (LET), i.e. energy transferred by an ionising particle per unit distance traversed. The Birk's constant, k_b is to be empirically determined. The heavier (i.e. slow moving) the ionising particle is, the higher is the LET. Thus, NR tracks are expected to be denser, shorter and more heavily quenched than the ER ones.

- **Escape electrons:** A third effect to be taken into account is the electrons escaping recombination with ions, which is again greater for NRs (dense tracks, probability of recombination is higher) than in ERs, even in the absence of an external electric field [167]. The quenching due to escape electrons can be expressed as [172]

$$q_{esc} = \frac{\alpha + 1 - \beta_{NR}}{\alpha + 1 - \beta^{122}}, \tag{3.10}$$

where n_{esc} is the number of escaped electrons, $\alpha = n_{ex}/n_i$ and $\beta = n_{esc}/n_i$. The superscript 122 refers to the $122\,keV$ ERs from ^{57}Co, which is a conventional [173] gamma source for energy calibration. The calculated value for LXe is $\beta^{122} \sim 0.31$ [173]. The values often used for α [165] for LXe are:

$$\begin{aligned} &\text{(ER)} \qquad \alpha = \begin{cases} 0.06, & \text{(calculated)} \\ 0.2, & \text{(measured)} \end{cases}, \\ &\text{(NR)} \qquad \alpha \sim 1. \end{aligned} \tag{3.11}$$

The reciprocal of f_{NR} is called the effective (or relative) scintillation efficiency, $\mathcal{L}_{eff}$. The experimental measurement of $\mathcal{L}_{eff}$ consists of measuring the denominator of eq. 3.6 for photo-absorption events of $122\,keV$ γ-rays from ^{57}Co. An empirical model by Manzur et al. [172] gives a relative scintillation efficiency

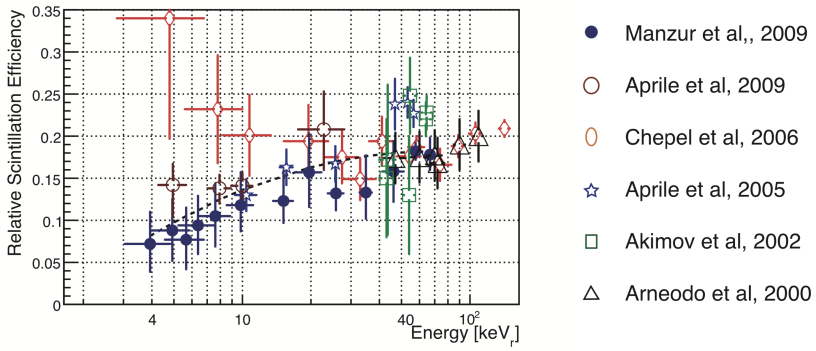

Figure 3.4: *Measurements of the relative scintillation efficiency in liquid xenon as a function of nuclear recoil energy from [172]. The dashed line corresponds to the empirical model described in the text.*

in terms of the previously mentioned quenching factors as

$$\mathcal{L}_{eff} = q_{ncl} \cdot q_{esc} \cdot q_{el}. \tag{3.12}$$

The measured values of $\mathcal{L}_{eff}$, as a function of nuclear recoil energy, is shown in fig. 3.4 where the dashed line represents the empirical model.

3.3 Dual phase xenon time projection chamber

3.3.1 Working principle

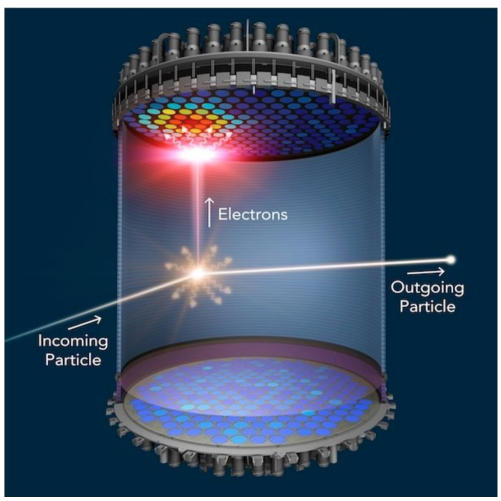

Figure 3.5: *Working principle of a dual phase time projection chamber.*

A dual phase xenon time projection chamber (TPC) uses xenon as a detection medium, both in liquid and gaseous phases. The chamber is usually of a cylindrical shape (fig. 3.5). It is divided into two regions, lower and upper,

hosting ultra-pure xenon in liquid and gaseous phases respectively. Liquid xenon, upon interaction with an incoming particle, promptly emits a scintillation light (primary scintillation signal, S1), accompanied by a number of ionisation electrons. A homogeneous electric field is applied vertically across the lower chamber (i.e. between the cathode at the bottom and the gate electrodes just below the liquid-gas interface) causing an upward drift of ionisation electrons towards the gaseous phase. These electrons are accelerated into the gaseous phase by a second stronger electric field across the upper chamber (i.e. between the gate and the anode at the top of the TPC). Their inelastic interactions with gas atoms produce an electroluminescence signal denoted as S2. Being proportional to the number of extracted electrons (i.e. to the primary ionisation), S2 is also called a secondary scintillation or ionisation.

The primary (S1) and secondary (S2) scintillation signals are detected by two arrays of photomultiplier tubes (PMTs), positioned at the bottom and at the top of the TPC respectively. A set of S1 and S2 signals provides some important information on an interaction occurring within the detector:

- **Energy deposition:** A linear combination of S1 and S2 signals reconstructs the total energy deposited by an incoming particle in the liquid xenon.
- **3D position reconstruction** The location of the event in the horizontal (xy) plane is given by the distribution of S1 signals in the bottom PMT array. The vertical (z) co-ordinate is determined by the time separation of S1 and S2 signals.
- **ER-NR discrimination:** The ratio of S2 and S1 signals is different for ER and NR, owing to the different densities of ionisation tracks, and ensures a strong background discrimination ($> 99\%$ rejection for ER).

3.3.2 Signal yields: S1 and S2

The quantities n_i and n_{ex}, the number of electron-ion pairs and excimers, are not directly measurable in practice. Only the VUV photons (n_γ) and the recombination-escaped electrons (n_e) can be observed in a detector. As discussed in section 3.2.2, both excitation and ionisation contribute to n_γ. Denoting the fraction of n_i that leads to VUV emission as r, n_γ and n_e can be expressed as

$$n_\gamma = n_{ex} + rn_i = (\alpha + r)n_i, \qquad n_e = (1 - r)n_i. \tag{3.13}$$

The size of the prompt scintillation signal should be directly proportional to n_γ:

$$S1 = g_1 n_\gamma, \tag{3.14}$$

where g_1 is the probability of one scintillation photon producing (at least) one photo-electron (phe) in the PMT. It depends on the geometrical light collection efficiency and PMT quantum efficiency. The electrons n_e are extracted in the gas phase where they generate the secondary ionisations. The $S2$ signal is thus proportional to n_e:

$$S2 = g_2 n_e, \tag{3.15}$$

where the constant g_2 depends on the electron extraction efficiency of the detector. The $S1$ and $S2$ signals are expressed in the units of detected photons (phd). The gain factors (g_1 and g_2) are expressed in $phd/quantum$. In terms of $S1$, $S2$, g_1 and g_2, eq. 3.5 can be re-written as

$$E_{dep} = fW_{ph}(1+\alpha)n_i = fW_{ph}(n_\gamma + n_e) = fW_{ph}\left(\frac{S1}{g_1} + \frac{S2}{g_2}\right). \tag{3.16}$$

Values of g_1 and g_2 are quantified with detector calibrations with sources of known distribution.

3.4 LUX-ZEPLIN (LZ) experiment

LUX-ZEPLIN (LZ) is a second generation direct detection experiment formed by two former collaborations: Large Underground Xenon (LUX) [174] and ZonEd Proportional scintillation in LIquid Noble gases (ZEPLIN) [175, 176]. ZEPLIN was a pioneer in the field of LXe detectors: a series of single (ZEPLIN-I, late 1990s) and dual (ZEPLIN-II and III, 2006-2011) phase experiments took place at the Palmer underground laboratory, Boulby, UK. The LUX experiment at the Sanford Underground Research Facility (SURF) in Lead, South Dakota was operated by more than 27 institutions in the US, UK, Portugal and Russia during 2009-2016. Its successor, the LZ detector, is currently being installed in the same Davis cavern at SURF (4850 ft underground) and the first science run is planned to start in 2020. The LZ collaboration consists of 257 scientists and engineers from 37 institutions in US, UK, Portugal and South Korea: the University of Edinburgh is one of them.

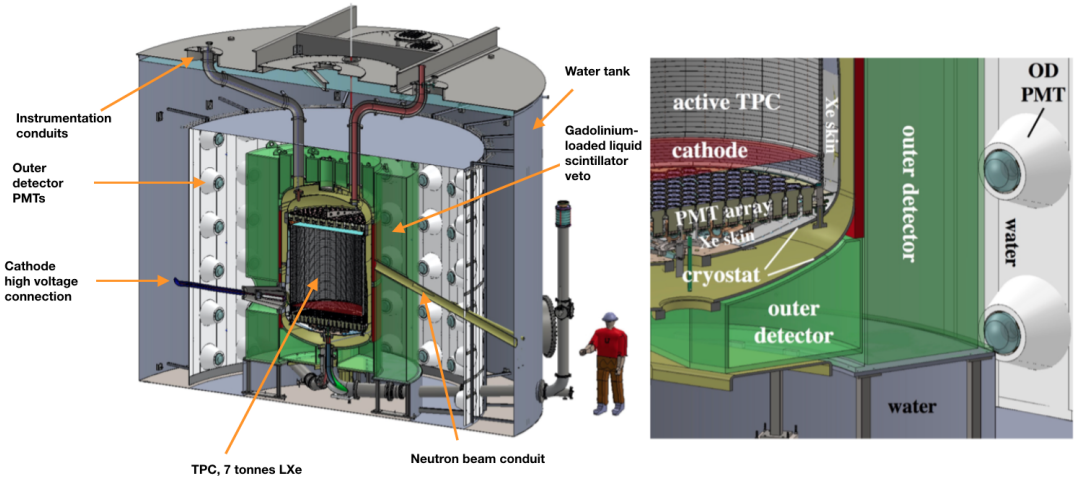

Figure 3.6: *(Left) A cutaway drawing of the LZ detector, figure modified from [63]. (Right) Expanded view of the cathode region [63]. 'OD PMT' indicates the outer detector photo-multiplier tubes.*

3.4.1 Detector design and veto strategy

Fig. 3.6 shows a cutaway design of the LZ detector housed inside the water tank inherited from LUX. The rock overburden the Davis cavern effectively reduces the cosmic muon flux and the 228 tonnes of ultrapure water in the tank will act as a 'veto' for the remnant, i.e. will tag muons and muon-induced fast neutrons. It will also shield the detector against the cavern radioactivity (γ-rays and neutrons). The inner Tyvek linings of the tank will improve the light efficiency. A cylindrical array of 120 water-proof 8″ Hamamatsu R5912 PMTs will be implemented in the wall of the water tank. These PMTs will detect Cherenkov light coming from the outer detector (OD) surrounding the LXe TPC.

The OD consists of 10 acrylic tanks filled with gadolinium-loaded liquid scintillator (GdLS). The liquid scintillator (e.g. linear alkylbenzene (LAB)) has a high moderating (i.e. slowing down or thermalising) power for the fast neutrons, and gadolinium (Gd) increases its thermal neutron capture[‖] cross-section. This powerful combination enables the OD to tag the single scatters induced by the internally generated[¶] fast ($\sim 1\,MeV$) neutrons in LXe, which would otherwise mimic a WIMP signal. To understand how this tagging is done, consider a fast neutron that undergoes a single scatter in LXe and escapes into the OD. The GdLS in the OD region first slows the neutron down and then captures it, intiating a cascade of $\sim 8\,MeV$ γ-rays. These gamma rays are easily distinguished from the background radioactivity (typically $\sim 2.6\,MeV$ γ-rays from ^{208}Tl) in the OD region. The OD thus acts as an 'anti-coincidence' detector (i.e. a neutron 'veto')

and effectively increases the detector's fiducial volume.

The OD surrounds an ultra-pure titanium-made cryostat vessel [177] maintained at $175K$ that contains the LXe TPC. The cryostat consists of three parts: an inner vessel, an outer vessel, and a cryostat support system. The multi-layer insulation (MLI) between the inner and outer vessels provides the contingency against rapid warm up in the event of an air or water leak in to the vacuum region. The LXe TPC is cylindrical with an equal height and diameter ($1.46\,m$) and a highly reflective polytetrafluoroethylene (PTFE) inner coating to maximise the light collection. The PTFE panels will have an embedded electric field cage consisting of 57 rings to define the vertical drift field. The electric field will be provided by four horizontal grids of electrodes made from thin stainless steel wires: a gate grid just below the liquid-gas interface, an anode grid at the top to extract the ionization electrons in the gaseous phase, a cathode grid at the bottom and a fourth additional grid below to shield the bottom PMTs from the cathode potential. The $\sim 13.8\,cm$ region between the cathode and the fourth additional grid will have a $'$reverse$'$ field and energy deposited here will only create S1 signals. The high voltage connection to the cathode will be established via a xenon-filled feed-through cable.

The detector will use ~ 10 tonnes LXe in total, with ~ 7 tonnes of active xenon as the WIMP-target within the TPC, $\sim 840\,kg$ LXe in the reverse field region and ~ 2 tonnes of LXe enveloping the TPC as a $'$skin$'$. The LXe skin, optically decoupled from the main LXe volume, comprises of the LXe beneath the bottom PMT array and the $\sim 4-8\,cm$ region between the outer surface of the PTFE panels and the inner titanium wall of the cryostat vessel. This skin will be instrumented with 131 Hamamatsu R8778 PMTs (93 $1''$ PMTs near the LXe level and 38 $2''$ ones near the bottom) and will effectively veto the γ-rays. I played an active role in the performance tests of the top skin PMTs at the University of Edinburgh which will be addressed in chapter 4.

The veto efficiency of the skin alone is limited, but the integrated (OD+skin) system enhances the overall veto performance. The design requirement is a veto efficiency of $> 90\%$ for neutrons and $> 70\%$ for gamma-rays escaping the TPC. The two stage (OD+skin) veto strategy of LZ is illustrated in fig. 3.7.

‖capture time $\sim 30\,\mu s$.

¶e.g. via (α, n) reaction or fission.

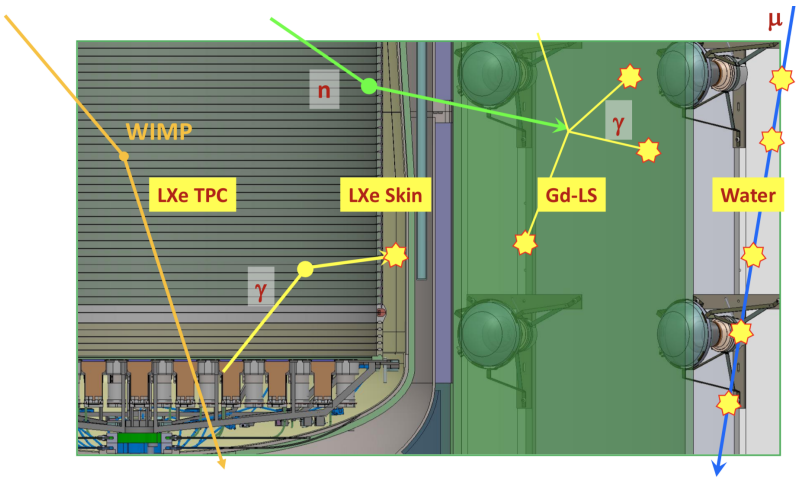

Figure 3.7: *Veto strategy of LZ detector. Picture from [178].*

Particle interactions within active LXe volume will be detected by 494 Hamamatsu R11410-22 PMTs (with 3″ diameter each), 241 at the bottom in a hexagonal array to maximise the S1 light collection and 253 at the top in a hybrid array (hexagonal at the centre but circular at the perimeter) for optimised position reconstruction of the wall events. These PMTs have ultra low background [179] and a $> 30\%$ quantum efficiency at the LXe VUV wavelength ($175\,nm$). The signals from the PMTs, once amplified and shaped, will flow to the data acquisition system (DAQ) to be digitized. Once digitized, they will be sent to the data collectors and stored in disks. The design of analog and digital electronics depends on the type of the PMT concerned (i.e. TPC, skin or OD).

The detector temperature will be controlled by an array of liquid nitrogen (LN)-cooled thermosyphons. The LXe purity will be ensured by a high capacity Xe circulation and purification system in every 2 to 3 days. A more detailed and comprehensive technical overview can be found in the LZ technical design report [180].

3.4.2 Calibration strategy

The calibration plan for the LZ detector is mostly based on the experience and technologies developed for LUX, with further refinements keeping the size difference in mind. For example, LUX used internally dispersed ^{83m}Kr for ER calibration but its half life ($1.86\,hr$) is shorter for a uniform mixing with the much larger LXe volume in LZ. An additional ER calibration source proposed for LZ is ^{131m}Xe produced via ^{131}I decay. ^{131m}Xe has a half life of 12 days

and decays into ^{131}Xe by a $163.9\,keV$ γ-ray emission. Tritium (^{3}H, via β-decay with $Q = 18.6\,keV$) and ^{14}C calibrations are also planned. The gaseous sources (krypton, xenon and tritiated methane) will be injected directly to the LXe via a gas-handling system.

For NR, a collimated beam of $2.4\,MeV$ neutrons from a deuterium-deuterium (DD) fusion generator will be employed, similar to the LUX. Another calibration source of interest is americium-lithium (AmLi) with a lower maximum neutron energy ($1.5\,MeV$) but an enhanced number of events ($< 10\,keV$). Photo-neutron sources with well-defined endpoint energies (e.g. ^{88}YBe) are also planned. For LXe skin calibrations, ^{220}Rn will be utilised. Dedicated source tubes containing water and organic scintillators will be employed to position the neutron or γ-ray calibration sources next to the inner cryostat.

3.4.3 Cleanliness, Xe self-shielding and fiducialization

LZ employs a wide range of screening procedures to control the radio-purity of detector materials. The manufacture of the components and their shipments to the detector site are subject to proper handling and cleaning protocols to ensure a minimum radioactive contamination. A real-time monitoring of internally generated electronegative and noble gas impurities is also ensured by a mass spectrometry [181] method developed and optimised for LZ.

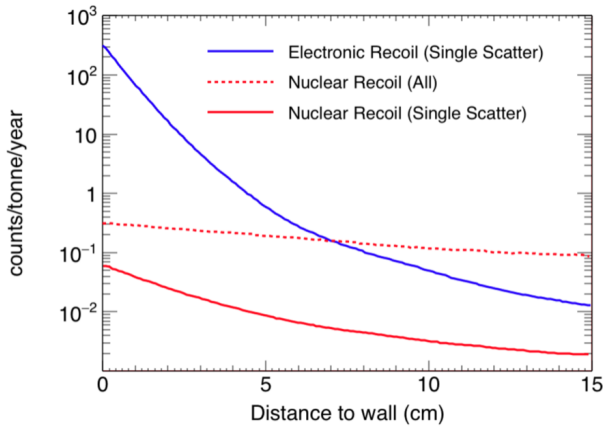

Figure 3.8: *LXe self-shielding as a function of distance from the TPC wall [180].*

A detector size larger than the mean interaction lengths of neutron and γ-rays exploits the xenon self-shielding to reject external n or γ radioactivity. The interaction rates due to these backgrounds exponentially (fig. 3.8) fall off with the distance from the TPC wall, allowing an inner fiducial region that is relatively free

from external n or γ backgrounds. A ten-fold mitigation of γ-rays and neutrons can be achieved by a LXe layer with a thickness of $\sim 2\,cm$ and $\sim 6\,cm$ respectively. Further increase in fiducial volume can be achieved from the nested veto system (OD+Xe skin) discussed earlier.

Fig. 3.9 shows the distribution of simulated single scattered NR events in a region of interest to a $40\,GeV/c^2$ WIMP search ($E_{NR} \approx 6 - 30\,keV$) [63], with and without the vetoes. The dashed line shows the fiducial mass, i.e. 5600 kg LXe.

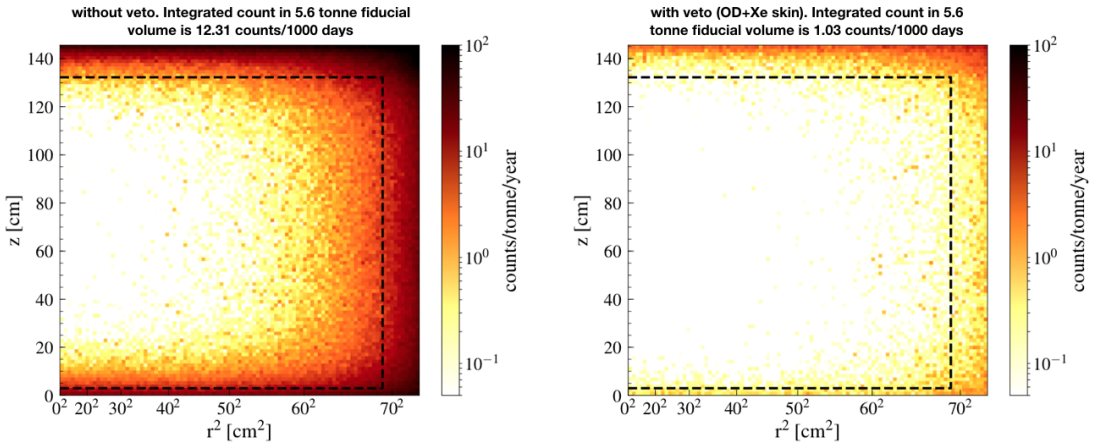

Figure 3.9: *Simulated distribution of single scatter NR events in a $40\,GeV/c^2$ WIMP search region from [63] in detector co-ordinates r and z. The dashed lines define the fiducial volume.*

3.4.4 Science goals and current status

The LZ detector is highly sensitive to a diverse array of physics signals. The primary candidates of interest are obviously the WIMPs, but a variety of other exotic candidates e.g. solar axions, galactic ALPs and HPs etc. will also be investigated. New insights of neutrino physics can be achieved via solar neutrino scattering (ER and coherent NR), double beta decays (neutrino-less and two-neutrino-) and solar neutrino magnetic moment studies. At the time of writing this thesis, the detector installation at SURF is ongoing. The TPC assembly is fully complete, awaiting a careful installation in the underground soon.

3.5 Other detection techniques

The LZ detector is only one example from a diverse array of detection technologies. As mentioned at the beginning of this chapter, several other direct, indirect and collider approaches can be adopted to investigate the particle identity of the dark matter. Some of them will be briefly addressed in this section.

Direct detections

Direct detection using activated inorganic scintillators (e.g. NaI(Tl), CsI(Tl) crystals) as target is well known for low energy threshold, a large stopping power (e.g. $3.7\,g/cm^3$ for NaI(Tl) and $4.5\,g/cm^3$ for CsI(Tl)) owing to the crystal density and a light emission wavelength (e.g. 415 nm for NaI(Tl) and 580 nm for CsI(Tl)) compatible with photo-sensor sensitivities. Since such detectors only detect the scintillation signals, no particle identification and ER/NR discrimination is possible. However, an annual modulation of the signal can be searched for to identify a DM interaction. The DArk MAtter (DAMA) experiment (employing NaI(Tl) crystal) and its successor DAMA/LIBRA at the Gran Sasso National Laboratory in Italy are worth-mentioning examples. Their recent phase-2 results [182] claim an annual modulation signature of $9.5\,\sigma$ in the region $1 - 6\,keV$. However, the interpretation of this signal in terms of DM is excluded by the non-observation of a modulation signal by sensitive xenon detectors like XENON100 [183], XMASS [184] and LUX [185]. Also, model-independent results by Annual modulation with NaI Scintillators (ANAIS) experiment [186, 187] and Korea Invisible Mass Search (KIMS) experiment [188] found no evidence of annual modulation signal in the same parameter space as DAMA/LIBRA has originally published, and hence disfavour their $9.5\,\sigma$ claim.

High radio-purity germanium detectors that operate at liquid nitrogen temperatures ($77\,K$) have a very low energy threshold ($\sim$ $0.5\,keV$), a high energy resolution ($\sim$ 0.15 around $1.3\,MeV$) and operate only in ionisation mode. Although the signal rise-time can be used to discriminate between surface background and bulk events, no complete ER-NR discrimination is possible. Two well-known examples are Coherent Germanium Neutrino Technology (CoGeNT) [189] at the Soudan Underground Laboratory in Minnesota and the Majorana Low Background Broad Energy Germanium (BEGe) detector at Kimballton (MALBEK) [190].

Cryogenic bolometers are based on the collection of phonons produced by the energy depositions in a crystal at very low temperatures. Both single-phase and double-phase bolometer techniques are possible with an additional ER-NR discrimination capability. For example, the Cryogenic Dark Matter Search (CDMS) [191] at Soudan and its successor SuperCDMS [192] at SNOLAB in Canada use both the ionisation and phonon signals in Ge and Si crystal substrates. Other examples are the Experience pour DEtecter Les WIMPs En Site Souterrain (EDELWEISS) and its successors (EDELWEISS-II and EDELWEISS-III) at the LSM (Modane Underground Laboratory) [193]. There are light and phonon readout bolometers as well, such as the Cryogenic Rare Event Search with Superconducting Thermometers (CRESST) and its successors (CRESST-II and CRESST-III) [194].

Other examples of direct detection experiments are the bubble chambers using superheated fluids (PICO-60[‡] detector [195] at SNOLAB), single phase liquid argon detectors e.g. the Dark matter Experiment using Argon Pulse-shape discrimination (DEAP) [196] and (Mini-) Cryogenic Low Energy Astrophysics with Noble liquids (miniCLEAN) [197] at SNOLAB, single phase liquid xenon detectors e.g. the XMASS detector [198] located at the Kamioka Observatory, directional searches by the Directional Recoil Identification From Tracks (DRIFT) experiment and its successor DRIFT-II [199] at the Boulby underground laboratory in the UK etc..

Indirect searches

Indirect searches look for primary or secondary products (e.g. γ-rays, neutrinos or positrons) of DM self-annihilation or decays (subject to stability constraints), preferably from highly dense astrophysical sources such as the solar centre, the centre of the galactic halo etc. They have two obvious challenges: the uncertainties in DM distribution in galactic halos, and a limited understanding of astrophysical backgrounds involved. Minimizing these uncertainties and ensuring a dense DM population at the same time is a tough task. For example, the galactic centre has a large DM concentration but a poorly understood dark matter profile [200, 201] and diffuse (and/or source) γ-ray backgrounds [202, 203]. Dark matter dominated dwarf galaxies with low-backgrounds are good alternatives, but the predicted

[‡]Merger of two experiments, Project In CAnada to Search for Supersymmetric Objects (PICASSO) and Chicagoland Observatory for Underground Particle Physics(COUPP).

fluxes are low [204–206].

Depending on the particular interaction or products involved, the indirect technique can either be space-based (e.g. Fermi Large Area Telescope (Fermi-LAT) [207], Alpha Magnetic Spectrometer (AMS) [208, 209]) or ground-based (e.g. Major Atmospheric Gamma-ray Imaging Cherenkov (MAGIC) [210], High Energy Stereoscopic System (H.E.S.S.) [211]). A wide range of energies, from keV to TeV scale, can be probed. Ground based telescopes have large effective collection areas and provide the strongest limits at high energies. Space based telescopes are more sensitive to low energies (below $\mathcal{O}(100\,GeV)$). A joint analysis of the ground- and space-based detectors, thus provides more stringent constraints. The first collaborative effort of this type was that by Fermi-LAT and MAGIC in 2016 [212] in an energy range $10\,GeV\,-\,100\,TeV$.

Indirect experiments have been able to provide stringent constraints (see section 2.2.2.2) on ALP-photon coupling. Worth mentioning here is the observation of an unidentified $3.5\,keV$ line in the x-ray spectrum of galaxy clusters [213] and the Andromeda galaxy [214] by the X-ray Multi-Mirror Mission (XMM-Newton[††]) [215], with no apparent astrophysical origin. A DM interpretation was proposed in [216] that the light ALPs produced by DM decays were later converted into photons in astrophysical magnetic fields, which might have had caused the $3.5\,keV$ line. Despite the ongoing debates on the theory [216–218], the most recent analysis of Chandra[‡‡] [219] data for NGC 1275[§§], based on this interpretation, constrains $g_{a\gamma} < (6-8)\times 10^{-13}\,GeV^{-1}$ for ALP masses $< 1\times 10^{-12}\,eV/c^2$.

Collider searches

Multi-purpose detectors like A Toroidal LHC ApparatuS (ATLAS) and the Compact Muon Spectrometer (CMS) operating at the Large Hadron Collider (LHC) are excellent means for collider DM searches. There are two search approaches of particular interest [220] – mono-X $+\not{E}_T$, and mediator searches.

In mono-X searches, a heavy dark matter mediator (Z') is produced by collision between SM particles (e.g. quark-antiquark annihilation) which later decays into

[††]named after physicist and astronomer Sir Isaac Newton.

[‡‡]named after the Nobel Prize-winning astrophysicist Subrahmanyan Chandrasekhar.

[§§]the active galactic nucleus at the center of the Perseus cluster.

a pair of dark matter particles. The event is triggered by a single ('mono-') detectable SM particle X (e.g. an energetic jet, photon or Z boson) to 'tag' its occurrence. The SM particle can be emitted either by the initial state particles (e.g. quarks) or by the final state ones (e.g. χ- particles). A 'missing' transverse* energy $\not{E}_T$ in the collision event can be attributed to the escaped dark matter particles. Example of a mono-jet process is illustrated in fig. 3.10a where the initial state radiation of a gluon can be detected as a jet. Mono-X searches are typically more sensitive [221] to very light DM masses ($\mathcal{O}(1)\,GeV$ for LHC).

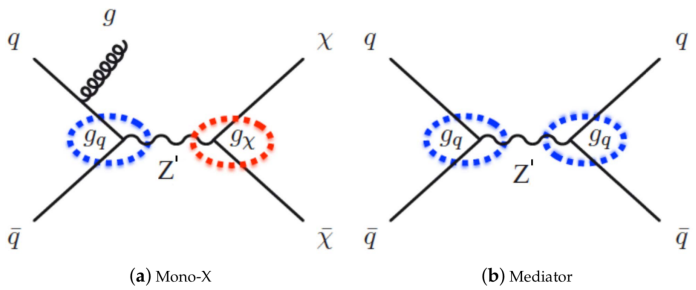

Figure 3.10: *Examples [220] of dark matter production in colliders. Couplings of Z' to SM quarks and DM are denoted by g_q and g_χ respectively.*

In mediator searches, Z' mediators once produced from SM-SM particle collisions (e.g. quark-antiquark annihilation), decay back into a SM-SM pair ('di'-) in the final states. This is a much more probable scenario when the $Z' \to \chi\bar{\chi}$ decay is suppressed, either due to lighter Z' mass ($m_\chi > m_{Z'}$) or large SM coupling ($g_q > g_\chi$). Since these searches do not involve $\chi\bar{\chi}$ productions, they are not very sensitive to m_χ, but are more sensitive to Z'-SM coupling (e.g strong Z'-quark coupling g_q in fig. 3.10b). The final state SM particles can also produce a narrow resonance, appearing as a *bump* in the $di-X$ (e.g. di-jet [222, 223], di-lepton [224] etc.) invariant mass spectrum.

3.6 Chapter summary

The aim of this chapter was to address the basic principles of the LZ detector and form a prelude for the main body of the dissertation. The key topics covered are:

*Measuring the missing energy is only possible in a direction transverse to the collider beam, owing to the uncertainty in post-collision energy of the partons (constituents of hadrons e.g. quarks/gluons) escaping along the beam line. The post-collision transverse momenta of partons are negligible.

- Direct detection experiments look for interactions of DM particles with a target material, either via electron recoil (ER) or nuclear recoil (NR).
- LXe-based instruments have high scintillation and ionisation signatures and uniquely strong self-shielding capabilities.
- Dual phase xenon TPCs use both signatures (scintillation and ionisation) to ensure a powerful ER-NR discrimination and 3D position reconstruction of particle interactions within.
- LZ is a multi-tonne scale, highly sensitive second generation detector exploiting the dual phase TPC technology with a 5.6 tonne fiducial mass.

A variety of other detection techniques was also briefly introduced at the end. The next chapter will describe the validation tests for the skin PMTs that are dedicated to read the S1 signals from the LXe skin.

Chapter 4

Skin Photomultiplier Tubes in LZ

The optical performance of the LXe skin crucially affects the overall veto efficiency of the combined (OD + skin) anti-coincidence system in LZ. The skin comprises of two regions: a cylindrical side region at the outer PTFE surface on the TPC wall and a dome region underneath the TPC. The skin contains $\sim 2\,tonnes$ of LXe and provides necessary isolation between the biased TPC and the electrically grounded inner cryostat. It also interacts with/absorbs γ-rays (or, neutrons to a lesser extent) producing scintillation photons. These photons are detected by 131 PMTs instrumented (fig. 4.1) within the LXe skin.

The $\sim 4\,cm$ wide skin at the top has 93 down-facing, specialized-for-LXe $1''$ Hamamatsu R8520-406 PMTs, just below the LXe surface. The bottom region is $\sim 8\,cm$ wide owing to the tapered shape of the vessel. It uses 20 $2''$ R8778 PMTs looking up: 18 symmetrically around the bottom and 2 in the cathode HV feed-through region to mitigate the photon absorption in the feed-through umbilical cord. The dome region contains another 18 $2''$ PMTs of the same type. Photon absorption on the metal envelopes of the TPC PMTs and R8778 PMTs are reduced by the use of reflecting PTFE sleeves.

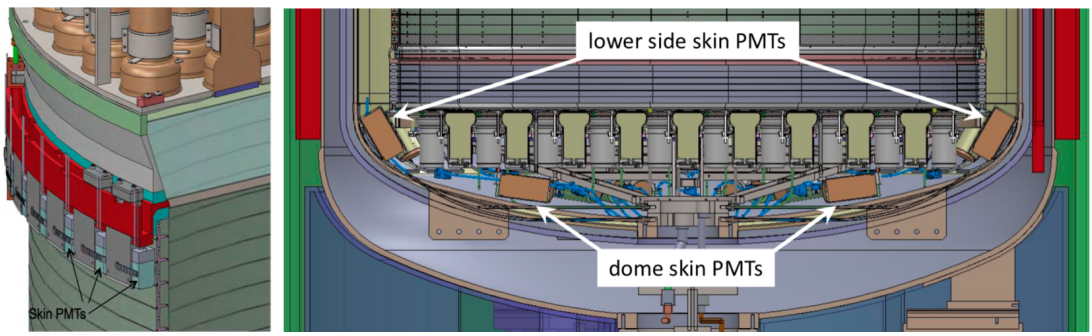

Figure 4.1: *Skin PMT arrangement in LZ from [180, 225]. (Left) Skin PMTs mounted near the top TPC array. (Right) Skin PMTs in the dome and lower side regions.*

The top skin PMTs, once delivered from Hamamatsu to Brown University (BU), were shipped to the University of Edinburgh (UOE) for extensive tests of their performance against Hammamatsu specifications and LZ design requirements. As a part of the Edinburgh group, I have had an active role in these tests for a significant period of my PhD.

4.1 Top skin PMTs in LZ

4.1.1 General features of Hamamatsu R8520-406 PMTs

A PMT is a vacuum tube equipped with a photo-sensitive cathode (photocathode) that emits photoelectrons upon light incidence on an input window, a series of dynodes where the electrons are multiplied by secondary emission effect, a focusing electrode to focus the electrons from cathode to the first dynode, and an anode that collects the electrons from the last dynode to produce an output signal. The Hamamatsu PMTs of R8520 series are well-known for their suitability in LXe detectors and have been previously used by XENON10 [226], XENON100 [97] and PandaX [227]. The R8520-406 PMTs (fig. 4.2a) are small with a square $1''\,(26\,mm)$ window and can easily fit into the narrow ($\sim 4\,cm$) width of the top LXe skin. They are of head-on* type, a typical cross-sectional view of which is shown in fig. 4.2b.

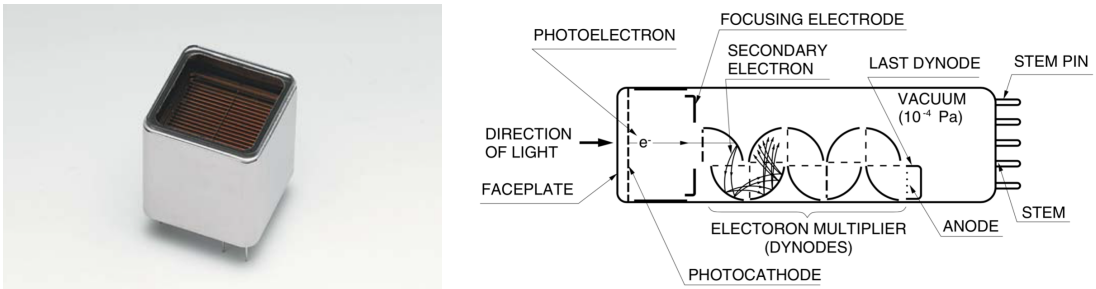

Figure 4.2: *(a) An $1''$ Hamamatsu R8520 PMT [228].*
(b) Schematic cross-section of a PMT [229].

The performance of a PMT depends on several factors, such as the composition and material used, dynode arrangement, temperature of operation, wavelength of

*the photo-cathode is mounted on the inner surface of the window. Another type is the side-on type where the photo-cathode is on the side of a glass bulb and it operates in the reflection mode.

incident light etc.. It is thus important to quantify the performance characteristics in terms of specific parameters, such as:

- **Spectrum response:** The conversion efficiency of a photocathode varies with the wavelength of incident light. The ratio of detected and incident photons, when plotted against the wavelength, is called the spectral response of the PMT. The long wavelength range of this curve depends on the composition of the photocathode material and the short wavelength range is determined by the window material. The bialkali (Sb-Rb-Cs, Sb-K-Cs) photocathode of the Hamamatsu R8520 PMT has a wide spectral response from ultraviolet to near-infrared, with a peak at $\sim 420\,nm$. The LXe VUV wavelength ($\sim 175\,nm$) stands at the short wavelength side of this range, thus making the R8520 PMT a good choice for the detector. Also, the silica glass as the window material offers a low VUV absorption.

- **Quantum efficiency:** The spectral response at a specific wavelength (λ), expressed as

$$QE = \left(\frac{\text{number of photoelectrons}}{\text{number of incident photons}}\right)_{\lambda} \times 100\%, \tag{4.1}$$

  is called the quantum efficiency (QE). It is related to the radiant sensitivity S (i.e. the ratio of the photoelectric current generated and the incident radiant power) as

$$QE = \frac{S \times 1240}{\lambda} \times 100\%, \tag{4.2}$$

  where λ is in nm and S is in A/W. R8520-406 has a typical QE of 30% at the VUV wavelength ($175\,nm$) of Xe [230].

- **Cathode blue sensitivity:** An essential parameter in scintillation counting is the cathode blue sensitivity. It is defined as the photoelectric current per incident light flux from a tugnsten filament lamp at 2856K, passed through a blue filter[†]. It is only measured at the room temperature and may affect the energy resolution of the detected signal. The R8520-406 PMT has a blue sensitivity index[‡] of 11.0 at $25°C$.

[†]Corning CS 5-58 polished to half stock thickness [229].

[‡]It is a dimensionless quantity. After passing through the blue filter the unit ′lumen′ can not be used any more for the incident light flux. Lumen is only defined for visible region of electromagnetic spectrum.

The typical features of the R8520-406 PMTs are summarised in table 4.1.

Table 4.1 *General features of R8520-406 PMTs by Hamamatsu [228].*

Parameter	Description
Spectral Response	$160 - 650\,nm$
Wavelength of maximum response	$420\,nm$
Window Material	Silica glass
Photocathode Material	Bialkali
Dynode	Metal channel, 10 Stages
Operating Ambient Temperature	$-110°C$ to $50°C$
Weight	$22.9\,g$

4.1.2 Functional tests for LZ

Although the characteristic properties of a PMT are provided by its manufacturer, a cross-check is necessary before its implementation in an actual experiment. 100 Hamamatsu R8520-406 PMTs were purchased for LZ: 93 PMTs for use in the top LXe skin and 7 PMTs as spare. They will be referred to as PMT001-100 in this dissertation, where the actual serial numbers are in the format LV1XXX (table 4.2).

Prior to all other functional tests, it is necessary to check the pressure resistance of individual PMTs, since a catastrophic pressure failure of a PMT could be experiment ending. Also, minor leaks will lead to a poor performance, especially in gain and afterpulsing. Hence the pressure test has to be done first (so that any leak might get picked up in the later gain and afterpulsing tests). LZ requires a minimum pressure resistance to 3 bar (gauge). The pressure tests were done in the class-100 clean rooms at the Scottish Microelectronics Centre (SMC) according to the LZ cleanliness requirements. The PMTs were also subject to high purity germanium (HPGe) screening at Boulby underground laboratory to confirm their consistency with the LZ radioactivity requirements. Following the base-attachment at Imperial College London, the tests of gain, resolution, afterpulse and dark rates of the PMTs were performed at the Astronomy Technology Centre (ATC) at UOE, using a LHe-cooled cryostat.

Table 4.2 *PMT number to LV- mapping in this work.*

PMT	Serial	PMT	Serial	PMT	Serial	PMT	Serial	PMT	Serial
1	LV1768	21	LV1736	41	LV1818	61	LV1843	81	LV1819
2	LV1793	22	LV1738	42	LV1824	62	LV1845	82	LV1822
3	LV1794	23	LV1747	43	LV1826	63	LV1850	83	LV1839
4	LV1795	24	LV1748	44	LV1831	64	LV1879	84	LV1842
5	LV1797	25	LV1753	45	LV1833	65	LV1881	85	LV1866
6	LV1798	26	LV1763	46	LV1834	66	LV1885	86	LV1867
7	LV1801	27	LV1764	47	LV1840	67	LV1888	87	LV1870
8	LV1802	28	LV1765	48	LV1847	68	LV1894	88	LV1895
9	LV1806	29	LV1773	49	LV1848	69	LV1897	89	LV1901
10	LV1807	30	LV1776	50	LV1849	70	LV1903	90	LV1904
11	LV1803	31	LV1735	51	LV1816	71	LV1821	91	LV1820
12	LV1799	32	LV1739	52	LV1825	72	LV1846	92	LV1823
13	LV1800	33	LV1741	53	LV1827	73	LV1884	93	LV1865
14	LV1790	34	LV1755	54	LV1828	74	LV1887	94	LV1868
15	LV1804	35	LV1761	55	LV1829	75	LV1889	95	LV1869
16	LV1791	36	LV1769	56	LV1832	76	LV1891	96	LV1871
17	LV1781	37	LV1774	57	LV1835	77	LV1893	97	LV1883
18	LV1813	38	LV1775	58	LV1837	78	LV1898	98	LV1886
19	LV1792	39	LV1779	59	LV1838	79	LV1899	99	LV1896
20	LV1796	40	LV1783	60	LV1841	80	LV1902	100	LV1900

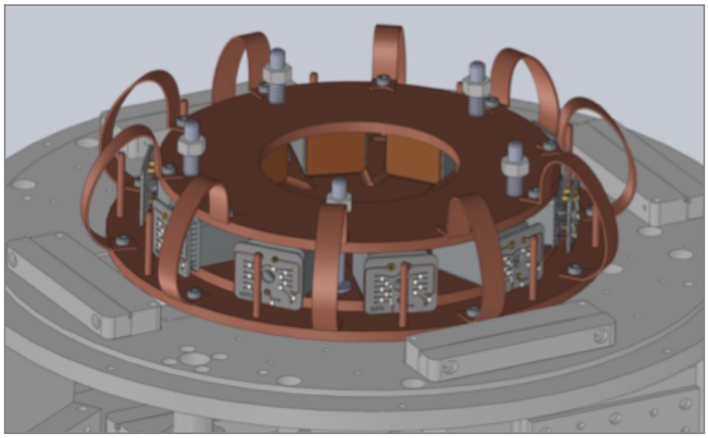

Figure 4.3: *The PMT layout in the LHe cooled cryostat for testing.*

Fig. 4.3 shows the design of the apparatus. 10 PMTs, each facing the centre of a circular layout, were loaded at a time. An approximately spherical symmetric illumination at the centre was provided by an external source via an optical fibre connection. Electrical insulation was provided by the sapphire (between the PMTs/their holders and the cryostat) and diamond wafers (between the PMT holders and the heating sensor). A high voltage power supply was used to bias all PMTs simultaneously. The output signals from the anodes were fed to a picoscope

where they were read out in a digital format. As a part of the UOE group, I was involved in the data analysis part of these tests, mostly for the dark rate computation.

4.2 Gain and resolution tests

4.2.1 Gain: definition

The accelerated photo-electrons, originally emitted by the photocathode, are successively multiplied by a cascade of secondary emissions at the dynodes which result into a large output current. If the average secondary emission ratio is δ and number of dynode stages is n, the current amplification (ratio of the output current to the input photo-electric current)

$$G = \delta^n, \tag{4.3}$$

is often called the $'$gain$'$ by the manufacturer. The secondary emission ratio is typically proportional to some power of the interstage voltage E:

$$\delta = AE^{\alpha}, \tag{4.4}$$

where A is a constant and the coefficient α depends on the material and geometry of the dynodes. Typical values are $\alpha \sim 0.7, 0.8$. If the cathode-to-anode voltage is V, the combination of eqs. 4.3 and 4.4 yields

$$G = (AE^{\alpha})^n = \left[A\left(\frac{V}{n+1}\right)^{\alpha}\right]^n = KV^{\alpha n}, \tag{4.5}$$

where $K = A^n/(n+1)^{\alpha n}$ is a constant. Since the gain is directly dependent on V, a stable power supply with minimum voltage fluctuations is necessary. The absolute maximum value of the cathode-to-anode voltage for R8520-406 PMT, as recommended by Hamamatsu, is $900V$.

However, the manufacturer's definition of gain does not consider the collection efficiency of the first dynode. In LZ, the gain is defined as an overall electron multiplication which includes the collection efficiency as well. In other words, the gain in LZ is defined as [231]

$$G_{LZ} = \frac{Q}{q_{in}}, \tag{4.6}$$

where Q is the total charge of the output signal and q_{in} is the input charge.

4.2.2 Testing procedure

Testing the PMT response against the $175\,nm$ VUV photons is costly[§] and time consuming. An alternative way is to use a $470\,nm$ blue LED light, since previous LUX measurements have already demonstrated a generally consistent gain difference of $10-20\%$ in the LED case. The LED gain can still be an useful parameter to test against the Hamamatsu specifications.

A low intensity 'fast' LED source driven at a rate $\sim 10-50\,kHz$ by a special circuit (an external 'trigger') was used to enable fast flashes (few ns long). It was connected to the apparatus via optical fibres. The probability of detecting k photons (i.e. k photoelectric conversions) by a PMT upon the light incidence on it follows the Poisson distribution

$$P_\lambda(k) = \frac{\lambda^k}{k!}e^{-\lambda}, \tag{4.7}$$

where λ is the expectation value, i.e. the average number of photons detected per LED pulses at a certain intensity (or amplitude). The LED amplitude was adjusted by slowly varying the LED driver voltage from $1\,V$ until 1 in 10 triggers produced prompt single photo-electron (SPE) pulses at the picoscope. This corresponds to $\lambda \approx 0.11177$, i.e. 10% chance of a SPE and an 0.56% chance of two photoelectron emissions. The output histogram was thus dominated by SPEs. The picoscope was set at its maximum resolution ($2\,ns$).

For the R8520-406 PMTs, Hamamatsu guarantees a minimum gain of $G = 0.6\times10^6$ at $-800\,V$, $25°C$. This gain was to be verified first in a warm ($\sim 25°C$) condition for different PMT bias voltages ($800\,V$, $850\,V$ and $900\,V$). Around 10000 waveforms were recorded for each particular arrangement. Following the warm measurements, the PMTs were cooled down and a second set of ('cold') measurements were obtained at $\sim -100°C$. The LZ requirement is $G > 0.6\times10^6$, both at $25°C$ and $-100°C$.

The same data recorded for gain were used to determine the SPE resolution according to the definition

$$R_{SPE} = \frac{\sigma}{\mu}, \tag{4.8}$$

where σ and μ are the standard deviation and the mean of the Gaussian function used to fit the SPE peak, respectively. Hamamatsu specifies a value of $<= 50\%$

[§]it would require more sophisticated apparatus, incluing a 175 nm light source.

at $25°C$. In LUX, a 35% SPE resolution resulted in a $> 90\%$ SPE detection by most (96%) PMTs [232]. Based on this knowledge, a $< 50\%$ resolution both at $(-900\,V,\, 25°C)$ and $(-900\,V,\, -100°C)$ is the baseline choice for LZ.

4.2.3 Analysis method

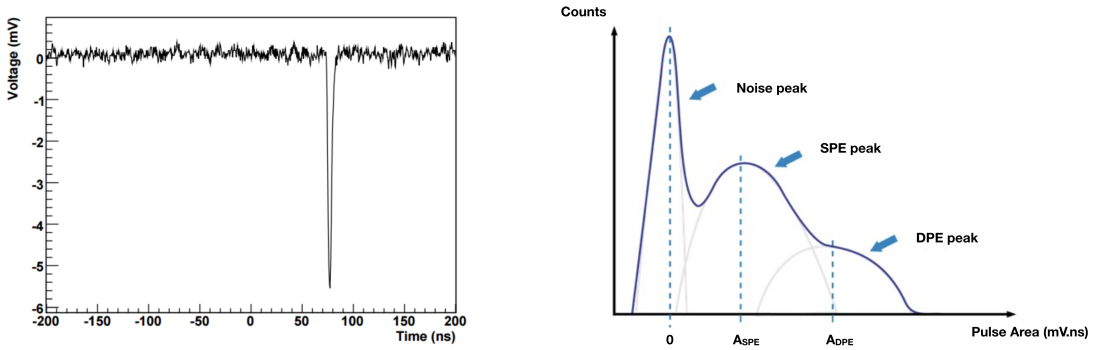

(a) *(b)*

Figure 4.4: *(a) A typical SPE waveform. The time = 0 ns tags the trigger. (b) An idealised SPE spectrum. Figure modified from [233].*

Fig. 4.4a shows a typical SPE waveform. The average voltage fluctuations in a SPE-free region (e.g. the first $50\,ns$) was defined as the baseline and was subtracted from every sample to place the new baseline at $0\,mV$. For a single PMT in a particular operating condition, each of the SPE peaks in 10000 recorded waveforms was fitted with a Gaussian function and a peak area was calculated with respect to the $0\,mV$ baseline.

The charge Q of an individual SPE pulse was found by dividing the pulse area (mV-ns) by the effective resistance of the PMT circuit (R_{eff}). Since the electron multiplication by a PMT is subject to statistical fluctuations, an average value of Q is was used in eq. 4.6 to calculate the gain. This was typically done by plotting a pulse area spectrum like the standardised one in fig. 4.4b. The large noise peak ($'$pedestal$'$) at the left of the standardised plot results from an integration of the baseline voltage and is prominent for low LED intensities. A baseline subtraction places the position of the peak at 0, but it fluctuates to positive and negative values due to the random nature of the noise. It is followed[¶] by a smaller SPE peak and an even smaller double photoelectron (DPE) peak. For higher LED intensities and high-statistic data, multi-PE peaks are also possible.

[¶]Note that fig. 4.4b is only a standardised plot. In the present case, the areas should be 10% and 0.5% of the pedestal following the Poisson trigger logic earlier.

For a particular PMT and a particular operating condition, the mean SPE area A_{SPE} was determined from the SPE spectrum by a Gaussian fit. The gain was then calculated by

$$G = \frac{A_{SPE}[mV\,ns] \times 10^{-12}}{R_{eff}.q_e}, \tag{4.9}$$

where $q_e = 1.6 \times 10^{-19}\,Coulombs$ is the charge of an electron. The value of the effective resistance ($R_{eff} = 50\,\Omega$) was determined by the resistances used in the PMTs and the acquisition software, and was confirmed by the measurements performed by the School's electrical technician.

4.2.4 Results

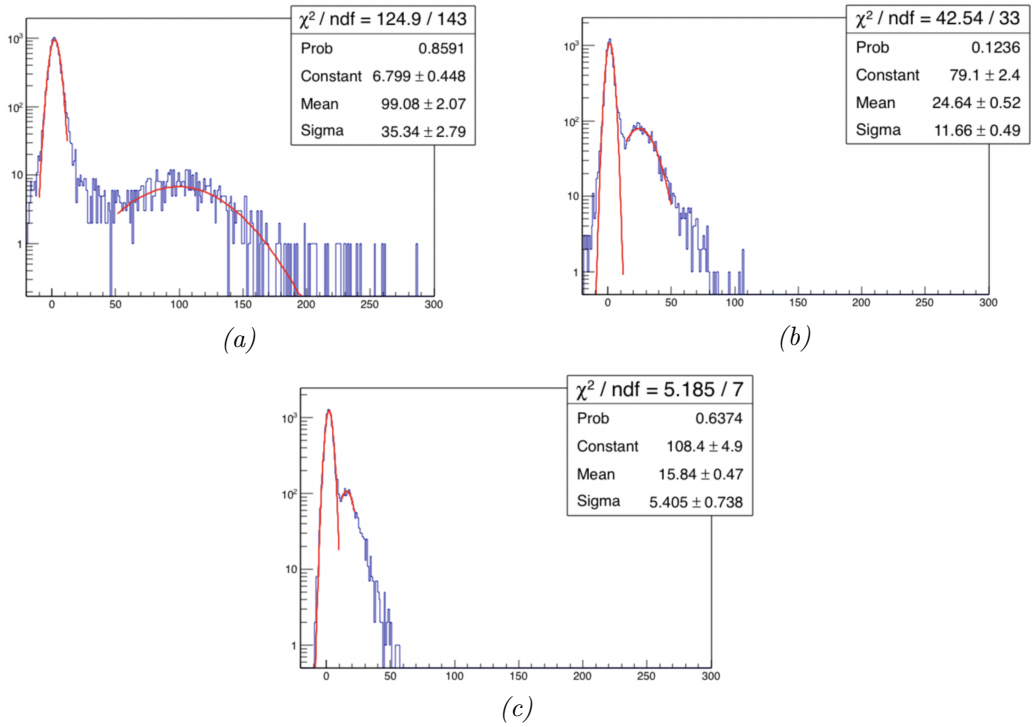

Figure 4.5: *SPE spectra at 170 K (cold) for the (a) highest gain- (PMT024, serial number LV1736), (b) typical gain- (PMT055, serial number LV1829), and (c) the lowest gain (PMT098, serial number LV1866). PMTs biased at −800 V.*

The spectrum analysis described in section 4.2.3 was performed for each of the 100 PMTs in both cold (170 K) and warm (300 K) conditions at voltages of 800, 850 and 900 V. The results described here are for those at 800 V bias. 95 PMTs satisfied the LZ gain requirement with a highest gain of ($G = 1.2 \times 10^7$) for PMT024 (fig. 4.5a, SPE resolution 37%), a lowest gain of ($G = 1.9 \times 10^6$) for PMT098 (fig. 4.5c, SPE resolution 34%) and typical responses in between for others (e.g. PMT055 in fig. 4.5b, gain $G = 3.1 \times 10^6$ and resolution=47%).

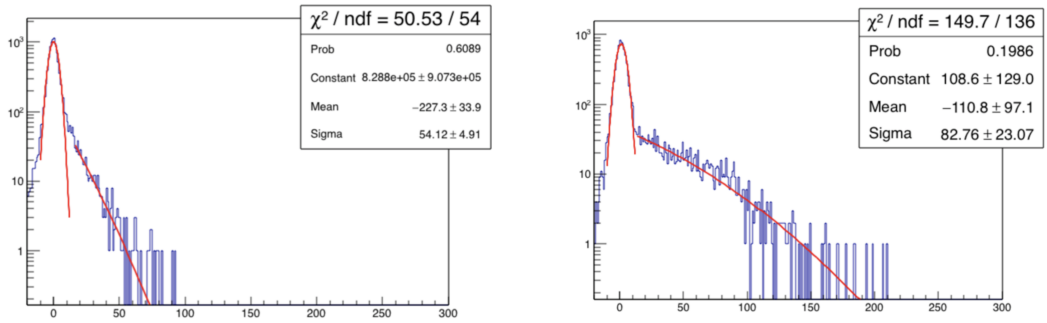

(a) *(b)*

Figure 4.6: *Example spectra for the PMTs that failed to show SPE. Spectra shown here are at 800 V and 170 K for (a) PMT006 (serial number LV1798) and (b) PMT027 (serial number LV1764).*

Their SPE resolutions fairly satisfied the 50% resolution requirement, with a few exceptions (fig. 4.7b) which were not extensively objectionable considering the uncertainties.

Five PMTs failed to fulfil the LZ requirements for gain and resolutions. They showed no SPE peak at 800 V when cooled to 170 K, and generally failed to generate one at higher voltages or temperatures. They were thus rejected for use in LZ. The spectra for two such PMTs are shown in figs. 4.6a and 4.6b.

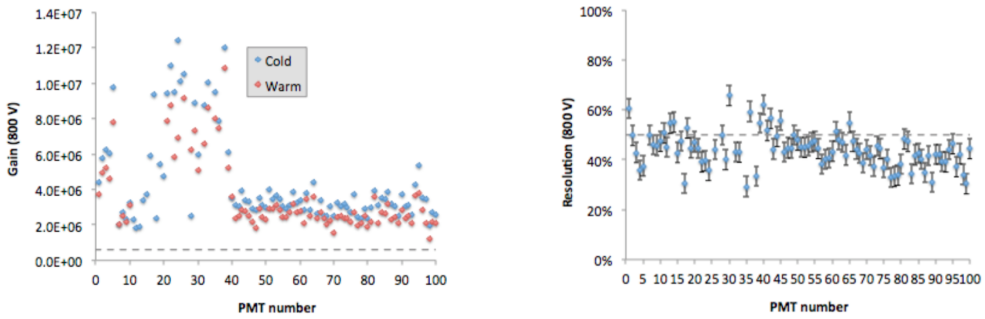

(a) *(b)*

Figure 4.7: *(a) Gains and (b) resolutions of 95 good PMTs.*

Fig. 4.7a shows the gain values of 95 good PMTs, both in cold and warm conditions. The cold gains were larger than the warm (room temperature) ones, as expected. The increase was $\sim$ 25% with a rms of 5%. The first 40 PMTs showed larger and scattered gains as compared to the PMTs $41-100$. This could, however, be correlated to the groups of PMT shipments delivered to Edinburgh from Brown. The testing apparatus, procedure, base attachment and manufacture were completely uniform and consistent for all the 100 PMTs so that the existence of such correlation due to changes in the testing procedures is unlikely.

4.3 Dark count rates

Some small random pulses are always present at the output even if a PMT operates in a complete darkness. Light detection by a PMT is critically affected by these ′dark counts′, because:

- The data acquisition system records unnecessary dark count data, requires extra storage and introduces a problematic dead-time for the instrument.
- An increased SPE rate due to the dark counts subsequently increases the rates of 2SPE, 3SPE etc. and effectively reduces the overall veto efficiency of the detector.

A lower rate of dark counts is necessary to avoid the random coincidences between PMTs (i.e. simultaneous dark peaks at two or multiple PMTs) that mimic actual scintillation signals.

4.3.1 Causes of dark counts

Dark counts can be caused by several sources, such as:

- **Thermionic electron emissions at photocathode:** The photo-sensitive material at the cathode has a low work-function and it exhibits thermionic emission even at the room temperature. These electrons are often multiplied by the dynode stages and are the major contributors to the dark counts. As obvious, thermionic emissions are temperature dependent and the dependency can be expressed in terms of Richardon's law:

$$I \propto T^{5/4}\, e^{-W/k_B T}, \tag{4.10}$$

  where I is the dark current (dark count per unit time), T is the absolute photocathode temperature, W is its workfunction, e is the electron charge and k_B is the Boltzman constant. Thus, both the photocathode material and its temperature affect the thermionic dark current. PMTs sensitive to longer wavelengths (e.g. red to infrared regions) have larger dark currents at room temperature. Bialcali photocathodes sensitive to UV wavelengths thus provide the lowest dark current.

- **Ohmic leakage:** The typical operating voltages of a PMT are high ($\sim 500V - 3000V$) but the output currents are very low ($\sim\ nA - \mu A$). Even an insulation, for example with a $10^{12}\,\Omega$ resistance, produces a current in the nA range (according to the Ohm's law). Using highly insulating material in the tube, avoiding dirt and humidity contaminated surfaces, and ensuring the optimal insulation of glass stem and base, and between the anode- and the other pins are necessary to minimise the ohmic leakage. As the thermionic contribution to the dark current increases with temperature, ohmic leakage is the dominant contributor at low voltage and low temperature operations.

- **Glass scintillations:** Electrons, if somehow deviate from their anticipated trajectories through the dynode chain, can strike the glass envelope and cause a scintillation. This can be avoided by putting a black conductive coating (connected to the cathode potential) around the glass envelope and wrapping the PMT by a black cover.

- **Field emission:** At high operating voltages, the presence of strong electric fields can cause spontaneous emission of electrons from electrodes leading to a dark current. Every PMT has a maximum rating of operating voltages and it is recommended [229] to operate the PMTs at voltages $100 - 300\,V$ lower than it.

- **Radioactive contributions:** Any natural radioactivity in the structural components, external cosmic backgrounds or environmental γ-rays may also cause additional noise currents.

4.3.2 Testing procedure

Dark counts are dominated by thermionic emissions at room temperatures. At LXe temperatures, however, the thermionic component is strongly suppressed and the non-thermal contributions (e.g. field emission, radioactivity etc.) remain. Hamamatsu specifies a dark count rate of $< 5\,kHz$ at room temperature. For LZ operation at LXe temperature, a requirement of $< 200\,Hz$ at $-100°C$ is specified.

The testing apparatus was similar to that used in gain tests except that the LED illumination was absent. Proper care was taken to ensure any light leakage into the PMTs during the testing. Total 267 long ($\sim 1\,ms$) waveforms were recorded for each of the 100 PMTs biased at $-800\,V$, both in cold and warm conditions.

4.3.3 Analysis technique

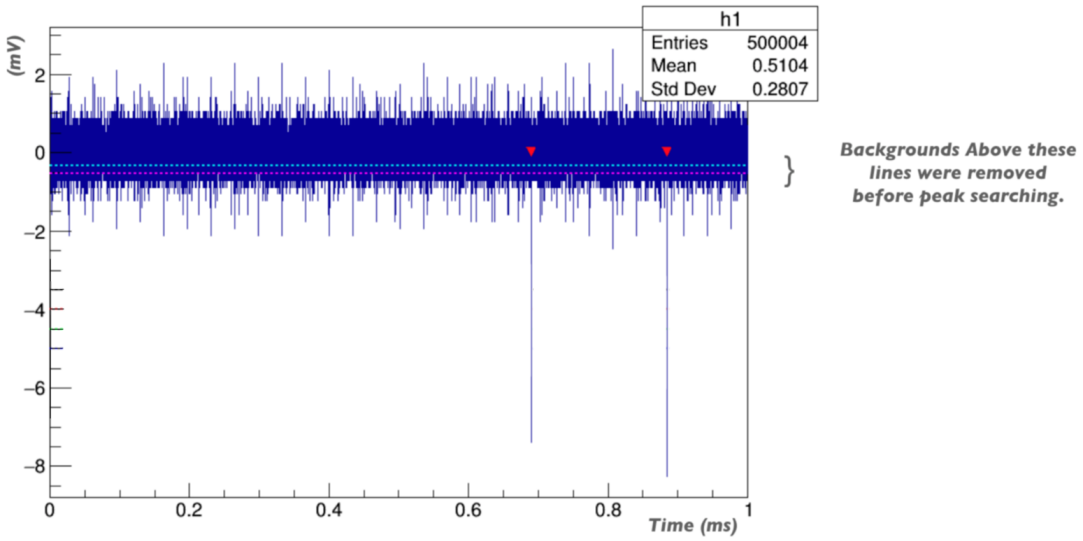

Figure 4.8: *A typical waveform from dark count test. The red-tagged peaks are the dark peaks. The cyan and pink dashed lines are the average and rms values of background fluctuations.*

A typical waveform (fig. 4.8) recorded in complete darkness appears as random (and rare) spikes (dark counts) superimposed in a fluctuating noisy background. These low amplitude noises have a characteristic frequency (hence the term ′ringing′) and are likely to be some kind of EM pick-ups. However, it is not so simple to identify a SPE-like dark peak out of this background using a simple algorithm. General peak finding algorithms e.g. the functions in the ′TSpectrum′ class in ROOT (an object-oriented data analysis framework by CERN) are well-suited for high-amplitude peaks over a fairly small background (like those in gain tests). But in dark rate tests, both the dark peaks and background fluctuations are random, no definite correlation between their heights is available. Defining a well-defined threshold can simplify the algorithm, but discriminating SPE-like dark peaks from random large ringing still poses a problem.

Keeping all these issues in mind, I developed a computational framework based on ROOT and C++ for this specific purpose of dark peak identification. The individual steps of the algorithm are:

1. **Baseline computation:** For a particular PMT and operating conditions, a few waveforms free from any high spiky structure were selected by eye. The average and standard deviation (σ) of the background fluctuations were computed using a coding script.

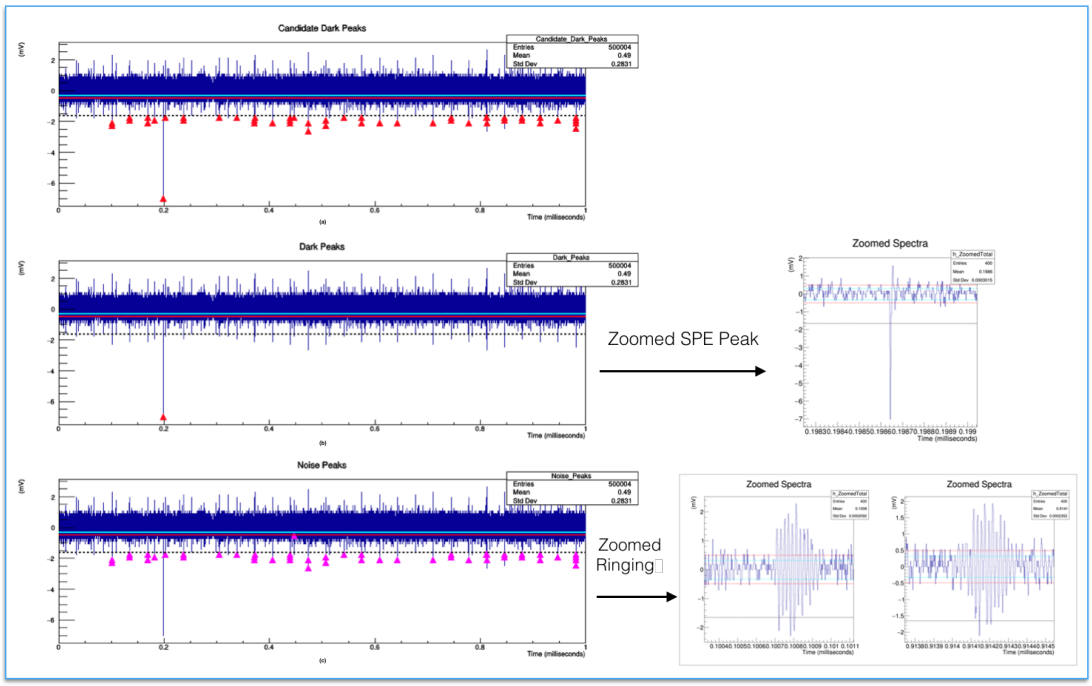

Figure 4.9: *Example of SPE -Ringing Discrimination:*
(a) initially searched Peaks over an 1-ms waveform,
(b) SPE Peaks found after precise peak searching,
(c) ringings which were initially suspected as a peak but got rejected in precise peak search. Examples of zoomed ringing and SPE peak are also shown.

2. **Threshold determination:** A minimum height of 5σ was defined for a pulse to be identified as a SPE and termed as the 'threshold'. It was kept constant for all 267 waveforms for that PMT, recorded in the particular operating conditions in question.

3. **Initial peak search:** Each of the 267 waveforms was investigated separately by the peak finding code with the threshold defined in step 2. Peaks with heights above this threshold were selected as a potential dark peak. The time bin at which the peak is detected was recorded. The run-time of the code was significantly reduced by neglecting background fluctuations in the positive side of the waveform (by removing backgrounds above the average background determined in step 1), since only the negative peaks are of interest.

4. **SPE peak-ringing discrimination:** To check whether a peak tagged in step 3 was a true SPE and not a random ringing, the part of the waveform around the recorded position was precisely investigated. The discrimination (fig. 4.9) was done by calculating peak frequencies in the region and/or the peak width of the candidate peak. This is based on the reasoning that the SPEs

are expected to be clean peaks, not fast oscillatory shapes. For example, most of the preliminarily tagged peaks above the 5σ threshold in the waveform 4.9a were later rejected (fig. 4.9c) by the code, and only one true SPE-like dark peak (fig. 4.9b) remained. The reason for not running this SPE-ringing discrimination code initially was to minimise the computational time.

5. **Sum up and rate determination:** Looping over all the 267 waveforms, the total number of dark counts (N_D) was determined and the dark rate (R_D) was calculated by

$$R_D = \frac{N_D}{t}, \tag{4.11}$$

where t is the total time in seconds. The entire process was repeated several times and an average R_D is determined.

4.3.4 Results

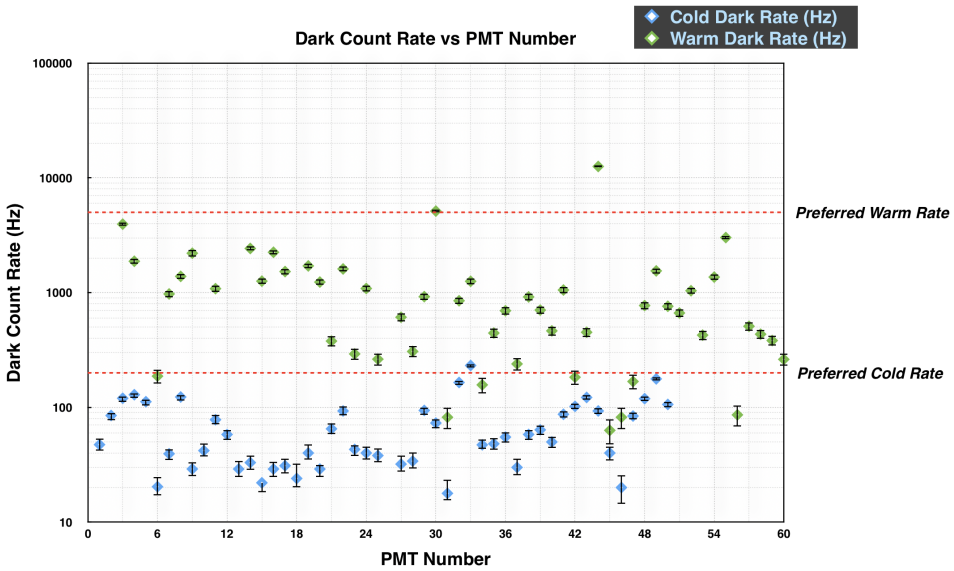

Figure 4.10: *Dark Count Rates in Hz for the first 60 PMTs.*

The dark count rates of all the 100 PMTs were computed according to the procedure described above. The cold and warm results for first 60 PMTs are shown in fig. 4.10. Cold rates were higher than the warm ones, as expected. Cold and warm rates were typically around $50-70\,Hz$ and $500-1000\,Hz$ respectively. A few PMTs slightly exceeded the LZ-preferred rates. No tube failed both cold and warm rate requirements.

4.4 Afterpulsing

Afterpulses [234] are spurious pulses with small amplitudes that appear after a primary signal pulse and are caused by ionisation of residual gases trapped inside the PMT dynode structure. Photoelectrons produced by incident light, while flowing through the tube, ionise these residual gases. The positive ions slowly drift towards the photocathode and produce additional photo-electrons upon impinging. These electrons are then multiplied by the dynode chain, thus producing the afterpulses. The time delay between the primary and afterpulses is approximately

$$\Delta t = \sqrt{\frac{2md}{qV}}, \tag{4.12}$$

where d and V are the distance and voltage between the photocathode and the first dynode respectively (as this is the region where most of the residual gas ions are expected), m is the mass of the ion and q is its charge. In general, the time delay is of the order of $\sim 1\,\mu s$. This is shorter than the delayed time ($\sim 10\,\mu s$) of late pulses produced by the backscattered photoelectrons.

An important parameter is the afterpulsing ratio (APR), defined as

$$APR = \frac{Q_{AP}}{Q_{SPE}}, \tag{4.13}$$

where Q_{AP} and Q_{SPE} are the total charge of the afterpulse and the main pulse respectively. Previous experience from LUX suggests that a new PMT should have very small residual gases showing an $APR \leq 5\%$ within $2\,\mu s$ after a main SPE pulse. An $APR \geq 5\%$ thus indicates a PMT with compromised health.

Around 5000 waveforms with $\sim 2\mu s$ durations and larger SPE heights were recorded for each of the 100 PMTs in both cold and warm conditions. The test requirement is $APR \leq 5\%$ within $2\,\mu s$ of LED pulse at $-900V$ and $25°C$ after pressure test. At the time of writing this thesis, the data analysis is complete and awaiting internal reviews.

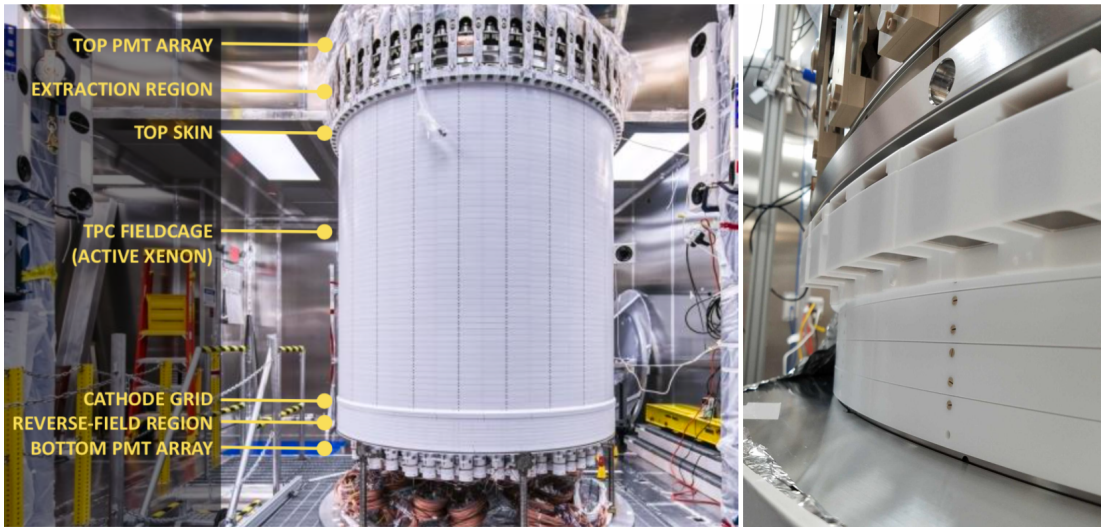

Figure 4.11: *(left) Assembled LZ TPC at SURF and (right) the top skin region [178].*

4.5 Chapter summary and current status

The results of the validation tests of top skin PMTs at Edinburgh can be summarised as:

- 95 out of 100 Hamamatsu R8520-406 PMTs fulfilled the gain and resolution requirements by LZ.
- Typical gains were found around $\sim 3.1 \times 10^6$. All PMTs fairly satisfied the $< 50\%$ resolution requirement of LZ.
- 5 PMTs failed to show SPE peaks when cooled to $170\,K$, and generally failed to produce one at higher temperatures. They were rejected and sent back.
- Cold and warm dark rates were measured to be around $50 - 70\,Hz$ and $500 - 1000\,Hz$ respectively.
- A few PMTs had dark rates slightly exceeding the LZ requirements, but no tube failed both the cold and warm rate requirements.
- Afterpulsing analysis is done and to be presented internally to the collaboration soon.

95 top skin PMTs that passed the validation tests were returned to, and received at, Brown University. After radon emanation at South Dakota School of Mines and Technology (SDSMT), they were sent to the SURF for installation. 93 top

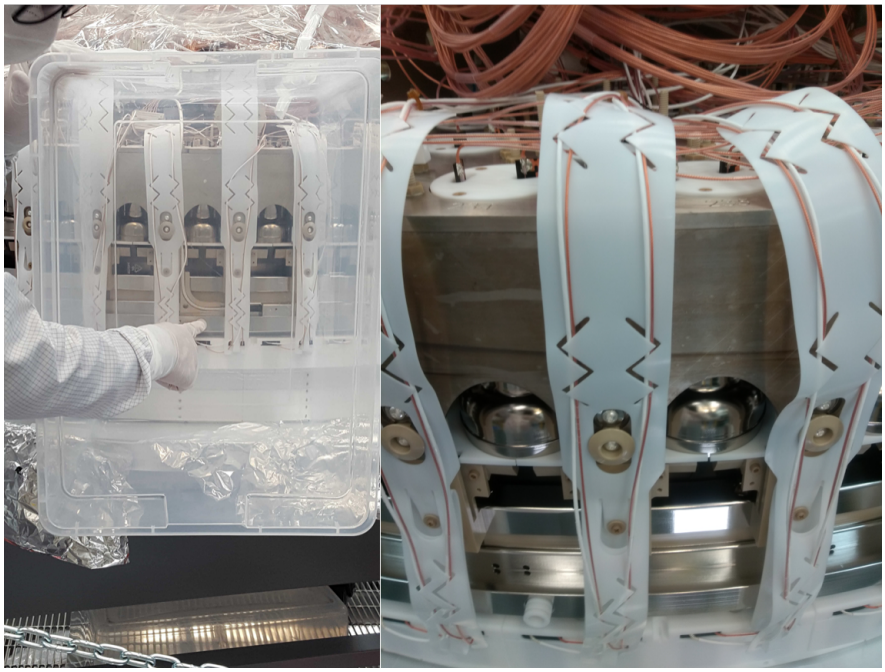

Figure 4.12: *Top skin cable routing at SURF.*

skin PMTs were successfully assembled in the LXe skin region (fig. 4.11) of the LZ detector. Fig. 4.12 shows two photos taken during the skin cable routing at SURF.

Chapter 5

Electron Recoil (ER) Backgrounds and Atomic Binding

A major challenge of any direct detection experiment is the presence of irreducible backgrounds at the detection site. Initiatives like deep underground operations, controlled material screening, LXe purification and proper design of shielding system only suppress the background but never remove it completely. In general, the NR backgrounds are more effectively controlled than the ER ones, thus making the low energy searches (e.g. HPs or ALPs) relatively difficult. It is crucial to characterise all possible sources of backgrounds in an experiment, take necessary actions to reduce it (if possible) and properly model their effect on the detection medium.

A vast majority of the expected backgrounds in LZ are of ER type, i.e. they interact with the atomic electrons. While interactions like photo-absorptions of γ-rays already include the atomic binding effect in the theoretical formulation, processes like Compton or neutrino-electron scattering usually adopt a free electron approximation (FEA). The FEA is simple but unrealistic: it yields excess events at low ER energies and affects the sensitivity of the particular analysis it is being used for. This chapter will investigate the extent of these effects, for reliability of various LZ analyses at present and in the near future.

5.1 Dominant backgrounds in LZ

5.1.1 Cosmogenic backgrounds

Major cosmogenic backgrounds of concern are the cosmic muons and muon neutrinos. These energetic particles are produced by the high energy collisions of cosmic ray nucleons with the gaseous nuclei in upper atmosphere ($\sim 15\,km$)

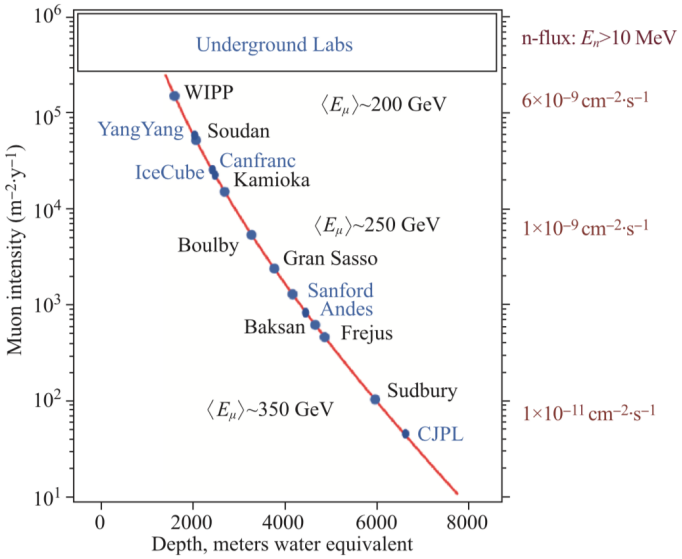

Figure 5.1: *Expected cosmic muon (left vertical scale) and neutrino (right vertical scale) fluxes [235] as a function of depth of the underground laboratory.*

and are continuously bombarding the Earth's surface. They can induce hadronic cascades and electromagnetic showers in a material, producing highly penetrating γ-rays and neutrons. Fast ($\sim MeV - GeV$) neutrons can either be generated by secondary particles of these cascades or directly by muon-interactions with the detecting medium, e.g.

$$\begin{aligned}
&\mu^- \rightarrow e^- + \bar{\nu}_e + \nu_\mu && (\mu\text{-decay}),\\
&\mu^- + p \rightarrow n + \nu_\mu && (\mu\text{-capture}),\\
&\mu^- + X \rightarrow X' + n && (\text{spallation}),\\
&\gamma + X \rightarrow X' + n && (\text{photo-nuclear interaction}),\\
&\pi + X \rightarrow X' + n && (\text{hadronic interaction}), \text{ etc.},
\end{aligned} \tag{5.1}$$

where X and X' are two different nuclei.

The neutrons produced by cosmic muon interactions can undergo elastic scattering with the target (e.g. LXe) nuclei and mimic a WIMP signal. A practical solution to reduce this background is to go deep underground* because the natural Earth materials (e.g. rock) effectively shield the detector from the cosmic muons. Fig. 5.1 plots the expected muon and neutrino fluxes as a function of depth into the Earth. The Davis Cavern at SURF receives a muon flux of $(5.31 \pm 0.17) \times 10^{-9}\, \mu/s/cm^2$ [236], which is about 3×10^6 less than that on the

*or deep ice/underwater.

surface. The flux of secondary neutrons at that depth[†] can be obtained either by using empirical depth-dependent functions [237] or by Monte Carlo (MC) simulations [238], and the calculated value is $\sim 0.5 \times 10^{-9}\, neutrons\, /cm^2/s$. The muons traversing the water shield ('muon veto') can be tagged by the Cherenkov light they produce. Water and the liquid scintillator in OD have low neutron yields, resulting in a low muon-induced neutron flux ($10^{-9}\, neutrons/kg/s$) [225].

A second background comes from the cosmogenic activation of detector materials, including the LXe itself. Exposure of detector materials to cosmic rays while being manufactured, assembled or transported on the Earth's surface, can cause production of radioisotopes within (table. 5.1). The largest contribution in LZ comes from the ^{46}Sc produced in the material (titanium) of the cryostat. The ideal way to mitigate this background is to move the components underground as soon as possible[‡].

Table 5.1 *Backgrounds due to cosmogenic activation.*

Source	Decay scheme	Component
^{46}Sc	(83.83 d, β-γ)	Cryostat (Ti), PMT array structure
^{60}Co	(5.3 y, β-γ)	Copper Components
^{3}H	(12.3 y, β)	LXe
^{127}Xe	(36.4 d, electron capture, followed by x-ray and Auger e^- cascades)	LXe
^{129m}Xe	(8.9 d, γ)	LXe
^{131m}Xe	(11.9 d, γ)	LXe

The cosmogenic activation of xenon is more problematic than those in other materials, since the radioisotopes produced reside in the LXe itself and cannot be shielded against. Non-xenon radioisotopes, e.g. tritium can be efficiently removed via a hot zirconium getter during the detector operation. However, this method is not applicable for the Xe radioisotopes (e.g. ^{127}Xe, ^{129m}Xe, ^{131m}Xe). ^{127}Xe decays via an electron capture [239], either from the K-shell (83.37% probability), L-shell (13.09% probability), M-shell (2.88% probability) or N-shell (0.66% probability), resulting in an orbital vacancy. The vacancy is filled by the electronic transitions from higher orbitals, leading to x-ray and Auger electron cascades (with total cascade energies of $32.2\, keV$, $5.2\, keV$, $1.1\, keV$ and $186\, eV$ respectively). The

[†]It has been measured at several underground labs, but not at the $4850\, ft$ ($4300\, m.w.e.$ rock overburden) level at SURF.

[‡]Cosmogenic activation of materials while in underground can be neglected because of the significantly lower cosmic-ray flux there.

cascades are followed by the emission of γ-ray (or internal conversion electrons) by de-excitation of the product ^{127}I itself. This facilitate a 'coincidence-tagging'[§] of ^{127}Xe background. The efficiency of such coincidence is limited at the edge of the LXe target [225]. However, most Xe radioisotopes decay quickly and their contributions are expected to be mitigated after months of commissioning and calibration runs of LZ. ^{129m}Xe and ^{131m}Xe will also serve as calibration sources in the early runs.

5.1.2 Laboratory and detector materials

The rock in the Davis cavern is naturally contaminated with ^{238}U ($29\pm15\,Bq/kg$), ^{232}Th ($13\pm3\,Bq/kg$) and ^{40}K ($220\pm60\,Bq/kg$) [240]. The neutrons and γ-rays resulting from the associated decay chains (fig. 5.2) constitute the major part of the background outside the detector. The LXe TPC will be primarily shielded against these γ-rays by the water tank. Further shielding will be provided by an inverted pyramid shaped shield on the cavern floor, made of 6 octogonal 5 cm steel plates just beneath the LXe target (where the rock is at the closest proximity). The neutrons will be efficiently attenuated [225] by the water and the liquid scintillator in OD.

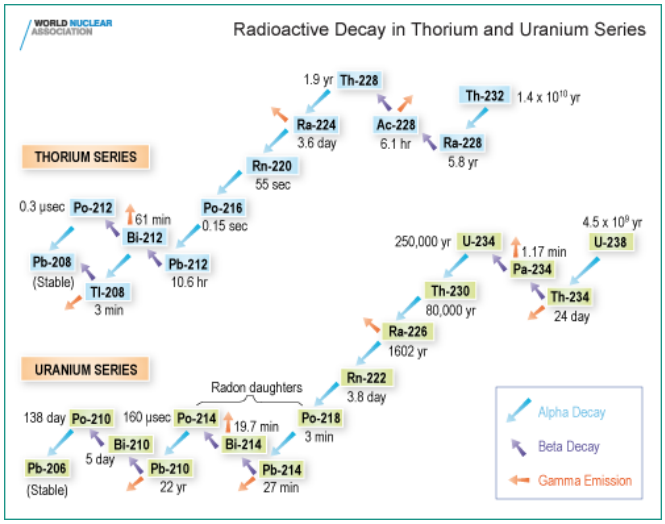

Figure 5.2: *U and Th decay chains. Source: World Nuclear Assosciation (WNA).*

The construction materials of various detector components have some intrinsic radioactivity as well. Based on the size, mass and proximity to the LXe,

[§]i.e. rejecting the ^{127}Xe-induced x-ray/Auger background by detecting the following ^{127}I-decay.

components with dominant contributions are the PMT arrays, the titanium cryostat and the TPC system itself. All materials to be used in the LZ detector are thus needed to be extensively screened [225] against these naturally occurring radioactive material (NORM)s, e.g. the γ-ray emitting ^{40}K, ^{137}Cs and ^{60}Co; ^{238}U, ^{232}Th and their progeny.

5.1.3 Surface contaminations

Exposure to airborne radon (particularly ^{222}Rn with $T_{1/2} = 3.82\,days$, produced in the ^{238}U decay chain) at any stage of detector assembly, construction or installation can deposit (or implant) radon progenies (e.g. ^{218}Po) on the surface of various detector components. β particles and γ-rays from short lived radio-contaminants (e.g. ^{206}Pb from ^{218}Po-decay) are largely mitigated in combination with the LXe self-shielding. However, the long lived ^{210}Pb ($T_{1/2} = 22.3\,years$) poses a real problem, as its progeny ^{210}Po decays by α-emission, leading to an (α, n) reaction that produces fast neutrons. The fast neutrons can undergo NR events mimicking a WIMP signal. Materials with large neutron yields (such as PTFE on the TPC walls) are more prone to such induced neutron background. LZ has a rigorous programme to control the exposure to radon rich air, to ensure a radon proof storage and assembly system, and to strictly follow the cleanliness protocol against radon and any generic dust contamination containing the NORMs.

5.1.4 Intrinsic Xe contaminations

The largest contributors to the overall background in LZ are the dispersed radioisotopes in the LXe, which can not be mitigated by the self-shielding. A xenon purification campaign with a gas chromatography system is designed at SLAC that reduces the trace amounts of naturally occurring ^{85}Kr and ^{39}Ar in xenon to the levels $< 0.015\,ppt$[¶¶¶] (g/g) and $< 0.45\,ppb$[¶¶¶] (g/g) respectively [225]. After the $Kr - Ar$ removal, LXe is stored for about six months in storage before moving into the underground. Proper care is taken to avoid any re-production of ^{85}Kr during storage or detector operation, either via air leaks or detector outgassing.

[¶¶¶] *ppt*= parts per trillion, *ppb*= parts per billion

Major backgrounds of concerns are the naked or semi-naked β emissions from ^{214}Pb (^{212}Pb), a progeny of the ^{222}Rn (^{220}Rn) sub-chain. The ^{222}Rn (^{220}Rn) are emanated out of the Xe-wetted detector materials in the active LXe volume. The naked β particles cannot be vetoed, and the γ rays in the semi-naked β decays are fast enough to escape the active volume and harder to tag (i.e. β-γ coincidence can not be used). ^{222}Rn emanations from Xe-wetted materials are either directly measured [241] or projected from existing literature.

5.1.5 Physics backgrounds

An interesting physics background in LZ is the two neutrino double beta decay ($2\nu\beta\beta$) of ^{136}Xe, a SM process that occurs when a single beta decay is energetically forbidden. Two electrons and anti-neutrinos are emitted in the process, followed by γ-ray emissions with 760.493 and 818.497 keV energies. The background rate used in LZ is based on EXO-200 [242] and KamLAND-Zen [243] measurements.

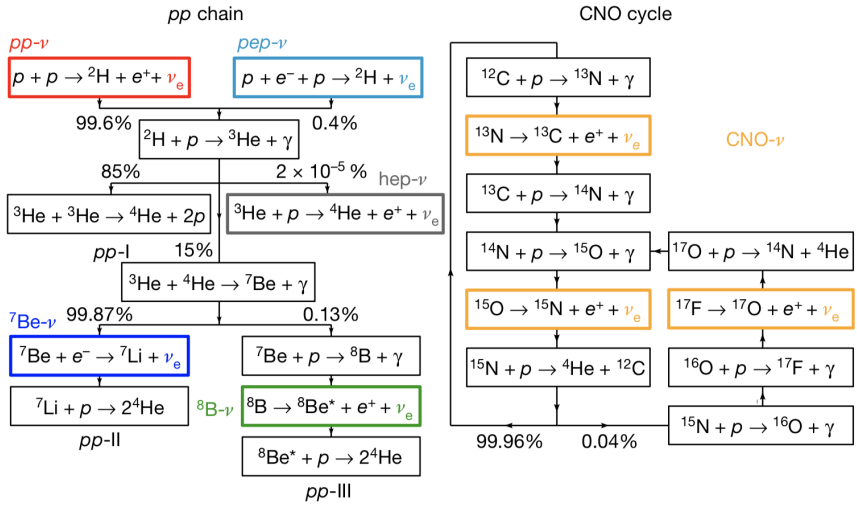

Figure 5.3: *Solar PP chain (left) and CNO cycles (right). Source: [244].*

The Earth is continuously bombarded upon by solar, atmospheric[‖] and diffuse supernova (DSN)[¶] neutrinos. At low energies ($< 10\,MeV$), the solar neutrino flux dominates the other two. Scattering of solar neutrinos with atomic electrons in xenon is a prominent ER background for LZ. Neutrinos are produced (fig. 5.3) in the solar core as a product of a series of nuclear fusion reactions. The major

[‖] produced from muon and pion decays in the atmosphere.
[¶] neutrinos resulting from a supernova in the Milky-Way galaxy.

($\sim 86\%$) contributions come from different stages of the proton-proton (PP) chain and the rest ($\sim 14\%$) comes from the CNO cycle. An emitted neutrino is named after the specific stage it is produced from. The ER neutrino background in LZ is dominated by the *pp* neutrinos, with smaller ^{7}Be and CNO contributions. A significant period of my PhD was spent in the studies of the ER solar neutrino background in LZ, with the atomic binding effect of the recoiling electron taken into account. This will be addressed in the next section.

The ^{8}B and *hep* neutrinos can coherently scatter off the LXe nuclei, constituting a very low NR background. However, the coherent neutrino-nucleus scattering ($CE\nu NS$) is also possible for diffuse supernova [245] and atmospheric neutrinos, which constitutes the biggest part of total NR background in LZ [63].

5.2 ER backgrounds: solar neutrinos

5.2.1 Incoming solar neutrino flux

A precise experimental measurement of the solar neutrino flux and identifying the individual components is technically challenging. Alternatively, theoretical estimates from the standard solar model (SSM) can be used. The SSM is a spherically symmetric quasi-static model of the Sun, constrained by its luminosity, radius, age and composition. The metallic composition of the solar interior plays an important role in building a SSM, and can be either high (as inferred by helioseismology[§§]) or low (implied by photospheric measurements [247]). This apparent inconsistency, known as the ′solar metallicity problem′, gives rise to a number of SSMs, each predicting different CNO neutrino fluxes. However, the effect of solar metallicity on the fluxes of neutrinos from the PP chain is negligible.

Table 5.2 summarises the solar neutrino fluxes used in LZ background estimations. The *pp*, *pep*, ^{7}Be and CNO neutrino fluxes are obtained from the luminosity-constrained analysis of the BORon solar neutrino EXperiment (BOREXINO)'s data, by Haxton et al [248]. For ^{8}B, the value measured by Neutral Current Detectors (NCDs) of Sudbury Neutrino Observatory (SNO) [249] is used. For *hep* neutrinos, the value used is from $GS98 - SFII$[¶¶] [248], a high

[§§]Solar interior studies by observing solar oscillation, i.e., vibrations on solar surface.

[¶¶]A modified version of the high metallicity SSM proposed by Grevesse and Sauval [246] in 1998, with the inclusion of the solar Fusion II cross-sections.

metallicity SSM. Note that the fluxes of CNO neutrinos have only an upper bound in Table 5.2, because of the uncertainty in our current knowledge on solar metallicity (i.e. the solar neutrino problem mentioned earlier).

Table 5.2 *Solar neutrino fluxes used in LZ. The pp, pep, ^7Be and CNO neutrino fluxes are from analysis of BOREXINO's data, by Haxton et al [248]. The ^8B and hep fluxes are from [249] and [248] respectively. See text for details.*

ν	Energy Spectra	E_ν^{max} (E_ν) for continuous (line) spectra (keV) [250]	flux ($cm^{-2}\,s^{-1}$)
pp	Continuous	420.3	$6.05\,(1^{+0.003}_{-0.011}) \times 10^{10}$
pep	Line	1442	$1.46\,(1^{+0.010}_{-0.014}) \times 10^{8}$
^7Be		862 (89.7%), 384 (10.3%)	$4.82\,(1^{+0.05}_{-0.04}) \times 10^{9}$
hep	Continuous	18773	$8.04\,(1 \pm 0.3) \times 10^{3}$
^8B		~ 15000	$5.25\,(1 \pm 0.03) \times 10^{6}$
^{13}N		1199	$\leq 6.7 \times 10^{8}$
^{15}O		1732	$\leq 3.2 \times 10^{8}$
^{17}F		1740	$\leq 59 \times 10^{6}$

The incoming energy spectra is continuous for pp, hep, ^8B, CNO neutrinos and mono-energetic for ^7Be and hep neutrinos. The maximum neutrino energies can be obtained by standard Q-value calculations, except for the neutrinos from ^8B decay ($^8B \rightarrow {}^8Be^* + e^+ + \nu_e$). The decay product $^8Be^*$ can be produced in a number of possible states so that the endpoint is computed from measured α-particle spectrum from the $^8Be^*$ decay. For hep neutrinos, the overall neutrino flux is very small and there is a large uncertainty in the low energy $^3He + p$ reaction cross-section.

The spectral shape of pp and CNO neutrino fluxes originates from standard theories of allowed and superallowed weak transitions and is parametrised as [135]

$$\frac{dN_\nu(E_\nu)}{dE_\nu} = A(Q + m_e - E_\nu)[(Q + M_E - E_\nu)^2 - m_e^2]^{\frac{1}{2}} E_\nu^2 F, \tag{5.2}$$

where E_ν is the neutrino energy, $Q = E_\nu^{max}$ is the maximum neutrino energy, m_e is the electron mass, A is a normalisation factor and F is a correction factor. For low-Z nuclei, F is close to unity for most of the solar neutrino species, and hence the present work considers $F = 1$. The normalisation factor A depends on the value of the neutrino flux being considered.

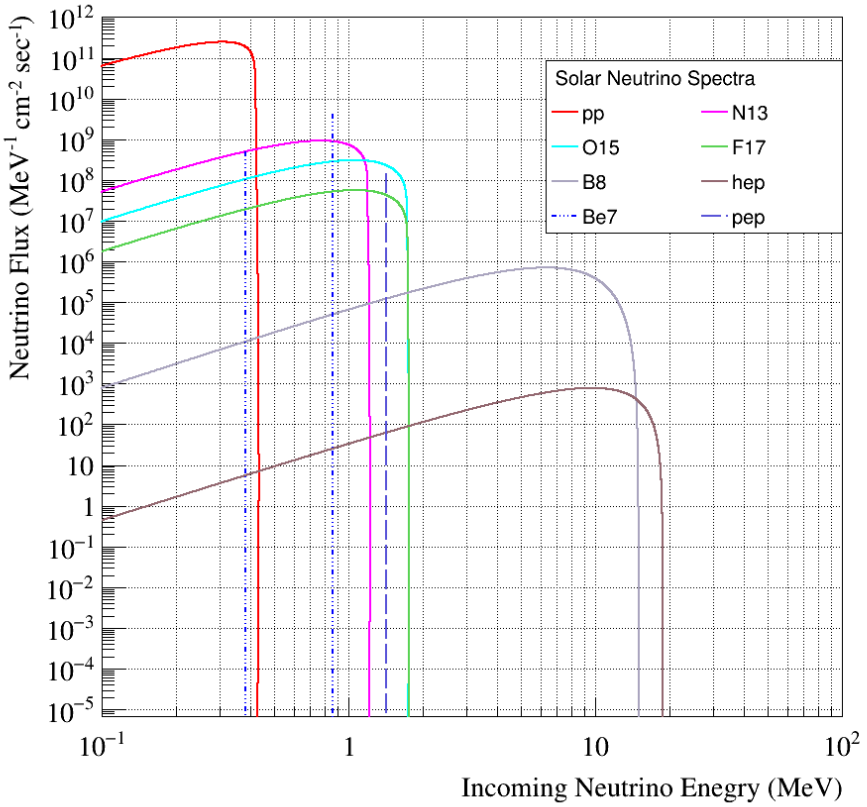

Figure 5.4: *Incoming solar neutrino fluxes used in this work. The pp, pep, ^{7}Be and CNO neutrino fluxes are from analysis of BOREXINO's data, by Haxton et al [248]. The ^{8}B and hep fluxes are from [249] and [248] respectively.*

The energy spectra (in MeV) for ^{8}B and *hep* neutrinos can be analytically approximated as [135]

$$\begin{aligned} \frac{dN_\nu(E_\nu)}{dE_\nu} &= 8.52 \times 10^{-6}(15.1 - E_\nu)^{2.75} E_\nu^2 \qquad (\ ^{8}B \text{ neutrinos}), \text{ and} \\ \frac{dN_\nu(E_\nu)}{dE_\nu} &= 2.33 \times 10^{-5}(18.8 - E_\nu)^{1.80} E_\nu^{1.92} \qquad (\ hep \text{ neutrinos}), \end{aligned} \tag{5.3}$$

respectively. Eqs. 5.3 are well-consistent with the tabulated data by Bahcall et al. [251, 252]. Fig. 5.4 illustrates the incoming energy spectra for different solar neutrino species: parametrised according to eqs. 5.2 and 5.3, and normalised to the flux values tabulated in table. 5.2.

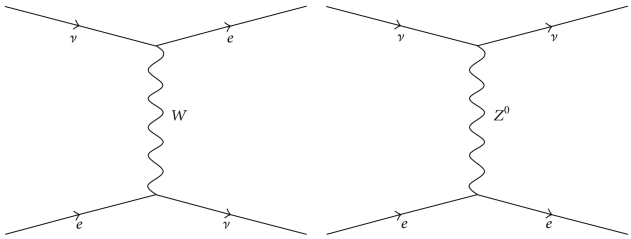

Figure 5.5: *Tree level Feynman diagrams for charged (left) and neutral (right) current channels of $\nu_e + e^- \rightarrow \nu_e + e^-$ scattering.*

5.2.2 Matrix elements and scattering kinematics

5.2.2.1 Matrix elements

The elastic neutrino-electron scattering,

$$\nu_l + e^- \rightarrow \nu_l + e^-, \tag{5.4}$$

proceeds through both the neutral current (NC, Z^0 exchange) and the charged current (CC, W exchange) channels for electron neutrinos ($l = e$) (see fig. 5.5) and only through the neutral current interaction for the other neutrino flavours ($l = \mu, \tau$). The full particle-physics description of the interaction process is encoded in the scattering amplitude $|\mathcal{M}|$, which in the low energy limit (i.e. for $|q|^2 << m_{W,Z}^2$ where q is the 4-momentum transfer and $m_{W,Z}$ are the masses** of W, Z^0) reads as [253]

$$\begin{aligned} |\mathcal{M}|_{CC} &= \frac{G_F}{\sqrt{2}} \left[\bar{u}_{\nu_2}\gamma_\mu(1-\gamma_5)u_{\nu_1}\right]\left[\bar{u}_{e_2}\gamma^\mu(1-\gamma_5)u_{e_1}\right] \qquad \text{(CC interaction)}, \\ |\mathcal{M}|_{NC} &= \frac{G_F}{\sqrt{2}} \left[\bar{u}_{\nu_2}\gamma_\mu(1-\gamma_5)u_{\nu_1}\right]\left[\bar{u}_{e_2}\gamma^\mu(g_V^{\nu e} - g_A^{\nu e}\gamma_5)u_{e_1}\right] \qquad \text{(NC interaction)} \end{aligned} \tag{5.5}$$

at tree level. u_{ν_1} (u_{e_1}), u_{ν_2} (u_{e_2}) are the initial and final neutrino (electron) spinors respectively, and $G_F = 1.1663788(7) \times 10^{-5} GeV^{-2}$ is the Fermi constant††. The vector ($g_V^{\nu e}$) and axial vector ($g_A^{\nu e}$) terms appear in $|\mathcal{M}|_{NC}$ because of the $V - A$

**$m_W = 80.4\,GeV$, $m_Z = 91.2\,GeV$.

††In analogy to the electromagnetic interaction, Fermi assumed a $'$4-point$'$ interaction (i.e. happening at a single point in the space-time) with no propagator to describe weak interactions (β-decay). His theory introduced a coupling factor $G_F/\sqrt{2}$, where G_F is termed as the Fermi constant. Although it is now known that weak interaction is mediated by $W^\pm, Z^0$ bosons and the 4-point interaction is incorrect, Fermi's theory can be considered as a low energy approximation.

nature of the NC interaction. $g_V^{\nu e}$ and $g_A^{\nu e}$ are defined as:

$$g_V^{\nu e} \equiv 2g_L^{\nu} g_V^{e} = \rho(-\frac{1}{2} + 2\sin^2\theta_W), \qquad g_A^{\nu e} \equiv 2g_L^{\nu} g_A^{e} = \rho(-\frac{1}{2}). \tag{5.6}$$

The values of vector (g_V^f), axial vector (g_A^f), left (g_L^f) and right (g_R^f) coupling constants for different fermion fields are summarised in table. 5.3. Here θ_W is the Weinberg angle and a standard value, $\sin^2\theta_W = 0.231$ [59] is used. $\rho = 1$ at the (SM) tree level.

Table 5.3 *Values for vector (g_V), axial-vector (g_A), left (g_L) and right (g_R) coupling constants for different fermion fields for pure NC interactions.*

Fermion (f)	g_L^f	g_R^f	$g_V^f = g_L^f + g_R^f$	$g_A^f = g_L^f - g_R^f$
ν_e, ν_μ, ν_τ	$+\frac{1}{2}\sqrt{\rho}$	0	$+\frac{1}{2}$	$+\frac{1}{2}$
e, μ, τ	$\sqrt{\rho}(-\frac{1}{2} + \sin^2\theta_W)$	$\sqrt{\rho}(+\sin^2\theta_W)$	$\sqrt{\rho}(-\frac{1}{2} + 2\sin^2\theta_W)$	$\sqrt{\rho}(-\frac{1}{2})$

For $\nu_e - e^-$ scattering, both CC and NC channels come into play and the corresponding amplitudes interfere with one another [254]. It is evident from eqs. 5.5 that the interference can be simply realised by shifting $g_V^{\nu e} \to g_V^{\nu e} + 1$ and $g_A^{\nu e} \to g_A^{\nu e} + 1$.

5.2.2.2 Kinematics

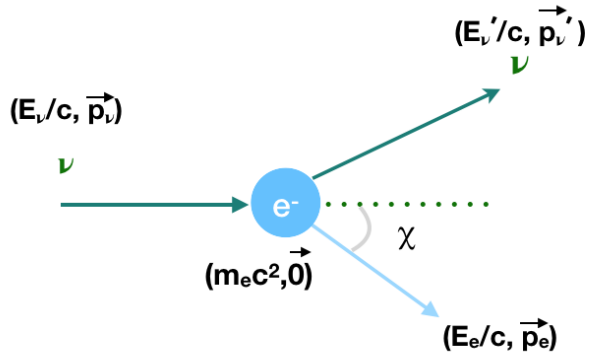

Figure 5.6: *Two-body kinematics of $\nu - e^-_{free}$ scattering.*

Consider next the kinematics of the scattering process (fig. 5.6). The electron is assumed to be free and initially at rest. In the ultra-relativistic limit ($m_\nu \to 0$),

the four momentum transfer squared (q^2) in the process is

$$q^2 = -\left(\frac{E_e}{c} - m_e c^2\right)^2 - |\,\vec{p}_e\,|^2 = -\left(\frac{E_e}{c} - m_e c^2\right)^2 - \left(\frac{E_e^2}{c^2} - m_e^2 c^2\right) = 2m_e T, \quad (5.7)$$

where $T = E_e - m_e c^2$ is the energy and $\vec{p}_e$ the three momentum transferred to the electron. Since there is no other body involved, T appears totally as the kinetic energy of the recoil electron. The scattering angle χ with respect to the incoming neutrino direction and the maximum T-value (corresponding to $\chi = 0°$) are

$$\cos\chi = \frac{E_\nu + m_e}{E_\nu}\sqrt{\frac{T}{T + 2m_e}}, \qquad T_{max} = \frac{2{E_\nu}^2}{2E_\nu + m_e} \quad (5.8)$$

respectively. To obtain the differential scattering cross-section in the laboratory frame, one needs to take the square of eq. 5.5 (i.e. $|\mathcal{M}|^2$), average over initial electron polarizations, sum over all final polarisation and spin states, and integrate over all unobserved momenta (e.g. outgoing neutrinos). The expression for the differential scattering cross-section (either for pure NC or NC+CC) is [255]

$$\begin{aligned}\frac{d\sigma(T, E_\nu)}{dT} = \frac{G_F^2 m_e}{2\pi}\Bigg[&(g_V^{\nu e} + g_A^{\nu e})^2 + (g_V^{\nu e} - g_A^{\nu e})^2\left(1 - \frac{T}{E_\nu}\right)^2 \\ &- \left((g_V^{\nu e})^2 - (g_A^{\nu e})^2\right)\frac{m_e T}{(E_\nu)^2}\Bigg]\end{aligned} \quad (5.9)$$

where

$$g_A^{\nu e} = \begin{cases} \frac{1}{2}, & (\text{for } \nu_e) \\ -\frac{1}{2}, & (\text{for } \nu_{\mu,\tau}) \end{cases}, \qquad g_V^{\nu e} = \begin{cases} +\frac{1}{2} + 2\sin^2\theta_W, & (\text{for } \nu_e) \\ -\frac{1}{2} + 2\sin^2\theta_W, & (\text{for } \nu_{\mu,\tau}) \end{cases}. \quad (5.10)$$

For anti-neutrinos, one should substitute $g_A \to -g_A$.

5.2.3 Flavour content of the incoming neutrinos

First proposed by Bruno Pontecorvo in 1957 [256, 257] and further developed by Maki, Nakagawa, and Sakata in 1962 [258], neutrino oscillation is a phenomenon where a neutrino propagating through the space can change from one flavour to another. This is due to the mixture between its flavour (ν_e, ν_μ, ν_τ) and mass (ν_1,

ν_2, ν_3) eigenstates:

$$\begin{bmatrix} \nu_e \\ \nu_\mu \\ \nu_\tau \end{bmatrix} = \begin{bmatrix} U_{e1} & U_{e2} & U_{e3} \\ U_{\mu 1} & U_{\mu 2} & U_{\mu 3} \\ U_{\tau 1} & U_{\tau 2} & U_{\tau 3} \end{bmatrix} \begin{bmatrix} \nu_1 \\ \nu_2 \\ \nu_3 \end{bmatrix} = U_{PMNS} \begin{bmatrix} \nu_1 \\ \nu_2 \\ \nu_3 \end{bmatrix}, \tag{5.11}$$

where U_{PMNS} is the unitary Pontecorvo-Maki-Nakagawa-Sakata matrix [258]:

$$U_{PMNS} = \begin{bmatrix} c_{12}c_{13} & s_{12}c_{13} & s_{13}e^{-i\delta} \\ -s_{12}c_{23} - c_{12}s_{23}s_{13}e^{i\delta} & c_{12}c_{23} - s_{12}s_{23}s_{13}e^{i\delta} & s_{23}c_{13} \\ s_{12}s_{23} - c_{12}c_{23}s_{13}e^{i\delta} & -c_{12}s_{23} - s_{12}c_{23}s_{13}e^{i\delta} & c_{23}c_{13} \end{bmatrix} P, \tag{5.12}$$

with $\delta \in [0, 2\pi]$. c_{ij} and s_{ij} are the cosine and sine of the Euler angles ($\theta_{ij} \in [0, \frac{\pi}{2}]$) respectively with i and j referring to the neutrino generation ($i < j = 1, 2, 3$). The matrix P in eq. 5.12 is simply an unit matrix:

$$P_{Dirac} = \begin{bmatrix} 1 & 0 & 0 \\ 0 & 1 & 0 \\ 0 & 0 & 1 \end{bmatrix} \tag{5.13}$$

for Dirac scenario (i.e. neutrinos are *not* their own antiparticles), providing only one CP violating Dirac phase δ.

When a neutrino propagates, the propagation eigenstate is governed by its mass eigenstate. Different mass eigenstates propagate with different frequencies, leading to a constructive interference between their flavour components. Thus, a solar neutrino initially produced as ν_e in the solar core, can oscillate into other flavours along their way to the Earth and end up being detected[‡‡‡] as a ν_μ or a ν_τ. The pattern of the neutrino oscillation depends on the medium they are propagating through (e.g. the solar material between the Sun's core and the surface). At low energies, the matter effect (also called the Mikheyev–Smirnov–Wolfenstein (MSW) effect) is negligible and the large mixing angle (LMA) MSW solution of solar neutrino problem[§§§] is applicable. Since the

[‡‡‡]Neutrino experiments, in general, search for weak CC interactions, i.e., identify the neutrinos by detecting the charged leptons produced alongside. In other words, experiments detect the ′flavour′ eigenstates, not the mass ones.

[§§§]A large discrepancy was found between the experimentally measured flux and the one predicted by standard solar model. The problem was resolved by the concept of neutrino oscillations [259, 260].

largest contribution to the solar neutrino flux comes from the low energy *pp* and ^{7}Be neutrinos (Fig. 5.4), it is a safe choice to assume that the solar neutrino oscillation is dominated by the vacuum between the Sun and the Earth.

The probability for a solar neutrinos arriving at the detector with a certain neutrino flavour is termed as the survival probability. The survival probability for ν_e is approximated as [261]

$$P_{(\nu_e)} = \cos^4\theta_{13}\left(1 - \frac{1}{2}\sin^2 2\theta_{12}\right) + \sin^4\theta_{13}, \tag{5.14}$$

where θ_{13} and θ_{12} are the cross-generation mixing angles defined earlier. The sum reads

$$\sum P_{(j)}\,(j = \nu_\mu, \nu_\tau) = 1 - P_{(\nu_e)}, \tag{5.15}$$

as obvious. The values of $\sin^2\theta_{13}$ and $\sin^2\theta_{12}$ used in the current work are [262]

$$\begin{aligned} &\sin^2\theta_{13} = 0.0219\,(\pm 0.0014) \quad \text{(reactor neutrino experiments), and} \\ &\sin^2\theta_{12} = 0.310\,(\pm 0.014) \quad\;\; \text{(Super-K + SNO data).} \end{aligned} \tag{5.16}$$

5.2.4 Recoil spectrum: free electron approximation (FEA)

The differential ER spectrum $(dN_e\,(T)/dT)$ induced by the $\nu + e^-_{free}$ scattering in LXe can be obtained by convolving the incoming flux (eq. 5.2 or 5.3) with the scattering cross-section (eq. 5.9), integrating over all neutrino energies, summing over all neutrino flavours and multiplying with the detector exposure time t and number of electrons (N_0) that participate in the scattering:

$$\frac{dN_e\,(T)}{dT} = N_0 \times t \times \sum_{i=\nu_e,\,\nu_\mu,\,\nu_\tau} P_{(i)} \int_{E_\nu^{min}}^{E_\nu^{max}} dE_\nu \left(\frac{dN_\nu^{(i)}(E_\nu)}{dE_\nu}\right)\left(\frac{d\sigma^{(i)}(T, E_\nu)}{dT}\right). \tag{5.17}$$

The survival probabilities $P_{(i)}$ for neutrino flavours $i = \nu_e$, ν_μ, ν_τ are calculated using eq. 5.14. Assuming all electrons in the target as free, the number N_0 reads

$$N_0 = (6.02 \times 10^{23})\,\frac{Z}{A} \tag{5.18}$$

for LXe (atomic number $Z = 54$ and atomic mass $A = 131.3\,g$).

The total differential event rate (eq. 5.17) and its ν_e-only and $\nu_{\mu,\tau}$-only components are plotted against the ER energy for *pp* neutrinos, as example, in

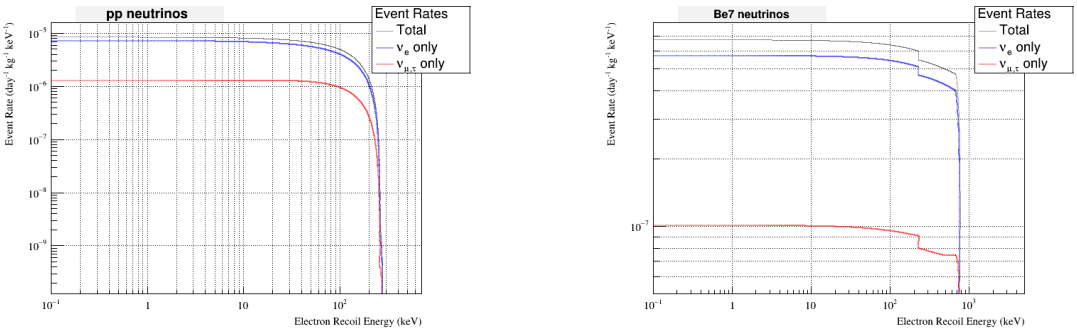

(a) *(b)*

Figure 5.7: *Total differential ER spectrum and its decomposition into ν_e-only and $\nu_{\mu,\tau}$-only components, for (a) pp and (b) ^7Be neutrinos.*

fig. 5.7a. The spectral shape will be similar for other neutrino components with continuous spectra (^{13}N, ^{15}O, ^{17}F, ^8B, *hep*). For ^7Be neutrinos, there are two mono-energetic peaks (Table. 5.2) with $E_\nu = 384$ and $862\,keV$. The corresponding T_{max} (eq. 5.8) are $\sim 230\,keV$ and $\sim 665\,keV$, respectively. This explains the distinct structure at $\sim 230\,keV$ in the recoil spectra (fig. 5.7b), ensuring that above $\sim 230\,keV$ the rate is only due to $862\,keV$ ^7Be neutrino line. Note that the *pep* neutrinos have only one energy so the spectral shape is similar to that of *pp* neutrinos.

Nevertheless, only the total (eq. 5.17) differential rate summed over all neutrino flavours is relevant and from now on, no explicit mention of neutrino flavours will follow. The spectra (eq. 5.17) for all solar neutrino components assuming a free electron approximation (eq.5.18) are illustrated (solid lines) in fig.5.8.

5.2.5 Recoil spectrum: stepping approximation (SA)

The FEA works well at high keV regions, i.e. at energies considerably higher than the binding energy of K-shell electron in LXe ($\sim 34.5\,keV$). For neutrinos with low fluxes and very high energy ranges (e.g. CNO neutrinos) this approximation is sufficient and eq. 5.17 can be used. However, for solar neutrinos (*pp*, ^7Be and ^{13}N) that have high fluxes at low energies, atomic binding plays a non-negligible role and must be taken into account. The simplest approach is to use a stepping function, θ:

$$\theta(T - B_k) = \begin{cases} 1 & \text{if } T \geq B_k \\ 0 & \text{if } T < B_k \end{cases}, \tag{5.19}$$

where B_k the binding energy of the $K-$th electron (i.e. ionisation threshold of the $K-$th shell) in LXe. The stepping approximation (SA) [263] simply assumes

that only the electrons having binding energies less than the energy deposited by the neutrino (T) participate in the scattering process. The stepping-modified version of eq. 5.9 reads

$$\frac{d\sigma^{(i)}(T, E_\nu)}{dT} = \sum_{k=1}^{Z=54} \theta(T - B_k) \frac{d\sigma^{(i)}_{free}(T, E_\nu)}{dT}, \tag{5.20}$$

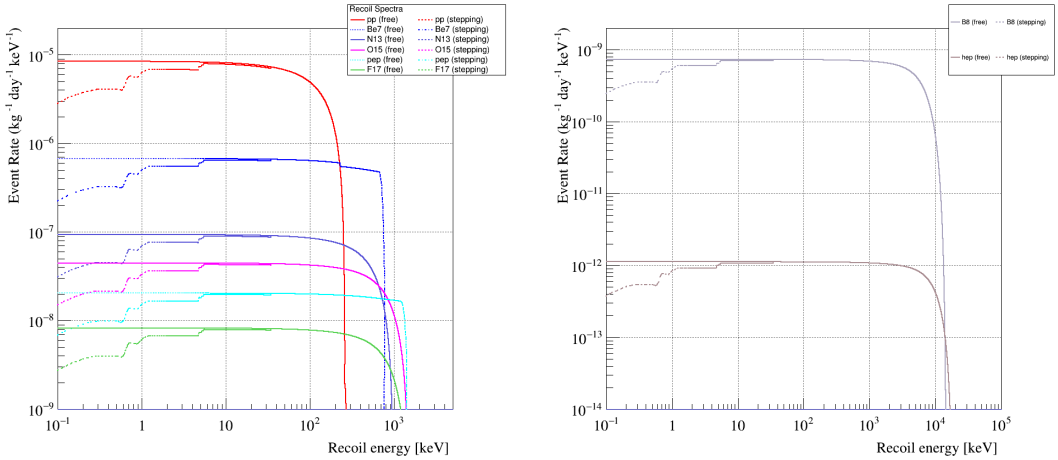

Figure 5.8: *Free electron vs stepping approximated rates of neutrino-electron scattering in xenon (left) for pp, pep, ^{7}Be and CNO neutrinos and (right) for ^{8}B and hep neutrinos.*

where the subscript ′free′ refers to the FEA. Comparative recoil spectra for free (solid lines) vs stepping approximations (dashed lines) for different solar neutrino components are depicted in fig. 5.8. The stepping effect at low energies, as obvious, reduces the number of scattering events as compared to the free-electron approximation. The stepping approximated spectrum (dashed-line) gradually approaches the free electron approximated one (solid line) with recoil energy, and become indistinguishable above ($34.5\,keV$), the binding energy of K-th shell electron in Xe.

5.2.6 Relativistic random phase approximation (RRPA)

Despite the successful application in background analyses for germanium detectors [264–266], the SA suffers from some theoretical drawbacks [264, 267]. For example, FEA and SA assume a two-body scattering, which is not true in reality. The more realistic scenario is the neutrino-induced atomic (A) ionisation,

$$\nu + A \rightarrow \nu + A^+ + e^-. \tag{5.21}$$

There are now three bodies in the final state and the constraint 5.7 obtained from two body kinematics is no longer valid. The momentum transfer squared in the ultra-relativistic limit ($m_\nu \to 0$) now depends on the neutrino scattering angle (χ) as well [266]:

$$q^2 = -4E_\nu^2 \sin^2\left(\frac{\chi}{2}\right) - m_\nu^2 \frac{T^2}{E_\nu^2}, \tag{5.22}$$

which can never be zero as long as the neutrino has a non-zero mass. This has an important implication on neutrino electromagnetic properties [266]. The cosine of the scattering angle χ is constrained by (required by the 4-momentum conservation)

$$min\left(1,\, max\left[-1,\, \frac{E_\nu^2 + (E_\nu - T)^2 - 2M_A\,(T - B)}{2E_\nu\,(E_\nu - T)}\right]\right) \leq \cos\chi \leq 1, \tag{5.23}$$

where M_A is the atomic mass and B is the binding energy of ejected electron. Due to the wider range of q^2 than the specified one (eq. 5.7), the sharp cut-off T_{max} (eq. 5.8) is no longer true as well.

More importantly, the SA does not consider atomic wave-functions to estimate the number of active electrons participating in the atomic ionisation process. Ab-initio calculations using the Hartree-Fock (HF) method [268, 269] and its modifications can be a good solution.

The (multi-configuration) relativistic random phase approximation (RRPA) formalism, recently developed by Jiunn-Wei Chen et al. [264, 270] is based on the time-dependent HF theory with some additional features. This is a better theoretical tool to account for the atomic wave-functions, because:

1. **Multi-configuration HF:** Open shell atoms with high Z may have more than one ground state configurations. The multi-configuration RRPA takes a linear combination of them to create a proper HF reference state.

2. **Relativistic corrections:** For high Z atoms, the relativistic corrections can no longer be neglected.

3. **Effect of two-electron correlations:** Important in many-electron atoms, the electron-electron correlations may affect the scattering cross-section and MCRRPA takes this into account.

For close-shelled atoms like Xe, the multi-configuration ground state is irrelevant, and a simple RRPA treatment suffices. The differential cross-section (eq. 5.9) is

now modified to contain information on initial ($|\Psi_i\rangle = |J_i, M_{J_i}, ...\rangle$) and final ($|\Psi_f\rangle$) atomic states, in terms of the atomic weak response functions:

$$\begin{aligned} R^{(i)}_{\alpha\beta} &= \frac{1}{2J_i+1} \\ &\times \sum_{M_{J_i}} \sum_{f} \langle \Psi_f \mid g_V^{(i)} \hat{\mathcal{J}}_\alpha - g_A^{(i)} \hat{\mathcal{J}}_{5\alpha} \mid \Psi_i \rangle \langle \Psi_f \mid g_V^{(i)} \hat{\mathcal{J}}_\beta - g_A^{(i)} \hat{\mathcal{J}}_{5\beta} \mid \Psi_i \rangle^* \\ &\times \delta(T + E_i - E_f), \end{aligned} \tag{5.24}$$

where $\hat{\mathcal{J}}$ are the current operators, g_A, g_V are the couplings defined in eq. 5.10 and $\alpha, \beta = 0, 1, 2, 3$ are the Lorentz indices. The quantisation axis $\alpha = 3$ is taken to be in the direction of $\vec{q}$. In the calculation, the recoil of heavy Xe^+ ion is neglected i.e. it is assumed that the deposited energy (T) entirely appears as the kinetic energy of ejected electron plus the atomic excitation energy. The expression for the differential cross-section now reads [270]

$$\begin{aligned} \frac{d\sigma^{(i)}(T, E_\nu)}{dT} = \frac{G_F^2}{\pi}(E_\nu - T)^2 \int d\cos\chi \cos^2\frac{\chi}{2} \Bigg[& R^{(i)}_{00} - \frac{T}{\mid \vec{q} \mid} R^{(i)}_{03+30} \\ & + \frac{T^2}{\mid \vec{q} \mid^2} R^{(i)}_{33} + \left(\tan^2\frac{\chi}{2} - \frac{q^2}{2 \mid \vec{q} \mid^2} \right) R^{(i)}_{11+22} \\ & + \tan\frac{\chi}{2} \sqrt{\tan^2\frac{\chi}{2} - \frac{q^2}{\mid \vec{q} \mid^2}} R^{(i)}_{12+21} \Bigg], \end{aligned} \tag{5.25}$$

where $\vec{q}$ is the three-momentum transfer.

Values of the differential cross-sections (eq. 5.25) for neutrino-ionisation of LXe have been computed by J.W. Chen et al. [270] upto $30\,keV$ ER energy with a theoretical error less than 5% in general and an average systematic uncertainty of 2–3% (fig. 5.9) in the energy window of 2–30 keV. Background suppressions of $\sim 23\%$ for pp and $\sim 20\%$ for ^7Be in the $2 - 30\,keV$ region were reported. The suppression for the pp component is stronger due to the lower averaged E_ν. The free and stepping calculations shown in fig. 5.9 are similar to that described in this thesis earlier, except that the authors used different pp and ^7Be neutrino fluxes:

$$\phi_{pp} = 5.98 \times 10^{10}\, cm^{-2}\, s^{-1},\ \phi_{^7Be} = 5.00 \times 10^{9}\, cm^{-2} s^{-1}. \tag{5.26}$$

The fluxes 5.26 differ than those used in LZ is by only ($\sim 1 - 3\%$).

A few comments can be made on the RRPA calculations in [270]. First, the exact RRPA-approximated shape of ER spectra for ^{13}N and other neutrino components are unavailable from the paper except an explicit statement that ^{13}N

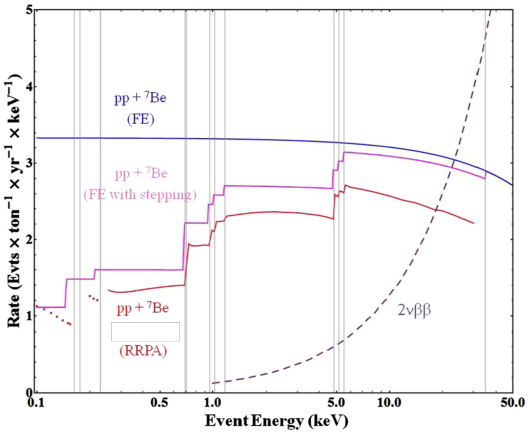

Figure 5.9: *Differential count rate of solar neutrino induced ER in LXe using free, stepping and RRPA approximations by J.W.Chen et al. [270]. The dashed curve is the neutrino background from $2\nu\beta\beta$ decay of ^{136}Xe.*

neutrinos would suffer similar background suppression as the ^7Be ones (because they have similar averaged E_ν). Obtaining a stable solution at very low energies ($\leq$ 250 eV) is numerically difficult, that is why the low energy points are not smooth in fig. 5.9. Finally, the behaviour of RRPA spectrum above 30 keV is not very clear from [270]. At least, it is expected that it will approach the FEA spectrum at some point above $T = 34.5\,keV$. For example, consider a simple case where the RRPA curve above 30 keV lies between the FEA spectrum and 80% of the FEA spectrum. The theory error above 30 keV would be then $\sim \pm 10\%$. However, since the ER $2\nu\beta\beta$ spectra starts to dominate above 20 keV (see fig. 5.9), the uncertainty arising from atomic binding treatment is expected to be less important in our analysis.

5.2.7 Implementation of RRPA, analyses and results

Implementation of RRPA values from [270] into the ER background model for LZ is done according to the following steps:

1. Read Data from Digitised J.W.Chen's plot (fig. 5.9) for $pp +^7 Be$ neutrinos, perform a linear interpolation by CERN ROOT to use them for $T \leqslant 30keV$.

2. Scale the RRPA spectra with respect to the stepping approximated spectra for $pp +^7 Be$ neutrinos up to 30 keV. The scaling factor varies with energy.

3. Assume that the scaling factor becomes constant at $T = 30\,keV$. Since it is not clearly known how the scale varies above $30keV$, a constant scale is a safer choice.

4. For ^{13}N neutrinos, J.W.Chen's RRPA values are unavailable, so the scaling factors computed in the above steps are used.

Note that in $30\,keV < T \leqslant 34.5\,keV$, atomic binding effect should obviously be considered, as the K-shell electron in Xe has a binding energy $\approx 34.5\,keV$. Using a scaling factor in this reason is a wise choice. Above $34.5\,keV$, although the energy transfer T is higher enough to extract the K-shell electron, the electron *should not be* considered to be *completely free*. Also, eq. 5.25 does not have a $'$stepping$'$-like factor, implying that a direct stepping to FEA/SA at $T \approx 34.5\,keV$ is not a good choice. Instead, the FEA/SA spectrum[§§§] above $\approx 34.5\,keV$ is scaled down with the constant scale mentioned above. The consistency of this hybrid model with the theoretical expectations was ensured through a series of discussions with J.W.Chen over email. It should be just kept in mind that the theory error above $30\,keV$ will be slightly higher than that below and it is expected to be less important as the ER $2\nu\beta\beta$ background dominates in this energy region.

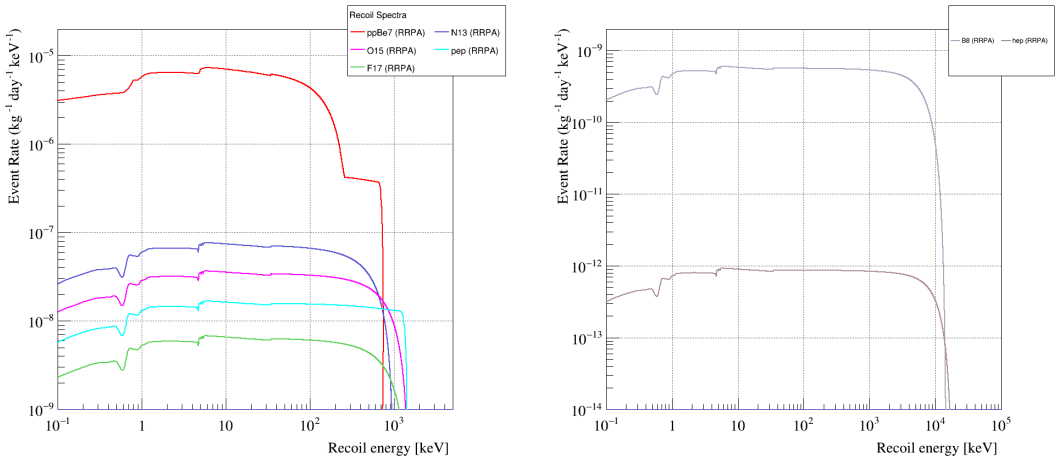

Figure 5.10: *Differential count rates of solar neutrino induced ER in LXe scaled to RRPA approximations (left) for $(pp + {}^7Be)$, pep and CNO neutrinos and (right) for ^8B and hep neutrinos. Details in text.*

The scaled spectra for all neutrino components are shown in fig. 5.10. The stepping behaviour at $\approx 0.7keV$ corresponds to the binding energy of $M_{IV}(3d_{5/2})$ shell electron. From fig. 5.9 it can be seen that the step at this energy is the highest, and when the stepping approximated spectra are scaled down for components other than $pp + {}^7Be$, the stepping structure at $\approx 0.7keV$ becomes prominent. For $pp + {}^7Be$ neutrinos, the structure appears less steep since J.W.Chen's low energy RRPA calculations were directly used in this energy region.

[§§§] Above $\approx 34.5\,keV$, the SA and FEA become indistinguishable.

Table 5.4 *Comparison of total number of neutrino-electron scattering events for different approximation schemes. The values are for 5600 kg fiducial volume and a 1000 live-day run. Fluxes from Table. 5.2 are used for the incoming solar neutrinos.*

ν	Total Number of Events in 1000 days, 5600 kg fid. vol.					
	WIMP ROI $(1.5-6.5\,keV)$			ALP/HP ROI $(1.5-100\,keV)$		
	FEA	SA	RRPA	FEA	SA	RRPA
pp+^{7}Be	252	216	187	4059	3974	3139
^{13}N	3	2	2	49	48	38
^{15}O	1	1	1	24	24	19
^{17}F	0	0	0	4	4	3
^{8}B	0	0	0	0	0	0
hep	0	0	0	0	0	0
pep	1	0	0	11	11	9

The calculated total number of events in the $5600\,kg$ fiducial volume of the LZ detector for the planned science run of 1000 livedays for various approximation schemes are shown in Table. 5.4. Two particular regions of interests (ROIs) are considered: $1.5-6.5\,keV\ ER$ for the WIMP searches [63], and $1.5-100\,keV\ ER$ for ALP/HP searches (described in detail in Chapter 6). The values imply that

- FEA and SA obviously provide an over-estimated neutrino-electron scattering rates at lower energies.
- Larger the recoil energy range (e.g. for CNO, ^{8}B and hep neutrinos), lower the effect of atomic binding on the total event rates.
- For both ROIs, the major contribution to ER background are due to pp and ^{7}Be neutrinos.
- For ALP/HP ROI, contributions from pep, ^{13}N and ^{15}O neutrinos are also non-negligible.
- Total number of events due to other neutrino components contribute $\leq 1\%$ of the $pp + {}^{7}Be + pep + {}^{13}N + {}^{15}O$ contribution and are neglected.

It is thus instructive to consider only pp, ^{7}Be, pep, ^{13}N and ^{15}O neutrino components for modelling the total ER background due to solar neutrinos. On average, an uncertainty[‡‡] of $\leqslant 2\%$ in the total number of events (which is more relevant for the background analysis) is assumed.

[‡‡]The total systematic uncertainty in the total number of events is mainly due that in incoming flux ($< 1\%$) [271], the neutrino oscillation ($< 1.6\%$) [271] and atomic binding treatment ($< 2-3\%$).

5.3 ER backgrounds: Compton Scattering

An important fraction of the ER background in LZ is due to the interactions of γ-rays arising from material/external radioactivity. The attenuation of photons in a material is mostly due to (see fig. 5.11)

- photoelectric effect: $\gamma + A \rightarrow A^+ + e^-$, where A is an atom,
- Compton scattering [272] (Incoherent, scattered photon has a lower frequency than the incident one): $\gamma + e^- \rightarrow \gamma^* + e^-$, and
- electron-positron pair production: $\gamma + A \rightarrow A + e^+ + e^-$.

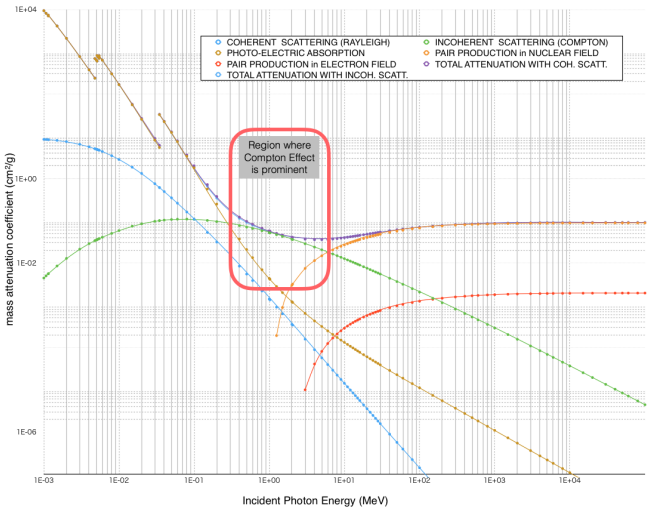

Figure 5.11: *Mass attenuation coefficient of Xe as a function of photon energy. Data from https://physics.nist.gov.*

The contribution of Rayleigh scattering (coherent, scattered photon has the same frequency, no ionisation or excitation happens) is usually minor, but needs to be known for a complete knowledge of the beam attenuation. The relative strengths of the interactions are determined by the atomic number (Z) of the material and incident γ-ray energy. Fig. 5.11 shows various attenuation channels for photons in Xe, with the region dominated by Compton scattering circled out.

In general, the detector ER background in LZ are modelled using BACCARAT, a computational framework based on GEANT4 [273] simulation toolkit. For a realistic background simulation, it is important to ensure a precise modelling of Compton scattering with an inclusion of the effect of atomic binding (and/or Doppler broadening). This section will summarise my work in this prospect.

5.3.1 Free electron approximation: Klein-Nishina formula

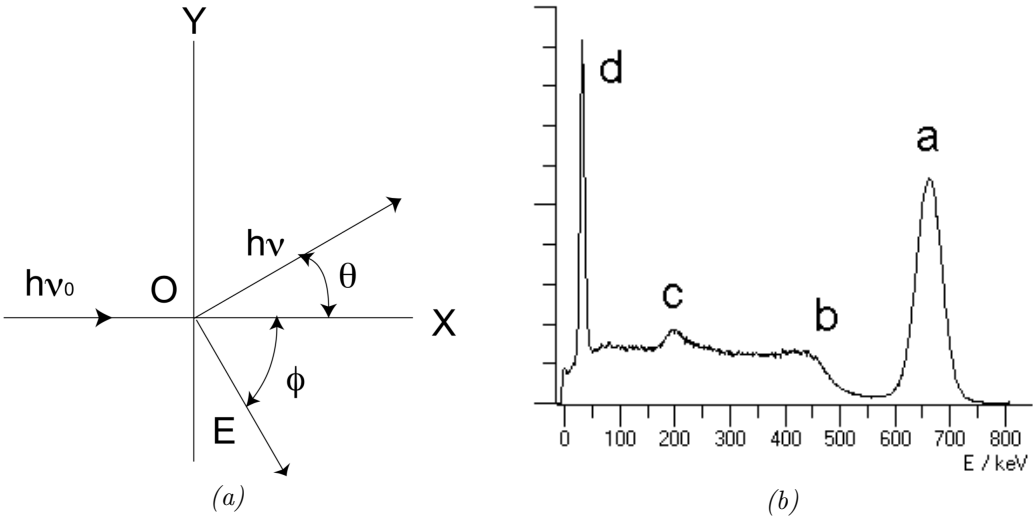

Figure 5.12: *(a) Compton scattering on a free electron.*
(b) A typical ER spectra in a sample preparation [274] due to Compton scattering of 622 keV γ-rays from ^{137}Cs. The Y axis is in arbitrary units. See text for details.

Assuming the electrons to be free and initially at rest (fig. 5.12a), the energies of the incident ($E_0 = h\nu_0$) and scattered ($E' = h\nu$) photons are related by

$$E' = \frac{E_0}{1 + \frac{E_0}{m_e c^2}(1 - \cos\theta)}, \tag{5.27}$$

where m_e is the mass of an electron and θ the scattering angle. The energy transfer is maximum when the photon backscatters, i.e. $\theta = \pi$. Backscattered photons appear as a sharp spectral feature in the recoil spectrum, known as the Compton edge. The differential cross-section per atom is given by the well-known Klein-Nishina [275] formula

$$\frac{d\sigma_c^{KN}}{d\epsilon} = \pi r_e^2 \frac{m_e c^2}{E_0} Z \left(\frac{1}{\epsilon} + \epsilon\right)\left(1 - \frac{\epsilon \sin^2\theta}{1 + \epsilon^2}\right), \tag{5.28}$$

where $Z = 54$ for Xe, $\epsilon = E'/E_0$, and $r_e \approx 2.8179\, fm$ is the classical electron radius.

Fig. 5.12b illustrates a typical instrumental ER response for a mono-energetic beam of $662\, keV$ γ-rays from ^{137}Cs (actually from its daughter ^{137m}Ba) interacting with a detection medium. The rightmost peak (a) arises in the case of complete absorption (photo-absorption) of the gamma rays in the medium. The

energy of the Compton scattered electrons forms a continuum, from the minimum (zero) to the maximum (Compton edge, point b). There is an enhanced number of counts at a point c in between ($\sim 184\,keV$ for $662\,keV$ γ-line), corresponding to the interaction of backscattered gamma-rays with detector shielding. In general, the backscatter ($\theta = \pi$ in eq. 5.27) reduces the photon energy to between 170 and 220 keV, irrespective of the incident energy. This is why the backscatter peak is always at the low energy side. Note that the leftmost peak (d) has nothing to do with the Compton scattering. It is the x-ray emitted in internal conversion processes of ^{137m}Ba that happen alongside the de-excitation by γ-emissions.

5.3.2 Relativistic impulse approximation (RIA)

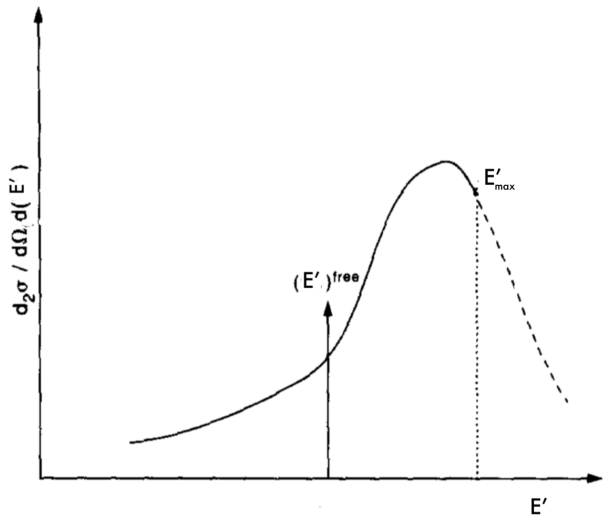

Figure 5.13: *Doppler broadening of scattered photon peak and the Compton defect. Figure from [276].*

So far it has been assumed that the electrons participating in Compton scattering were free and initially at rest. In the absence of atomic binding, the doubly differential cross-section (DDCS) $\frac{d^2\sigma}{dE'd\Omega}$ should be a mono-energetic line ($(E')^{free}$, shown by a delta function in energy in fig. 5.13). However in reality, the electrons are bound to the atom and move around the nucleus. This affects the Compton line in three ways:

1. **Doppler Broadening:** The pre-collision momenta of bound electrons result in an energy distribution ('Doppler' broadening, fig. 5.13) instead of a mono-energetic peak.

2. **Compton defect:** The centre of the peak is slightly shifted from the FEA

value. The direction and magnitude of this defect depend on the atomic sub-shell of the electron in question [277].

3. **Kinematic cut-off:** The kinematics imposes a maximum energy of the scattered photon as

$$E'_{max} = E_0 - E_B, \tag{5.29}$$

where E_B is the binding energy of the electron in the shell.

There are several theoretical schemes to account for these features, e.g. the incoherent scattering factor approximation, i.e. multiplication of the Klein-Nishina formula 5.28 by the incoherent scattering factor S [278, 279]:

$$\left(\frac{d\sigma}{d\Omega}\right)_{incoh} = \left(\frac{d\sigma_c^{KN}}{d\Omega}\right) S(E_0, \theta, Z). \tag{5.30}$$

The effect of atomic binding is hidden in the magnitude of S, which can be calculated from non-relativistic Waller-Hartree theory [280]. The factorization (eq. 5.30) can also be achieved naturally by a relativistic version of Du Mond's impulse approximation [281]. While comparative overviews of different approaches can be found in [282, 283], the current work will stick to the relativistic impulse approximation (RIA) in two frameworks: Ribberfors [284, 285] and Monash [286, 287].

5.3.2.1 Ribberfors′ model

The relativistic impulse approximation (RIA) was first used by Ribberfors [284, 285] to account for the Compton scattering of a bound electron and the Doppler broadening. In this approximation, the scattering is treated as that from a distribution of free electrons, i.e. an electron in a shell i is treated as free, but with a constrained momentum distribution $\rho(\vec{p}_i)$. $\rho(\vec{p}_i)$ is numerically derived from relativistic (necessary for heavier elements) many-body calculations of the atomic ground state of the scatterer. A sum over all the orbitals is needed if several electron states are involved:

$$\rho(\vec{p}) = \sum_{i}^{occ} |\psi_i(\vec{p})|^2. \tag{5.31}$$

For a system at rest, mean $\vec{p}$ is zero and $\rho(\vec{p})$ can be viewed as a stationary wave packet of free-electron states. Assuming that the energy transfer is much larger than the electron binding energy, the scattering cross-section will be similar to

that for the free electrons, but weighted by a probability of a certain FE state appearing in the wave packet. The simplified doubly-differential cross-section (DDCS) in RIA is

$$\left(\frac{d^2\sigma_c}{dE'd\Omega}\right)_{RIA} = Y\,.\,J. \tag{5.32}$$

The factor Y, independent of the atomic structure of the target material, includes all the kinematics and dynamics of the scattering process:

$$Y \approx \frac{r_e^2 m_e^2 E'}{2E_0|\vec{k'}-\vec{k}|(m^2+p_z^2)^{1/2}}\bar{X}(R,R'), \tag{5.33}$$

where z axis represents the direction of momentum transfer, k and k' are the momenta of the incident and scattered photon respectively, and X is a slowly varying function:

$$\bar{X}(R,R') = \frac{R}{R'} + \frac{R'}{R} + 2m_e^2\left(\frac{1}{R}-\frac{1}{R'}\right) + m_e^4\left(\frac{1}{R}-\frac{1}{R'}\right)^2. \tag{5.34}$$

R and R' are defined as

$$\begin{aligned} R &= E_0\left((m_e^2+p_z^2)^{1/2} + \frac{(E_0 - E'\cos\theta)p_z}{|\vec{k'}-\vec{k}|}\right), \\ R' &= R - E_0E'(1-\cos\theta). \end{aligned} \tag{5.35}$$

The second factor (J) in eq. 5.32 is the Compton profile:

$$J_i(p_z) = \sum_i^{occ} J_i(p_z), \text{ where } J(p_z) \equiv \int\int\int \rho(\vec{p})dp_xdp_y, \tag{5.36}$$

and it determines the probability distribution of energy of the scattered photon, i.e. gives the shape of the Doppler broadening. For low energy and momentum transfer (i.e. non-relativistic limit, $p_z = 0$) $\bar{X}$ reduces to a Klein-Nishina type of expression and the Klein-Nishina DDCS becomes

$$\left(\frac{d^2\sigma_c}{dE'd\Omega}\right)_{KN} = \frac{r_e^2 m_e E'}{2E_0|\vec{k'}-\vec{k}|}\bar{X}_{KN}(R,R')\,J(p_z). \tag{5.37}$$

Integrating eq. 5.37 with respect to E', the typical Klein-Nishina cross-section per solid angle ($d\sigma_c^{KN}/d\Omega$) can be reproduced. Having both RIA and Klein-Nishina versions of the scattering cross-sections, further calculations reproduce eq. 5.30 if

the scattering function is identified as

$$S(E_0, \theta, Z) = \sum_{i}^{occ} n_i(p_{i.max}), \text{ where } n_i(p_{i.max}) = \int_{-\inf}^{p_{i,max}} dp_z J_i(p_z). \tag{5.38}$$

Further details can be found in Ribberfors′ original paper [284]. The relation between E'-values for the Ribberfors′ and Klein-Nishina case is [288]

$$E' = E'_{KN}\left(1 - \frac{p_z|\vec{k}_0 - \vec{k}}{m_e c E_0}\right). \tag{5.39}$$

Since p_z depends on quantum mechanics of the electron's orbit, there is no unique value of E' for a specific (E_0, θ): i.e. Doppler broadening appears.

The RIA treatment of Ribberfors is widely used in interdisciplinary studies, and is also adopted by Geant4 and other MC simulation frameworks [289–292].

5.3.2.2 Monash model

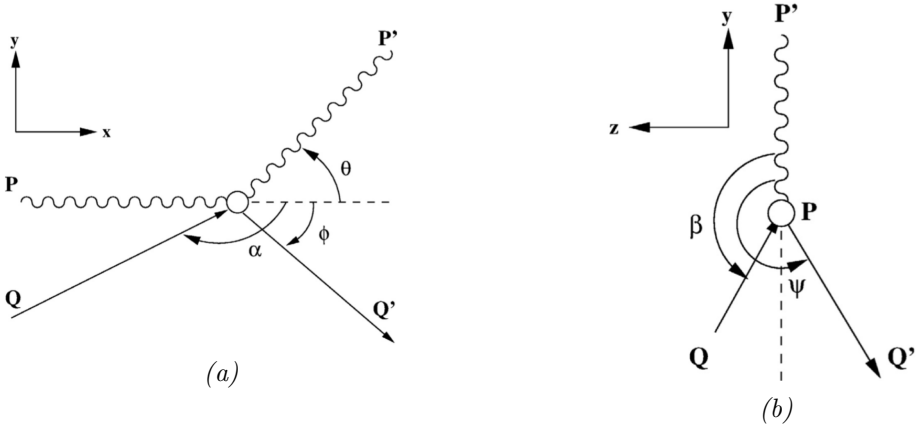

Figure 5.14: *(a), (b) Three dimensional diagram of Compton scattering from [287]. P (P′) and Q (Q′) are the initial (final) four momenta of photon and electron respectively.*

Ribberfors′ DDCS formula only considers a two-dimensional scattering kinematics: the components of pre-collision electron momentum are constrained to lie on the photon plane (plane defined by the incident and scattered photons). As a result, the momentum of the ejected electron is forced to be in the photon plane to ensure the energy-momentum conservation. A wide range of

***e.g. the fully relativistic second-order S-matrix QED independent particle (entirely no electron-electron correlation) approximation (IPA) model by Kaliman et al. [293].

alternative approaches exist in literature that intend to modify or even extend the DDCS formula (eq. 5.32) to a triply differential cross-section (TDCS) one***. A recently developed model [286, 287] by J.M.C. Brown et al. at Monash University, approaches the same problem in a rather simple first principle framework. They employed a two body fully relativistic three-dimensional (figs. 5.14a and 5.14b) RIA framework and modified eq. 5.27 as

$$E' = \frac{\gamma m_e c(c - u\cos\alpha)}{1 - \cos\theta + \frac{\gamma m_e c(c - u\cos\theta\cos\alpha - u\sin\theta sin\alpha\cos\beta}{E_0}}, \tag{5.40}$$

where u is the speed of the target electron, $\gamma = (1 - (u^2/c^2))^{-1/2}$ and α, β and θ are the angles illustrated in figs. 5.14a and 5.14b. The remaining angles, i.e. the polar (ϕ) and azimuthal (ψ) angles of the recoil electron ejection are treated in RIA by assuming a minimal influence of electromagnetic field potential of the atom and using a simplified kinetic energy of the scattered electron,

$$E'_e = E_0 - E' - E_B. \tag{5.41}$$

The RIA-modified expressions for all the post-collision energies and momenta (in terms of the various angles) then determine the scattering function 5.38. Using the value of S, eq. 5.30 provides the incoherent differential cross-section.

5.3.3 Monte Carlo modelling of Compton scattering

It has been previously mentioned that BACCARAT, a GEANT4-based LZ simulation framework, is used for ER modelling of the detector background. The EM interactions with matter, down to very low energies, can be modelled with one of several built-in physics models in GEANT4, such as the Livermore model [294], the Penelope model [295] and the Monash model [287, 296].

Monte Carlo modelling of Compton scattering in GEANT4 is based on the following algorithm:

1. **Target Element**: One element in the target material is selected. The cross-sections of Compton scattering from that element are obtained by a direct interpolation of existing data tables, e.g. from a set of Livermore data libraries [297–301]. These publicly available libraries, produced by a mixture of experimental data and theoretical techniques, include electron binding effects averaged over all atomic states.

2. **Photon scattering angle** θ: The photon scatter angle θ is randomly sampled from the scattering function corrected Klein-Nishina formula. The incoherent scattering form factors are interpolated from the data libraries mentioned above. Both Livermore and Monash physics follow this step.

3. **Target electron's shell and momentum**: The Compton profile encodes all the information of the momenta of atomic electrons and is read by the GEANT4 physics list from an appropriate data library. A particular atomic shell is randomly sampled based on the shell occupancy of the particular element. The value of p_z is sampled from the tabulated Hartree-Fock Compton profiles [302] of the corresponding shell. This step is the same for both Livermore and Monash physics.

4. **Scattered photon energy**: The Doppler broadened scattered-photon energy is calculated according to eq. 5.39 (Livermore physics) or eq. 5.40 (Monash physics).

5. **Compare photon energy transfer with the binding energy**: If the energy transferred by photon is less than the electron binding energy, the process resets to step 3. Otherwise, it proceeds to step 6. This step is only followed in Monash physics. Livermore physics considers a free electron approximation at this stage.

6. **Scattered electron energy and ejection direction**: The scattered electron energy and ejection angles are determined by Ribberfors′ model 5.3.2.1 (Livermore physics) or Monash model (Monash physics).

7. **Iteration**: Steps 4-6 are repeated for different energies and momenta of scattered photon.

By default, BACCARAT uses the Low energy Livermore physics for Compton modelling. It is interesting to check the comparative performance of Livermore (G4EmLivermorePhysics) and Monash physics (G4LowEPPhysics) and their effect on the LZ background model, which will be dealt in the next section.

5.3.4 Analyses and results

5.3.4.1 Pre-analysis cut results

BACCARAT simulations with realistic background sources in different detector components were performed: first with low energy Livermore physics (G4EmLivermorePhysics) and then with low energy Monash (G4LowEPPhysics) physics. The plots of energy depositions, without any analysis cut are shown in figs. 5.15 and 5.16.

Note that the energy deposition events include all γ-ray interactions (where possible) – *including but not limited to* the Compton scattering. Also, for U and Th sources, individual stages in the decay chain are also taken into account.

The fractional differences in recoil spectra due to Livermore and Monash physics, as a function of recoil energy, are shown in figs. 5.17 and 5.18. The difference is particularly more prominent for radioactivity from $^{238}U/^{232}Th$ decay chains, possibly due to the contributions from different decay products in the chain. In addition to these findings, some common trends can be noticed in all results, such as:

- At very low energies, the Monash physics gives fewer events than Livermore. This is due to the refined treatment of atomic binding in Monash physics.
- The fractional difference increases from negative to positive with energy, and attains a maximum at $\sim 34.5\,keV$, binding energy of K-shell electron in LXe.
- At higher energies ($> 100\,keV$), the difference minimises.

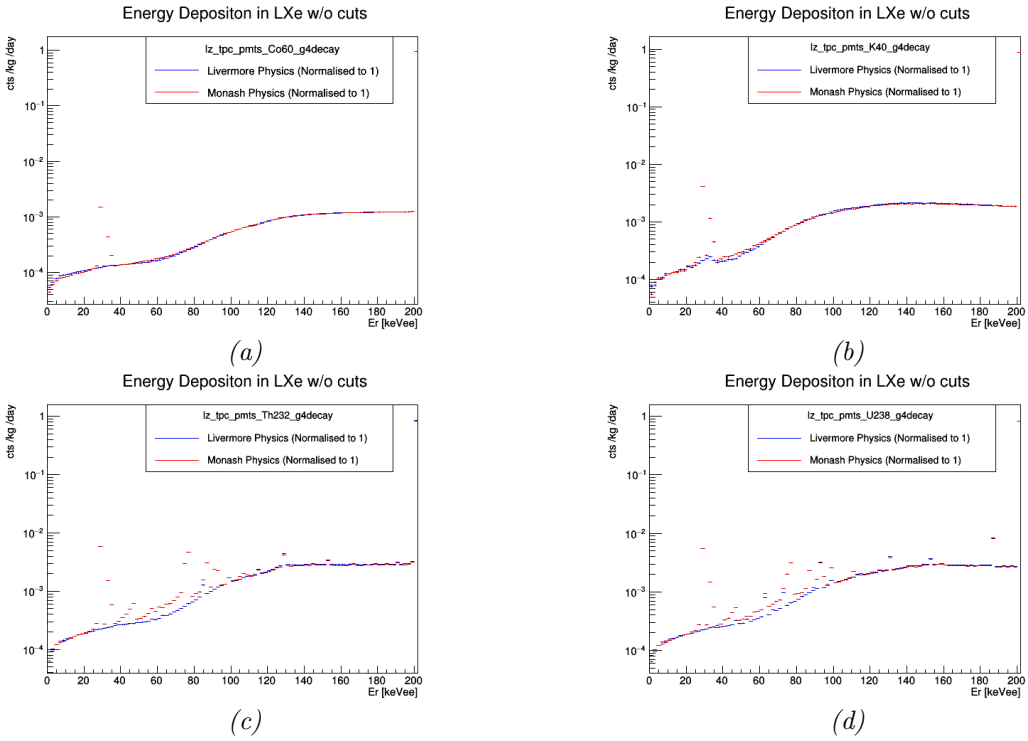

Figure 5.15: *Simulated energy depositions in LXe (without analyses cuts) for (a) ^{60}Co, (b)^{40}K, (c) ^{232}Th and (d) ^{238}U radioactivity in TPC PMTs.*

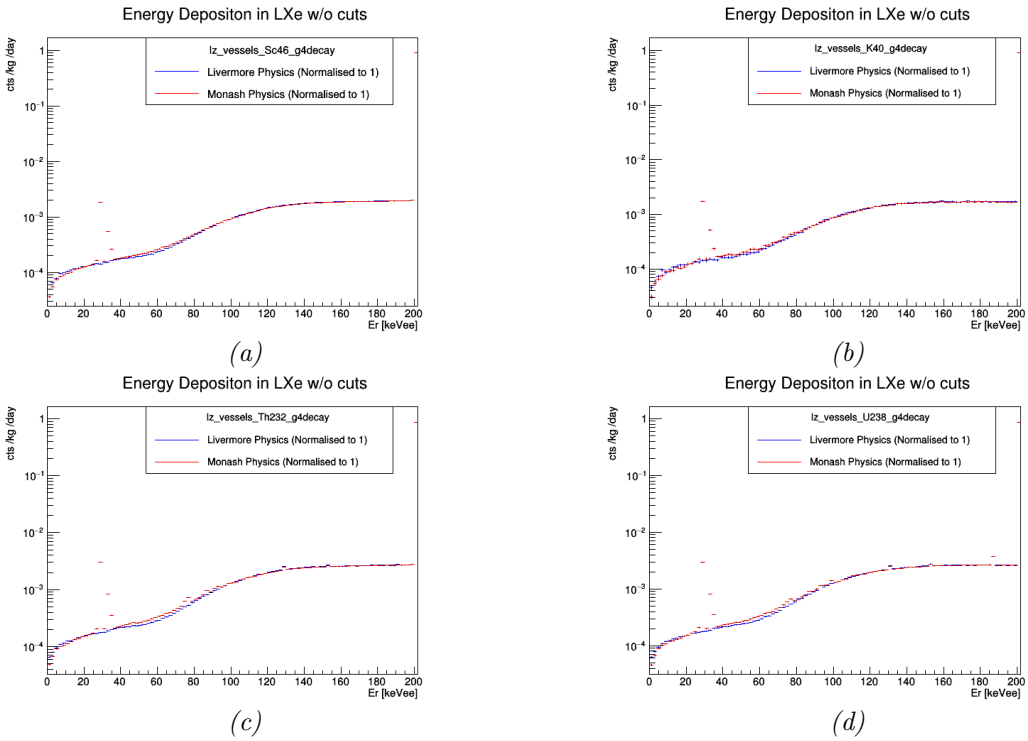

Figure 5.16: *Simulated energy depositions in LXe (without analyses cuts) for (a) ^{46}Sc, (b)^{40}K, (c) ^{232}Th and (d) ^{238}U radioactivity in detector vessel.*

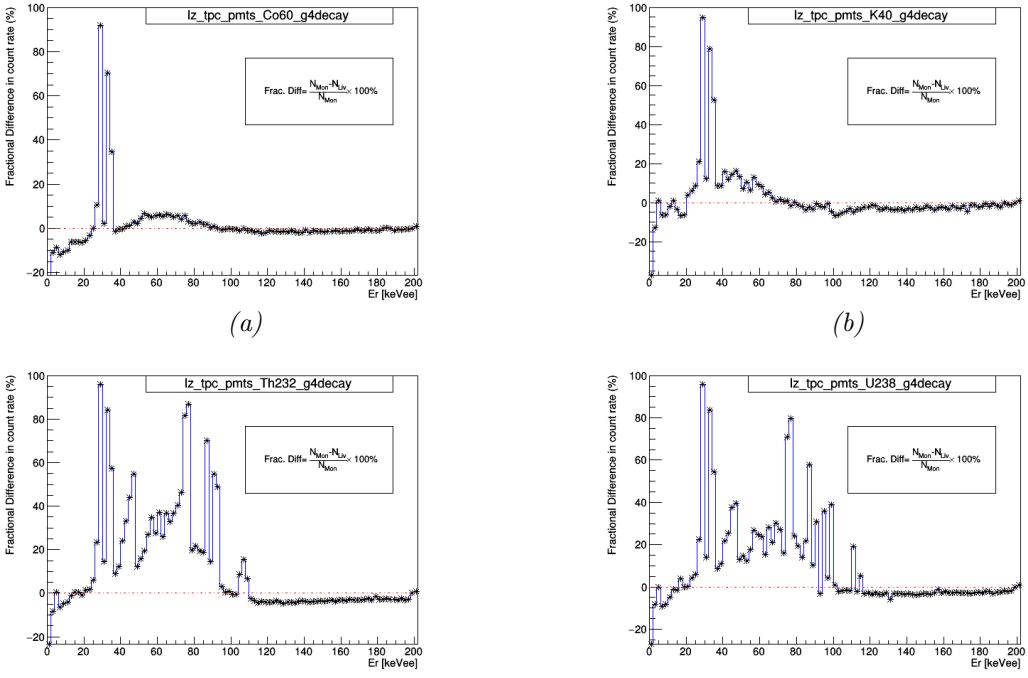

Figure 5.17: *Fractional difference in simulated energy deposition in LXe for (a) ^{60}Co, (b)^{40}K, (c) ^{232}Th and (d) ^{238}U radioactivity in TPC PMTs.*

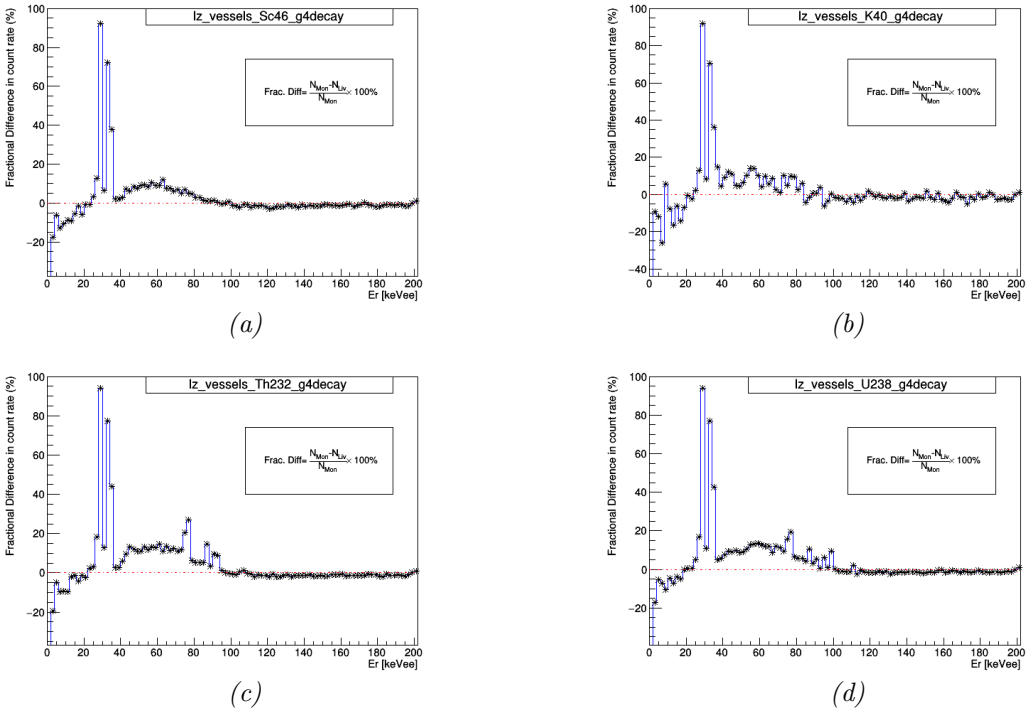

Figure 5.18: *Fractional difference in simulated energy deposition in LXe for (a) ^{46}Sc, (b)^{40}K, (c) ^{232}Th and (d) ^{238}U radioactivity in detector vessel.*

5.3.4.2 Post-analysis cut results

So far no analysis cut was applied on the simulated results. In standard LZ analyses, three analysis cuts are to be applied:

1. **Single scatter (SS) cut** to reject multi-scattered neutrons and γ-rays, based on the LUX experience [303]. The cut is specified by $\sigma_r < 3\,cm$ and $\sigma_z < 0.2\,cm$ where σ_r and σ_z are the energy-weighted standard deviations of radial and vertical hit positions, respectively.

2. **Fiducial volume cut** to remove events outside the predefined fiducial volume ($r < 68.8\,cm, 1.5\,cm < z < 132.1\,cm$ from the center of active LXe volume).

3. **OD+skin veto cuts** to remove the vetoed events.

Additionally, a ROI cut is to be applied according to the particular analysis in question. Since this study is for comparison purposes, only the standard ER ROI ($0-100\ keV$) and WIMP ROI ($1.5-6.5\ keV$) are considered. The corresponding number of events are tabulated in Table. 5.5. Note that, as mentioned in section 5.3.4.1, the events are *not only* the Compton ones.

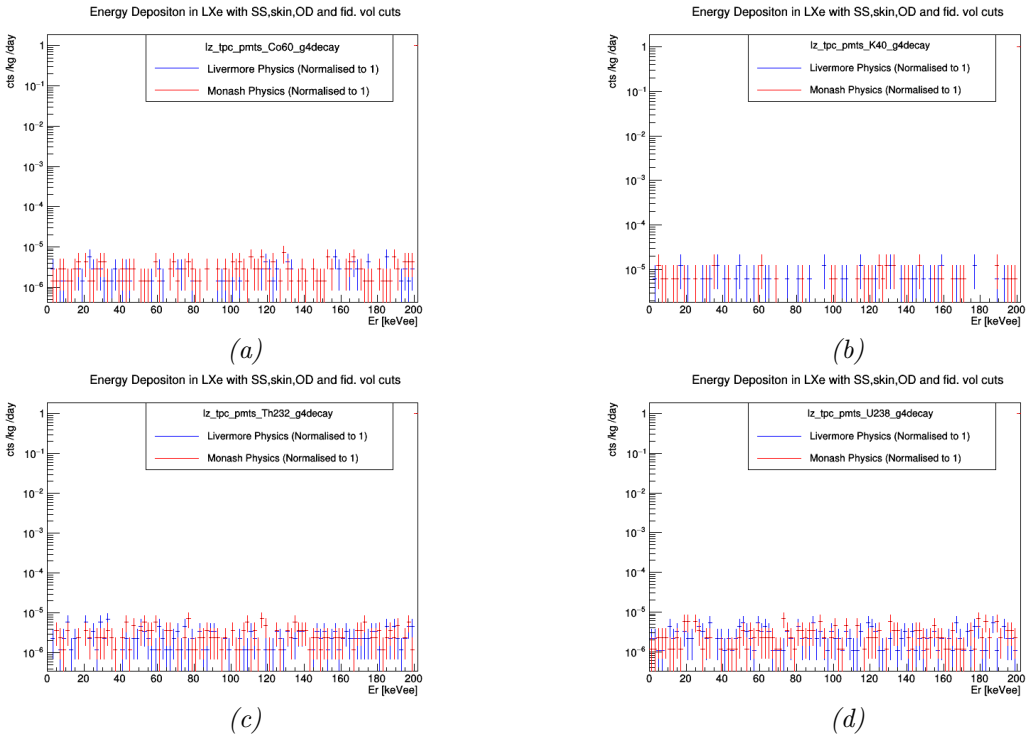

Figure 5.19: *Simulated energy deposition in LXe after applying analysis cuts for (a) ^{60}Co, (b)^{40}K, (c) ^{232}Th and (d) ^{238}U radioactivity in TPC PMTs.*

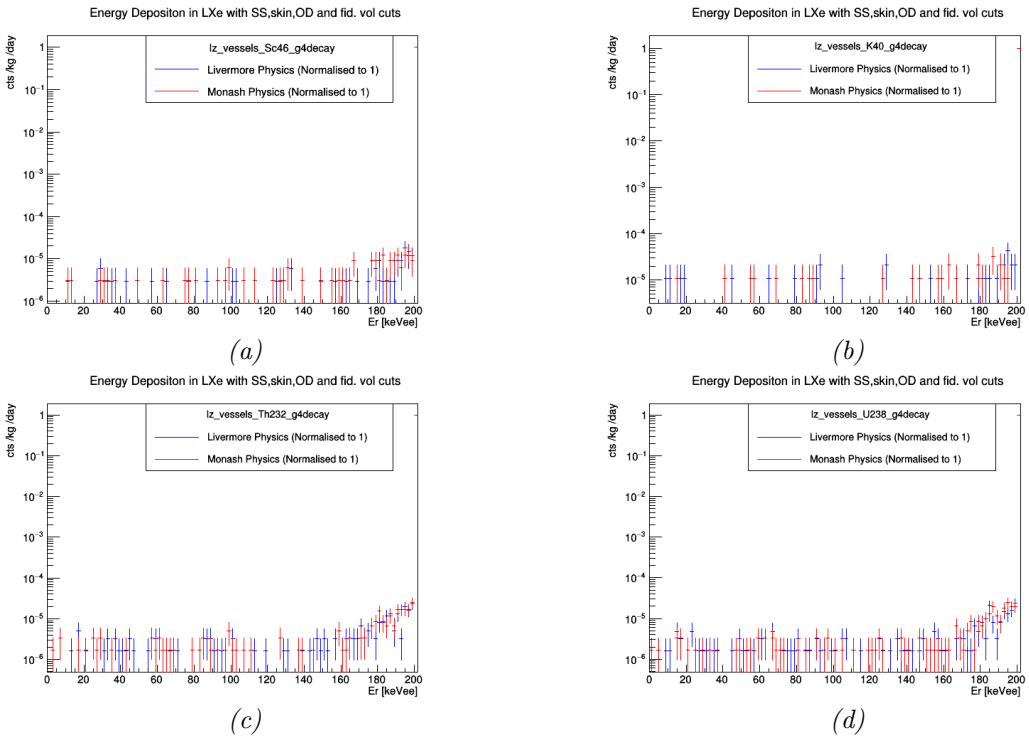

Figure 5.20: *Simulated energy deposition in LXe after applying analysis cuts for (a) ^{60}Co, (b)^{40}K, (c) ^{232}Th and (d) ^{238}U radioactivity in detector vessel.*

Table 5.5 *Detector components and background sources simulated in this work.*

Component and Source		Model	Total no. of events			
			Simulation results: $(0-100$ keV)			Scaled results: $(1.5-6.5$ keV)
			Decays Simulated	w/o cuts	with SS, skin, OD, Fiducial cut	1000 days at 1 $mBq\ /kg$, with all cuts
TPC PMTs	^{60}Co	Livermore	3.98×10^8	26376	4	0.87
		Monash	3.9×10^8	23394	3	0.66
	^{40}K	Livermore	3.97×10^8	2558	3	0.65
		Monash	3.97×10^8	2385	3	0.65
	^{232}Th	Livermore	3.95×10^8	51955	3	0.66
		Monash	3.93×10^8	50579	4	0.88
	^{238}U	Livermore	3.98×10^8	49674	4	0.87
		Monash	3.81×10^8	45570	4	0.91
Vessels	^{46}Sc	Livermore	3.98×10^8	11334	0	0
		Monash	3.96×10^8	10135	0	0
	^{40}K	Livermore	3.98×10^8	727	0	0
		Monash	3.97×10^8	647	0	0
	^{232}Th	Livermore	3.98×10^8	13903	0	0
		Monash	3.91×10^8	12237	3	0.66
	^{238}U	Livermore	3.99×10^8	12833	0	0
		Monash	3.99×10^8	11706	1	0.22

It appears from Table. 5.5 that, with all the analysis cuts (SS+skin+OD vetoes) the number of events in the fiducial volume are too few[†††] (as expected from vetoes) to compare, i.e. the effect of atomic binding (Livermore vs Monash physics) on background counts is negligible. Hence for the realistic detector backgrounds and standard analysis cuts, Livermore model serves as a good approximation for Compton scattering. However, the increased fractional differences at low energies (figs. 5.17 and 5.18) may affect other low energy searches with the LZ detector in near future. Also, in future generation-3 (G3) detectors with larger fiducial volumes ($\sim 50-100\,tonnes$), the atomic binding effect will be more prominent and a migration to Monash physics will be necessary.

Thus, the present work recommends a migration to Monash physics for the LZ background model, which is currently being considered by the LZ background and simulation working group.

[†††]The number of signal events we expect in the ROI is very much model-dependent. For example, without a prior knowledge of the unknown parameter κ (see eq. 6.4), it is not possible to provide an exact number of expected signal events due to a HP mass. Hence we do not present any comparison of the background events (Table. 5.5) with the number of signal events.

5.4 Chapter summary

Before proceeding to the next chapter, the key aspects that came out of chapter 5 should be noted down:

- Irreducible ER backgrounds present a major issue in dark matter searches and should be modelled accurately.
- The free electron approximation is a simpler way to treat the solar neutrino-electron scattering and the Compton scattering of γ-ray backgrounds, but is unrealistic at low energies (i.e. at least for $\leq 34.5\,keV$, the binding energy of K-shell electron in LXe).
- The relativistic random phase approximation provides a better treatment of solar neutrino-electron scattering and has been *recently implemented* in the ER background model in LZ.
- The three-dimensional Compton scattering framework (Monash physics) with relativistic impulse approximation was tested against the Ribberfors model-based Livermore physics by performing GEANT4 simulations from realistic detector backgrounds. The fractional differences are the maximum around $\sim 34.5\,keV$, the binding energy of the K-shell electron in LXe.
- Standard analysis cuts on the simulation results reduce the number of background events in the fiducial volume (as expected), ensuring that the Livermore model is a good approximation for WIMP, HP/ALP analyses.
- However, the low energy deviations of Monash model from the Livermore physics may have a considerable effect on other low energy searches in LZ in near future.
- A migration to Monash model is recommended and the suggestion is currently being considered by the LZ background and simulation working group.

Implementing the binding corrections to solar-neutrino backgrounds and being assured that the Livermore physics is a good approximation for the present work, the next stage is to use the complete LZ background model to evaluate the ALP/HP sensitivity reach of LZ: discussed in the next chapter.

Chapter 6

Hidden Photon and Axion-Like Particle Searches in LZ

The science goal of the LZ experiment is multi-dimensional. WIMPs being the major signal of interest, a diverse array of other non-WIMP signals are also to be investigated as a part of the programme. With the first science run scheduled in 2020, the projection of the sensitivity reach of LZ for each of these signals is a key necessity beforehand.

The theoretical concepts of hidden photons (HPs) and axion-like particles (ALPs) and the possibility for them to constitute the mysterious dark matter have already been discussed in Chapter 2. A brief technical overview and working principle of the LZ detector have been summarised in Chapter 3, followed by a detail hands-on study of the performance testing of LZ skin-PMTs in Chapter 4. The importance of precise modelling of ER backgrounds in the detection medium and the effect of atomic binding of electrons have been emphasized in Chapter 5. All of them constitute a prelude of the current chapter, which presents the analysis details of the sensitivity projections for HP and ALP searches, for 5600 kg fiducial volume and a 1000 live-day run, with the LZ detector.

6.1 Signal models

The viable parameter space (m_V, κ) for HP physics spreads over a wide mass range: from $10^{-15}\,eV$ to $10^{12}\,eV$. Existing cosmological bounds (appendix A) and experimental constraints (section. 2.3.2.5) still leave a vast (m_V, κ) region to explore (fig. 2.7). The present and future searches for HPs can be categorised according to the HP mass range, as shown in Table. 6.1.

In general, the low energy (eV and less) searches are based on photon-HP

Table 6.1 *Experimental searches for Hidden photons.*

Interaction exploited	HP mass ($\times 1/c^2$)	Experiments
photon-HP oscillation or conversion	neV-peV or less	DM Radio Pathfinder experiment [304]
	μeV	Haloscope searches [133] e.g. Axion Dark Matter eXperiment (ADMX) [305].
		Broadband searches e.g. WISP Dark Matter eXperiment (WISPDMX) [306]
	meV	light shining through walls experiments, e.g. ALPS [132]
	eV	Dish antenna searches [307]
HP Absorption	keV	WIMP-search experiments e.g. XENON100 [308], XMASS [309], LZ
HP production + decay	$sub-GeV$	Electron beam dump experiments [310]
		Fixed target experiments [311]
		Proton beam dump experiments [312]
	GeV - TeV	Hadron colliders e.g. ATLAS and CMS at the LHC [313], LHCb [314]
		e^-e^+ colliders [315]

oscillations (sec. 2.3.2.2), while the intermediate ($sub-GeV$) and high ($GeV-TeV$) energy searches are mostly focussed on decays of HPs produced in the detector via bremsstrahlung or other mechanisms. On the other hand, liquid scintillator detectors like LZ can probe a completely different HP signature: the so called hidden-photoelectric effect.

Since HPs always interact with SM particles via the kinetic mixing, all approaches simply probe different regions of the same parameter space (m_V, κ). However, this is not the same for ALPs. Since ALPs directly couple to SM particles (i.e. no kinetic mixing), experiments that search for ALPs usually probe a specific coupling, e.g. ALP-photon (sec. 2.2.2.2) or ALP-electron (sec. 2.2.2.3). ALP-searches in LZ will focus on the later, the ALP-electron coupling, by searching for a signature termed as the axio-electric effect.

6.1.1 Hidden photo- (and axio-) electric effect(s)

Absorption of a bosonic particle like a HP (ALP) by a bound electron, known as the hidden photo- (axio-) electric effect, is very similar to the photoelectric effect caused by ordinary photons [73], except that

- the photon energy ω is replaced by the HP (ALP) rest mass m_{HP} (m_{ALP});

- the space dependent factor $\exp(i\vec{k}.\vec{r})$ (where k is the photon spatial momentum) in the absorbed photon wave-function is replaced by $\exp(im_{HP}\,\vec{v}.\vec{r})$ (where v is the velocity of incoming HP/ALP particle).

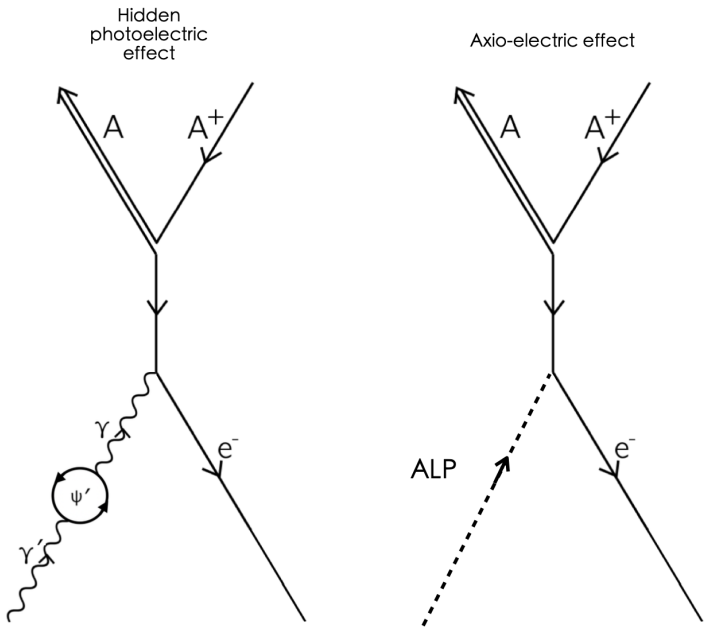

Figure 6.1: *Feynman diagrams of (left) hidden photo-electric and (right) axio-electric effects.*

Feynman diagrams of hidden photoelectric effect by HPs and axio-electric effect by ALPs follow in fig. 6.1. For the HP/ALP interpretation of CDM, the particles are non-relativistic and a DM density of $0.3\,GeV/cm^3$ can be assumed. This corresponds to $v \sim 10^{-3}c$, and the oscillating factor can be approximated to 1 (i.e. $\exp(im_{HP}\,\vec{v}.\vec{r}) \approx 1$). The simplified relations between the HP (and ALP) absorption cross-sections and ordinary photo-electric cross-section are [73]

$$\frac{\sigma_{HP}v_{HP}}{\sigma_{PE}(\omega = m_{HP})c} \approx \frac{\alpha'}{\alpha} \qquad \text{(Hidden photo-electric effect)} \tag{6.1}$$

and

$$\frac{\sigma_{ALP}v_{ALP}}{\sigma_{PE}(\omega = m_{ALP})c} \approx \frac{3m_{ALP}^2}{4\pi\alpha f_\alpha^2} \qquad \text{(Axio-electric effect).} \tag{6.2}$$

Here $f_a \equiv 2m_e/g_{Ae}$ is the dimensionful coupling constant for ALPs, α is the electromagnetic fine structure constant and α' is its analogue for HP:

$$\alpha = \frac{e^2}{4\pi} \qquad \text{and} \qquad \alpha' = \frac{g_h^2}{4\pi}. \tag{6.3}$$

e and g_h are the visible and gauge couplings respectively. Combining eq. 6.3 with eq. 2.20, one obtains

$$\kappa = \left(\frac{\alpha'}{\alpha}\right)^{1/2}. \tag{6.4}$$

The expected interaction rates in the detector simply read as [73]

$$R_{HP}\,[kg^{-1}\,day^{-1}] \simeq \frac{4\times10^{23}}{A}\frac{\alpha'}{\alpha}\frac{\sigma_{PE}\,[barn]}{m_{HP}\,[keV]} \tag{6.5}$$

and

$$R_{ALP}\,[kg^{-1}\,day^{-1}] \simeq \frac{1.2\times10^{19}}{A} g_{Ae}^2 \sigma_{PE}\,[barn]\, m_{ALP}\,[keV]. \tag{6.6}$$

$A = 131.3$ is the atomic mass of LXe, as usual.

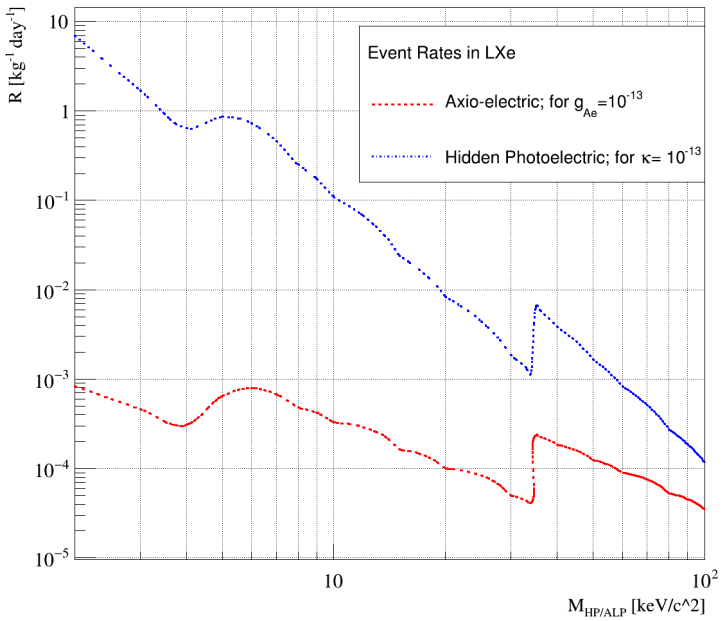

Figure 6.2: *Interaction rates in LXe for hidden photo-electric effect and axio-electric effect as a function of incident mass, assuming* $\kappa = 10^{-13}$ *and* $g_{Ae} = 10^{-13}$ *receptively.*

The variations of the interaction rate $R_{HP/ALP}$ as a function of the incident HP/ALP mass $m_{HP/ALP}$ in keV are shown in fig. 6.2, assuming $\kappa = 10^{-13}$ and $g_{Ae} = 10^{-13}$ respectively. Standard photo-electric cross-sections for LXe are used for the calculations.

The event rates (eqs. 6.5, 6.6) are independent of the HP/ALP velocity distribution in the galactic halo, suggesting an absence of modulation terms due to the Earth's motion, at least to an experimentally relevant level [73]. A very small modulation still may arise due to the difference of flux and can be neglected.

6.1.2 Region of interest (ROI)

There are two unknowns in each of the eqs. 6.5 and 6.6: the HP/ALP mass and the κ or g_{Ae}. The searches for HP/ALP hence scan over a range of mass, limited by the signal yields of the detector and availability of an appropriate background model. For a particular mass-value, the aim is to constrain (reduce the parameter space of allowed values) or measure the kinetic mixing parameter κ for HPs and coupling g_{Ae} for ALPs. For HP/ALP masses $< 40\,keV/c^2$ and $> 120\,keV/c^2$, indirect limits are still the leading ones. The most stringent limit between $40 - 120\,keV/c^2$ is due to the XMASS [309] (800 live-days data, $327\,kg$ of LXe, $30\,cm$ fiducial radius) direct detection experiment. Given a much bigger fiducial volume ($5600\,kg$) and planned science run (1000 live days) of the LZ detector, it is expected to achieve a better sensitivity than the XMASS-2018 results.

In a hidden photo- (axio-) electric effect, the entire HP/ALP rest mass is converted into energy and absorbed by the atomic electron, i.e. the energy deposition (E_{dep}) is essentially equal to the incoming mass ($m_{HP/ALP}\,[keV/c^2]$), as the particles$'$ kinetic energies are $<<$ $m_{HP/ALP}c^2$. The mass range scanned over thus defines an equivalent range of energy deposition in the detector. At the time this analysis was commenced, the available background model for LZ was only upto $100\,keV$. Taking into account the smearing of the energy deposition spectrum (figs. 6.4b and 6.5b in the next section) by the finite experimental resolution, a reduced upper bound ($70\,keV$) of the search range was selected. While writing the thesis, a high ER background model is available that implies the possibility of extending the search further above. This idea will be revisited at the end of this chapter. The lowest HP/ALP mass scanned in the present work is $2\,keV$, because $1.1\,keV$ is the ER threshold for the detector.

6.1.3 Probability density functions (PDFs)

The expected energy deposition spectrum in the detector (i.e. $R_{HP/ALP}$ vs E_{dep} plot) should be a mono-energetic peak centred at the value of the incident mass ($m_{HP/ALP}$) and smeared by the experimental resolution. A more informative way to model the signal events is to define a probability density function (PDF), i.e. probability distribution of signal events in a multi-dimensional phase space. The current analysis is based on a 2-dimensional PDF, in a $\log_{10} S2_c$ vs $S1_c$ space. The subscripts $'$c$'$ imply that the S1, S2 signals are corrected: S1 against the spatial

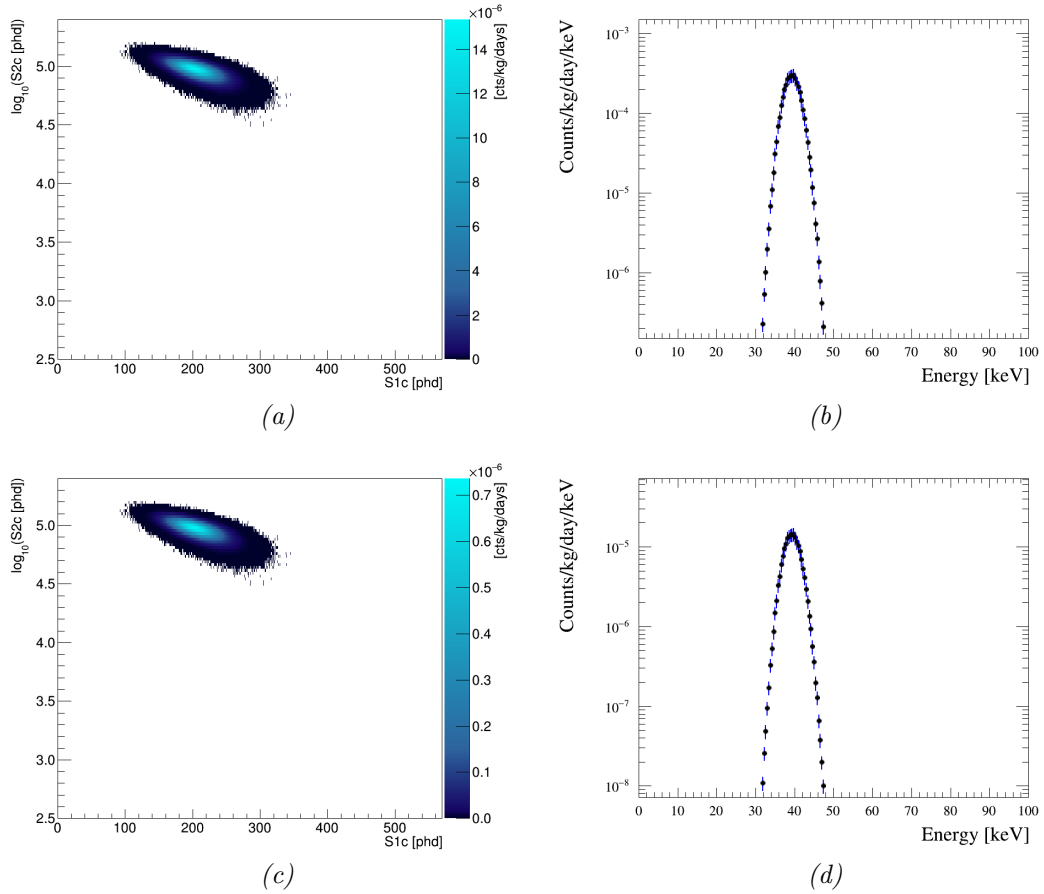

Figure 6.3: *(a) Signal model and (b) reconstructed energy for a* $40\,keV/c^2$ *HP (assuming* $\kappa = 10^{-13}$*) and (c) signal model and (d) reconstructed energy for a* $40\,keV/c^2$ *ALP (assuming* $g_{Ae} = 10^{-13}$*).*

variation of light collection, and S2 against the event position and the electron lifetime effects [63].

The theoretical energy depositions are calculated from eq. 6.5 for HPs and eq. 6.6 for ALPs, using $\kappa = 10^{-13}$ and $g_{Ae} = 10^{-13}$ receptively. It does not much matter what arbitrary value of κ (or g_{Ae}) value is used, as it will be factored out in the statistical analysis (see section 6.3) later. The theoretical spectrum is translated into the signal PDF using the Noble Element Simulation Technique (NEST) version 2.0.0 [316, & references therein]. NEST provides precise models of scintillation light and ionisation charge yields in liquid, gaseous and solid xenon, and some additional tools (e.g. pulse shape models for S1, S2 etc.).

A number of signal models in the mass range $(2 - 70\,keV)$ for HPs and ALPs are built. The PDFs appear as 'blobs' in the $\log_{10} S2_c$ vs $S1_c$ space (fig. 6.3). The experimental energy depositions can be reconstructed using the version of

eq. 3.16 for ER searches:

$$E_{dep}^{ER} = (13.7\,eV)\left(\frac{S1}{g_1} + \frac{S2}{g_2}\right) \qquad \text{(For ER, } f_{ER} = 1\text{)}, \tag{6.7}$$

with the standard g_1, g_2 values for LZ, i.e.

$$g_1 = 0.118735 \text{ phd/photon}, \qquad g_2 = 79.2291\,\text{phd/electron}. \tag{6.8}$$

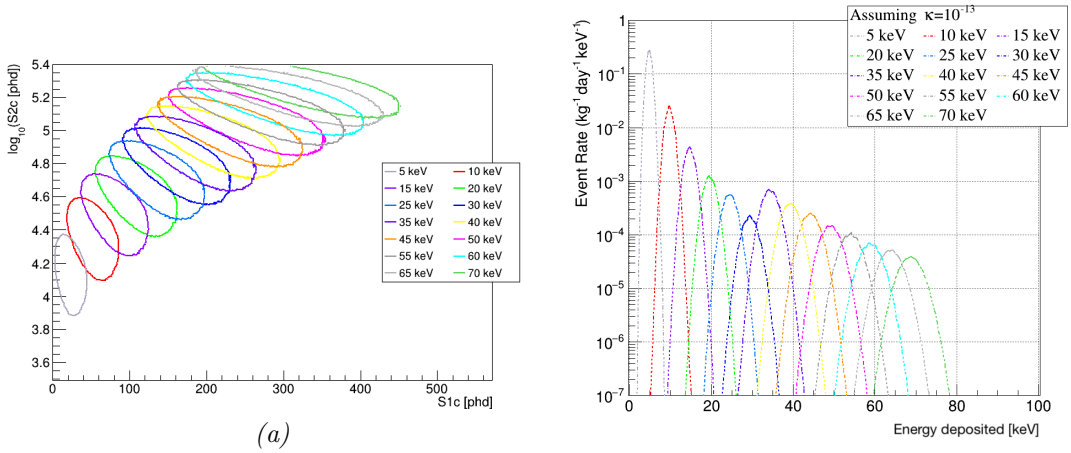

(a) *(b)*

Figure 6.4: *(a) Contour plots of the signal models for various masses of HPs and (b) corresponding energy deposition spectra in the detector, assuming* $\kappa = 10^{-13}$.

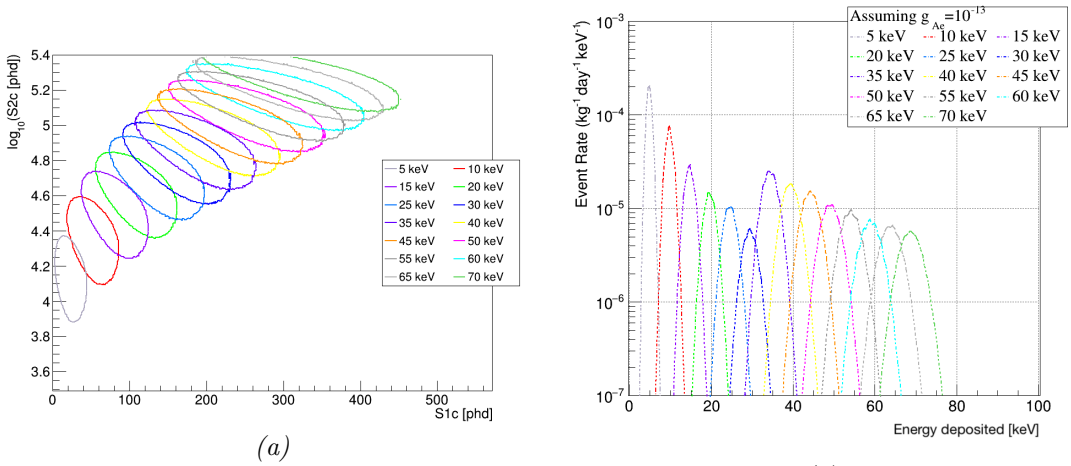

(a) *(b)*

Figure 6.5: *(a) Contour plots of the signal models for various masses of ALPs and (b) corresponding energy deposition spectra in the detector assuming* $g_{Ae} = 10^{-13}$.

Fig. 6.3 shows the examples of the signal PDF with the reconstructed energy for a $40\,keV/c^2$ HP and a $40\,keV/c^2$ galactic ALP. The contour plots with

corresponding energy depositions for multiple signal models are also shown in fig. 6.4 for HPs and in fig. 6.5 for ALPs. Larger the energy deposition, higher the contours, as expected. The energy ROI ($2 - 70\,keV$) can be re-defined for the $S1_c$-$\log_{10} S2_c$ space by introducing the following analysis cuts:

- the S1 pulses must have at least 3-fold coincidence in the TPC-PMTs (i.e. a S1 pulse must have been seen by at least three TPC-PMTs);
- the $S2 \geq 415\,phd$ (5 emitted electrons),
- the $\log_{10}(S2_c[phd])_{max} = 5.4$, and
- the total $S1c \leq 570\,phd$.

The first three cuts are those being planned for the most LZ analyses. The $S1c$ cut is larger than that used in other LZ analyses[‡], because of the wider energy ROI in the present case.

The relative scales of the peak amplitudes in the energy deposition plots (figs. 6.4b and 6.5b) depend on the photo-electric cross-sections of LXe (which reflect the atomic shell structure) and the particular κ and g_{Ae} choices in eqs. 6.5 and 6.6 respectively. The relative variations of peak widths are due to the energy dependent resolution of the detector, which gets worse at higher energies.

6.2 Background model

The common sources of background in LZ, as discussed in section 5.1, usually form two distinct bands (ER and NR) in the $S1_c$-$\log_{10} S2_c$ space. Most of the backgrounds sit in the ER band which, however, also contains the HP/ALP signal model(s). An accurate consideration of the ER backgrounds is thus crucial for any low energy ER searches/analyses.

The present work is mostly based on the background model used for the WIMP sensitivity projection [63], except that the ER pp $+^7$ Be $+^{13}$ N solar neutrino background is replaced by the RRPA-scaled result (section 5.2.7), including the contributions from all $CNO + pep$ neutrinos. The WIMP sensitivity paper [63] also includes J.W.Chen's RRPA-corrections for $pp +^7 Be$ neutrinos but only in a relevant low energy region.

[‡]For NR searches for WIMPs, $S1c \leq 80\,phd$ is used [63]. The expected ER background rejection using the $S2/S1$ ratio is $> 99.5\%$ for a 50% NR signal acceptance [63].

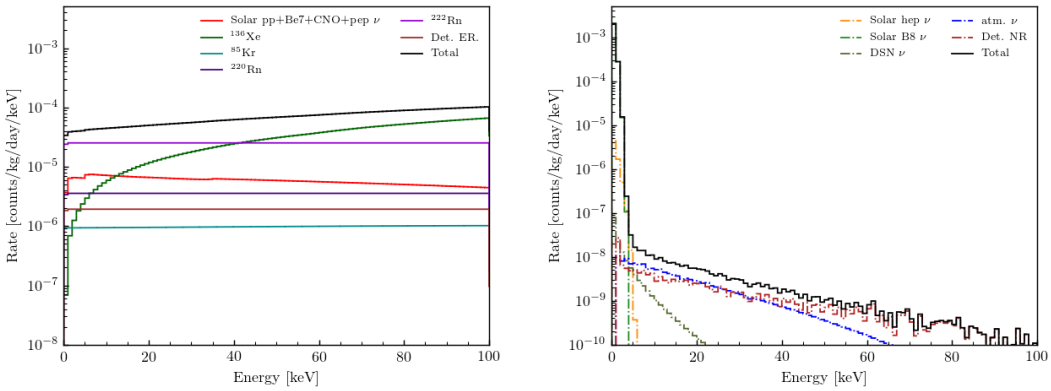

(a) *(b)*

Figure 6.6: *Background spectra: (a) ER and (b) NR.*

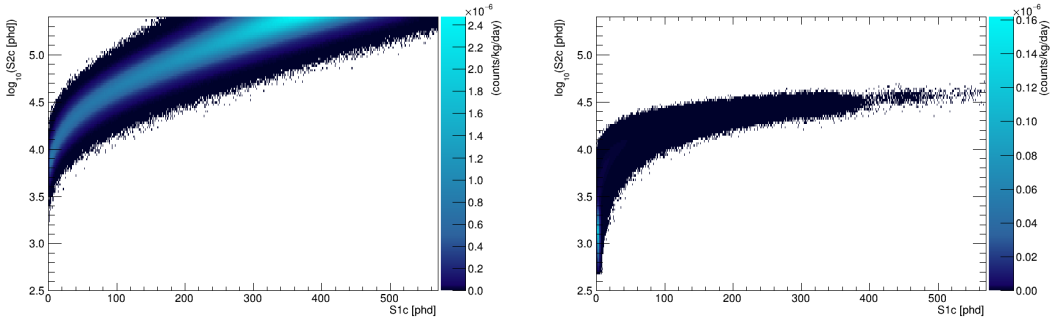

(a) *(b)*

Figure 6.7: *Background PDFs: (a) ER and (b) NR.*

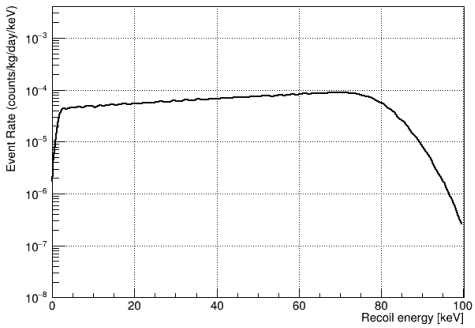

Figure 6.8: *Reconstructed energy: total (ER+NR) background.*

The ER and NR components of the background (Table 6.2), with an energy cut at $100\,keV$, are shown in fig. 6.6. Note that the contributions from surface contaminations, laboratory and cosmogenic backgrounds are included in the DetER and DetNR background components. The background model PDFs (figs. 6.7) are then generated in NEST with the S1c, logS2c cuts introduced in section 6.1.3. The reconstructed energy spectra for the total (ER+NR)

background model (fig. 6.8) is flat upto $\sim 75\,keV$, and it slowly rolls off to 0 beyond that energy (owing to the analysis cuts). This further justifies the choice of $70\,keV$ as the upper bound of the HP/ALP ROI, taking the smeared energy depositions (figs. 6.4 and 6.5) into account.

6.3 Statistical analysis

Statistics is an important tool for direct detection experiments that look for ′predicted but yet-unseen′ DM interactions with ordinary matter. Given a known background model and relevant detector parameters, the most important questions a statistical theory deals with are:

- **In the absence of real data:**
  - **(Sensitivity projection)** What region of parameter space (e.g. (m_{HP}, χ) for HPs) can be probed by the detector at $X\%$ confidence limit?
  - **(Discovery significance projection)** What region of parameter space (e.g. (m_{HP}, χ) for HPs) will imply a $Z - sigma$ discovery (e.g. $Z = 3$)?
- **Data are available, but no signal (excess events above background) observed:**
  - **(Exclusion limit)** Which region of parameter space (e.g. (m_{HP}, χ) for HPs) can be ruled out (at $X\%$ confidence limit)?
- **Data are available, some signal observed:**
  - **(Discovery significance)** What is the statistical significance of the observation, i.e. what $Z - sigma$ discovery is it?

Statistics answers these questions by making a ′statistical inference′, i.e. given a set of data (mock data for projections, real data for exclusion limits and discovery significance), it draws scientific conclusions about the validity of a particular probabilistic model or determines certain parameter values. This section will summarise the basics of the frequentist* approach adopted in the HP/ALP analysis.

*In the frequentist approach, probability is interpreted as the frequency of the result of a repeatable experiment. For instance, $P(A)$ is the frequency of occurrence of an outcome A upon repeating the experiment a large number of times ($N \to \infty$) in identical conditions. The

6.3.1 Statistical preliminaries

6.3.1.1 Hypothesis

A hypothesis is an educated ′assumption′ about something, expressed in the form of a ′statement′ which can be experimentally tested. Any hypothesis, in general, is characterized by a set of parameters $\{\sigma, \nu\}$:

- **Parameter of interest (POI) (σ):** This is the parameter of primary concern.
- **Nuisance parameters (ν):** These are the other unknown (e.g. the systematic uncertainties of various variables in the model) parameters which are the most likely to affect the outcome of the statistical analysis.

6.3.1.2 Likelihood

The frequentist probability of observing some data D that is consistent with a hypothesis H is defined as [317]

$$P(D|H) = \lim_{N\to\infty} \frac{N(D|H)}{N}, \tag{6.9}$$

where $N(D|H)$ is the number of experiments that result in D consistent with H, out of total N number of repeated experiments. $P(D|H)$ is thus nothing but an anticipation of a certain outcome of the experiment, given a hypothesis H. If $P(D|H)$ is expressed as a function of the parameters $\{\sigma, \nu\}$ of the hypothesis H, it is called the likelihood of H or a likelihood function $L(\sigma, \nu|D)$:

$$L(\sigma, \nu|D) = P(D|\sigma, \nu). \tag{6.10}$$

Likelihood thus quantifies how likely a set of observed data supports a certain hypothesis, H. Although it is expressed in terms of the conditional probability $P(D|\sigma, \nu)$, probability and likelihood are completely distinct terminologies. By definition, probabilities of all possible outcomes (i.e. all possible D ′s) must add

probability here is an objective concept, i.e. is not influenced by a prior knowledge or certainty. On the contrary, in Bayesian statistics, probability is ′subjective′, i.e. it needs some ′degree of belief′ prior the experiment, which is later updated by the experimental data. For example, $P(A)$ is interpreted as the degree of belief that the hypothesis A is true.

to 1 for a particular hypothesis H, i.e. $\sum_{\sigma,\nu} P(D|\sigma,\nu) = 1$. But the same is not true for likelihoods $L(\sigma,\nu|D)$, i.e sum of likelihoods across different hypotheses do not sum up to 1.

6.3.1.3 Profile likelihood ratio (PLR)

The likelihood 6.10 contains both the POI (σ) and nuisance parameters (ν). It is useful to define a conditional maximum likelihood estimate (CMLE) ($\hat{\hat{\nu}}(\sigma)$), which is the value of ν that maximises the likelihood function $L(\sigma,\nu|D)$ for a given dataset D under the condition of a fixed value of σ. This process is known as $'$profiling$'$ and $\hat{\hat{\nu}}(\sigma)$ is often called the profiled value of ν. The profile likelihood ratio for a certain value of POI, σ_{test} is then defined as

$$\lambda(\sigma_{test}) = \frac{L(\sigma_{test}, \hat{\hat{\nu}})}{L(\hat{\sigma}_{test}, \hat{\nu})}, \tag{6.11}$$

where $\hat{\sigma}_{test}$ and $\hat{\nu}$ are the best values of σ and ν respectively, obtained from a global fit of L with data D (known as maximum likelihood estimate, (MLE)).

6.3.1.4 Hypothesis test

A hypothesis test is a standard statistical procedure to determine whether to $'$accept$'$ or $'$reject$'$ a certain hypothesis, by investigating its consistency with a set of data. The basic steps in a frequentist hypothesis test are:

1. Construct two hypotheses: null (H_0) and alternative (H_1). H_0 is the hypothesis that one is trying to disprove, and H_1 is the alternative one.
2. Define a test statistic (q_σ) as a function of the dataset D, i.e. $q_\sigma = q_\sigma(\sigma)$.
3. For a particular choice of $\sigma = \sigma_{test}$, construct the distribution models of q_σ under H_0 and H_1 separately. The distribution histograms are populated by performing a large number of pseudo-experiments.
4. Evaluate the test statistic $q_{\sigma,obs}$ on the observed data for $\sigma = \sigma_{test}$.
5. Choose the size or significance level of the test (α) and define a critical region (w) of the D-space such that the probability under H_0 to find $x \in w$ is no more than α.

6. Define a probability-value (p-value) as

$$p = \int_{q_{\sigma,obs}}^{\infty} f(q_\sigma|H_0)dq_\sigma. \tag{6.12}$$

and reject H_0 if $p < \alpha$.

6.3.2 PLR method for hypothesis testing

6.3.2.1 Likelihood function

LZ uses a constrained extended unbinned likelihood function:

$$\begin{aligned} L(\sigma,\nu|D) =& \text{Poiss}(n_0|\mu) \\ & \times \prod_{e=1}^{n_0} \frac{1}{\mu}\left[\mu_s(\sigma) f_s(x_e|m_{HP/ALP}) + \sum_{b=1}^{N_b} \mu_b f_b(x_e|\nu)\right] \\ & \times \prod_{p=1}^{N_p} f_p(g_p|\nu_p), \end{aligned} \tag{6.13}$$

which consists of three terms:

- **(First) Poisson term:** The function of the term is to ′extend′ the likelihood by including the Poisson probability of seeing n_0 events with observables $x = \{S1_c, log_{10}S2_c\}$ in dataset D, when expecting μ. If μ_s and μ_b are the expected numbers of events for signal and individual background components respectively, $\mu = \mu_s + \sum_b \mu_b$.
- **(Second) Event probability model**: This is the product of probability models for each observed event and hence the likelihood is ′unbinned′. Individual event probabilities are modelled as weighted sums of signal (given a mass $m_{HP/ALP}$) and background (given ν) PDFs, $f_s(x_e|m_{HP/ALP})$ and $f_b(x_e|\nu)$ respectively, where N_b is the total number of background components.
- **(Third) Constraint term:** This is the Gaussian constraint on a subset p of the nuisance parameters. g denotes global observables, i.e. auxiliary measurements.

The same form of likelihood function 6.13 is used for all LZ analyses, only the choices of POI and nuisance parameters vary. In HP/ALP analysis, the number of signal events are considered as POI, i.e. $\sigma = \mu_s$. The set of nuisance parameters consists of the three major ER backgrounds (see Table. 6.2), including a combined

Table 6.2 *ER and NR backgrounds included in the analysis. The first three ER backgrounds are considered as the nuisance parameters in PLR.*

	Component	Expected events	Relative uncertainty	Constraint
ER	Combined ($Rn + Kr$)	14154	8.6%	1215.2
	$2\nu\beta\beta$	13186.3	50%	6593.2
	DetER	915.7	20%	183.1
	Solar ν	2845.4	2%	56.9
NR	DetNR	3.53	20%	0.7
	DSN ν	0.14	50%	0.07
	hep ν	0.84	12%	0.1
	^8B ν	33.5	15%	5.0
	atm ν	0.65	30.8%	0.2

$Rn + Kr$ model (intrinsic $^{85}Kr + {}^{220}Rn + {}^{222}Rn$). For the later, the relative uncertainties for ^{85}Kr, ^{220}Rn and ^{222}Rn are added in quadrature. Since the solar-ν (pp + ^7Be + CNO + pep) ER background is well-constrained (2% relative uncertainty), it is not considered as a nuisance parameter.

6.3.2.2 Confidence intervals and hypothesis test inversion

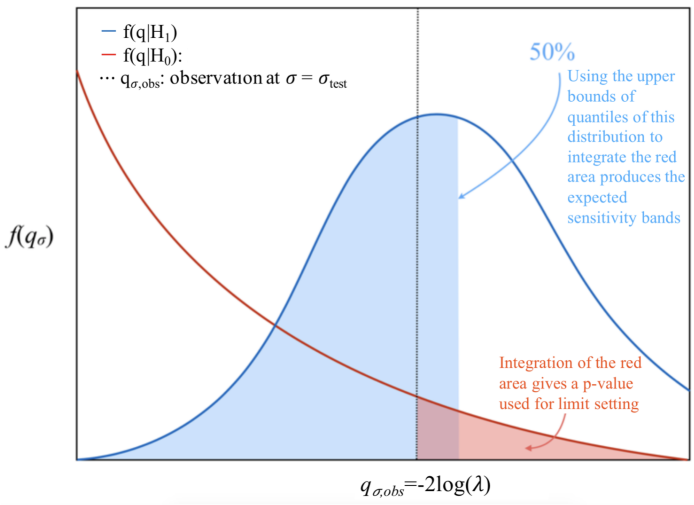

Figure 6.9: *An one-sided hypothesis testing. Image Courtesy: Lucie Tvrznikova.*

The aim is to set an upper limit on the POI, computed from the statistics of the observed data to 90% confidence limit (CL). The confidence interval (the present work only considers the upper limit) has a one-to-one correspondence with the hypothesis test, i.e. it consists of hypothesis tests for each value in the interval. The idea is to perform hypothesis tests for different σ_{test} values and

finding p-values as a function of σ to estimate the limits. An example of an one-sided[†] hypothesis test is illustrated in fig. 6.9. The H_0 and H_1 hypotheses are constructed as

- H_0 (red curve): data contains both the signal and background events.
- H_1 (blue curve): data contains only the background events (i.e. $\sigma = 0$).

The test statistic is defined in terms of the profile likelihood ratio $\lambda(\sigma)$ as

$$q_\sigma \equiv -2\ln(\lambda(\sigma)). \tag{6.14}$$

As $\sigma \to \hat{\sigma}$, $\lambda \to 1$ and $q \to 0$. The steps mentioned in section 6.3.1.4 are then followed, except that the lower limit of the integral 6.12 is now chosen to be the median ($'$expected$'$) value of test statistic distribution under H_1 (rightmost edge of the blue-shaded region in fig. 6.9 that contains 50% of the background distribution):

$$p = \int_{q_{\sigma,med,H_1}}^{\infty} f(q_\sigma|H_0)dq_\sigma. \tag{6.15}$$

The process is repeated for different values of σ and the p-values under the corresponding null hypotheses (i.e. area under the test statistic distribution under H_0) are calculated according to eq. 6.15. The last step is to $'$invert$'$ the hypothesis test, i.e. plotting the p-values as a function of σ and reject the POI values for $p < 0.1$. The maximum acceptable POI is called the median 90% (i.e. $\alpha = 1-0.9$) confidence level (CL) upper limit, given H_1. Note that a two-sided test (where both tails of the distribution is explored) gives both lower and upper limits.

[†]only one tail of the distribution is examined.

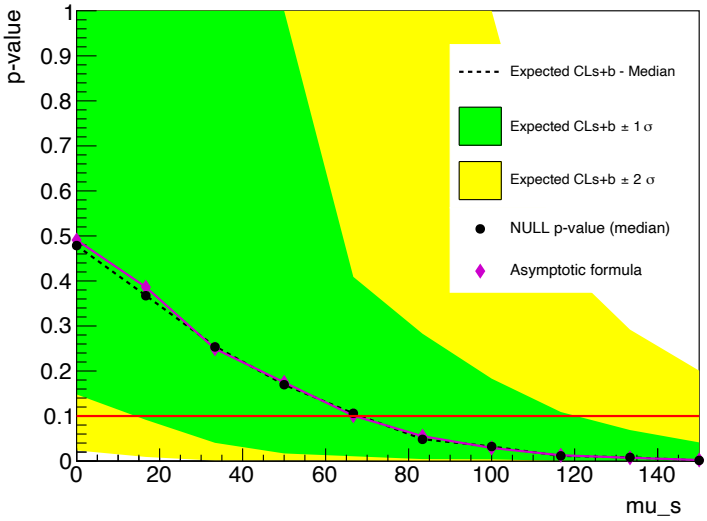

Figure 6.11: *The p−values determined from fig. 6.10 as a function of the POI (μ_s). The point of intersection of the p−value curve with the red $1-\alpha = 0.1$ line is the upper limit on the POI, above which H_0 is incompatible.*

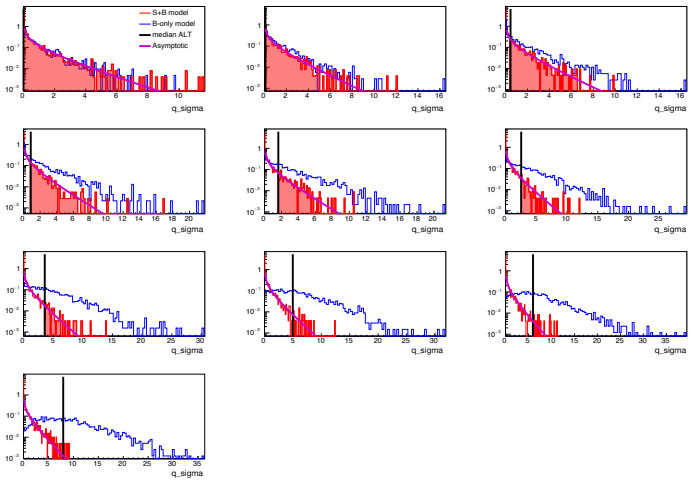

Figure 6.10: *Distributions of the test statistic q_σ for the null hypothesis H_0 (red histogram) and alternative hypothesis H_1 (blue histogram) for 10 different number of signal events (μ_s) generated by a 40 keV HP. The black vertical line is the q_{obs}, test statistic evaluated on pseudo-data generated from the background only model (H_1).*

Figs. 6.10 and 6.11 illustrate an example of the statistical analysis for a signal model of $40\,keV/c^2$ HP. For a given number of signal events (μ_s), the hypothesis test produces $\sim$ 5000 pseudo-experiments according to both H_1 and H_0, populating two distributions of the test statistic q_σ. The q_σ distributions under the null (H_0, red histogram) and alternative (H_1, blue histogram) hypotheses

for 10 different number of signal events (σ_{test}) are shown in fig. 6.10. The test statistic evaluated on pseudo-data generated from the background only model (H_1) for $\sigma = \sigma_{test}$ is shown by the black vertical line. The frequentist hypothesis test inversion to obtain the expected 90% CL is shown in fig. 6.11, where the $'$inverted$'$ p-values for each of the ten plots are plotted against σ. The red line is for $p = 1 - \alpha = 0.1$, and its intersection point with the p-value curve gives the median 90% confidence level (CL) upper limit on POI, above which H_0 is incompatible. Similarly, the $\pm 1\sigma$ (green) and $\pm 2\sigma$ (yellow) $'$Brazil$'$ bands (named after the flag) are obtained by repeating the entire process for different values ($0.16, 0.84, 0.025, 0.975$ quantiles of the q_{σ,H_1} PDF) of the lower limit of the integral 6.12.

6.3.2.3 From PLR to final results

Once an upper limit on the number of signal events is obtained, the expression for the interaction rate in the detector, i.e. eq. 6.5 for HP and eq. 6.6 for ALP, can be used to obtain a limit on the kinetic mixing κ and coupling g_{Ae} respectively. The idea is to exploit the proportionality $R_{HP} \propto \kappa^2 = \frac{\alpha'}{\alpha}$ as

$$\frac{\alpha'}{\alpha}(90\%\, CL) = \frac{\alpha'}{\alpha}(0)\left(\frac{\mu_{HP}(90\%\, CL)}{\mu_{HP}(0)}\right), \tag{6.16}$$

and $R_{ALP} \propto g_{Ae}^2$ as

$$g_{Ae}(90\%\, CL) = g_{Ae}(0)\left(\frac{\mu_{ALP}(90\%\, CL)}{\mu_{ALP}(0)}\right)^{1/2}, \tag{6.17}$$

where $\frac{\alpha'}{\alpha}(0) = 10^{-26}$ and $g_{Ae}(0) = 10^{-13}$ are the initially assumed values of HP kinetic mixing squared and ALP-electron coupling respectively (see section 6.1) and $\mu_{HP}(0)$, $\mu_{ALP}(0)$ are the corresponding numbers of signal events. $\mu_{HP}(90\%\, CL)$, $\mu_{ALP}(90\%\, CL)$ are the upper limits on POI obtained from the PLR analysis.

Note that eqs. 6.5 and 6.6 can also be combined as

$$\frac{R_{HP}}{R_{ALP}} = 3.3 \times 10^4 \frac{\alpha'}{\alpha} g_{Ae}^{-2} \frac{1}{m_{HP} m_{ALP}}, \tag{6.18}$$

i.e. one may just use the scaling to convert the constraint on α'/α into g_{Ae} or vice versa, using eq. 6.18.

The entire procedure is repeated for a number of HP (and ALP) masses from $2 - 70\,keV$. The final results follow in section 6.4.

6.4 Results and discussion

6.4.1 Sensitivity projections

Figs. 6.12 and 6.13 show the LZ projected sensitivities (90% C.L., for 1000 live days and 5.6 tonne fiducial mass) to the kinetic mixing squared ($\kappa^2 = \frac{\alpha'}{\alpha}$) for HPs and ALP-electron coupling (g_{Ae}) for ALPs, as a function of HP and ALP mass respectively. The conventional Brazilian bands, i.e. $\pm 1\sigma$ (green) and $+2\sigma$ (yellow) bands are also shown. Note that the -2σ region is omitted as it is expected to be ′power constrained′ [318]. Results from other experiments are taken from [309, 319, 320] for HPs and from [319–321] for ALPs.

A scan over HP masses ($2 - 70\,keV/c^2$) constrains the expected $\frac{\alpha'}{\alpha}$ no larger than $\sim 3.48 \times 10^{-28}$ (at $\sim 70\,keV$). While at very low energies ($\leqslant 15\,keV$) the indirect (Red Giant) limit on κ^2 is still the most stringent, LZ is expected to give a *better limit* at intermediate energies, i.e $\geqslant 15\,keV$ and $\leqslant 70\,keV$. Roughly, an improvement of ~ 2 orders of magnitude over the existing results is expected.

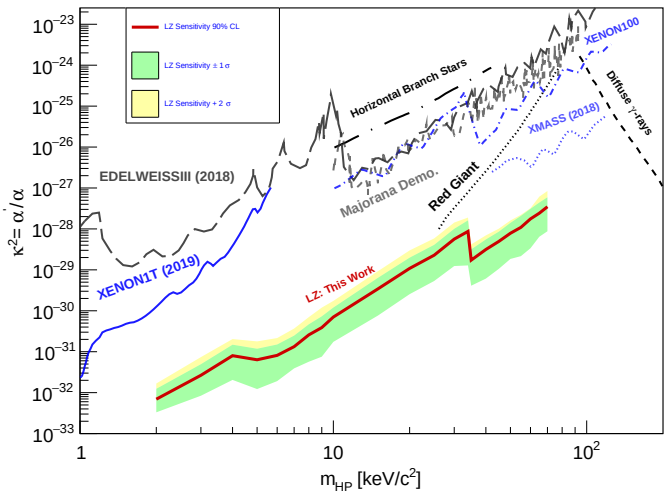

Figure 6.12: *Red curve: 90% C.L. sensitivity on kinetic mixing squared, $\kappa^2 = (\frac{\alpha'}{\alpha})$ for hidden photons. $\pm 1\sigma$ (green) and $+2\sigma$ (yellow) bands are also shown. Results from other experiments are taken from [309, 319, 320].*

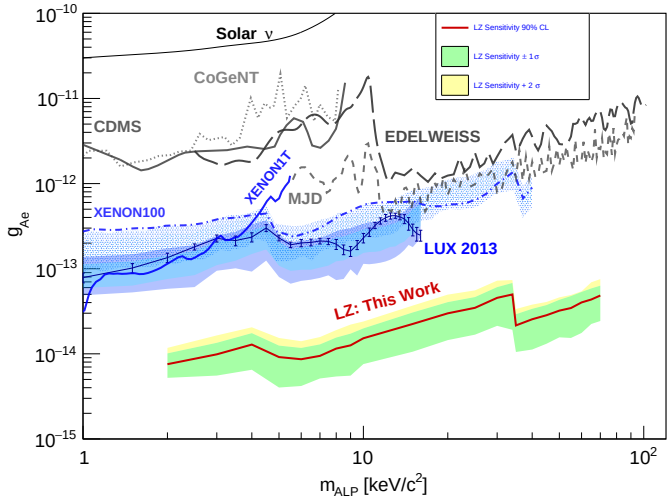

Figure 6.13: *Red curve:* 90% *C.L. sensitivity on ALP-electron coupling.* $\pm 1\sigma$ *(green) and* $+2\sigma$ *(yellow) bands are also shown. Results from other experiments are taken from [319–321].*

For ALPs, LZ is expected to give a *more stringent* limit than the published results to date. Again $\sim$ 2 orders of magnitude improved sensitivity is expected, with g_{Ae} no larger than $\sim 4.98 \times 10^{-14}$ (at $\sim 34\,keV$). The ALP result (fig. 6.13) is obtained by the scaling method (eq. 6.18) and a same result will follow if one uses a full PLR treatment.

6.4.2 Effect of Rn+Kr background

Intrinsic Xe contaminants constitute a major ER background in LZ, largely due to the naked or semi-naked β's from $^{212,214}Pb$ progenies of $^{220,222}Rn$. However, there is an uncertainty as to how well LZ will be able to meet its intrinsic background (especially radon) goals. It is thus important to investigate the variation of the median sensitivity for κ^2 and g_{Ae} in different $Rn + Kr$ scenarios, other than the projected one.

As mentioned in section 6.3.2.1, the $^{220,222}Rn$ and ^{85}Kr backgrounds are combined together into a single component while treating in the PLR. The combined $Rn + Kr$ background is dominant only over the lower regions of the parameter space (see fig. 6.6). This can be quantified by dividing the HP/ALP ROI into three smaller regions and tabulating the total number of ER events within (Table 6.3).

Table 6.3 *Estimated number of ER background events in smaller ROI regions for an exposure of 1000 days in 5600 kg fiducial mass.*

ROI range (*keV*)	Number of ER background events (1000 days, 5600 kg fid. vol)				*Rn + Kr* dominance
	^{136}Xe $2\nu\beta\beta$	*Solar* ν	Det. ER	*Rn + Kr* (Projected)	
0 - 20	647	759	217	3338	Dominant
21 - 60	5422	1327	422	6516	Dominant but comparable with $2\nu\beta\beta$
61 - 100	11532	1095	422	6523	sub-dominant

Any variation of the projected $Rn + Kr$ background will change its dominance from that shown in Table. 6.3, and affect the PLR results for a given HP/ALP mass. To investigate this, two representative HP masses are chosen ($15\,keV/c^2$ and $70\,keV/c^2$). The variations of the total background for five different $Rn+Kr$ levels ($0.1\times, 0.31\times, 1\times, 3.1\times, 10\times$ projected value) in the signal neighbourhood, defined by the full width at half maximum (FWHM) of the reconstructed energy peak (fig. 6.4b), are shown in figs. 6.14a and 6.14b for 70 and $15\,keV/c^2$ HP respectively.

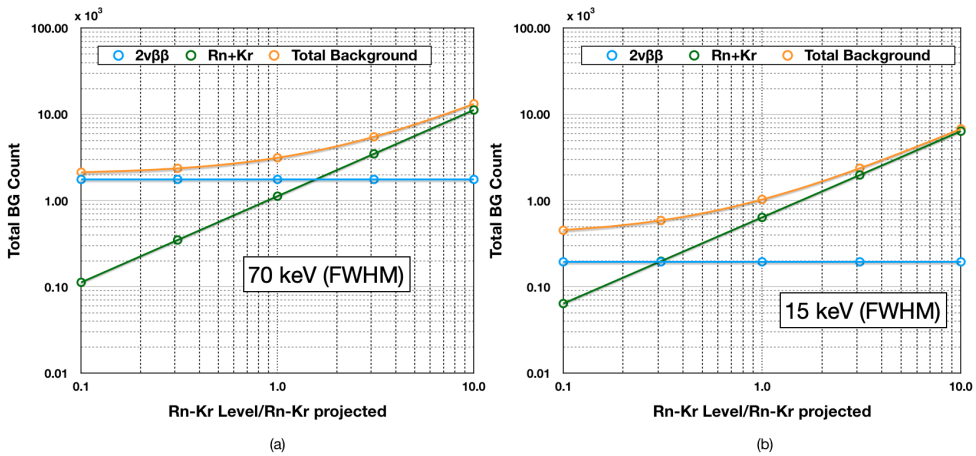

Figure 6.14: *Variations of $Rn + Kr$, $2\nu\beta\beta$ and total backgrounds (for an exposure of 1000 days in a 5600 kg fiducial mass) in the signal neighbourhoods for (a) $70\,keV/c^2$ and (b) $15\,keV/c^2$ HP.*

The entire PLR treatment (sections 6.3 and 6.4.1) is then repeated for both masses, at different $Rn+Kr$ levels. The results are summarised in fig. 6.15. Since PLR runs are time consuming, the effect of Rn-Kr variation on ALP sensitivity

are simply obtained (fig. 6.16) using the scaling method (eq. 6.18).

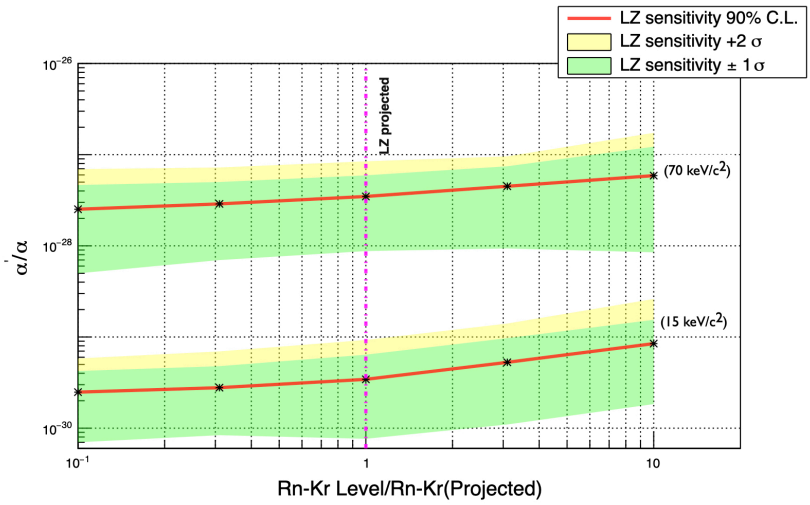

Figure 6.15: *Variation of the 90% C.L. sensitivity on kinetic mixing squared for $15\,keV/c^2$ and $70\,keV/c^2$ HPs. The $\pm1\sigma$ and $+2\sigma$ bands are also shown.*

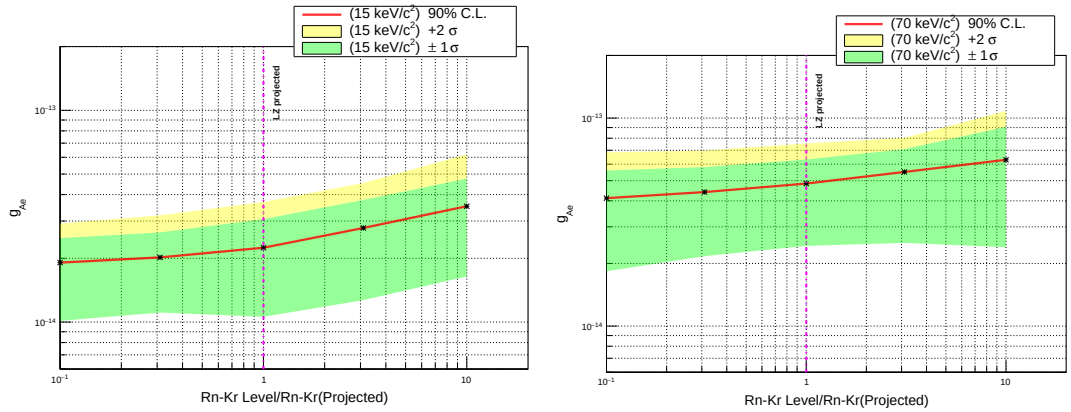

(a) *(b)*

Figure 6.16: *Variation of the 90% C.L. sensitivity on ALP-electron coupling for (a) $15\,keV/c^2$ and (b) $70\,keV/c^2$ ALPs. The $\pm1\sigma$ and $+2\sigma$ bands are also shown.*

For a given HP (ALP) mass, the median sensitivity for $\frac{\alpha'}{\alpha}$ (g_{Ae}) varies as $\propto (R_{BG})^{1/2}$ ($\propto (R_{BG})^{1/4}$), where R_{BG} denotes the number of background events in the signal neighbourhood. This is expected since the sensitivity to R_{HP} (R_{ALP}) should be proportional to the Poisson fluctuations ($R_{BG}^{1/2}$) of the background rate, and R_{HP} (R_{ALP}) and $\frac{\alpha'}{\alpha}$ (g_{Ae}) share a linear (squared) relationship (eqs. 6.5 and 6.6).

The effect of $Rn + Kr$ variation is more pronounced for lower mass (e.g. $15\,keV$) than the higher one (e.g. $70\,keV$), because of two reasons. First, the Xe photo-electric cross-section (σ_{PE} in eqs. 6.5 and 6.6) at $15\,keV$ is ten times larger than that at $70\,keV$ (see figs. 5.11 or 6.2). The second reason is the dominance of $Rn + Kr$ component in the neighbourhood of the $15\,keV$ signal (fig. 6.14b).

The rates R_{HP} and R_{ALP} vary differently with respect to the masses m_{HP} and m_{ALP}: inversely for HPs (eq. 6.5) and linearly for ALPs (eq. 6.6). This explains the remaining differences between fig. 6.15 and fig. 6.16a for $15\,keV/c^2$ HP/ALP and between fig. 6.15 and fig. 6.16b for $70\,keV/c^2$ HP/ALP. For ALPs, the σ-bands for the two masses are overlapped, and hence they are plotted separately in figs. 6.16a and 6.16b.

Nevertheless, even with an unrealistically higher level of Rn-Kr background (e.g. $10\times$ the projected one), the projected sensitivities for intermediate energies, (i.e $\geqslant 15\,keV$ and $\leqslant 70\,keV$) are still better than the existing experimental bounds, both for HPs and ALPs.

6.4.3 Spatial distribution of events

The results discussed so far are based on the analysis of two dimensional PDFs that use two experimental observables: $S1_c$ and $log_{10}\,S2_c$. No spatial information in terms of the radial (r) and vertical (z) components was explicitly mentioned. Since both the signal and background PDFs are treated in the same manner, it is expected that the sensitivity projection is unaffected by the absence of (r, z) in the PDFs. However, in the long run (especially when the real data will be available) they will be definitely included in the analysis, i.e. a four dimensional PDF ($S1_c$, $log_{10}\,S2_c$, r and z) will be used.

6.5 Summary and future prospects

This chapter presented a detailed insight into the sensitivity reach of the LZ direct detection experiment for HP and ALP searches. The interaction signatures, i.e. the hidden photo-electric and axio-electric effect, both provide mono-energetic electron recoil spectra. A complete statistical analysis based on the frequentist PLR method was applied using two-dimensional ($S1_c$, $log_{10}\,S2_c$) signal and background PDFs. A wide range of HP/ALP mass ($2 - 70\,keV/c^2$)

was investigated, and projected upper limits on the HP kinetic mixing squared $\frac{\alpha'}{\alpha}$ and ALP-electron coupling g_{Ae} at 90% CL were drawn. The projections showed more than $\sim$ 2 orders of magnitude improvement over the existing experimental bounds. A study of sensitivity performance over a variation of $Rn + Kr$ background was also done at the end, resulting in a promising outcome that the sensitivity would still lead the existing ones.

Looking to the future, further improvement is still possible. The present work is based on a background model having an explicit energy cut at $100\,keV$. At the time this thesis is being written, high energy background simulations are available for use. The implementation of an improved background model with a higher energy range (i.e. exceeding $100\,keV$) is thus the obvious next step in the game. In the long run, the analysis will be facilitated by the real data from LZ science run(s), expectedly providing world-leading limits on the hidden photon kinetic mixing and ALP-electron coupling.

Chapter 7

Conclusions

The quest for identifying the particle nature of the mysterious dark matter combines the round-the-clock efforts of physicists and researchers from a diverse array of theoretical and experimental collaborations. The present work plays a part in this gigantic scientific expedition by exploring the low energy electron recoil science capabilities of LUX-ZEPLIN (LZ), the cutting-edge second generation direct detection experiment.

Overview

Chapter 1 constitutes the cosmological prelude of the thesis, essentially beginning with the observational evidence of dark matter abundance in the cosmos. The chapter also brings together some cosmological aspects of dark matter, e.g. the concept of cold dark matter, dark matter content of the universe and the galactic halo model. **Chapter 2** describes the theoretical models to further strengthen the concept, by outlining a landscape of particle candidates for dark matter, e.g. weakly interacting massive particles (WIMPs). Special attention was paid to the hidden photon (HP) and axion-like particle (ALP) interpretations of the dark matter, followed by a brief review of existing constraints on relevant parameters, i.e. the kinetic mixing squared (κ^2) for hidden photons and coupling to electrons (g_{Ae}) for ALPs.

Experimental realisation of rare dark matter interactions is not a straight-forward task. **Chapter 3** encapsulates different detection approaches in this context, with detail working principle and technical overview of the LZ detector.

Chapter 4 covers the hardware-centric part of the thesis work and reports the performance tests of 100 Hamamatsu R8520-406 PMTs (93 for instrumentation in the top LXe skin region of the LZ detector, and the rest were spare) that were conducted in Edinburgh. **Chapter 5** investigates the extents of the atomic

binding effect on ER backgrounds and reports the ***first implementation*** of available relativistic random phase approximation (RRPA) to the solar neutrino background model in LZ. Finally, **Chapter 6** demonstrates the beyond-the-WIMP science capability of LZ: the ***first*** sensitivity projections for HPs and ALPs over a wide mass range ($2 - 70\,keV/c^2$) were reported.

Findings and contributions

Diligent functional tests are crucial for reliability of the detector performance during science runs. Sophisticated peak-finding algorithms with the capability of peak-EM ringing discrimination were developed and successfully applied for dark count analysis of the skin PMTs, as described in chapter 4. Based on all test results, 95 PMTs out of 100 passed the LZ validation requirements and 5 ′rejected′ PMTs were returned to the manufacturer. The best 93 PMTs have been successfully assembled in the skin region of the LZ detector at SURF. This was an active and direct participation of the author in the detector commissioning as a part of the LZ collaboration.

The sensitivity reach of direct detection experiments are limited by the presence of irreducible detector backgrounds, most of which sit in the electron-recoil (ER) band. Backgrounds like Compton or neutrino ERs are *usually* modelled adopting a free electron approximation – which is simple but unrealistic. The author's implementation of the RRPA-corrected solar neutrino background in the analysis framework takes it one step towards a better and precise low energy ER background model. The binding effect on Compton scattering was also studied in terms of GEANT4 Monash physics. Excess events at the low-energy side of the recoil spectra, prior to the application of the analysis cuts, were reported. However, simulation outputs of realistic detector backgrounds with standard analysis cuts resulted in too few events to show any noticeable difference. The migration to Monash physics is thus not an urgent need for the standard LZ analyses, but is recommended for the long run. Also, for future generation-3 detectors with larger (hundreds-tonne scale) volumes, Monash physics is a ′must′.

Chapter 6 presents the study of the sensitivity performance of the LZ detector for direct detection of HPs and ALPs. The projected upper limits of κ^2 (for HPs) and g_{Ae} (for ALPs), for 5600 kg fiducial volume and a 1000 live-day run, showed more than ~ 2 orders of improvement over the existing experimental bounds. The uncertainty in meeting LZ′s intrinsic background goal was also accounted for by conducting a quick study at the end. The result is promising: the sensitivities will

still be world-leading ones even with an unrealistically high intrinsic $Rn + Kr$ background.

Implications and discussion

The implication of the work described in this thesis is broad. The RRPA-corrected solar neutrino background is now being actively used in all low energy ER analyses in LZ. For generation-3 dark matter detectors, atomic binding treatment will be more important and the results coming out of the background studies will come handy. At the time of writing this thesis, the implementation of Monash physics list in future versions of BACCARAT is being considered by the simulation and background working group and will go through the chains of usual validations and approval processes internal to the collaboration shortly.

The first LZ science run is scheduled in 2020. The analysis framework built for the sensitivity projections will be used as a foundation of the HP/ALP searches on real LZ data, providing world-leading limits of κ^2 and g_{Ae}.

Important physics can also be extracted from the results obtained. Model dependent conversion of the limits on ALP-electron (g_{Ae}) coupling into the ALP-photon ($g_{A\gamma\gamma}$) coupling can be an interesting area of study. The CAST collaboration attempted something similar back in 2013 [322] and constrained the product $g_{Ae}g_{A\gamma\gamma}$ for solar axions with masses smaller than $10\,meV$. A recent study by the China Dark Matter Experiment (CDEX) reported [323] a model-independent constraint on the product $g_{NN}^{eff} \times g_{Ae}$, where g_{NN}^{eff} is the effective axion-nuclear coupling. The possibility of doing something similar for ALPs is worth investigating.

Finally, there exists hybrid ALP+HP models that predict an ALP-photon-hidden photon coupling ($g_{A\gamma\gamma'}$), similar as the ALP coupling to two photons. Depending on the role of kinetic mixing in the model, experimental limits on κ^2 from solar hidden photon searches can shed some light on expected values of $g_{A\gamma\gamma'}$.

Appendix A

Alternative Production Mechanisms for ALPs and HPs

A.1 ALP production in the early universe

A.1.1 Post-inflation scenario

In the post-inflation scenario, the spontaneous symmetry breaking (SSB) occurred after inflation. It will have left an inhomogeneous ALP field, leading to a formation of ALP clumps due to its attractive self-interaction. These clumps, known as mini-clusters, will have had an additional 'impact' on cosmological structure formation. The mini-cluster mass at self-interaction freeze-out is expressed in terms of a freeze-out temperature T_λ as

$$M_{mc} \sim \rho_\phi(T_\lambda) d_H(T_\lambda)^3, \tag{A.1}$$

where $d_H = H^{-1}$ is the Hubble horizon. The constraint $M_{mc} \lesssim 4\times10^3 M_\odot$ imposed by the CDM power spectrum provides a bound on T_λ and m_ϕ (ALP mass) as [324]

$$T_\lambda > 2 \times 10^{-5}\, GeV \text{ and } m_\phi > H(T = 2 \times 10^{-5}\, GeV) \sim 10^{-20}\, eV. \tag{A.2}$$

Topological defects like cosmic strings and domain walls are also to be considered in the post-inflation scenario. However, the exact contribution of these effects is subject to a long-standing debate and beyond the scope of this dissertation. For details, see [103].

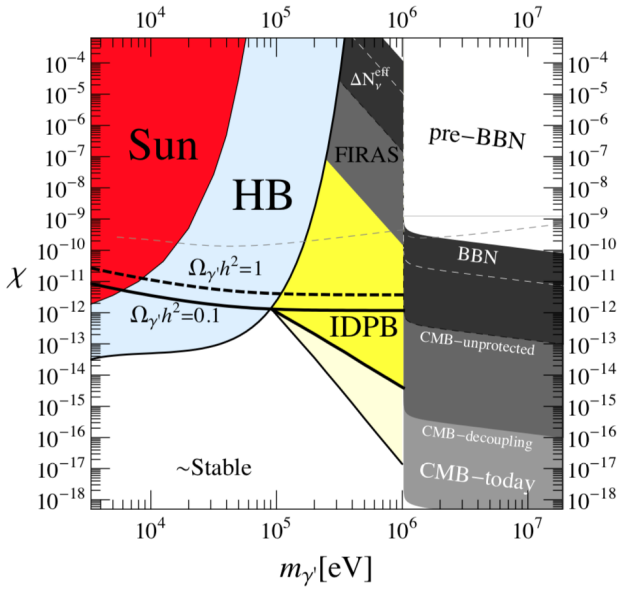

Figure A.1: *Cosmological bounds from [325] on HPs in the mass mixing plane. HP Mass and kinetic mixing parameter are represented by $m_{\gamma'}$ and χ respectively.*

A.2 HP production in the early universe

A.2.1 Thermal production

Hidden photons can also be produced thermally [325] via resonant photon-HP conversion in the primordial photon bath. In contrast to the less-restricted non-thermal scenarios, thermally produced HPs are very much constrained in astrophysics and cosmology. The mechanism consists of a conversion efficiency determined by the effective value of κ. Resonant photon-HP conversion dominates for light ($m_V < 2m_e$, m_e is the electron mass) dark photons, and the region $10\,eV \lesssim m_V < 100\,keV$ is experimentally excluded [326]. However, the relatively warmer HPs with a mass $\sim 100\,keV$ or above are still suitable DM candidates and can be considered as 'super-WIMPs'.

Cosmological constraints on thermally produced hidden photons are shown in fig. A.1. Values of (m_V, κ) that produce the correct CDM relic density follow the solid line labelled $\Omega'_\gamma h^2 = 0.1$. The region above is excluded by overproduction [325]. The exclusion regions labelled 'Sun' and 'HB' comes from studies of HP induced anomalous energy loss in the sun and horizontal branch (HB) stars respectively.

If the resonant HP production occurred after BBN but prior the CMB decoupling, it would increase the effective number of relativistic neutrino species N_ν^{eff} and the baryon to photon ratio at decoupling [327]. Photon-HP conversion could also cause a CMB distortion and constraints from Cosmic Background Explorer (COBE)'s Far-InfraRed Absolute Spectrophotometer (FIRAS) are also shown in fig.A.1.

Light HPs that decay into photons ($HP \rightarrow 3\gamma$) could leave a footprint in the astrophysical γ-background. Model (i.e 2 body/3 body considerations) independent constraints from the intergalactic diffuse photon background (IDPB) measurements [325] based on this idea are shown by the yellow region in fig. A.1. The dark yellow region is only for production via kinetic mixing with photons. For other production mechanisms, the region extends to the light yellow band. Decays of heavy ($m_V > 2m_e$) HPs into e^+, e^- pairs before CMB decoupling are strongly constrained by the studies of big bang nucleosynthesis [325]. Decaying heavy HPs after the CMB decoupling are also excluded because the present day CMB anisotropies would reveal these signatures otherwise.

The white band in the lower left corner of the plot corresponds to the long-lived (longer than the age of the universe) or $'$stable$'$ HP dark matter, provided the kinetic mixing as the dominant early universe production mechanism. This excludes the $'$thermally produced$'$ HPs with mass in the MeV scale or above as the cold dark matter candidate.

A.2.2 Production from Inflationary fluctuations

Graham et al. [328] introduced another mechanism to produce massive vector bosons from inflationary perturbations which can reproduce a calculable relic abundance as

$$\frac{\Omega_V h^2}{\Omega_c h^2} \approx \sqrt{\frac{m_V}{6 \times 10^{-6} eV}} \left(\frac{H_I}{10^{14} GeV} \right)^2, \tag{A.3}$$

where H_I is the Hubble scale of inflation with a current bound $H_I \lesssim 10^{14}\, GeV$. This provides a lower bound on HP DM mass as $m_V \gtrsim 10^{-5}\, eV$. Note that a lighter HP can still constitute a portion of DM, but not the whole of it. An upper bound $m_V \lesssim 10^8\, GeV$ also exists due to the condition of $m < H$ during inflation.

List of Acronyms

ALP Axion-Like Particle. 1, 24

BSM Beyond the Standard Model. 1

CDM Cold Dark Matter. 9
CL Confidence Limit. 132
CMB Cosmic Microwave Background. 7

DM Dark Matter. 1

ER Electron Recoil. 1

FEA Free Electron Approximation. 83, 97

HP Hidden Photon. 1, 24

LUX Large Underground Xenon. 44
LXe Liquid Xenon. 1
LZ LUX-ZEPLIN. 1

NORM Naturally Occurring Radioactive Materials. 86
NR Nuclear Recoil. 44

PDF Probability Density Function. 123
PLR Probability Likelihood Ratio. 130
PMT Photo-Multiplier Tube. 53
POI Parameter Of Interest. 129

RIA Relativistic Impulse Approximation. 107
ROI Region Of Interest. 102
RRPA Relativistic Random Phase Approximation. 99

SA Stepping Approximation. 97
SM Standard Model. 1

TPC Time Projection Chamber. 52

WIMP Weakly Interacting Massive Particle. 1
WISP Weakly Interacting Slim Particle. 24

List of Publications (LUX and LZ)

[1] D. Akerib et al. The LUX-ZEPLIN (LZ) experiment. *Nuclear Instruments and Methods in Physics Research Section A: Accelerators, Spectrometers, Detectors and Associated Equipment*, 953:163047, 2020.

[2] D. Akerib et al. Measurement of the gamma ray background in the davis cavern at the sanford underground research facility. *Astroparticle Physics*, 116:102391, 2020.

[3] D. S. Akerib et al. Improved measurements of the β-decay response of liquid xenon with the LUX detector. *Phys. Rev. D*, 100:022002, Jul 2019.

[4] D. S. Akerib et al. First direct detection constraint on mirror dark matter kinetic mixing using LUX 2013 data. *Phys. Rev. D*, 101:012003, Jan 2020.

[5] D. S. Akerib et al. Extending light wimp searches to single scintillation photons in LUX. *Phys. Rev. D*, 101:042001, Feb 2020.

[6] D. S. Akerib et al. Projected Sensitivity of the LUX-ZEPLIN Experiment to the $0\nu\beta\beta$ decay of ^{136}Xe. 2019.

[7] D. S. Akerib et al. Search for two neutrino double electron capture of ^{124}Xe and ^{126}Xe in the full exposure of the LUX detector. 2019.

[8] D. S. Akerib et al. Improved Modeling of β Electronic Recoils in Liquid Xenon Using LUX Calibration Data. 2019.

[9] D. S. Akerib et al. Simulations of Events for the LUX-ZEPLIN (LZ) Dark Matter Experiment. 2020.

Bibliography

[1] L. Kelvin. Baltimore Lectures on Molecular Dynamics and The Wave Theory of Light. 1904.

[2] P. Bowler and I. Morus. *Making Modern Science: A Historical Survey.* University of Chicago Press, 2010.

[3] O. Lodge. The Ether of Space. *The North American Review*, 187(630):724–736, 1908.

[4] H. Poincaré. The Milky Way and Theory of Gases. 1906.

[5] E. Hubble and M. L. Humason. The Velocity-Distance Relation among Extra-Galactic Nebulae. *The Astrophysical Journal*, 74:43, July 1931.

[6] F. Zwicky. The redshift of extragalactic nabulae. *Helvetica Physica Acta*, 6:110–127, 1933.

[7] F. Zwicky. On the masses of nebulae and of clusters of nebulae. *Astrophysical Journal*, pp. 86–217, 1937.

[8] S. Smith. The mass of the Virgo cluster. *Astrophysical Journal*, 6:23, 1936.

[9] M. Schwarzschild. Mass distribution and mass-luminosity ratio in galaxies. *Astronomical Journal*, 59:273, September 1954.

[10] E. Holmberg. On the Clustering Tendencies among the Nebulae. *Astrophysical Journal*, 92:200, September 1940.

[11] B. V. Alexeev. Chapter 4 - the dark matter problem. In B. V. Alexeev, editor, *Nonlocal Astrophysics*, pp. 141 – 176. Elsevier, 2017.

[12] V. C. Rubin et al. Extended rotation curves of high-luminosity spiral galaxies. IV - Systematic dynamical properties, SA through SC. *The Astrophysical Journal*, 225:L107–L111, November 1978.

[13] K. Lundmark. Über die Bestimmung der Entfernungen, Dimensionen, Massen und Dichtigkeit fur die nächstgelegenen anagalacktischen Sternsysteme. *Meddelanden fran Lunds Astronomiska Observatorium Serie I*, 125:1–13, 1930.

[14] H. W. Babcock. The rotation of the Andromeda Nebula. *Lick Observatory*

Bulletin, 19:41–51, 1939.

[15] J. H. Oort. Some Problems Concerning the Structure and Dynamics of the Galactic System and the Elliptical Nebulae NGC 3115 and 4494. *The Astrophysical Journal*, 91:273, April 1940.

[16] F. D. Kahn and L. Woltjer. Intergalactic Matter and the Galaxy. *The Astrophysical Journal*, 130:705, November 1959.

[17] K. C. Freeman. On the Disks of Spiral and S0 Galaxies. *The Astrophysical Journal*, 160:811, June 1970.

[18] D. H. Rogstad and G. S. Shostak. Gross Properties of Five Scd Galaxies as Determined from 21-CENTIMETER Observations. *The Astrophysical Journal*, 176:315, September 1972.

[19] V. C. Rubin et al. Rotation velocities of 16 SA galaxies and a comparison of Sa, Sb, and SC rotation properties. *The Astrophysical Journal*, 289:81–98, February 1985.

[20] O. J. LODGE. Gravitation and Light. *Nature*, 104(2614):354–354, 1919.

[21] O. Chwolson. Über eine mögliche Form fiktiver Doppelsterne. *Astronomische Nachrichten*, 221:329, June 1924.

[22] D. Clowe et al. A Direct Empirical Proof of the Existence of Dark Matter. *The Astrophysical Journal*, 648(2):L109–L113, Aug 2006.

[23] R. A. Alpher and R. C. Herman. On the Relative Abundance of the Elements. *Phys. Rev.*, 74:1737–1742, Dec 1948.

[24] A. G. Doroshkevich and I. D. Novikov. Mean Density of Radiation in the Metagalaxy and Certain Problems in Relativistic Cosmology. *Soviet Physics Doklady*, 9:111, August 1964.

[25] A. A. Penzias and R. W. Wilson. A Measurement of Excess Antenna Temperature at 4080 Mc/s. *The Astrophysical Journal*, 142:419–421, July 1965.

[26] Planck Collaboration et al. Planck 2013 results. I. Overview of products and scientific results. *Astronomy and Astrophysics*, 571:A1, November 2014.

[27] N. W. Boggess et al. The COBE mission - Its design and performance two years after launch. *The Astrophysical Journal*, 397:420–429, October 1992.

[28] A. R. Liddle and D. H. Lyth. Inflation and mixed dark matter models. *Monthly Notices of the Royal Astronomical Society*, 265(2):379–384, 11 1993.

[29] J. R. Primack and M. A. K. Gross. *Hot dark matter in cosmology*, pp. 287–308. 2001.

[30] N. Banik et al. Novel constraints on the particle nature of dark matter from stellar streams. *arXiv e-prints*, pp. arXiv:1911.02663, November 2019.

[31] A. Drlica-Wagner et al. Probing the Fundamental Nature of Dark Matter with the Large Synoptic Survey Telescope. *arXiv e-prints*, pp. arXiv:1902.01055, February 2019.

[32] L. J. Rosenberg. Direct Searches for Dark Matter: Recent Results. *Proceedings of the National Academy of Science*, 95(1):59–66, January 1998.

[33] L. Roszkowski et al. WIMP dark matter candidates and searches—current status and future prospects. *Rept. Prog. Phys.*, 81(6):066201, 2018.

[34] E. W. Kolb and M. S. Turner. *The early universe*, volume 69. 1990.

[35] K. Griest and M. Kamionkowski. Unitarity limits on the mass and radius of dark-matter particles. *Phys. Rev. Lett.*, 64:615–618, Feb 1990.

[36] G. R. Blumenthal et al. Formation of galaxies and large-scale structure with cold dark matter. *Nature*, 311:517–525, October 1984.

[37] A. G. Riess et al. Observational Evidence from Supernovae for an Accelerating Universe and a Cosmological Constant. *The Astronomical Journal*, 116(3):1009–1038, sep 1998.

[38] S. Perlmutter et al. Measurements of Ω and Λ from 42 High-Redshift Supernovae. *The Astrophysical Journal*, 517(2):565–586, jun 1999.

[39] N. Aghanim et al. Planck 2018 results. VI. Cosmological parameters. *arXiv e-prints*, pp. arXiv:1807.06209, July 2018.

[40] S. M. Carroll. The Cosmological Constant. *Living Reviews in Relativity*, 4:1, February 2001.

[41] P. J. E. Peebles. Large-scale background temperature and mass fluctuations due to scale-invariant primeval perturbations. *Astrophysical Journal, Part 2 - Letters to the Editor*, 263:L1–L5, December 1982.

[42] J. R. Bond et al. Formation of galaxies in a gravitino-dominated universe. *Physical Review Letters*, 48:1636–1639, June 1982.

[43] G. R. Blumenthal et al. Galaxy formation by dissipationless particles heavier than neutrinos. *Nature*, 299:37, September 1982.

[44] https://www.nobelprize.org/prizes/physics/2019/summary.

[45] S. D. M. White. The cold dark matter universe. In J. M. Dickey, editor, *The Minnesota lectures on Clusters of Galaxies and Large-Scale Structure*, volume 5 of *Astronomical Society of the Pacific Conference Series*, pp. 197–229, 1988.

[46] C. Giunti and C. W. Kim. *Fundamentals of Neutrino Physics and Astrophysics*. 4 2007.

[47] P. Mróz et al. Rotation Curve of the Milky Way from Classical Cepheids. *The Astrophysical Journal*, 870(1):L10, Jan 2019.

[48] J. Caldwell and J. Ostriker. The mass distribution within our Galaxy - A three component model. *The Astrphysical Journal*, 251:61–87, December 1981.

[49] R. A. Flores and J. R. Primack. Observational and theoretical constraints on singular dark matter halos. *Astrophys. J.*, 427:L1–4, 1994.

[50] B. Moore. Evidence against dissipationless dark matter from observations of galaxy haloes. *Nature*, 370:629, 1994.

[51] L. Hernquist. An analytical model for spherical galaxies and bulges. *The Astrphysical Journal*, 356:359–364, June 1990.

[52] J. F. Navarro et al. The Structure of Cold Dark Matter Halos. *The Astrphysical Journal*, 462:563, May 1996.

[53] J. Dubinski and R. G. Carlberg. The structure of cold dark matter halos. *The Astrphysical Journal*, 378:496–503, September 1991.

[54] J. I. Read et al. Dark matter heats up in dwarf galaxies. *Monthly Notices of the Royal Astronomical Society*, 484(1):1401–1420, 01 2019.

[55] M. Pierre et al. Sensitivity of CTA to dark matter signals from the Galactic Center. *Journal of Cosmology and Astroparticle Physics*, 2014(06):024–024, jun 2014.

[56] J. F. Navarro et al. A Universal density profile from hierarchical clustering. *Astrophys. J.*, 490:493–508, 1997.

[57] J. Einasto. On the Construction of a Composite Model for the Galaxy and on the Determination of the System of Galactic Parameters. *Trudy Astrofizicheskogo Instituta Alma-Ata*, 5:87–100, 1965.

[58] Salucci, P. et al. The dark matter density at the Sun′s location. *Astronomy and Astrophysics*, 523:A83, 2010.

[59] M. Tanabashi et al. Review of Particle Physics. *Phys. Rev. D*, 98:030001, Aug 2018.

[60] J. Binney and S. Tremaine. *Galactic dynamics*. Princeton, NJ, Princeton University Press, 1987, 747 p., 1987.

[61] M. Hoeft et al. Velocity dispersion profile in dark matter halos. *Astrophys. J.*, 602:162–169, 2004.

[62] G. Battaglia et al. The radial velocity dispersion profile of the Galactic halo: constraining the density profile of the dark halo of the Milky Way. *Monthly Notices of the Royal Astronomical Society*, 364(2):433–442, 12 2005.

[63] D. S. Akerib et al. Projected WIMP sensitivity of the LUX-ZEPLIN dark matter experiment. *Phys. Rev. D*, 101:052002, Mar 2020.

[64] C. McCabe. Astrophysical uncertainties of dark matter direct detection experiments. *Phys. Rev. D*, 82:023530, Jul 2010.

[65] M. Benito et al. Handling the uncertainties in the Galactic Dark Matter distribution for particle Dark Matter searches. *Journal of Cosmology and Astroparticle Physics*, 2019(3):033, March 2019.

[66] F. Mignard. Local galactic kinematics from Hipparcos proper motions. *Astronomy and Astrophysics*, 354:522–536, February 2000.

[67] F. J. Kerr and D. Lynden-Bell. Review of galactic constants. *Monthly Notices of the Royal Astronomical Society*, 221:1023–1038, August 1986.

[68] J. Bovy et al. Galactic Masers And The Milky Way Circular Velocity. *The Astrophysical Journal*, 704(2):1704–1709, Oct 2009.

[69] P. J. McMillan and J. J. Binney. The uncertainty in Galactic parameters. *Monthly Notices of the Royal Astronomical Society*, 402(2):934–940, Feb 2010.

[70] M. J. Reid et al. Trigonometric Parallaxes of Massive Star-Forming Regions. VI. Galactic Structure, Fundamental Parameters, and Noncircular Motions. *The Astrophysical Journal*, 700:137–148, July 2009.

[71] K. Freese et al. Colloquium: Annual modulation of dark matter. *Rev. Mod. Phys.*, 85:1561–1581, Nov 2013.

[72] T. M. Undagoitia and L. Rauch. Dark matter direct-detection experiments. *Journal of Physics G: Nuclear and Particle Physics*, 43(1):013001, Dec 2015.

[73] M. Pospelov et al. Bosonic super-WIMPs as keV-scale dark matter. *Phys. Rev.*

D, 78:115012, Dec 2008.

[74] J. I. Collar and F. T. Avignone. Diurnal modulation effects in cold dark matter experiments. *Phys. Lett.*, B275:181–185, 1992.

[75] J. I. Collar and F. T. Avignone. Effect of elastic scattering in the Earth on cold dark matter experiments. *Phys. Rev. D*, 47:5238–5246, Jun 1993.

[76] R. Bernabei et al. Model independent result on possible diurnal effect in DAMA/LIBRA-phase1. *The European Physical Journal C*, 74(3):2827, Mar 2014.

[77] J. Clarke and R. Foot. Plasma dark matter direct detection. *Journal of Cosmology and Astroparticle Physics*, 2016(01):029–029, Jan 2016.

[78] D. S. Akerib et al. First direct detection constraint on mirror dark matter kinetic mixing using LUX 2013 data. 2019.

[79] J. W. Moffat. Scalar–tensor–vector gravity theory. *Journal of Cosmology and Astroparticle Physics*, 2006(03):004–004, Mar 2006.

[80] M. Milgrom. A Modification of the Newtonian dynamics as a possible alternative to the hidden mass hypothesis. *Astrophys. J.*, 270:365–370, 1983.

[81] J. D. Bekenstein. Relativistic gravitation theory for the modified Newtonian dynamics paradigm. *Phys. Rev. D*, 70:083509, Oct 2004.

[82] I. Ferreras et al. Confronting MOND and TeVeS with strong gravitational lensing over galactic scales: An extended survey. *Phys. Rev. D*, 86:083507, Oct 2012.

[83] Tisserand, P. et al. Limits on the MACHO content of the Galactic Halo from the EROS-2 Survey of the Magellanic Clouds. *A&A*, 469(2):387–404, 2007.

[84] G. Jungman et al. Supersymmetric dark matter. *Phys. Rept.*, 267:195–373, 1996.

[85] M. Byrne et al. Bounds on charged, stable superpartners from cosmic ray production. *Phys. Rev. D*, 66:075007, Oct 2002.

[86] P. Smith et al. A search for anomalous hydrogen in enriched D2O, using a time-of-flight spectrometer. *Nuclear Physics B*, 206(3):333 – 348, 1982.

[87] T. Falk et al. Heavy sneutrinos as dark matter. *Physics Letters B*, 339(3):248 – 251, 1994.

[88] C. Arina and N. Fornengo. Sneutrino cold dark matter, a new analysis: Relic abundance and detection rates. *JHEP*, 11:029, 2007.

[89] M. Peiro and S. Robles. Low-mass neutralino dark matter in supergravity

scenarios: phenomenology and naturalness. *JCAP*, 1705(05):010, 2017.

[90] O. Klein. Quantentheorie und fünfdimensionale relativitätstheorie. *Zeitschrift für Physik*, 37(12):895–906, Dec 1926.

[91] T. Appelquist et al. Bounds on universal extra dimensions. *Phys. Rev.*, D64:035002, 2001.

[92] G. Servant and T. M. P. Tait. Is the lightest Kaluza-Klein particle a viable dark matter candidate? *Nucl. Phys.*, B650:391–419, 2003.

[93] H.-C. Cheng et al. Kaluza-Klein dark matter. *Phys. Rev. Lett.*, 89:211301, 2002.

[94] G. Gelmini and P. Gondolo. DM Production Mechanisms. pp. 121–141, 2010.

[95] D. S. Akerib et al. First Results from the LUX Dark Matter Experiment at the Sanford Underground Research Facility. *Phys. Rev. Lett.*, 112(9):091303, March 2014.

[96] D. S. Akerib et al. Results from a Search for Dark Matter in the Complete LUX Exposure. *Phys. Rev. Lett.*, 118(2):021303, January 2017.

[97] E. Aprile et al. Dark Matter Results from 225 Live Days of XENON100 Data. *Phys. Rev. Lett.*, 109:181301, Nov 2012.

[98] J. L. Feng and J. Kumar. Dark-Matter Particles without Weak-Scale Masses or Weak Interactions. *Phys. Rev. Lett.*, 101(23):231301, December 2008.

[99] H. Baer et al. Dark matter production in the early Universe: beyond the thermal WIMP paradigm. *Phys. Rept.*, 555:1–60, 2015.

[100] J. Preskill et al. Cosmology of the invisible axion. *Physics Letters B*, 120(1):127 – 132, 1983.

[101] L. Abbott and P. Sikivie. A cosmological bound on the invisible axion. *Physics Letters B*, 120(1):133 – 136, 1983.

[102] M. Dine and W. Fischler. The not-so-harmless axion. *Physics Letters B*, 120(1):137 – 141, 1983.

[103] P. Arias et al. WISPy cold dark matter. *Journal of Cosmology and Astroparticle Physics*, 2012(06):013–013, Jun 2012.

[104] N. Cabibbo. *Elementary Particles*. Enrico Fermi International School of Physics. Elsevier Science, 1987.

[105] G. Alonso-Álvarez and J. Jaeckel. Exploring ALPs beyond the canonical. *arXiv*

e-prints, pp. arXiv:1712.07500, December 2017.

[106] A. E. Nelson and J. Scholtz. Dark light, dark matter, and the misalignment mechanism. *Phys. Rev. D*, 84:103501, Nov 2011.

[107] R. D. Peccei. QCD, strong CP and axions. *J. Korean Phys. Soc.*, 29:S199–S208, 1996.

[108] Y. Chikashige et al. Are there real goldstone bosons associated with broken lepton number? *Physics Letters B*, 98(4):265 – 268, 1981.

[109] F. Wilczek. Axions and Family Symmetry Breaking. *Phys. Rev. Lett.*, 49:1549–1552, Nov 1982.

[110] J. E. Kim. Light pseudoscalars, particle physics and cosmology. *Physics Reports*, 150(1):1 – 177, 1987.

[111] M. B. Green et al. *Superstring Theory: 25th Anniversary Edition*, volume 2 of *Cambridge Monographs on Mathematical Physics*. Cambridge University Press, 2012.

[112] J. Jaeckel and A. Ringwald. The Low-Energy Frontier of Particle Physics. *Annual Review of Nuclear and Particle Science*, 60(1):405–437, 2010.

[113] M. Cicoli et al. The type IIB string axiverse and its low-energy phenomenology. *Journal of High Energy Physics*, 2012(10):146, Oct 2012.

[114] P. Sikivie. *Axion Cosmology*, pp. 19–50. Springer Berlin Heidelberg, Berlin, Heidelberg, 2008.

[115] G. G. Raffelt. Axions: Motivation, limits and searches. *J. Phys.*, A40:6607–6620, 2007.

[116] D. Aloni et al. Coupling QCD-scale axion-like particles to gluons. *Phys. Rev. Lett.*, 123:031803, 2019.

[117] M. Bauer et al. Collider probes of axion-like particles. *Journal of High Energy Physics*, 2017(12):44, December 2017.

[118] M. J. Dolan et al. A taste of dark matter: flavour constraints on pseudoscalar mediators. *Journal of High Energy Physics*, 2015(3):171, Mar 2015.

[119] E. Izaguirre et al. Searching for Axionlike Particles in Flavor-Changing Neutral Current Processes. *Phys. Rev. Lett.*, 118(11):111802, 2017.

[120] H. Fukuda et al. Model of visible QCD axion. *Phys. Rev. D*, 92:015021, Jul 2015.

[121] K. Mimasu and V. Sanz. ALPs at colliders. *Journal of High Energy Physics*, 2015:173, June 2015.

[122] Search for new light resonances decaying to jet pairs and produced in association with a photon or a jet in proton-proton collisions at $\sqrt{s} = 13$ TeV with the ATLAS detector. Technical Report ATLAS-CONF-2016-070, CERN, Geneva, Aug 2016.

[123] C. Abel et al. Search for Axionlike Dark Matter through Nuclear Spin Precession in Electric and Magnetic Fields. *Phys. Rev. X*, 7:041034, Nov 2017.

[124] G. G. Raffelt. Astrophysical axion bounds. *Lect. Notes Phys.*, 741:51–71, 2008. 51(2006).

[125] G. Raffelt and L. Stodolsky. Mixing of the photon with low-mass particles. *Phys. Rev. D*, 37:1237–1249, Mar 1988.

[126] H. Primakoff. Photo-Production of Neutral Mesons in Nuclear Electric Fields and the Mean Life of the Neutral Meson. *Phys. Rev.*, 81:899–899, Mar 1951.

[127] J. M. Overduin and P. S. Wesson. Dark matter and background light. *Phys. Rept.*, 402:267–406, 2004.

[128] S. Andriamonje et al. An Improved limit on the axion-photon coupling from the CAST experiment. *JCAP*, 0704:010, 2007.

[129] E. Arik et al. Probing eV-scale axions with CAST. *JCAP*, 0902:008, 2009.

[130] Y. Inoue et al. Search for solar axions with mass around 1 eV using coherent conversion of axions into photons. *Phys. Lett.*, B668:93–97, 2008.

[131] J. Redondo and A. Ringwald. Light shining through walls. *Contemp. Phys.*, 52:211–236, 2011.

[132] R. Bähre et al. Any Light Particle Search II — Technical Design Report. *Journal of Instrumentation*, 8(09):T09001–T09001, Sep 2013.

[133] P. Sikivie. Experimental Tests of the Invisible Axion. *Phys. Rev. Lett.*, 51:1415–1417, Oct 1983.

[134] G. G. Raffelt. Astrophysical axion bounds diminished by screening effects. *Phys. Rev. D*, 33:897–909, Feb 1986.

[135] G. G. Raffelt. *Stars as laboratories for fundamental physics*. 1996.

[136] J. Redondo. Solar axion flux from the axion-electron coupling. *JCAP*, 1312:008, 2013.

[137] M. Dine et al. A simple solution to the strong CP problem with a harmless axion. *Physics Letters B*, 104(3):199 – 202, 1981.

[138] J. E. Kim. Weak-Interaction Singlet and Strong CP Invariance. *Phys. Rev. Lett.*, 43:103–107, Jul 1979.

[139] N. Viaux et al. Neutrino and axion bounds from the globular cluster M5 (NGC 5904). *Phys. Rev. Lett.*, 111:231301, 2013.

[140] M. Giannotti et al. Stellar Recipes for Axion Hunters. *JCAP*, 1710(10):010, 2017.

[141] M. Goodsell et al. Naturally Light Hidden Photons in Large Volume String Compactifications. *JHEP*, 11:027, 2009.

[142] M. Ahlers et al. Probing hidden sector photons through the Higgs window. *Phys. Rev. D*, 78:075005, Oct 2008.

[143] M. Cicoli et al. Testing string vacua in the lab: from a hidden CMB to dark forces in flux compactifications. *Journal of High Energy Physics*, 2011(7):114, Jul 2011.

[144] B. Patt and F. Wilczek. Higgs-field portal into hidden sectors. 2006.

[145] J. Redondo. Atlas of solar hidden photon emission. *JCAP*, 1507(07):024, 2015.

[146] H. An et al. Direct detection constraints on dark photon dark matter. *Physics Letters B*, 747:331 – 338, 2015.

[147] L. B. Okun. Limits Of Electrodynamics: Paraphotons? *Sov. Phys. JETP*, 56:502, 1982. [Zh. Eksp. Teor. Fiz.83,892(1982)].

[148] B. Holdom. Two U(1)'s and Epsilon Charge Shifts. *Phys. Lett.*, 166B:196–198, 1986.

[149] S. A. Abel et al. Kinetic Mixing of the Photon with Hidden U(1)s in String Phenomenology. *JHEP*, 07:124, 2008.

[150] K. Schmitz and S. und frühes Universum Hamburg Germany Teilchen. Kinetic Mixing in Field Theory. 07 2019.

[151] F. Brummer and J. Jaeckel. Minicharges and Magnetic Monopoles. *Phys. Lett.*, B675:360–364, 2009.

[152] K. R. Dienes et al. Kinetic mixing and the supersymmetric gauge hierarchy. *Nucl. Phys.*, B492:104–118, 1997.

[153] M. Pospelov et al. Secluded WIMP Dark Matter. *Phys. Lett.*, B662:53–61, 2008.

[154] A. M. Sirunyan et al. A search for pair production of new light bosons decaying

into muons in proton-proton collisions at 13 TeV. *Phys. Lett. B*, 796:131–154, 2019.

[155] A. Mirizzi et al. Microwave Background Constraints on Mixing of Photons with Hidden Photons. *JCAP*, 0903:026, 2009.

[156] ATLAS Collaboration. Search for long-lived neutral particles decaying into lepton jets in proton–proton collisions at $\sqrt{s} = 8$ TeV with the ATLAS detector. *arXiv e-prints*, pp. arXiv:1409.0746, September 2014.

[157] A. Belyaev et al. Lhc discovery potential of the lightest nmssm higgs boson in the $h_1 \to a_1 a_1 \to 4\mu$ channel. *Phys. Rev. D*, 81:075021, Apr 2010.

[158] T. Lin. Dark matter models and direct detection. *PoS*, 333:009, 2019.

[159] E. Aprile and T. Doke. Liquid Xenon Detectors for Particle Physics and Astrophysics. *Rev. Mod. Phys.*, 82:2053–2097, 2010.

[160] J. A. Northrop et al. Further Work with Noble Element Scintillators. *IRE Transactions on Nuclear Science*, 5(3):81–87, Dec 1958.

[161] W. H. Lippincott et al. Scintillation yield and time dependence from electronic and nuclear recoils in liquid neon. *Phys. Rev.*, C86:015807, 2012.

[162] *Technology of Noble Gas Detectors*, chapter 8, pp. 239–276. John Wiley and Sons, Ltd, 2006.

[163] A. Gando and e. a. Gando. *Phys. Rev. Lett.*, 122:192501, May 2019.

[164] A. Gando et al. *Phys. Rev. C*, 85:045504, Apr 2012.

[165] V. Chepel and H. Araujo. Liquid noble gas detectors for low energy particle physics. *JINST*, 8:R04001, 2013.

[166] G. Alner et al. First limits on nuclear recoil events from the ZEPLIN I galactic dark matter detector. *Astroparticle Physics*, 23(5):444 – 462, 2005.

[167] T. Doke et al. Absolute Scintillation Yields in Liquid Argon and Xenon for Various Particles. *Jap. J. Appl. Phys.*, 41:1538–1545, 2002.

[168] C. E. Dahl. *The physics of background discrimination in liquid xenon, and first results from XENON10 in the hunt for WIMP dark matter*. PhD thesis, Princeton U., 2009.

[169] M. S. J. Lindhard, V. Nielsen and P. Thomsen. *Mat. Fys. Medd. Dan. Vid. Selsk.*, 33, 1963.

[170] A. Hitachi. Properties of liquid xenon scintillation for dark matter searches. *Astroparticle Physics*, 24(3):247 – 256, 2005.

[171] J. B. Birks and F. A. Black. Deterioration of Anthracene under Particle Irradiation. *Proceedings of the Physical Society. Section A*, 64(5):511–512, May 1951.

[172] A. Manzur et al. Scintillation efficiency and ionization yield of liquid xenon for mono-energetic nuclear recoils down to 4 keV. *Phys. Rev.*, C81:025808, 2010.

[173] E. Aprile et al. Simultaneous Measurement of Ionization and Scintillation from Nuclear Recoils in Liquid Xenon for a Dark Matter Experiment. *Phys. Rev. Lett.*, 97:081302, Aug 2006.

[174] D. Akerib et al. The Large Underground Xenon (LUX) experiment. *Nuclear Instruments and Methods in Physics Research Section A: Accelerators, Spectrometers, Detectors and Associated Equipment*, 704:111 – 126, 2013.

[175] V. N. Lebedenko et al. Results from the first science run of the ZEPLIN-III dark matter search experiment. *Phys. Rev. D*, 80:052010, Sep 2009.

[176] D. Akimov et al. The ZEPLIN-III dark matter detector: Instrument design, manufacture and commissioning. *Astroparticle Physics*, 27(1):46 – 60, 2007.

[177] D. Akerib et al. Identification of radiopure titanium for the LZ dark matter experiment and future rare event searches. *Astroparticle Physics*, 96:1 – 10, 2017.

[178] H. Araujo. A Xenon Detector For The LZ Experiment. In *LIDNE-2019*, Manchester, Aug 2019.

[179] D. S. Akerib et al. An Ultra-Low Background PMT for Liquid Xenon Detectors. *Nucl. Instrum. Meth.*, A703:1–6, 2013.

[180] B. J. Mount et al. LUX-ZEPLIN (LZ) Technical Design Report. 2017.

[181] D. S. Leonard et al. A simple high-sensitivity technique for purity analysis of xenon gas. *Nuclear Instruments and Methods in Physics Research A*, 621(1-3):678–684, Sep 2010.

[182] R. Bernabei et al. First Model Independent Results from DAMA/LIBRA–Phase 2. *Universe*, 4(11):116, 2018. [Nucl. Phys. Atom. Energy19,no.4,307(2018)].

[183] E. Aprile et al. Search for Electronic Recoil Event Rate Modulation with 4 Years of XENON100 Data. *Phys. Rev. Lett.*, 118:101101, Mar 2017.

[184] K. Abe et al. Direct dark matter search by annual modulation in XMASS-I.

Physics Letters B, 759:272 – 276, 2016.

[185] D. S. Akerib et al. Search for annual and diurnal rate modulations in the LUX experiment. *Phys. Rev. D*, 98:062005, Sep 2018.

[186] J. Amaré et al. First Results on Dark Matter Annual Modulation from the ANAIS-112 Experiment. *Phys. Rev. Lett.*, 123(3):031301, 2019.

[187] J. Amaré et al. ANAIS-112 status: two years results on annual modulation. *arXiv e-prints*, pp. arXiv:1910.13365, October 2019.

[188] H. S. Lee et al. Search for low-mass dark matter with csi(tl) crystal detectors. *Phys. Rev. D*, 90:052006, Sep 2014.

[189] C. E. Aalseth et al. Search for An Annual Modulation in Three Years of CoGeNT Dark Matter Detector Data. 2014.

[190] G. K. Giovanetti et al. A Dark Matter Search with MALBEK. *Phys. Procedia*, 61:77–84, 2015.

[191] R. Agnese et al. Improved WIMP-search reach of the CDMS II germanium data. *Phys. Rev. D*, 92:072003, Oct 2015.

[192] R. Agnese et al. Projected sensitivity of the SuperCDMS SNOLAB experiment. *Phys. Rev. D*, 95:082002, Apr 2017.

[193] E. Armengaud et al. Performance of the EDELWEISS-III experiment for direct dark matter searches. *Journal of Instrumentation*, 12(08):P08010–P08010, aug 2017.

[194] F. Petricca et al. First results on low-mass dark matter from the CRESST-III experiment. In *15th International Conference on Topics in Astroparticle and Underground Physics (TAUP 2017) Sudbury, Ontario, Canada, July 24-28, 2017*, 2017.

[195] C. Amole et al. Dark Matter Search Results from the PICO−60 C_3F_8 Bubble Chamber. *Phys. Rev. Lett.*, 118:251301, Jun 2017.

[196] M. G. B. and. DEAP-3600 Dark Matter Search at SNOLAB. *Journal of Physics: Conference Series*, 375(1):012027, Jul 2012.

[197] J.-J. Wang. MiniCLEAN Dark Matter Experiment. 2017.

[198] K. Abe et al. XMASS detector. *Nucl. Instrum. Meth.*, A716:78–85, 2013.

[199] J. B. R. Battat et al. First background-free limit from a directional dark matter experiment: results from a fully fiducialised DRIFT detector. *Phys. Dark Univ.*,

9-10:1–7, 2015.

[200] F. Stoehr et al. Dark matter annihilation in the halo of the Milky Way. *Mon. Not. Roy. Astron. Soc.*, 345:1313, 2003.

[201] D. Merritt. Dark matter at the centres of galaxies. pp. 83–98, 2010.

[202] V. Vitale et al. Indirect Search for Dark Matter from the center of the Milky Way with the Fermi-Large Area Telescope. *arXiv e-prints*, pp. arXiv:0912.3828, Dec 2009.

[203] F. Acero et al. Localizing the VHE gamma-ray source at the Galactic Centre. *Mon. Not. Roy. Astron. Soc.*, 402(3):1877–1882, Mar 2010.

[204] T. Bringmann et al. Dark Matter signals from Draco and Willman 1: Prospects for MAGIC II and CTA. *JCAP*, 0901:016, 2009.

[205] L. Pieri et al. Could the Fermi-LAT detect gamma-rays from dark matter annihilation in the dwarf galaxies of the Local Group? *Astron. Astrophys.*, 496:351, 2009.

[206] G. D. Martinez et al. Indirect Dark Matter Detection from Dwarf Satellites: Joint Expectations from Astrophysics and Supersymmetry. *JCAP*, 0906:014, 2009.

[207] M. Ackermann et al. Searching for Dark Matter Annihilation from Milky Way Dwarf Spheroidal Galaxies with Six Years of Fermi Large Area Telescope Data. *Phys. Rev. Lett.*, 115(23):231301, 2015.

[208] L. Bergstrom et al. New Limits on Dark Matter Annihilation from Alpha Magnetic Spectrometer Cosmic Ray Positron Data. *Phys. Rev. Lett.*, 111:171101, Oct 2013.

[209] G. Giesen et al. AMS-02 antiprotons, at last! Secondary astrophysical component and immediate implications for Dark Matter. *JCAP*, 1509(09):023, 2015.

[210] J. Aleksić et al. Optimized dark matter searches in deep observations of Segue 1 with MAGIC. *Journal of Cosmology and Astroparticle Physics*, 2014(02):008–008, Feb 2014.

[211] H. Abdallah et al. Search for Dark Matter Annihilations towards the Inner Galactic Halo from 10 Years of Observations with H.E.S.S. *Phys. Rev. Lett.*, 117:111301, Sep 2016.

[212] M. L. Ahnen et al. Limits to Dark Matter Annihilation Cross-Section from a Combined Analysis of MAGIC and Fermi-LAT Observations of Dwarf Satellite Galaxies. *JCAP*, 1602(02):039, 2016.

[213] E. Bulbul et al. DETECTION OF AN UNIDENTIFIED EMISSION LINE IN THE STACKED x-RAY SPECTRUM OF GALAXY CLUSTERS. *The Astrophysical Journal*, 789(1):13, jun 2014.

[214] A. Boyarsky et al. Unidentified Line in X-Ray Spectra of the Andromeda Galaxy and Perseus Galaxy Cluster. *Phys. Rev. Lett.*, 113:251301, 2014.

[215] P. D. Alvarez et al. Observational consistency and future predictions for a 3.5 keV ALP to photon line. *Journal of Cosmology and Astroparticle Physics*, 2015(04):013–013, apr 2015.

[216] M. Cicoli et al. 3.55 keV photon line and its morphology from a 3.55 keV axionlike particle line. *Phys. Rev. D*, 90:023540, 2014.

[217] C. Dessert et al. The dark matter interpretation of the 3.5-kev line is inconsistent with blank-sky observations. *Science*, 367(6485), 3 2020.

[218] A. Boyarsky et al. Technical comment on the paper of Dessert et al. "The dark matter interpretation of the 3.5 keV line is inconsistent with blank-sky observations". 4 2020.

[219] C. S. Reynolds et al. Astrophysical limits on very light axion-like particles from Chandra grating spectroscopy of NGC 1275. 7 2019.

[220] N. Trevisani. Collider searches for dark matter (ATLAS + CMS). *Universe*, 4:131, 11 2018.

[221] G. Busoni et al. Recommendations on presenting LHC searches for missing transverse energy signals using simplified s-channel models of dark matter. 2016.

[222] R. Sekhar Chivukula et al. Distinguishing dijet resonances at the LHC. *Phys. Rev.*, D91(5):055019, 2015.

[223] Search for new phenomena in dijet events using 37 fb-1 of pp collision data collected at s =13 tev with the ATLAS detector. *Physical Review D - Particles, Fields, Gravitation and Cosmology*, 96(5), 2017. Export Date: 30 October 2017.

[224] M. Aaboud et al. Search for new high-mass phenomena in the dilepton final state using 36 fb^{-1} of proton-proton collision data at $\sqrt{s} = 13$ TeV with the ATLAS detector. *JHEP*, 10:182, 2017.

[225] D. S. Akerib et al. LUX-ZEPLIN (LZ) Conceptual Design Report. 2015.

[226] L. de Viveiros. PhD thesis, Brown University, May 2010.

[227] S. Li et al. Performance of Photosensors in the PandaX-I Experiment. *JINST*,

11(02):T02005, 2016.

[228] Hamamatsu. Photomultiplier tube r8520-406/r8520-506, 2019.

[229] Hamamatsu. Photomultiplier tubes and assemblies for scintillation counting and high energy physics. `https://www.hamamatsu.com/resources/pdf/etd/High_energy_PMT_TPMZ0003E.pdf`, 2017.

[230] E. Aprile et al. Measurement of the quantum efficiency of Hamamatsu R8520 photomultipliers at liquid xenon temperature. *Journal of Instrumentation*, 7(10):P10005, Oct 2012.

[231] B. López Paredes et al. Response of photomultiplier tubes to xenon scintillation light. *Astropart. Phys.*, 102:56–66, 2018.

[232] D. S. Akerib et al. Calibration, event reconstruction, data analysis, and limit calculation for the LUX dark matter experiment. *Phys. Rev.*, D97(10):102008, 2018.

[233] N. Krybus. *General aspects of calibration of the Muenster dual phase xenon TPC*. PhD thesis, The University of Munster, Oct 2016.

[234] G. A. Morton et al. Afterpulses in Photomultipliers. *IEEE Transactions on Nuclear Science*, 14(1):443–448, Feb 1967.

[235] B.-L. Young. A survey of dark matter and related topics in cosmology. *Frontiers of Physics*, 12(2):121201, Oct 2016.

[236] N. Abgrall et al. Muon flux measurements at the Davis campus of the Sanford Underground Research Facility with the MAJORANA Demonstrator veto system. *Astroparticle Physics*, 93:70 – 75, 2017.

[237] D.-M. Mei and A. Hime. Muon-induced background study for underground laboratories. *Phys. Rev. D*, 73:053004, Mar 2006.

[238] V. A. Kudryavtsev. Muon simulation codes MUSIC and MUSUN for underground physics. *Comput. Phys. Commun.*, 180:339–346, 2009.

[239] D. S. Akerib et al. Ultralow energy calibration of LUX detector using ^{127}Xe electron capture. *Phys. Rev. D*, 96:112011, Dec 2017.

[240] D. S. Akerib et al. Measurement of the Gamma Ray Background in the Davis Cavern at the Sanford Underground Research Facility. 2019.

[241] E. H. Miller et al. Constraining Radon Backgrounds in LZ. *AIP Conf. Proc.*, 1921(1):050003, 2018.

[242] N. Ackerman et al. *Phys. Rev. Lett.*, 107:212501, 2011.

[243] A. Gando et al. *Phys. Rev.*, C85:045504, 2012.

[244] M. Agostini et al. Comprehensive measurement of PP-chain solar neutrinos. *Nature*, 562:505–510, 10 2018.

[245] R. F. Lang et al. Supernova neutrino physics with xenon dark matter detectors: A timely perspective. *Phys. Rev.*, D94(10):103009, 2016.

[246] N. Grevesse and A. Sauval. Standard solar composition. *Space Science Reviews*, 85(1):161–174, May 1998.

[247] M. Asplund et al. The Chemical Composition of the Sun. *Annual Review of Astronomy and Astrophysics*, 47(1):481–522, 2009.

[248] W. Haxton et al. Solar Neutrinos: Status and Prospects. *Annual Review of Astronomy and Astrophysics*, 51, 08 2012.

[249] N. Tolich. Final results from SNO. *J. Phys. Conf. Ser.*, 375:042049, 2012.

[250] J. N. Bahcall. Neutrino - Electron Scattering and Solar Neutrino Experiments. *Rev. Mod. Phys.*, 59:505, 1987.

[251] J. N. Bahcall and B. R. Holstein. Solar neutrinos from the decay of ^{8}B. *Phys. Rev. C*, 33:2121–2127, Jun 1986.

[252] J. N. Bahcall and R. K. Ulrich. Solar models, neutrino experiments, and helioseismology. *Rev. Mod. Phys.*, 60:297–372, Apr 1988.

[253] K. A. Kouzakov and A. I. Studenikin. Theory of neutrino-atom collisions: the history, present status and BSM physics. *Adv. High Energy Phys.*, 2014:569409, 2014.

[254] J. A. Formaggio and G. P. Zeller. From eV to EeV: Neutrino cross sections across energy scales. *Rev. Mod. Phys.*, 84:1307–1341, Sep 2012.

[255] E. D. Commins and P. H. Bucksbaum. *Weak Interactions of Leptons and Quarks*. 1983.

[256] C. Andreopoulos. Experimental study of the phenomenon of neutrino oscillations with the MINOS experiment. 6 2003.

[257] B. Pontecorvo. Neutrino Experiments and the Problem of Conservation of Leptonic Charge. *Sov. Phys. JETP*, 26:984–988, 1968. [Zh. Eksp. Teor. Fiz.53,1717(1967)].

[258] Z. Maki et al. Remarks on the Unified Model of Elementary Particles. *Progress of Theoretical Physics*, 28(5):870–880, 1962.

[259] J. C.-D. et al. The Current State of Solar Modeling. *Science*, 272:1286–1292, 1996.

[260] J. N. Bahcall et al. Solar Models: Current Epoch and Time Dependences, Neutrinos, and Helioseismological Properties. *The Astrophysical Journal*, 555(2):990, 2001.

[261] J. N. Bahcall and C. Peña-Garay. Solar models and solar neutrino oscillations. *New Journal of Physics*, 6:63–63, Jun 2004.

[262] K. Abe et al. Solar neutrino measurements in Super-Kamiokande-IV. *Phys. Rev. D*, 94:052010, Sep 2016.

[263] V. I. Kopeikin et al. Scattering of reactor antineutrinos by electrons. *Physics of Atomic Nuclei*, 60(11):1859–1864, Nov 1997.

[264] J.-W. Chen et al. Atomic ionization of germanium by neutrinos from an ab initio approach. *Physics Letters B*, 731:159 – 162, 2014.

[265] J.-W. Chen et al. Constraints on millicharged neutrinos via analysis of data from atomic ionizations with germanium detectors at sub-keV sensitivities. *Phys. Rev. D*, 90:011301, Jul 2014.

[266] J.-W. Chen et al. Constraining neutrino electromagnetic properties by germanium detectors. *Phys. Rev. D*, 91:013005, Jan 2015.

[267] J.-W. Chen et al. Ionization of hydrogen by neutrino magnetic moment, relativistic muon, and WIMP. *Phys. Rev. D*, 88:033006, Aug 2013.

[268] V. Yu. Dobretsov et al. Inelastic neutrino scattering by atomic electrons. *Sov. J. Nucl. Phys.*, 55:1180–1186, 1992. [Yad. Fiz.55,2126(1992)].

[269] S. Fayans et al. Effect of atomic binding on inelastic νe scattering. *Physics Letters B*, 291(1):1 – 6, 1992.

[270] J.-W. Chen et al. Low-energy electronic recoil in xenon detectors by solar neutrinos. *Physics Letters B*, 774:656 – 661, 2017.

[271] L. collaboration. Neutrino task force report. Internal report, 2015.

[272] A. H. Compton. A Quantum Theory of the Scattering of X-rays by Light Elements. *Phys. Rev.*, 21:483–502, May 1923.

[273] S. Agostinelli et al. GEANT4: A Simulation toolkit. *Nucl. Instrum. Meth.*,

A506:250–303, 2003.

[274] https://www.ld-didactic.de/software/524221en/Content/Appendix/ComptonSpectrum.htm.

[275] O. Klein and Y. Nishina. Über die streuung von strahlung durch freie elektronen nach der neuen relativistischen quantendynamik von dirac. *Zeitschrift für Physik*, 52(11):853–868, Nov 1929.

[276] P. Bergstrom and R. Pratt. An overview of the theories used in Compton scattering calculations. *Radiation Physics and Chemistry*, 50(1):3 – 29, 1997. Inelastic Scattering of X-Rays and Gamma Rays.

[277] B. J. Bloch and L. B. Mendelsohn. Atomic L-shell Compton profiles and incoherent scattering factors: Theory. *Phys. Rev. A*, 9:129–155, Jan 1974.

[278] J. H. Hubbell et al. Atomic form factors, incoherent scattering functions, and photon scattering cross sections. *Journal of Physical and Chemical Reference Data*, 4(3):471–538, 1975.

[279] s. Roy et al. An alternative method to calculate inelastic scattering cross sections of photons. *Radiation Physics and Chemistry - RADIAT PHYS CHEM*, 71:679–680, 10 2004.

[280] I. Waller et al. On the intensity of total scattering of X-rays. *Proceedings of the Royal Society of London. Series A, Containing Papers of a Mathematical and Physical Character*, 124, 1929.

[281] J. W. M. Du Mond. Compton Modified Line Structure and its Relation to the Electron Theory of Solid Bodies. *Phys. Rev.*, 33:643–658, May 1929.

[282] R. H. Pratt et al. Compton scattering revisited. *Radiation Physics and Chemistry*, 79:124–131, February 2010.

[283] B. Chatterjee et al. Investigations on Compton scattering: New directions. *Radiation Physics and Chemistry*, 75(12):2165 – 2173, 2006. New Directions in the Study of Interaction of Energetic Photons with Matter.

[284] R. Ribberfors and K. F. Berggren. Incoherent-x-ray-scattering functions and cross sections $(\frac{d\sigma}{d\Omega'})_{\text{incoh}}$ by means of a pocket calculator. *Phys. Rev. A*, 26:3325–3333, Dec 1982.

[285] R. Ribberfors. Relationship of the relativistic Compton cross section to the momentum distribution of bound electron states. *PHYSICAL REVIEW B*, 12:2067–2074, September 1975.

[286] D. Townsend, editor. *Proceedings, 2011 IEEE Nuclear Science Symposium and Medical Imaging Conference (NSS/MIC 2011)*, Piscataway, USA, 2011. IEEE, IEEE.

[287] J. Brown et al. A low energy bound atomic electron Compton scattering model for geant4. *Nuclear Instruments and Methods in Physics Research Section B: Beam Interactions with Materials and Atoms*, 338:77 – 88, 2014.

[288] R. M. Kippen. The GEANT low energy Compton scattering (GLECS) package for use in simulating advanced Compton telescopes. *New Astronomy Reviews*, 48:221–225, February 2004.

[289] D. Brusa et al. Fast sampling algorithm for the simulation of photon Compton scattering. *Nuclear Instruments and Methods in Physics Research Section A: Accelerators, Spectrometers, Detectors and Associated Equipment*, 379(1):167 – 175, 1996.

[290] F. Salvat and J. M. Fernández-Varea. Overview of physical interaction models for photon and electron transport used in Monte Carlo codes. *Metrologia*, 46(2):S112–S138, Mar 2009.

[291] PENELOPE, and algorithm and computer code for Monte Carlo simulation of electron-photon showers, Oct 1996.

[292] Y. Namito et al. Implementation of the Doppler broadening of a Compton-scattered photon into the EGS4 code. *Nuclear Instruments and Methods in Physics Research Section A: Accelerators, Spectrometers, Detectors and Associated Equipment*, 349(2):489 – 494, 1994.

[293] Z. Kaliman et al. Triply differential cross section for Compton scattering. *Physical Review A - Atomic, Molecular, and Optical Physics*, 57(4):2683–2691, 1998.

[294] G. A. P. Cirrone et al. Validation of the Geant4 electromagnetic photon cross-sections for elements and compounds. *Nucl. Instrum. Meth.*, A618:315–322, 2010.

[295] L. Pandola et al. Validation of the Geant4 simulation of bremsstrahlung from thick targets below 3 MeV. *Nucl. Instrum. Meth.*, B350:41–48, 2015.

[296] J. Allison et al. Recent developments in Geant4. *Nucl. Instrum. Meth.*, A835:186–225, 2016.

[297] D. E. Cullen et al. EPDL 97 : the Evaluated Photon Data Library , '97 Version , I by. 1997.

[298] https://www.oecd-nea.org/tools/abstract/detail/iaea1435/.

[299] S. Perkins et al. Tables and graphs of electron-interaction cross sections from 10 eV to 100 GeV derived from the LLNL Evaluated Electron Data Library (EEDL), Z = 1–100. 11 1991.

[300] S. Perkins et al. Tables and graphs of atomic subshell and relaxation data derived from the LLNL Evaluated Atomic Data Library (EADL), Z = 1–100. 10 1991.

[301] J. SCOFIELD. 6 - radiative transitions. In B. CRASEMANN, editor, *Atomic Inner-Shell Processes*, pp. 265 – 292. Academic Press, 1975.

[302] F. Biggs et al. Hartree-Fock Compton profiles for the elements. *Atomic Data and Nuclear Data Tables*, 16(3):201 – 309, 1975.

[303] D. Akerib et al. Position reconstruction in LUX. *Journal of Instrumentation*, 13(02):P02001–P02001, Feb 2018.

[304] M. Silva-Feaver et al. Design Overview of the DM Radio Pathfinder Experiment, 2016.

[305] A. Wagner et al. A Search for Hidden Sector Photons with ADMX. *Phys. Rev. Lett.*, 105:171801, 2010.

[306] L. Hoang Nguyen et al. First results from the WISPDMX radio frequency cavity searches for hidden photon dark matter. 2019.

[307] J. Suzuki et al. Experimental Search for Hidden Photon CDM in the eV mass range with a Dish Antenna. *JCAP*, 1509(09):042, 2015.

[308] E. Aprile et al. Search for bosonic super-WIMP interactions with the XENON100 experiment. *Phys. Rev. D*, 96:122002, Dec 2017.

[309] K. Abe et al. Search for dark matter in the form of hidden photons and axion-like particles in the XMASS detector. *Physics Letters B*, 787:153 – 158, 2018.

[310] S. Andreas. Hidden Photons in beam dump experiments and in connection with Dark Matter, 2012.

[311] R. Essig et al. *Journal of High Energy Physics*, 2011(2):1–35, Feb 2011.

[312] A. A. A.-A. and. Search for Dark Matter in the beam-dump of a proton beam with MiniBooNE. *Journal of Physics: Conference Series*, 912:012017, Oct 2017.

[313] D. Curtin et al. Illuminating dark photons with high-energy colliders. *Journal of High Energy Physics*, 2015(2), Feb 2015.

[314] P. Ilten et al. Dark photons from charm mesons at LHCb. *Physical Review D*, 92(11), Dec 2015.

[315] R. Essig et al. *Phys. Rev. D*, 80:015003, Jul 2009.

[316] M. Szydagis et al. Noble Element Simulation Technique v2.0, July 2018.

[317] J. Conrad. Statistical Issues in Astrophysical Searches for Particle Dark Matter. *Astropart. Phys.*, 62:165–177, 2015.

[318] G. Cowan et al. Power-Constrained Limits. 2011.

[319] E. Aprile et al. Light Dark Matter Search with Ionization Signals in XENON1T. *Phys. Rev. Lett.*, 123(25):251801, 2019.

[320] E. Armengaud et al. Searches for electron interactions induced by new physics in the EDELWEISS-III germanium bolometers. *Phys. Rev. D*, 98:082004, Oct 2018.

[321] D. S. Akerib et al. First Searches for Axions and Axion-like Particles with the LUX Experiment. *Phys. Rev. Lett.*, 118(26):261301, 2017.

[322] K. Barth et al. CAST constraints on the axion-electron coupling. *Journal of Cosmology and Astroparticle Physics*, 2013(05):010–010, May 2013.

[323] Y. Wang et al. Improved limits on solar axions and bosonic dark matter from the CDEX-1B experiment using profile likelihood ratio method. 2019.

[324] K. M. Zurek et al. Astrophysical effects of scalar dark matter miniclusters. *Phys. Rev. D*, 75:043511, Feb 2007.

[325] J. Redondo and M. Postma. Massive hidden photons as lukewarm dark matter. *JCAP*, 0902:005, 2009.

[326] H. An et al. Direct Detection Constraints on Dark Photon Dark Matter. *Phys. Lett.*, B747:331–338, 2015.

[327] J. Jaeckel et al. Signatures of a hidden cosmic microwave background. *Phys. Rev. Lett.*, 101:131801, 2008.

[328] P. W. Graham et al. Vector Dark Matter from Inflationary Fluctuations. *Phys. Rev.*, D93(10):103520, 2016.